Computational Analysis of Turbulence and Thermal Characteristics in Fluid Film Thrust Bearings

A DISSERTATION

PRESENTED TO

THE FACULTY OF THE DEPARTMENT OF MECHANICAL AND AEROSPACE ENGINEERING
OF THE SCHOOL OF ENGINEERING AND APPLIED SCIENCE

University of Virginia

IN PARTIAL FULFILLMENT
OF THE REQUIREMENTS FOR DEGREE
DOCTOR OF PHILOSOPHY

BY

XIN DENG

DECEMBER 2022

APPROVAL SHEET

THIS THESIS

IS SUBMITTED IN PARTIAL FULFILLMENT OF THE REQUIREMENTS
FOR THE DEGREE OF

DOCTOR OF PHILOSOPHY

XIN DENG

THIS DISSERTATION HAS BEEN READ AND APPROVED BY THE EXAMINING COMMITTEE

HOUSTON WOOD (ADVISOR)

CHRISTOPHER GOYNE (CHAIRMAN)

ROGER FITTRO

HAIBO DONG

ANDRES CLARENS

BAOXING XU

ACCEPTED FOR THE SCHOOL OF ENGINEERING AND APPLIED SCIENCE:

DEAN, SCHOOL OF ENGINEERING AND APPLIED SCIENCE

DECEMBER 2022

Abstract

A thrust bearing is a type of rotary bearing that permits rotation between parts and is designed to support a load parallel to the axis of rotation. The film pressure that separates the surfaces is created by the surface's relative motion (rotation) as the lubricant is dragged into the converging wedge between the surfaces. The stationary and rotating surfaces are separated by the thin film of lubricants, such as oil, air, water, or other process fluid. The main performance characteristics of a thrust bearing are film thickness, load capacity, and temperature. Demand for turbo machines to run faster and the increasing use of nontraditional, low viscosity lubricants also demand new analysis tools that properly account for their physical properties. The oil lubrication in high speed or water lubrication is challenging for traditional turbulence modeling in bearing as the high rotating speed or the low viscosity of water produces highly turbulent bearings. Due to the inherent shortcomings, the traditional zero-equation can be improved to enable better prediction accuracy and less empiricism. There is a temperature drop region with the increase in speed. However, the physics causing such temperature drop is not well understood.

A series of studies are conducted to comprehensively analyze turbulence and thermal characteristics in thrust bearings through computational analysis. The finite element model is used to model three methods of modeling wall shear stress. Then sensitivity study of the three methods is performed for water and oil lubrication. Moreover, it compared the results between those three methods. For typical turbulence models, the value of y^+ must be within a certain range to maintain accuracy. Preserved the y^+ value to make water-lubricated thrust bearing models valid and optimized parameters in the Ng-Pan turbulence model. A new mixed zero-equation and one-equation turbulence model was developed in the new thrust bearing modeling code package “ThrustX”. It is a Thermo-hydrodynamic (THD) code consisting of looping between turbulence equation, Reynolds’ equation, film energy equation, and pad & runner conduction equation. A full fluid-solid CFX model was developed for a center pivot fluid-film thrust-bearing experimental model to study the physics of temperature drop in the transitional region. A novel physics finding causing the temperature drop in the transitional region was proposed, studied, and verified. A rigid verification between the experiment, benchmark FE code, and CFX was performed. The CFX model is verified by using an experimentally measured pad temperature map and by matching the temperature drop shown in the experiment to capture the cooling effect in the transitional region. The full fluid-solid CFX model has four groove regions – inlet and outlet grooves between the pads, a groove at the inner diameter groove, and a groove at the outer diameter.

All modeling results show good agreement with the available test data. The minimum film thickness with method three excluded is consistently larger. For water-lubricated conditions, the influence of the core turbulence region is not as obvious as that for oil-lubricated conditions. Minimum film thickness shows a significantly improved fit with the cross-film element number modified from the benchmark. The proposed modified Ng-Pan turbulence model fits well with the benchmark, showing a significant improvement in fit over the original Ng-Pan model at high Reynolds number cases. The eddy viscosity from the mixed zero-equation and one-equation turbulence model is very close to Eddy Viscosity Transport (EVT) and DNS results. The turbulence model in the mixed zero-equation and one-equation turbulence model is much improved compared to Ng-Pan zero-equation. The SST turbulence model captures the temperature drop in the transitional region and produces a very different thermal picture from the laminar groove models. It is found that the turbulence in the groove is the significant factor that causes the temperature drop, rather than turbulence developing in the film, from traditional understanding. The turbulence in the groove created eddies in the flow in the groove, and such enhanced mixing and conduction in the groove, produce a nearly uniform, reduced temperature at the leading edge of the film. As the groove flow becomes increasingly turbulent, the leading-edge temperature drops due to the increased turbulence in the groove conducting more heat away, with better heat transfer to the surrounding surfaces. The study of temperature drop in the transitional region to the thrust bearing modeling can significantly improve the understanding of predicting the overall thermal performance characteristics and dynamic coefficients for fluid film lubricated thrust bearings.

Acknowledgments

After seven years of the Ph.D. program, I have quite a long list of people to thank, all of whom helped make this dissertation possible. I would first like to thank my academic advisors. My sincerest thanks to Houston Wood for serving as my academic advisor for my entire Ph.D. program and Roger Fittro for serving as part of my Ph.D. program before Roger Fittro moved on from the lab. They are always supportive and caring. Thank you to Cori Watson-Kassa for her research collaboration and background knowledge of the CFD. Thank you to Minhui He for his background knowledge of the bearing and bearing finite element software. Thank you to Robert Rockwell for his background knowledge of finite element modeling. Thank you to all those serving on my committee and to all of the Rotating Machinery and Controls Laboratory (ROMAC) companies who have helped fund this work.

There are many more people to thank in the Mechanical and Aerospace Department, School of Engineering & Applied Science, and International Studies Office. Thanks to Brian Weaver, Michael Branagan, and Harrison Gates for their collaboration when I started my Ph.D. program. Thanks to Lori Pedersen and Brenda Perkins for their assistance in my Ph.D. program. Thanks to Richard Tanson for making sure I stayed on track to graduate. Thanks to ROMAC Alumni for their help with my job search, including Feng He, Yve Zhao, Long Di (Dee), Jie Zhou, Saeid Dousti, Barry Blair, and Jianming Cao. Thanks to the many, many great graduate students who shared their knowledge with me and helped me. The following were particularly instrumental to my Ph.D. program experience - Nathaniel Gibbons, Neal Morgan, Zihao Huang, Pedro Herrera, Wisher Paudel, Ben Thomas, Pan Han, Qingchang Liu, Madeline Collins, Jeffrey Bennett, Syed Ali Asad Rizvi, Day Griffin, Thomas Gresham, Paul Gancitano, Jason Kaplan, and Brad Nichols. If I have left you out, please forgive me. You all were much appreciated.

I would never be where I am today without my family's love and support. Thank you to my best friend and the love of my life, Ran Bi. You have been by my side every step of the way and provided me with the constant love and support necessary to complete this arduous task. It will be a wonderful lifetime memory of my wedding during my Ph.D.

program. I will always miss those who came to my wedding ceremony in UVA Chapel and my wedding reception in Early Mountain Vineyards on March 15, 2018. Thank you to my father and mother for always believing in me and always being there for whatever I needed. Thank you to my father-in-law and mother-in-law for their support and patience.

Table of Contents

List of Figures

List of Tables

Nomenclature

$\mathbf{y}$	Distance from the wall [m]
$\boldsymbol{\nu}$	Kinematic viscosity [m^2 / s]
$\boldsymbol{y^+}$	Nondimensional first layer height [1]
$\boldsymbol{\delta^+}$	Dimensionless thickness of viscous sublayer [1]
$\boldsymbol{\alpha, \beta}$	Constants used in δ^+ [1]
$\boldsymbol{Rep}$	Reynolds number at pivot location [1]
$\boldsymbol{k}$	Kinetic Energy of turbulent fluctuations [kg · m^2 / s^2]
$\boldsymbol{\nu_T}$	Kinematic eddy viscosity [m^2 / s]
$\boldsymbol{t}$	Time [s]
$\boldsymbol{\tau_{ij}}$	Specific Reynolds Stress tensor
$\boldsymbol{l}$	Turbulence length scale [m]
$\boldsymbol{\sigma_k}$	Constant
$\boldsymbol{S_{ij}}$	Mean strain-rate tensor [/ s]
$\boldsymbol{\delta_{ij}}$	Kronecker delta [1]
$\boldsymbol{x, y, z}$	Cartesian coordinate [m]
$\boldsymbol{u, v, w}$	Velocity components in x, y, z directions [m / s]
$\boldsymbol{\mu}$	Dynamic molecular viscosity [Pa · s]
$\boldsymbol{\rho}$	Density [kg / m^3]
$\boldsymbol{C}$	Constant [1]
$\boldsymbol{A^+}$	Constant [1]
$\boldsymbol{h}$	Film thickness [m]
$\boldsymbol{\varepsilon_m}$	Eddy-diffusivity for momentum [m^2/s]
$\boldsymbol{\tau_w}$	Wall shear stress [Pa]
$\boldsymbol{u^+}$	Dimensionless term used in eddy-viscosity model [1]
$\boldsymbol{z^+}$	Dimensionless term used in eddy-viscosity model [1]
$\boldsymbol{\kappa}$	Von Karman constant used to define eddy-viscosity model [1]
$\boldsymbol{\tau_0}$	Shear stress at z=0 [Pa]
$\boldsymbol{r, \theta, z}$	Coordinates in cylindrical coordinate system [m, degree, m]
$\boldsymbol{u_r, u_\theta, u_z}$	Velocities in cylindrical coordinate axes [m / s]

τ_h	Shear stress at z=0 [Pa]
z_m	Point in film at which eddy-viscosity for lower wall has the same value as that of the upper wall
z^{++}	Dimensionless term used in eddy-viscosity model [1]
τ_c	Shear stress at the core of turbulent pipe flow [Pa]
μ^*	Eddy viscosity [Pa · s]
β	Transition constant [m^4 · s / N]
$\Gamma_0, \Gamma_1, \Gamma_2$	Functions in turbulent Reynolds equation definition [m^2 s / kg]
$\hat{p}$	Constant cross-film pressure [N / m^2]
ω	Rotor speed [m / s]
υ_d	Diffusion flow [mol · m^{-2} / s]
c_p	Specific heat at constant pressure [J / (kg · K)]
T	Temperature [K]
k^*	Turbulent thermal conductivity [W / (m · K)]
k	Thermal conductivity [W / (m · K)]
Q	Heat source per unit volume per unit time [W / m^3]
$\hat{y}_i$	Predicted values
y_i	Regression's dependent variable
n	Times [1]
u_*	Friction velocity at the nearest wall [m / s]
α, β	Constants used in δ^+ [1]
Re_p	Reynolds number at pivot location [1]
d^*	First layer thickness calculated for a uniform mesh [m]
u	Moving surface velocity [m / s]
Ω	Rotor angular speed [rad / s]
D	Diameter of the rotor [m]
N	Number of elements across the film [1]
H_{min}	Minimum film thickness [m]
H_{piv}	Film thickness at pivot location [m]
u_i	Mean velocity in tensor notation [m / s]

x_j	Position vector in tensor notation [m]
C_D	closure coefficient, 0.08 [1]
σ_k	Turbulence closure coefficient [1]
p	Pressure [Pa]
U	Surface speed [m / s]
C_p	Center position [m]
X_j	Journal horizontal position [m]
Y_j	Journal vertical position [m]
θ_p	Pivot angular location [degree]
J	Jacobian
N_i	Shape function
r, s, t	Local coordinate
τ	Shear stress [Pa]
μ_T	Turbulent dynamic viscosity [Pa · s]
i, j, k	Unit vectors in x, y, and z directions
K_x, K_y, K_z	Coefficients for second-order derivative term
M_x, M_y, M_z	Coefficients for first order derivative term
P	Coefficient for first order term
A, B	Coefficients for linear equation

Subscripts

oil	Oil lubrication
water	Water lubrication

Abbreviations

TEHD	Thermo-elasto-hydrodynamic
RMS	Root mean square

1. Introduction

1.1 Overview of Previous Work

1.1.1 Basic working principle in thrust bearings

Figure 1 shows a thrust bearing applied in a hydro-generator. A thrust bearing is a type of rotary bearing that permits rotation between parts and is designed to support a load parallel to the axis of rotation. A typical tilting-pad fluid film thrust bearing is shown in Figure 2 [1]. The geometry and coordinate systems for a tilting-pad, fluid-film thrust bearing are shown in Figure 3 [2]. Hydrodynamic lubrication is where a layer or wedge of lubricant supports the bearing material, and no contact is made directly between the rotating shaft and bearing surfaces. Demand for turbo machines to run faster and more efficiently under higher loads with longer maintenance cycles requires more accurate design and analysis tools to ensure their high-performance operation without unexpected failures. Likewise, the increasing use of nontraditional, low viscosity lubricants also demands new analysis tools that properly account for their physical properties.

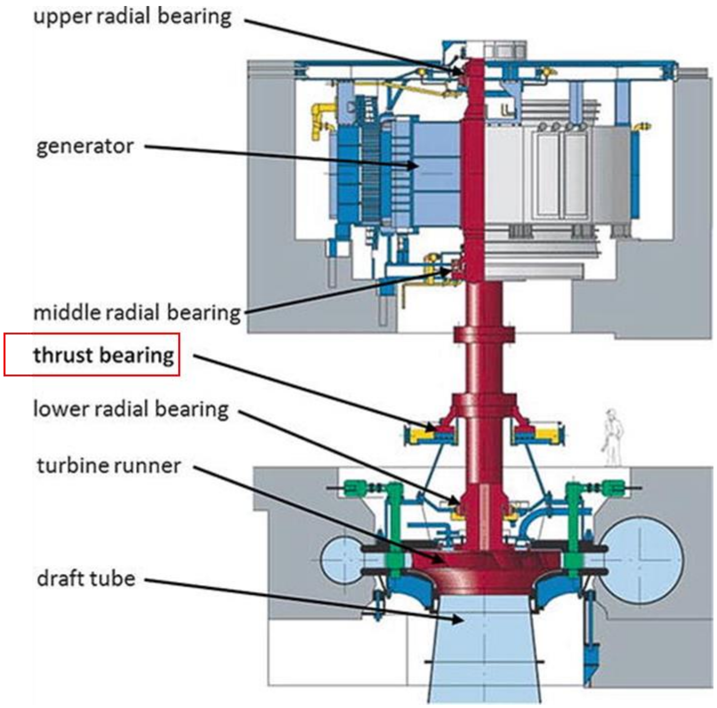

Figure 1: A typical tilting-pad fluid film thrust bearing

Figure 2: A typical tilting-pad fluid film thrust bearing [1]

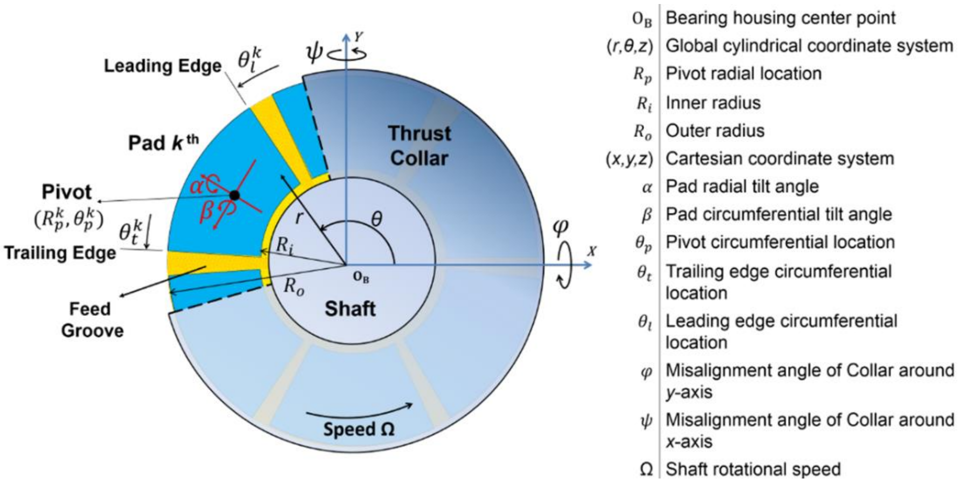

Figure 3: Geometry and coordinate system for a tilting pad thrust bearing [2]

The working principle of fluid film bearings is shown in Figure 4. A convergent wedge of fluid produces hydrodynamic lift as the fluid is dragged into the gap by viscous shearing. The stationary and rotating surfaces are separated by the thin film of lubricants, such as oil, air, water, or other process fluid. The film pressure that separates the surfaces is created by the surface's relative motion (rotation) as the lubricant is dragged into the converging wedge between the surfaces. The main performance characteristics of a thrust bearing are film thickness, load capacity, temperature, and power loss.

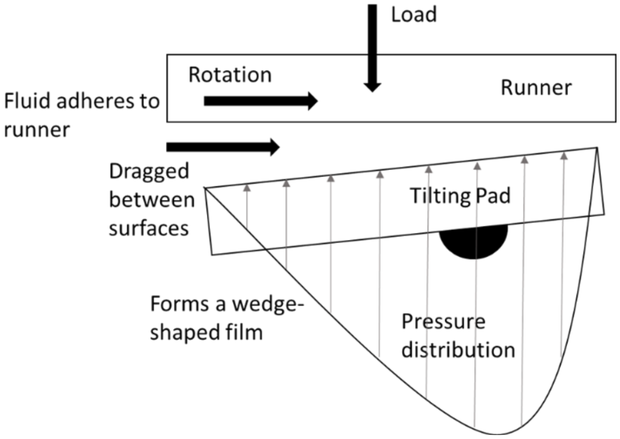

Figure 4: Working principle of fluid film thrust bearings: convergent wedge

1.1.2 Internal flow in thrust bearings

Flow in film region

Figure 5 [3] shows the velocity vectors on the axial midplane of a pad and halfway through the film thickness to show the physical flow within the thrust bearings. The velocity is circumferential mainly due to the runner's shear drag. Due to the influence of the circumferential velocity, the inlet flow is at the leading edge, and the hot oil carry-over is at the trailing edge. The velocity vectors also have radial components that cause inner and outer radius leakage. The Inner Diameter (ID) leakage (due to centrifugal pumping effects) and hot oil carry-over are internally circulated, and the net flow leaving the bearing is the Outer Diameter (OD) leakage [3].

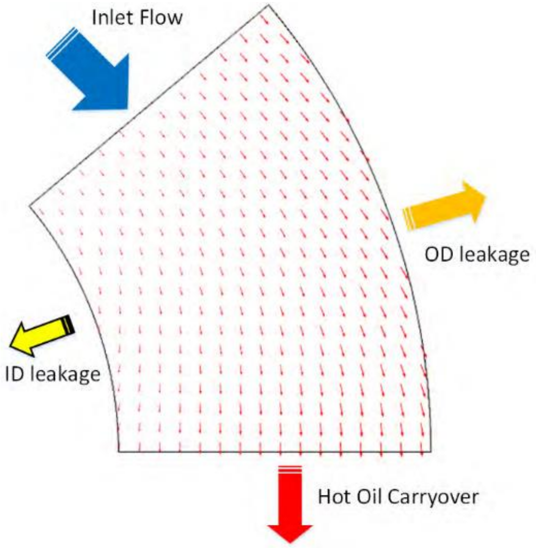

Figure 5: Velocity field on the axial mid-plane and oil flow across edges [3]

Flow in thrust bearing system

How the lubricant flows within the thrust bearing housing is crucial to a bearing's thermal performance. Figure 6 shows the flow in conventional thrust-bearing housing. Thrust bearings work in pairs in two directions [4]. If the shaft goes left, the left pad holds the load, while if the shaft goes right, the right-hand side pad holds the load. The lubricant is supplied into the bearing through radial holes behind the pads. The fluids enter the Inner diameter groove, then passes into the film between the pad and runner, and finally exit the Outer Diameter Groove (ODG) and Trailing Edge (TE) Groove, which is the Leading Edge (LE) Groove for the next pad. After the lubricant reaches the inside bearing bore, it is distributed circumferentially due to the rotating shaft, mixed with the ID leakage, and feeds the radial grooves between pads. A tangentially oriented drain hole eventually collects the exit flow on top. The numbers indicating parts are shown below: 1-Inner Diameter Groove (IDG); 2-Film; 3-Pad; 4-Runner; 5-Shaft; 6-Outer Diameter Groove (ODG); 7-Leading Edge (LE) groove; 8-Trailing Edge (TE) groove.

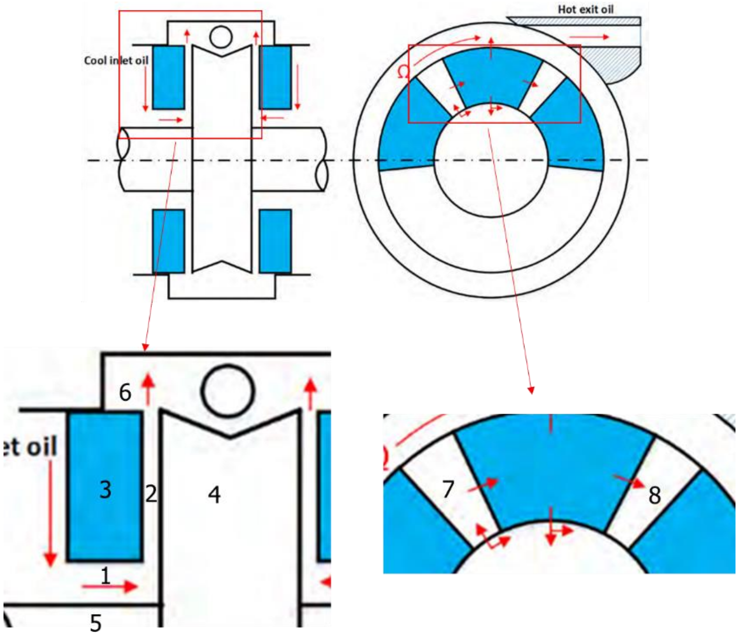

Figure 6: Flow in a conventional thrust bearing housing

Hot oil carry-over

The inaccurate leading-edge temperature is the most significant uncertainty in thrust bearings [5]. Presently, researchers have a general empirical method for understanding the process of hot oil carry-over. Existing hot oil carry-over models approximate the average leading edge temperature. However, the current hot oil carry-over models are not detailed and accurate. Therefore, researchers do not understand the groove flow in detail, which is necessary for accurate leading edge temperature predictions.

The relatively hot lubricant exiting the previous pad is called hot oil carry-over. Its mixing with supply oil is the phenomenon that makes inlet temperature less accurate [6]. In high-speed applications, temperature rather than film thickness is the limiting criterion. Figure 7 [3] schematically shows the oil flow between two pads. Lubricant entering a pad (Q_{in}) is composed of two streams: oil leaving the trailing edge of the upstream pad (Q_{out}) and oil from outside (Q_{supply}). The oil from the upstream pad is relatively hot due to internal viscous shearing. The pad temperature is greatly influenced by the temperature of the oil entering the pad, which in turn depends upon the proportion of the lubricant carried over on the collar as hot oil from the previous pad. The mean temperature of the oil entering the pad can be considerably higher than the fresh oil supplied to the bearing [7]. The quantitative distribution of trailing edge oil and fresh oil flow strongly depends on the tangible operating boundary conditions [8].

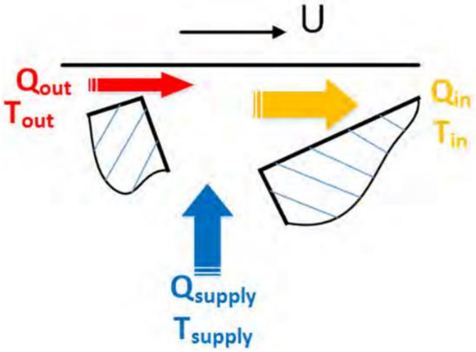

Figure 7: Flow between two pads [3]

Heshmat and Pinkus comprehensively discuss phenomena that impact the mixing process between the supplied fresh oil and the trailing edge flow of the upstream pad [9]**.** Heshmat and Pinkus [9] and Mitsui [10] use experimental data for their analyses and recommend empirical mixing factors to be applied in theoretical bearing codes. The fluid flow in the inlet cannot be described by the Reynolds equation but provides boundary conditions for its numerical solution [8]. Therefore, different researchers investigated fluid flow in the inlet region applying computational fluid dynamic (CFD) tools [11] [12] [13] [14]. The most widely used theory is Mitsui's hot oil carry-over model [10] [15]. In Mitsui's model, the groove mixing temperature is a function of flux, supply temperature, trailing edge temperature, and an empirical value of the hot oil carry-over factor. There have been other hot oil carry-over models developed in the past by Pinkus and Sternlicht [16] (1962), Neal [17] [18] [19] (1970), Ettles [6] [20] [21] (1969), Vohr [22] (1981) and Heshmat and Pinkus [9] (1986). Although these models are more complex than Mitsui's model, they require experimental data to correlate several empirical constants and, in practice, have shown no clear advantage over Mitsui's model.

Groove turbulence

Processes at the inlet region contribute to the boundary condition for the leading edge of the downstream pad. As a result, they substantially impact the lubricant film's temperature characteristic. For decades, researchers have tried to understand it and find a way to predict the groove mixing temperature. Different researchers [11] [12] [14] used computational fluid dynamic methods to study fluid flow in the inlet region in journal bearings. Hagemann [8] [13]used a conduction-convection hot oil carry-over model in a journal bearing. Yang [23] [24] [25] [26] (2019, 2021) had a severe study of journal bearings. Yang’s study included multiphase thermal flow in transitional turbulence, considering thermal deformation, with two-way fluid-structure interaction; and, stiffness and damping, and pad flexibility with the machine learning method. Grzegorz [27] simulated the lubricant flow in the leading-edge groove in a thrust bearing.

Groove turbulence affects turbulence within the film and groove mixing but was often not accounted for in legacy finite element modeling and commercial CFD modeling. This study demonstrates the utility of a groove model to remove the empiricism associated with a hot oil carry-over model in fluid film thrust bearings. The hot oil carry-over methods are predominantly empirical methods that use one value of temperature across the entire leading edge. Those hot oil carry-over models do not explicitly account for heat transfer in the groove and are, therefore, incomplete. The full fluid-solid-groove model used here includes the hot oil carry-over process in the calculation and gives an improved prediction of temperature variation across the entire film leading edge surface.

1.1.3 Turbulence: fundament

Turbulence, or eddying motion, is a local swirling motion of a fluid where the vorticity is very intense [28], as shown in Figure 8. A wide range of sizes of eddying motion appears, producing vigorous mixing momentum and effective turbulent stress. As shown in Figure 9, the larger-scale turbulent motions carry most of the energy while randomly stretching the vortex elements that comprise the smaller eddies, cascading energy to them in the form of turbulent kinetic energy. The state of a turbulent flow at a given position depends upon upstream history. As shown in Figure 10, considering turbulence’s fluctuating properties, after imagining having done a Fourier analysis of the fluctuating flow, wavelength and wavenumber [29] are introduced. With it, more mathematical methods can be applied. The energy dissipation rate is set by the long-wavelength motion, while the energy is dissipated by viscosity in the shortest wavelengths.

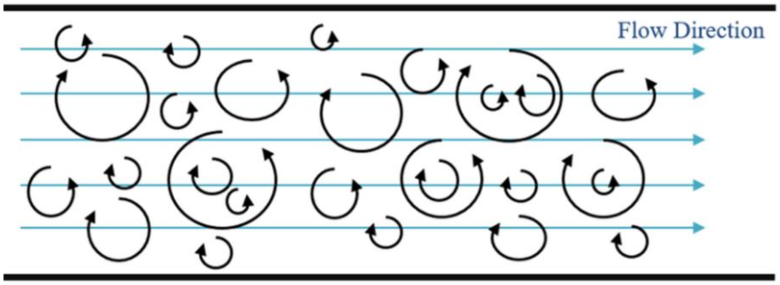

Figure 8: Turbulent eddy motion

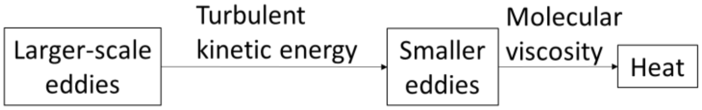

Figure 9: Turbulent eddy motion

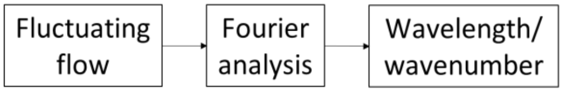

Figure 10: Turbulent spectra concept

Finding the smallest eddy scale is intuitive as it is easier to find, and it is desirable to test whether turbulence is a continuum problem. When the eddy is smaller, its motion tends to have a smaller time scale. When the eddy is small enough, the rate of larger-scale eddies supplying is equal to the rate of smaller eddies' energy dissipation. The smallest scales are called Kolmogorov scales (1941) [30], and it only depends on the rate of larger-scale eddies supplying ε and molecular viscosity ν. And the length, time, and velocity scales are $\left({\nu^3}/{\varepsilon}\right)^{1/4}$, $({\nu}/{\varepsilon})^{1/2}$, $(\nu\varepsilon)^{1/4}$. Most turbulence models use Taylor's equation (1935) $\varepsilon \sim \frac{k^{3/2}}{l}$ as a length scale. The overall development of the theoretical understanding of turbulence is depicted in Figure 11.

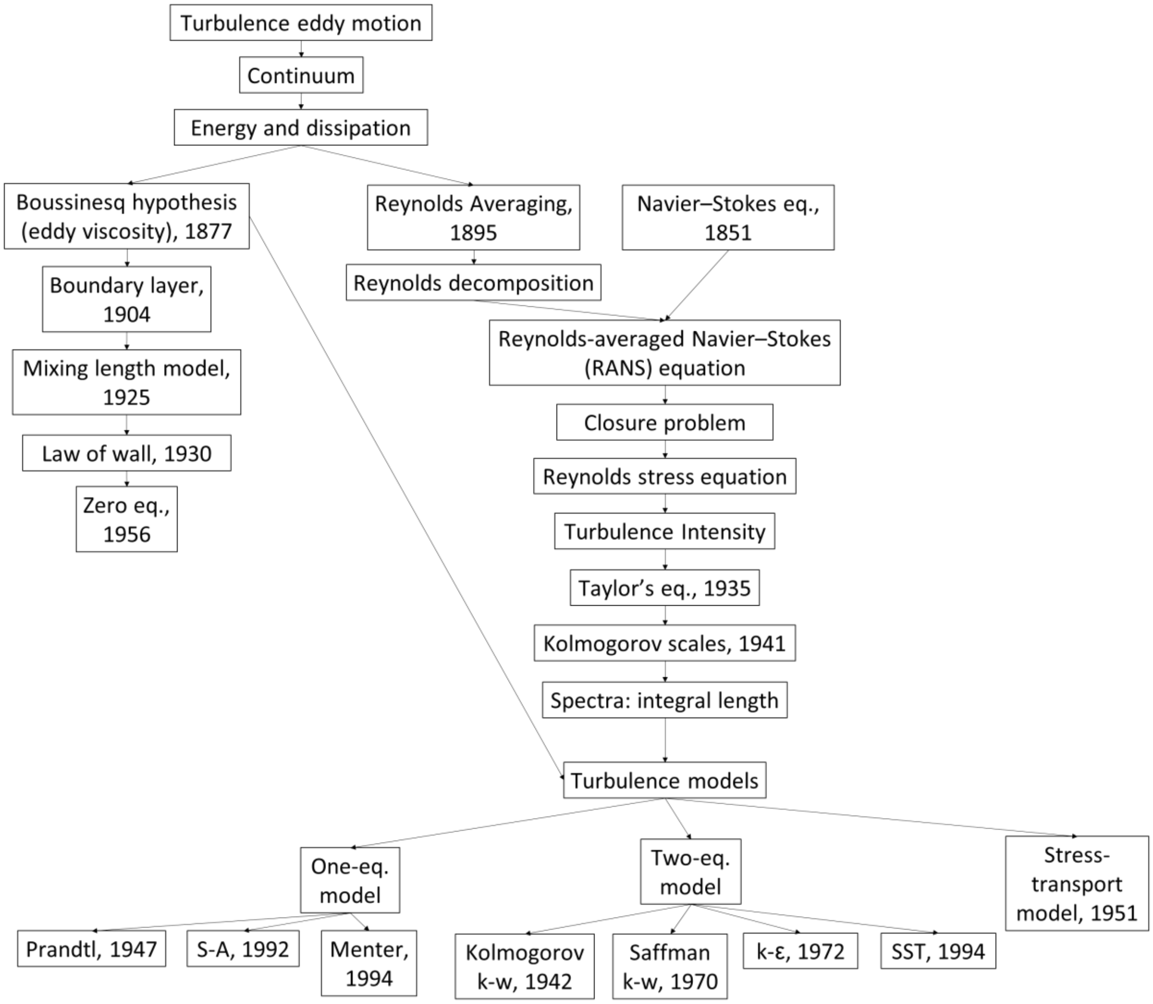

Figure 11: Development of turbulence

1.1.4 Turbulence: general modeling

Navier–Stokes (N-S) equations describe the motion of viscous fluid substances, which is fundamental to viscous flow theory. The incompressible steady flow equation is shown in Eq. 1. u is velocity, ∇ is gradient, υ is kinematic viscosity of the fluid, ∇w is the gradient of pressure over density.

$$(u \cdot \nabla)u - \nabla^2(\upsilon u) = -\nabla w \qquad \text{Eq. 1}$$

In particular to turbulence theory of Reynolds averaging (1895) [31], Reynolds decomposition is used to separate the expectation value of a quantity from its fluctuations [32]. The method is shown in Eq. 2, where the expectation $\bar{u}$ is the steady (time-averaged) component, and the fluctuation u' is the expectation value subtracted from this quantity.

There is no analytical theory to predict the evolution of turbulent flows, the random fluctuation is extremely sensitive to initial conditions, and the N-S equation can only be solved directly for simple flow cases. For most real turbulent flows, numerical simulations using turbulence models are the only way to predict the evolution of turbulence.

$$u = \bar{u} + u' \qquad \text{Eq. 2}$$

The purpose of Reynolds decomposition is to isolate slowly changing values and fluctuation values. This is the first step, and the next step is to try to remove the fluctuation terms. The Reynolds-averaged Navier–Stokes equations (RANS) is the result. RANS is the time-averaged equation of N-S eq, and it can be used with approximations based on knowledge of the properties of flow turbulence to give approximate time-averaged solutions to the N-S eq [32]. In order to achieve this, the mass conservation equation shown in Eq. 3 is also necessary. Taking N-S eq. in the x direction as an example, shown in Eq. 4, the term $\overline{u\frac{\partial u}{\partial x}}$ in N-S becomes four terms $\overline{\bar{u}\,\frac{\partial \bar{u}}{\partial x}}$, $\overline{\bar{u}\frac{\partial u'}{\partial x}}$, $\overline{u'\frac{\partial \bar{u}}{\partial x}}$, $\overline{u'\,\frac{\partial u'}{\partial x}}$. The second and third term are eliminated after time averaging, the fourth term becomes $\frac{\partial\left(\overline{u'u'}\right)}{\partial x}$ after applying mass conservation. $\overline{u'_{\imath}u'_{\jmath}}$ is a symmetric tensor, so it has six unknown quantities, plus pressure and three velocities, there are ten unknown quantities. However, there are only four equations, including one mass conversation and N-S equations in three directions. How to solve the term $\overline{u'_{\imath}u'_{\jmath}}$ is the so called "closure problem", and the term $\rho\overline{u'}\overline{u'}$ is called Reynolds stress.

$$\frac{\partial u}{\partial x} + \frac{\partial v}{\partial y} + \frac{\partial w}{\partial z} = 0 \qquad \text{Eq. 3}$$

$$\rho\left(u\frac{\partial u}{\partial x} + v\frac{\partial u}{\partial y} + w\frac{\partial u}{\partial z}\right) = -\frac{\partial p}{\partial x} + \frac{\partial}{\partial x}\left(\mu\frac{\partial u}{\partial x}\right) + \frac{\partial}{\partial y}\left(\mu\frac{\partial u}{\partial y}\right) + \frac{\partial}{\partial z}\left(\mu\frac{\partial u}{\partial z}\right) \qquad \text{Eq. 4}$$

The Reynolds stress equation is the second-moment related to answering the "closure problem". The Reynolds stress equation uses the exact Reynolds stress transport equation as the formation and is the complete classical turbulent model. The components of the Reynolds stress tensor are directly computed, accounting for the directional effects of the Reynolds stresses and the complex interactions in turbulent flows. The Reynolds stress equation is derived by multiplying the N-S equation by a fluctuating property and time averaging the product. The derivation process is shown in Figure 12. The final format of the Reynolds stress equation and the physical meanings of each term is shown in Figure 13.

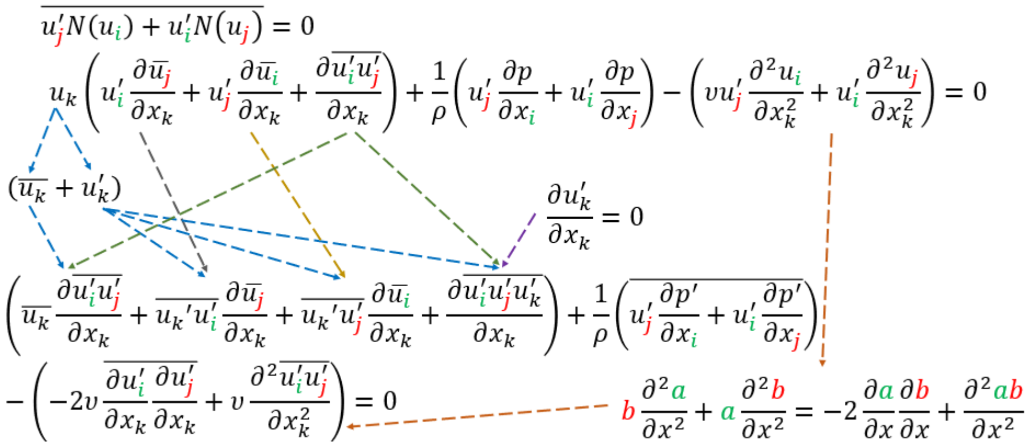

$$\overline{u_j'N(u_i)+u_i'N(u_j)}=0$$

$$u_k\left(u_i'\frac{\partial \bar{u}_j}{\partial x_k}+u_j'\frac{\partial \bar{u}_i}{\partial x_k}+\frac{\partial \overline{u_i'u_j'}}{\partial x_k}\right)+\frac{1}{\rho}\left(u_j'\frac{\partial p}{\partial x_i}+u_i'\frac{\partial p}{\partial x_j}\right)-\left(\upsilon u_j'\frac{\partial^2 u_i}{\partial x_k^2}+u_i'\frac{\partial^2 u_j}{\partial x_k^2}\right)=0$$

$$(\overline{u_k}+u_k')$$

$$\frac{\partial u_k'}{\partial x_k}=0$$

$$\left(\overline{u_k}\frac{\partial \overline{u_i'u_j'}}{\partial x_k}+\overline{u_k'u_i'}\frac{\partial \bar{u}_j}{\partial x_k}+\overline{u_k'u_j'}\frac{\partial \bar{u}_i}{\partial x_k}+\frac{\partial \overline{u_i'u_j'u_k'}}{\partial x_k}\right)+\frac{1}{\rho}\left(\overline{u_j'\frac{\partial p'}{\partial x_i}+u_i'\frac{\partial p'}{\partial x_j}}\right)$$

$$-\left(-2\upsilon\overline{\frac{\partial u_i'}{\partial x_k}\frac{\partial u_j'}{\partial x_k}}+\upsilon\frac{\partial^2 \overline{u_i'u_j'}}{\partial x_k^2}\right)=0$$

$$b\frac{\partial^2 a}{\partial x^2}+a\frac{\partial^2 b}{\partial x^2}=-2\frac{\partial a}{\partial x}\frac{\partial b}{\partial x}+\frac{\partial^2 ab}{\partial x^2}$$

Figure 12: Derivation of Reynolds stress equation

$$\overline{u_k}\frac{\partial \overline{u_i'u_j'}}{\partial x_k}=P_{ij}-\varepsilon_{ij}+\Pi_{ij}-\frac{\partial \overline{u_i'u_j'u_k'}}{\partial x_k}+\upsilon\frac{\partial^2 \overline{u_i'u_j'}}{\partial x_k^2}$$

Viscous diffusion

Turbulent transport

Production tensor $P_{ij}=-\left(\overline{u_k'u_i'}\frac{\partial \bar{u}_j}{\partial x_k}+\overline{u_k'u_j'}\frac{\partial \bar{u}_i}{\partial x_k}\right)$

Dissipation tensor $\varepsilon_{ij}=2\upsilon\overline{\frac{\partial u_i'}{\partial x_k}\frac{\partial u_j'}{\partial x_k}}$

Velocity-pressure-gradient tensor

$$\Pi_{ij}=-\frac{1}{\rho}\left(\overline{u_j'\frac{\partial p'}{\partial x_i}+u_i'\frac{\partial p'}{\partial x_j}}\right)$$

$$=\overline{\frac{p'}{\rho}\left(\frac{\partial u_j'}{\partial x_i}+\frac{\partial u_i'}{\partial x_j}\right)}-\frac{\partial}{\partial x_k}\left(\frac{\overline{p'u_j'}}{\rho}\delta_{jk}+\frac{\overline{p'u_i'}}{\rho}\delta_{ik}\right)$$

$$=R_{ij}-\frac{\partial}{\partial x_k}T_{kij}^{(p)}$$

Pressure-strain-rate tensor

Pressure transport tensor

Figure 13: Reynolds stress equation

The Boussinesq hypothesis (Boussinesq, 1877) solves the closure problem. It is the second answer to remove the fluctuation terms and is the "approximations based on knowledge of properties of flow turbulence" mentioned in the last paragraph by introducing the concept of eddy viscosity. Boussinesq relates the Reynolds stress to the velocity gradient through the eddy viscosity to close the system of RANS. The Boussinesq equation is shown in Eq. 5, or simply as $-\overline{u_i'u_j'}=2\upsilon_T S_{ij}$. υ_T is kinematic eddy viscosity, S_{ij} is strain-rate tensor shown in Eq. 6, and k is the turbulence kinetic energy shown in Eq. 7.

$$-\overline{u_i'u_j'} = 2\upsilon_T S_{ij} - \frac{2}{3}k\delta_{ij} \tag{Eq. 5}$$

$$S_{ij} = \frac{1}{2}(\nabla u + (\nabla u)^T) \tag{Eq. 6}$$

$$k = \frac{1}{2}\overline{u_i'u_i'} \tag{Eq. 7}$$

The mixing length model (1925) [33] describes momentum transfer by turbulent Reynolds stresses using eddy viscosity. The mixing length is conceptually analogous to the concept of “mean free path”: a fluid parcel will conserve its properties for a characteristic length, ξ', before mixing with the surrounding fluid. Using the concept of mixing length, the fluctuation terms can be seen as the average value deviation from its surrounding environment after it has moved over the mixing length ξ'. Therefore, using the Boussinesq equation, mixing length eddy viscosity is equal to the velocity gradient divided by ξ'^2.

To improve the ability to predict properties of turbulent flows and to develop a more realistic mathematical description of the turbulent stresses, Prandtl (1945) postulated a model in which the eddy viscosity depends upon the turbulent kinetic energy. This additional equation considers that turbulent stresses (eddy viscosity) are affected by flow history and is thus a one-equation turbulence model.

1.1.5 Turbulence: modeling in bearings

Care must include the dominant flow phenomena in high-speed oil or water-lubricated applications. As the flow regime in these bearings is almost always turbulent or transitioning to turbulent flow, this portion of the modeling approach is significant in producing an accurate system model. As lubrication in thrust bearings is one kind of drag flow, it is essential to model the wall shear stress between the fluid, the static pad, and the moving runner. Turbulence in the groove also influences the thin film turbulence and the groove conductivity. This research work includes groove turbulence as part of a more comprehensive turbulence model than has been done previously.

The flow in bearings can range from laminar to turbulent. The flow in thrust bearings transitions from laminar to turbulent when the lubricant has low viscosity, like water, or the shaft speed is very high. For example, with water lubrication, the Reynolds number can easily be larger than 40000. The Reynolds number is defined as $Re = \rho\omega r h_{min}/\mu$, where ρ, ω, r, h_{min}, and μ are the density, angular velocity, radius of the pad, minimum film thickness, and viscosity. A laminar-based or zero-equation turbulence model analysis method and tool cannot predict accurate performance characteristics in such high Reynolds number applications. For example, traditional analysis methods usually predict the film thickness to be a negative value.

For the application of thrust bearings, the numerical methods of RANS and Large Eddy Simulation (LES) have been used by researchers, of which RANS is the most commonly used. The RANS methods used in turbulence studies can be divided into zero-equation, one-equation, and two-equation turbulence models. Zero-equation models simplify the analysis by assuming an algebraic relationship between the mean flow's eddy viscosity and length scales. The most significant difference between one-equation and two-equation turbulence models is that one-equation models relate the turbulent length scale to some typical flow dimension. In contrast, two-equation models determine the turbulent length scale as part of the solution. More details will be discussed later in section 3. Since the late 1960s [34], researchers have predominantly used zero-equation models in finite element (FE) bearing analysis codes.

Constantinescu employed Prandtl’s mixing length concept for calculating journal and thrust bearings subjected to turbulence lubrication [35] [36] [37] [38] [39] [40] [41]. Ng and Pan [34] [42] [43] utilized the concept of eddy viscosity to represent the turbulent stresses in terms of the mean velocity gradient. Hirs [44] [45] adopted a bulk-flow approach requiring no physical representation of the turbulent transport mechanism. Hirs also compared Hirs's bulk-flow, Ng's law-of-wall, and Constantinescu's mixing length method. Hirs's approach is completely different in that it is based solely on experimental observations.

On the other hand, two-equation turbulence models (k-ε, k-ω, and SST) are typically used in commercial Computational Fluids Dynamics (CFD) software packages, which have been the basis of many industrial bearing studies. Typically, either turbulence or laminar flow condition is chosen for the whole flow regions. Also, for the turbulent flow, either one-equation or two-equation turbulence flow is chosen. They usually study bearing characteristics [46] [47] [48] [49] and not turbulence modeling. Large eddy simulation

(LES) is less used than RANS in CFD. Zhu [50] chose LES as coherent turbulent structures can be obtained with acceptable computational cost using LES.

Another significant modeling uncertainty in fluid-film thrust bearings is the bearing temperature drop associated with the transitional region: the fluid flow transitioning from laminar to turbulence flow as the runner speed increases. Moreover, to the knowledge of this researcher, no study has identified the exact regions of turbulence and the onset of turbulence in the bearings. That is to say, one flow pattern is assumed in the whole flow region with the bearings.

Oil lubrication at high speeds and water lubrication are two challenging areas for modeling and operational predictions due to the high rotating speed or low viscosity of water resulting in highly turbulent bearing operation. The conventional method to model turbulence in bearings uses empirical function based on the law of wall [51] to solve eddy viscosity. The law of wall states the relation between non-dimensional distance to wall and nondimensional velocity. There are three regions for the inner layer. The first region is the laminar sublayer, where the nondimensional velocity equals to the nondimensional distance to the wall. The second region is the log-law region [52]. In this region, $u^+ = \frac{1}{\kappa} lny^+ + C^+$, where y^+ is the nondimensional distance to wall, u^+ is the nondimensional velocity to wall, κ is the Von Karman constant, C^+ is a constant.

1.1.6 Turbulence: experimental method

According to Newton's law of viscous flow: shear stress = (dynamic viscosity) * (rate of deformation). Equilateral hyperbola states $\left(\frac{H_p}{K_2 U^3 \rho}\right)\left(\frac{Uh}{\nu}\right) = 1$. Eq. 14 shows the dimensionless values of the equilateral hyperbola. Until a critical Reynolds number is achieved, the experimental points follow the theoretical curve for laminar flow conditions. Above this critical value, the horsepower increases and shows what appears to be a transition region, after which the curve tends to approach a horizontal asymptote [53].

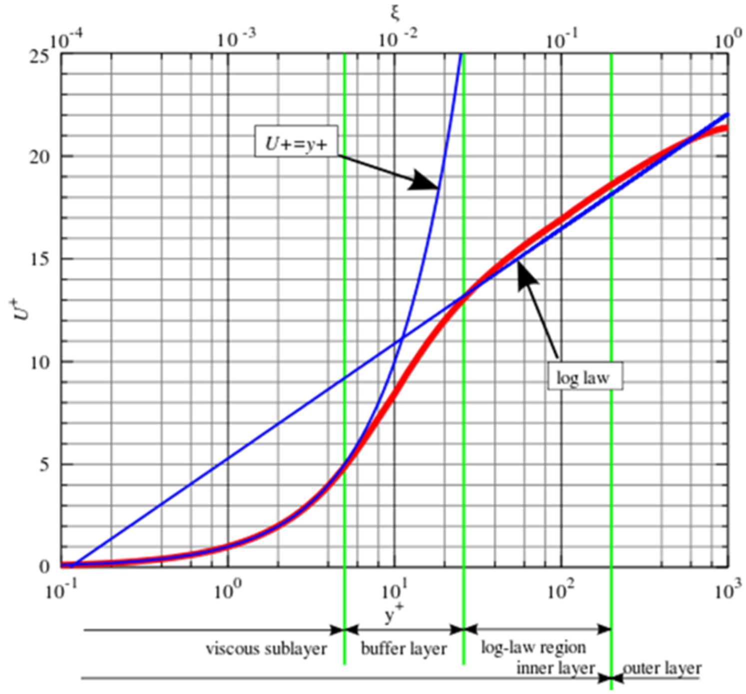

[54]

Figure 14: Law of wall

Besides the numerical methods to study turbulence in thrust bearings, experimental methods are also used, as shown in Figure 15. The quantities measured in experiments are usually temperature and power loss, and there are no direct kinetic energy observations. From experimental results [53], the Reynolds number for the boundaries between laminar, transitional turbulence, and turbulent flow for a tilting pad thrust bearing are as follows: $Re < Re_L=580$, a lower critical Reynolds number, which is the start, and transitions to fully turbulent at $Re > Re_U=800$, an upper critical Reynolds number.

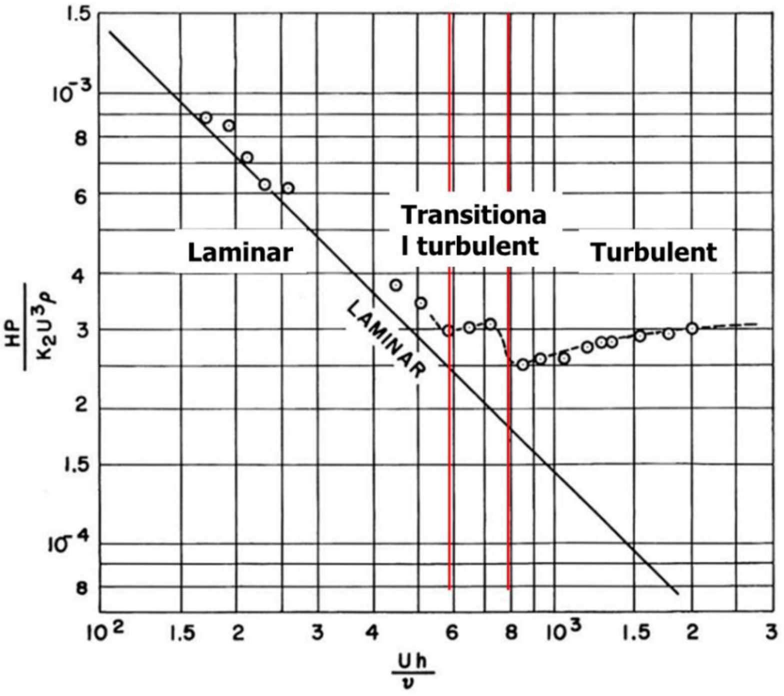

Figure 15: Comparison of Experiment and theory

1.1.7 Turbulence: transitional region

It is well known that bearing power loss and temperature will diverge from laminar predictions after a certain shaft speed is reached and surpassed [55] [56] [4] [57] [58] [59]. Traditionally, this phenomenon has been associated with turbulent flow in the film, and the transition point is of obvious interest to bearing designers. For years, researchers studied the performance characteristics of bearings undergoing a transition from laminar to turbulence through experiments [55] [60] [56] [61]. These experiments provide temperature profiles with speed and recorded temperature contours on the pad surface and thus are good references for studying the transitional region in thrust bearings. Researchers have also tried to understand the influence of turbulence on bearing performance using numerical methods (FE) to study turbulence in bearings since the late 1990s [49]. Importantly, these bearing studies have all used the zero-equation turbulence model and therefore do not calculate turbulent kinetic energy. In particular, the influence of the groove flow on the turbulent kinetic energy has not been carefully studied.

Gregory was the first to study transitional region in thrust bearings. Capitao and Mikula continued Gregory's study and provided temperature profiles on pad surface correlated with shaft speed and thus are an excellent experimental reference for a detailed study of the transitional region. Gregory (1974) [55] [62] focused on the power loss of thrust bearings at high operating speeds, while Capitao (1976) [56] [61] studied the effects of high-operating speeds on tilting pad thrust bearing performance, and first summarized the process of the phenomenon of temperature drop with increasing speed, as shown in Figure 16. He stated the process is a temperature peak, followed by a dramatic temperature decrease, then temperature rapidly climbing again. Mikula (1988-1991) [63] [5] [64] [65] further examined the same model that Gregory and Capitao studied and experimentally measured the temperature drop and power loss with the increasing operating speed. Thermal effects in thrust bearings are a major concern for high-speed applications. When the flow changes from laminar to turbulent, there is an overall temperature change, as seen in Figure 16. The temperature drop region begins at higher speeds as the load increases, showing that higher load cases have less turbulence than lower load cases. This is because the film is thinner for higher loads, which diminishes the turbulence. Yang [23] [24] [25] [26] (2019, 2021) had a severe simulation exploring machine learning method application in a journal bearing. His model included multiphase thermal flow in a transitional region, considering thermal deformation, with two-way fluid-structure interaction; and, stiffness and damping, and pad flexibility with the machine learning method. However, his model does not have groove regions.

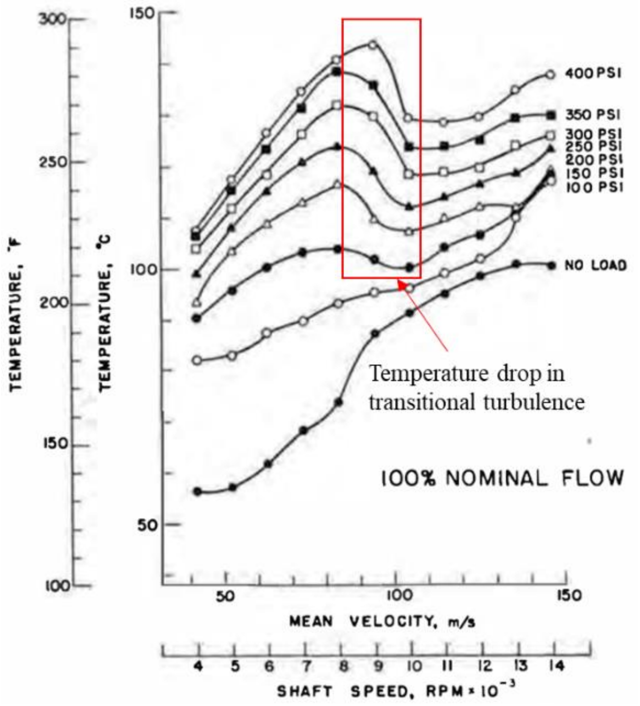

Figure 16: Temperature change in the transitional region [56]

1.1.8 CFD modeling in bearing groove

The Reynolds equation is the foundation for the fluid flow calculation used in traditional thermo-(elasto)-hydrodynamic lubrication (TEHD) assessments. Assuming conjugate heat transfer (CHT) boundary conditions between the individual components, the energy equation of the lubricant coating, as well as the heat conduction equations of the pads and the runner, can be determined using the fluid flow, e. g [66] [67] [68]. However, these analyses do not describe fluid flow in the spaces between pads nor the secondary flows that pass the remaining pad-free surfaces [69]. Therefore, TEHD codes require estimated convection coefficients for the free surfaces to evaluate heat flow across the outer boundaries of the bearing model [69].

Different researchers [11] [12] [14] used computational fluid dynamic methods to study fluid flow in the inlet region in journal bearings. Hagemann [13] [8] used a conduction-convection hot oil carry-over model in a journal bearing. Grzegorz [27] studied the lubricant flow in the leading-edge groove in a thrust bearing through CFD.

1.2 Scope of Current Work

The methodological and applied research, as well as a considerable portion of the theoretical and collaborative work discussed in this dissertation, addresses the general topic of thermo-elasto-hydrodynamic (TEHD) bearing and turbulence modeling and analysis. The details of the scope of the current work are described below.

Chapter two of this dissertation focused on modeling Reichardt's formula for eddy-viscosity in the fluid film of tilting pad thrust bearings with an experimental tilting-pad fluid-film thrust bearing. The research questions in chapter two are: Q1 - What are the effects of various modeling methods for applying Reichardt's equation in eddy viscosity calculations for turbulent bearings? Q2 - What best method(s) to use and under what conditions? Rotating machinery has rotating and static surfaces, and those two surfaces influence wall shear stress. In chapter two, the three widely used eddy viscosity modeling methods were analyzed to determine their effects on modeling the wall shear stress and the related effect associated with bearing performance. The three different finite element method models were analyzed using the Ng-Pan turbulence model to calculate the eddy viscosity. The sensitivity studies of the three methods were studied with both water and oil lubrication, and with runner thermal deformation on and off. From the results of this study, the temperature and film thickness predictions of the three methods were compared to optimize the turbulence modeling using the Ng-Pan method. The modeling results were studied to understand the influence of the three wall shear stress modeling methods.

Chapter three of this dissertation focuses on studying the methodology of turbulence parameter correction in water-lubricated thrust bearings. The research questions in chapter three are: Q1 - Is the traditional oil lubrication modeling equation adequate for water lubrication? Q2 - What are the additional modifications needed for water lubrication modeling, due to the different thermal characteristics of oil and water? Since water lubrication results in much larger turbulence than oil lubrication, the y+ value difference between oil and water lubrication is quite significant. This different y+ behavior requires a different meshing solution for water versus oil lubricated bearings. As cross-film meshing is much more sensitive than circumferential and radial meshing, chapter three is focused on studying the cross-film. Chapter three first created a strategy for determining the cross-film element number for water lubrication. Then compared the film thickness, pressure, and power loss between cases of a benchmark before and after optimization. The optimized parameters were used in the Ng-Pan turbulence model, and a sensitivity study of various parameters for the optimized case was performed.

Chapter four focuses on applying a mixed zero-equation and one-equation turbulence model. The research questions in chapter four are: Q1 - Is there a way to remove the two boundary values to decrease the uncertainty? Q2 - If there is more than one other way, what is the best choice? Q3 - How is the new model better than the traditional model? Due to inherent shortcomings, the traditional zero-equation needs to be improved to enable better prediction accuracy. Chapter four introduces the physics of zero-equation and one-equation turbulence models. A novel model is developed, combining a one-equation model with an empirical length scale as the mixed zero-equation and one-equation turbulence model of a fluid film thrust bearing. This mixed zero-equation and one-equation turbulence model was combined with the Reynolds equation, energy equation, and heat conduction equation and compared against DNS and ANSY CFX for evaluation purposes, using Couette and Poiseuille flow as example validation cases.

Chapter five examines the temperature drop in the transitional region. The research questions in chapter five are: Is it correct that the temperature drop across a range of increasing velocity, as seen in Fig. 16, can be attributed to the onset of turbulence in the fluid film? (1) If the answer is yes, what turbulence contributes to the temperature drop? Further questions are: (a) What turbulence model should be used? (b) What is the physical mechanism that leads to the temperature drop? Moreover, (2) If the answer to (1) is no, will a laminar flow model correctly capture the temperature drop? Further questions are: for the turbulence model, what happens in the groove that behaves in specific temperature changes in the transitional region? Could the impacting physics be eddy? Conduction? Production? A well-documented, experimental, center-pivot fluid film thrust bearing was selected for the work in this chapter, and a full fluid-solid CFX model was built. In addition to the research questions listed above, examining several different phenomena related to bearing performance and modeling was necessary. These include the crowning of the pad surface, the individual contributions of the film, pad, runner, and groove regions to CFX modeling results, and the impact of leading-edge temperature on load capacity.

2. Modeling Reichardt’s Formula for Eddy-Viscosity in The Fluid Film of Tilting Pad Thrust Bearings

Oil-lubricated bearings are widely used in high-speed rotating machines such as those used in the aerospace, power generation, and automotive industries that often require this lubrication. However, environmental issues and risk-averse operations have made water-lubricated bearings increasingly popular. Due to different viscosity properties between oil and water, the low viscosity of water increases Reynolds numbers drastically and therefore makes water-lubricated bearings prone to significant turbulence effects. The turbulence model is affected by eddy-viscosity, while eddy-viscosity depends on wall shear stress. Therefore, effective wall shear stress modeling is necessary for producing an accurate turbulence model. Improving the accuracy and efficiency of methodologies of modeling eddy-viscosity in the turbulence model is essential, especially considering the increasingly widespread application of water-lubricated bearings for various industrial applications and also the traditional oil-lubricated bearings in high-speed machinery. This research aims to study the sensitivity of different methodologies for solving eddy-viscosity for turbulence modeling.

Eddy-viscosity and flow viscosity form the effective viscosity are the coefficient of the shear stress in the film. The turbulence model and Reynolds equation are bound together to solve when the hydrodynamic analysis is performed. Therefore improving the accuracy of the turbulence model is also vital to improving a bearing model’s ability to predict film pressure values, which will determine the velocity and velocity gradients in the film. The velocity gradients in the film are the other terms that determine the shear stress. The research questions in chapter two are: Q1 - What are the effects of various modeling methods for applying Reichardt’s equation in eddy viscosity calculations for turbulent bearings? Q2 - What best method(s) to use and under what conditions? This work used three approaches applying Reichardt’s formula to model eddy-viscosity in the fluid film. These methods are for determining where one wall’s effects begin and the other wall’s effects end. Trying to find a suitable model to capture the wall’s effects of these bearings, aiming to improve the turbulence model's accuracy, would be of high value to the bearing industry. Since wall shear stress determines the temperature, temperature determines the viscosity. Viscosity determines the film profile and load capacity. The results of this study could aid in improving future designs and models of oil and water-lubricated bearings.

2.1 Introduction

As shown in Figure 17, Lubricated fluid film bearings are essential components of the rotating machinery they support. The inability to use oil-lubricated bearings in many applications with strict environmental or other design-driven limitations makes these applications challenging. The low viscosity of water produces highly turbulent bearings with less load capacity and lower stiffness and damping forces acting on the shaft than their oil-lubricated counterparts. Because water is not an ideal bearing lubricant, accurately modeling these bearings for design purposes is critical to producing a reliable design. This can pose a design challenge as designers seek to produce a reliable machine supported by bearings that adequately support the applied loads and control the vibration during operation.

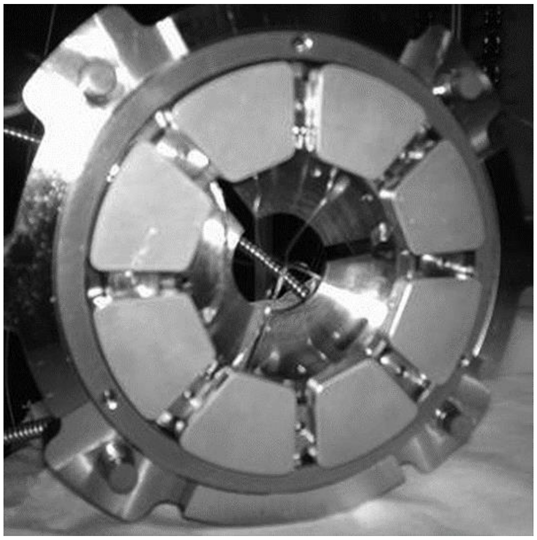

Figure 17. Photo of typical water-lubricated thrust bearing

Fortunately, Reynold’s Equation-based solution [70] techniques applied to oil-lubricated bearings can also be applied here [71] [72]. However, care must be taken to include the dominant flow phenomena in high-speed oil or water-lubricated applications. As the flow regime in these bearings is almost always turbulent, this portion of the modeling approach is significant to producing an accurate model of the system. For the TEHD analysis of turbulent bearings, the method presented by He [72] was based on the theory developed by Elrod and Ng [43] [34] [42] with a modification by Suganami and Szeri [73] to account for transitional turbulence. The turbulence is modeled using an eddy viscosity calculated through Reichardt’s formula.

This study aimed to analyze the application of Reichardt’s formula for eddy-viscosity, considering wall effects, to modeling a turbulent, oil or water-lubricated tilting pad thrust bearing. The three primary methods of this modeling approach were carried out and compared for a range of speed and loading conditions to determine if significant discrepancies between the three methods could be found. These different methods determine where one wall's effects begin and the other wall's effects end. Several model outputs were compared, and the primary causes of discrepancies are discussed in detail. The knowledge generated by this work can aid in developing thorough, accurate modeling approaches for these critical bearing applications.

Wall boundary's impact on turbulence

Turbulence, or eddying motion, is a local swirling motion of a fluid where the vorticity is very intense and, therefore, effective turbulent stress. There are three main ways of modeling turbulence in bearings. They are Constantinescu’s (1959) [35] [36] [37] [38] [39] [40] [41] mixing length theory using the concept of the free path, Ng’s (1965) [43] [34] [42] application of law-of-wall and the concept of eddy viscosity, and Hirs’s (1973) [44] bulk-flow considering pressure gradient. Elord & Ng (1967) [42] proposed a method of setting a core middle region of modeling wall shear stress in bearing. Clauser (1956) [74] studied the turbulence boundary layer in the broadened analysis framework compared to the laminar boundary layer. Brockett (1996) [71] mentioned three ways of modeling eddy viscosity considering wall shear stress, but he did not compare them. The ideas of the three methods are shown in Figure 18.

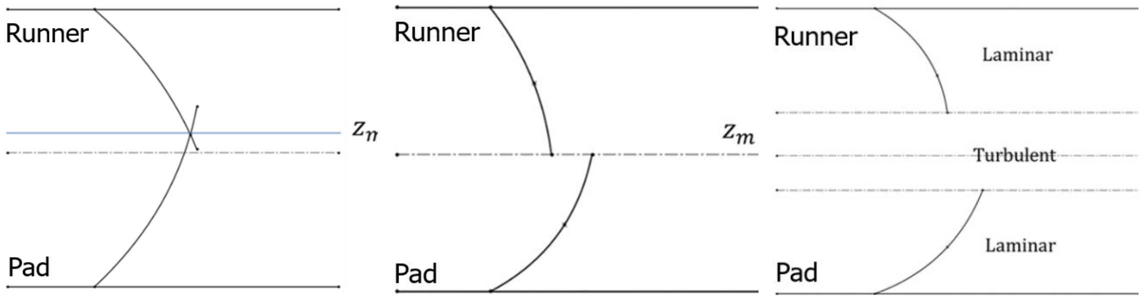

a) method 1 ***b) method 2*** ***c) method 3***

Figure 18: three methods of modeling eddy viscosity considering wall shear stress

This study aimed to analyze the application of Reichardt's formula for eddy-viscosity considering wall effects, and to model a turbulent, with oil or water-lubricated tilting pad thrust bearing. The three primary methods of this modeling approach were carried out and compared for a range of speed and loading conditions to determine if significant discrepancies between the three methods could be found. These different methods determine where one wall's effects begin and the other wall's effects end. Several model outputs were compared, and the primary causes of discrepancies found were discussed in detail. The knowledge generated by this work can aid in developing thorough, accurate modeling approaches for these critical bearing applications. The research plan was to use an FE code to model three methods of modeling wall shear stress. Then do a sensitivity study of those three methods, and compare the results between those three methods.

2.2 Reichardt Formula for Eddy-Viscosity

The law of wall describes the relationship between non-dimensional distance to wall and non-dimensional velocity. Nondimensional velocity is a function of shear stress, and non-dimensional distance to the wall is also a function of shear stress. Therefore, nondimensional velocity is a function of nondimensional distance to the wall. The partial derivative of the non-dimensional velocity to the non-dimensional distance to the wall is the term on the left-hand side of Reichardt's formula.

The exact form of the eddy-diffusivity for momentum ϵ_m is unknown. Many experiments on wall turbulence show that the mean velocity $\bar{u}$ near the wall is a function of the fluid viscosity μ and density ρ, distance from the wall z, and the wall shear stress τ_w. When the dimensional analysis is applied to these parameters, two dimensionless groups emerge:

$$u^+ = \frac{\bar{u}}{\sqrt{\frac{|\tau_w|}{\rho}}} \qquad \text{Eq. 8}$$

$$z^+ = \frac{z}{\nu}\sqrt{\frac{|\tau_w|}{\rho}} \qquad \text{Eq. 9}$$

Therefore:

$$u^+ = G(z^+) \qquad \text{Eq. 10}$$

This functional relationship is known as the "law of the wall" and can be deduced from other means [75]. This equation, coupled with the Boussinesq Hypothesis, leads to the equation: $\tau_{ij} = -\bar{p}\delta_{ij} + \mu(1 + \frac{\epsilon_m}{\nu})\bar{D}_{ij}$ at the wall and along with the non-dimensional Eq. 8 and Eq. 9 is enough to write the one-dimensional turbulence equation:

$$\frac{du^+}{dz^+} = \frac{1}{1 + \frac{\epsilon_m}{\nu}} \qquad \text{Eq. 11}$$

Integrating this equation yields

$$u^+ = \int_0^{z^+} \frac{dz^+}{\left(1 + \frac{\epsilon_m}{\nu}\right)} \qquad \text{Eq. 12}$$

As Huebner states [76], Reichardt asked the question, "What is the best functional representation for ϵ_m/ν in Eq. 11 so that the equation closely agrees with the empirically determined relationship between the two non-dimensional groups expressing the law of the wall?"

Reichardt then proposed the following relationship:

$$\frac{\epsilon_m}{\nu} = \kappa\left[z^+ - \delta_l^+ \tanh\left(\frac{z^+}{\delta_l^+}\right)\right] \qquad \text{Eq. 13}$$

In which κ is an empirically determined constant that ranges from 0.3 to 0.4, and δ_l^+ is also an empirically determined constant that ranges from 5 to 15, respectively [13]. Reichardt originally proposed $\kappa = 0.4$ and $\delta_l^+ = 11$ [14]. Ng optimized the constants based on published experimental data, which resulted in $\kappa = 0.4$ and $\delta_l^+ = 10.7$ yielding accurate results over the range $0 < z^+ < 1000$ [13]. He states that κ should decrease to 0.3 as z^+>1000.

2.3 Methods of Applying Reichardt's Formula

Several approaches have been used in applying Reichardt's formula. Each method also ignores the reciprocal influence of the walls [42]. Three methods to apply Reichardt's formula are as follows. These different methods determine where one wall's effects begin and the other wall's effects end. The general idea is that the top-half film uses shear from the top surface, and the bottom-half film uses shear from the bottom surface. The main difference between the three methods is primarily related to how the middle of the film is treated. Method one uses the middle surface, where the top and bottom surfaces have the same values. Method two uses the exact middle of the film, so the y^+ is not continuous in the middle. Method three uses the concept of the core region. In the Reichardt formula, the eddy is proportional to the y+, so the eddy becomes more prominent near the middle. The boundary of the core region is defined when $\frac{\varepsilon}{\nu}|_{core} = 0.07y^+$.

Method one

The shear value in Reichardt's formula was originally intended to be the shear stress at the wall. The shear stress at the lower wall in a lubrication problem can be approximated as:

$$\begin{aligned}\tau_0 = \sqrt{\tau_{rz}^2 + \tau_{\theta z}^2} &\approx \mu\left(1 + \frac{\epsilon_m}{\nu}\right)\sqrt{\left(\frac{\partial u_r}{\partial z}\right)^2 + \left(\frac{\partial u_\theta}{\partial z}\right)^2}\,|_{z=0} \\ &= \mu\sqrt{\left(\frac{\partial u_r}{\partial z}\right)^2 + \left(\frac{\partial u_\theta}{\partial z}\right)^2}\,|_{z=0}\end{aligned} \qquad \text{Eq. 14}$$

And for the upper wall, there is also an approximation

$$\tau_h = \sqrt{\tau_{rz}^2 + \tau_{\theta z}^2}|_{z=h} \approx \mu\left(1 + \frac{\epsilon_m}{\nu}\right)\sqrt{\left(\frac{\partial u_r}{\partial z}\right)^2 + \left(\frac{\partial u_\theta}{\partial z}\right)^2}\,|_{z=h}$$

$$= \mu\sqrt{\left(\frac{\partial u_r}{\partial z}\right)^2 + \left(\frac{\partial u_\theta}{\partial z}\right)^2}\,|_{z=h} \qquad \text{Eq. 15}$$

0 and h refer to the lower and upper walls, respectively. Continuity of the eddy-viscosity in the film is imposed. Since the eddy-viscosity in Eq. 13 is a unique function of $z^+ = (z/\nu)\sqrt{|\tau_w|/\rho}$, this leads to:

$$\frac{z_m}{\nu}\sqrt{\frac{|\tau_0|}{\rho}} = \frac{h - z_m}{\nu}\sqrt{\frac{|\tau_h|}{\rho}} \qquad \text{Eq. 16}$$

in which z_m is the point in the film at which the eddy-viscosity functions, as determined from the two surfaces, have the same value:

$$z_m = h\left[\frac{\sqrt{|\tau_h|}}{\sqrt{|\tau_h| + \sqrt{|\tau_0|}}}\right] \qquad \text{Eq. 17}$$

Reichardt’s formula can be rewritten as:

$$\frac{\epsilon_m}{\nu} = \kappa\left[z^{++} - \delta_l^+ \tanh\left(\frac{z^{++}}{\delta_l^+}\right)\right] \qquad \text{Eq. 18}$$

In which:

$$z^{++} = \frac{z}{\nu}\sqrt{|\tau_0|/\rho}\ if\ z \leq z_m \qquad \text{Eq. 19}$$

$$z^{++} = \frac{(h-z)}{\nu}\sqrt{|\tau_h|/\rho}\ if\ z > z_m \qquad \text{Eq. 20}$$

The cross-film derivative of eddy-viscosity is not continuous at z_m. This method was employed by Ng [34] and Huebner [76]. Elrod and Ng state that this method may lead to incorrect results when the shear vanishes at the wall [75]. Elrod and Ng proposed a solution to overcome this problem that leads to method one discussed here, which can be visualized in Figure 19. The method I is to apply Reichardt’s formula from both the upper and lower walls with an equilibrium position that needs to be calculated.

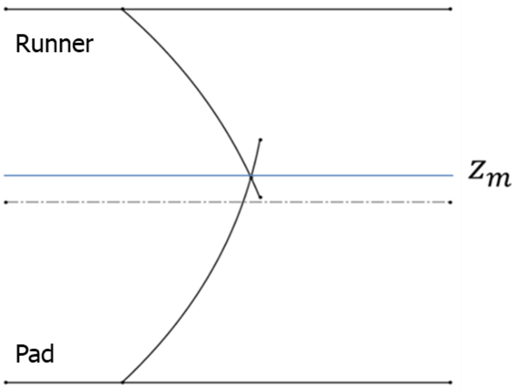

Figure 19. Graph of method one

Method two

A second approach, initially suggested by Elrod [42], is shown in Figure 20. Method two is very similar to method one, but it assumes that the eddy-viscosity can be calculated from the local value of shear stress $|\tau|$ in the film.

$$|\tau| = \sqrt{\tau_{rz}^2 + \tau_{\theta z}^2} \qquad \text{Eq. 21}$$

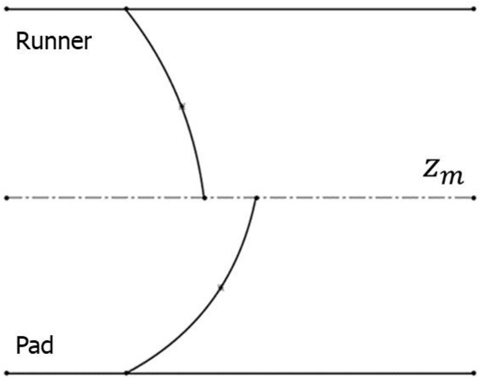

Figure 20. Graph of method two

In this case, $z_m = h/2$, and the cross-film derivative of eddy-viscosity is not continuous at z_m. The eddy-diffusivity in the upper one-half of the flow is influenced by the upper wall, while the eddy-diffusivity in the lower half of the flow is influenced by the lower wall [34]. Elrod stated that this method was more consistent with data published on turbulence boundary layers in the presence of adverse pressure gradients. [44] states that this may lead to anomalies in the eddy-viscosity when the shear stress vanishes in the channel. They recommend allowing the eddy-viscosity to vary with local shear stress as long as a monotonically increasing value of ϵ_m/υ is obtained. This method was employed by Ng and Pan [34] and Suganami and Szeri [73] [77].

Visualized method two is shown in Figure 21. Method two is to apply Reichardt's formula from both the upper and lower walls with an equilibrium position at the center of the fluid film. The cross-film derivative of eddy-viscosity is not continuous at z_m. The eddy-diffusivity in the upper one-half of the flow is influenced by the upper wall, while the lower wall influences the eddy-diffusivity in the lower half of the flow.

Method three

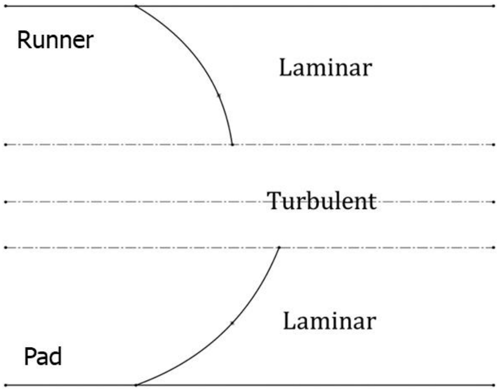

Figure 21. Graph of method three

The last method is similar to method two except that the eddy-viscosity is allowed to vary from Richardt's formula in the core of the flow. The core region is fully turbulent. Safar and Szeri [75] used:

$$\frac{\epsilon_m}{\nu}|_{core} = 0.07 z_0^+ \qquad \text{Eq. 22}$$

In the core region:

$$z_0^+ = \frac{h}{2\nu}\sqrt{\frac{|\tau_c|}{\rho}} \qquad \text{Eq. 23}$$

$$|\tau_c| = (|\tau_0| + |\tau_h|)/2 \qquad \text{Eq. 24}$$

Safar and Szeri [75] state that effective viscosity depends on local shear and temperature. Elrod [42] also states that method three was consistent with experimental data for turbulent pipe flow. Szeri [75] stated a form of Clauser's formula [74] for the core eddy viscosity, and Clauser's formula is independent of the transverse coordinate. They allowed the eddy-diffusivity value from Reichardt's formula to approach the core value but not surpass it.

Method three was visualized in Figure 12. Method three contains a core region that contains turbulent flow only, as shown in the middle. It contains three inner interfaces in the direction from the pad to the runner.

2.4 Model Analysis

The influence of modeling Reichardt's formula is studied through a sensitivity study. The bearing modeled for this analysis was a sector pad thrust bearing with a line pivot consisting of nine tilting pads, details of which are provided in Figure 22, Figure 23, and Table 2. **Error! Reference source not found.** shows how the modeling was performed in each set. The modeling was performed in the updated version of THRUST 5.3 developed by the Rotating Machinery and Controls Laboratory at the University of Virginia. A bearing load of 75400 lbf was calculated with multiple operating speeds, including fourteen different operating speeds for both including and excluding method three with method one and method two for oil lubricated conditions. Nine operating speeds were considered for both, including and excluding method three with method one and method two for water lubricated conditions. Eleven operating speeds were considered for including and excluding runner thermal deformation for oil lubricated conditions. Nine operating speeds for including and excluding runner thermal deformation for water lubricated conditions were then performed.

Turbulence in the film and thermal effects should be included in these three methods: allowing for turbulence in the film. Pad thermal deformation was also included. Runner thermal deformation is used as a comparing variable, allowing thermal conduction from the film to the runner and pad bearing surfaces. The turbulence correction factor can modify the film's thermal conductivity from the bearing. Runner temperature can vary axial-symmetrically with an insulated boundary condition at the inner radius. Temperature is allowed to vary three-dimensionally within the pad according to thermal boundary conditions applied to the pad.

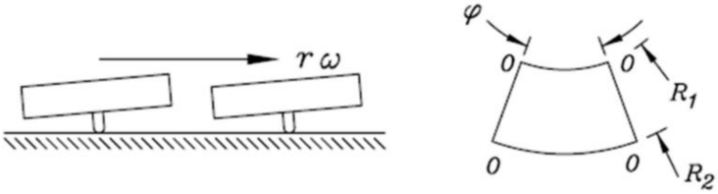

Figure 22. Schematic of a thrust bearing

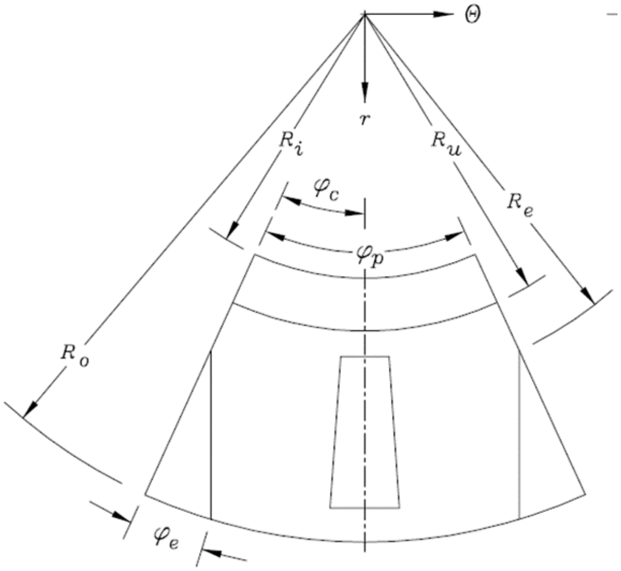

Figure 23. Structure of a thrust bearing

Table 1. Bearing Characteristics and Operating Conditions

Parameter	Value	Unit
Number of pads	9	
Runner inside radius	5.8	in
Runner outside radius	10.2	in
Runner axial thickness	2	in
Pad arc angle	30	deg
Groove arc angle	10	deg
Lubricant thermal conductivity	1.74E-06	Btu in/(sec°F)
Viscosity (oil) at T=100, 160 °F	4.13E-06	reyn
Viscosity (oil) at T=210 °F	6.50E-07	reyn
Viscosity (water) at T=100, 160, 210 °F	5.00E-08	reyn

Lubricant (oil) density	850	kg/m^3
Lubricant (water) density	970	kg/m^3
Oil supply temperature	120	°F
Applied bearing load	75400	lbf
Rotational speed	1000-80000	rpm

Table 2. Sensitivity study

	Oil	Water	Method 1	Method 2	Method 3	Runner thermal deformation
Set 1	✓	X	✓	X	✓	X
Set 2	✓	X	✓	X	X	X
Set 3	✓	X	X	✓	✓	X
Set 4	✓	X	X	✓	X	X
Set 5	X	✓	✓	X	✓	X
Set 6	X	✓	✓	X	X	X
Set 7	X	✓	X	✓	✓	X
Set 8	X	✓	X	✓	X	X
Set 9	✓	X	✓	X	✓	✓
Set 10	✓	X	✓	X	✓	X
Set 11	X	✓	✓	X	✓	✓
Set 12	X	✓	✓	X	✓	X

The other settings of this model are as follows: the iteration process matches the film thickness to the load. Iterations on pad tilt angles and pivot film thickness to match the load applied to the pad are performed. Linearized centrifugal inertia [78] term is included in the Reynolds equation solution. The tilting pad bearing pivot is rigid. No cutout is presented on the lower surface along the inner radius, neither at the leading or trailing edges of the pad on the outer diameter. The button material is specified, and the axial deflection on the underside of the button area of the pad is not zero. Only the edges of the button underside area are zeroed, allowing the center of the button underside to deflect.

This is to minimize the effects of too much thermal crowning. Pad and runner mechanical deformation are included. The Roeland viscosity-temperature model is used. Cavitation effects on the pressure and temperature distribution in the film are allowed during the pressure solution algorithm for oil but not allowed for water. Additional details on the modeling approach are found in [71].

2.5 Experimental Verification

The experimental data used for validation purposes was from the literature [79] [80] [81] [82]. The model is a thrust bearing consisting of a point tilting sector pad. The experimental device is shown in Figure 24, Figure 25, Figure 26, and Figure 27. The monitoring point 75/75 is shown in Figure 25. The bearing characteristic and operating conditions are given in Table 3. All the measurements are performed under steady-state conditions. The results of the comparison between the calculation and the experiment are presented in Figure 28. The results of the simulation and experiment were very close. The largest error between the simulation and experiment was 5%, which indicated that the simulation was quite accurate.

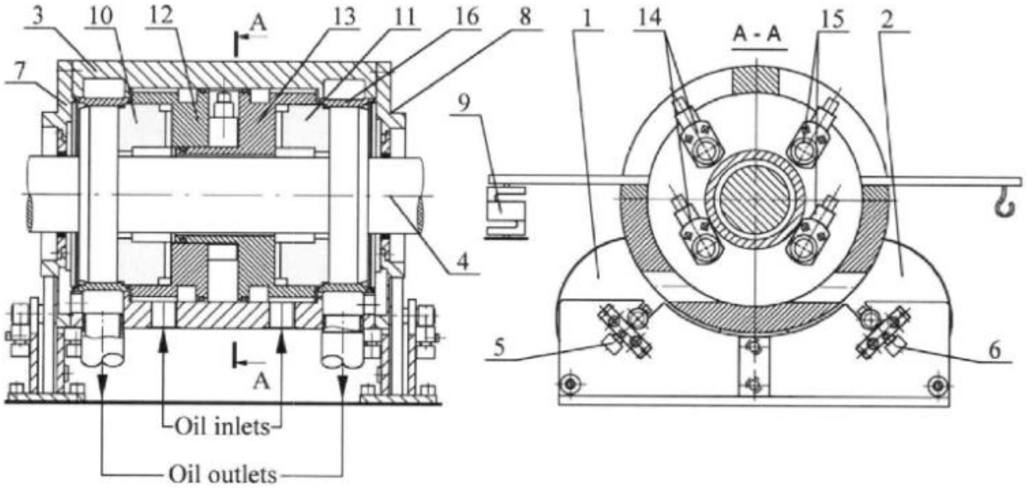

Figure 24. Schematic diagram of the test rig [80]

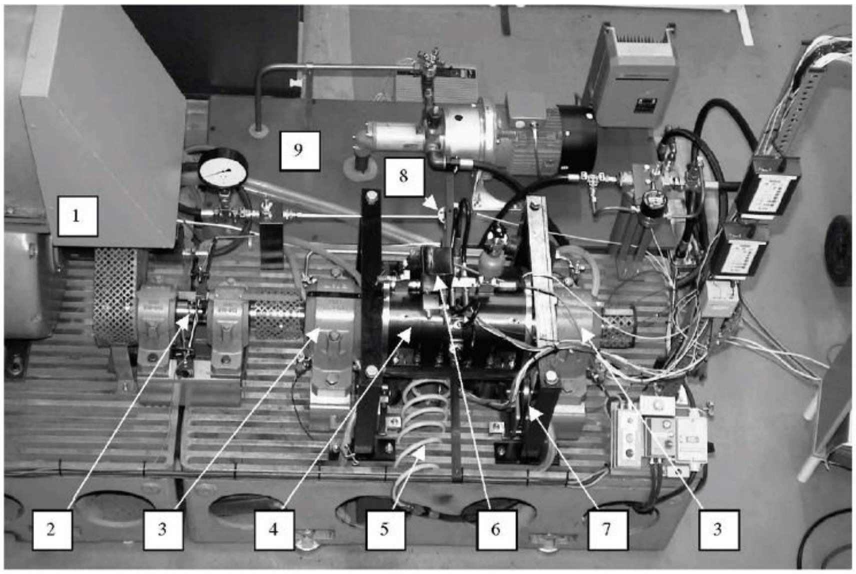

Figure 25. Photograph of the facility: (1) motor, (2) intermediate shaft, (3) journal bearings, (4) housing with test bearings, (5) flexible line for oil supply, (6) hydraulic system, one of four steel discs supporting the (7) housing, (8) load cell, (9) oil reservoir [80]

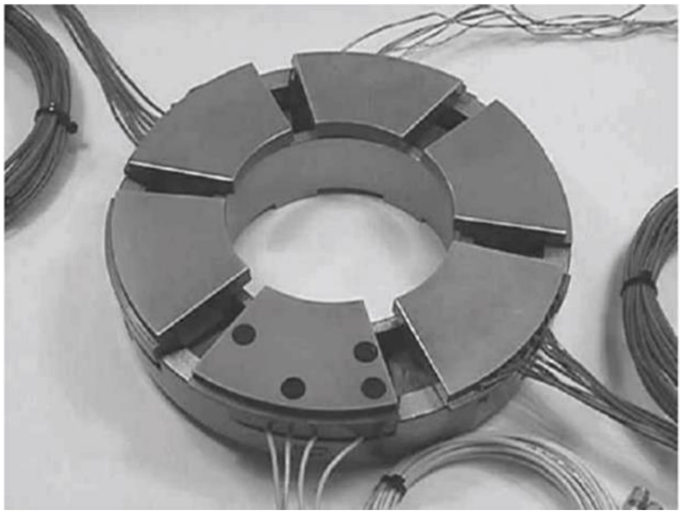

Figure 26. Photograph of the instrumented bearing [80]

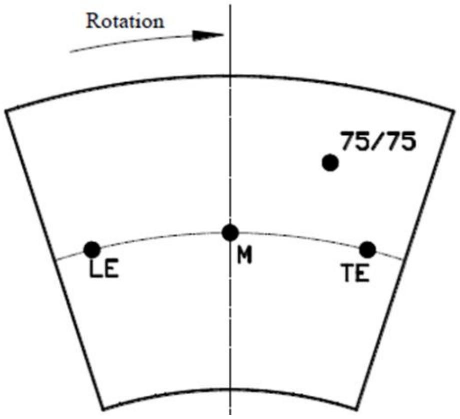

Figure 27. Schematic diagram of the monitoring point

Table 3. Bearing Characteristics and Operating Conditions

Parameter	Value	Unit
Number of pads	6	
Outer diameter	9	in
Inner diameter	4.5	in
Pad angle	50	deg
Pad thickness	1.1, 2.28	in
Pivot position (offset)	60	%
Pivot type	Spherical	
Collar diameter	9.1	in
Collar thickness	2	in
Viscosity at T=104 °F	5.66E-06	reyn
Viscosity at T=212 °F	7.80E-07	reyn
Lubricant density	855	kg/m^3
Feeding temperature	86-140	°F
Bearing area	40.5	inch^2
Bearing load	0.5-2	Mpa
Rotational speed	1500-3000	rpm

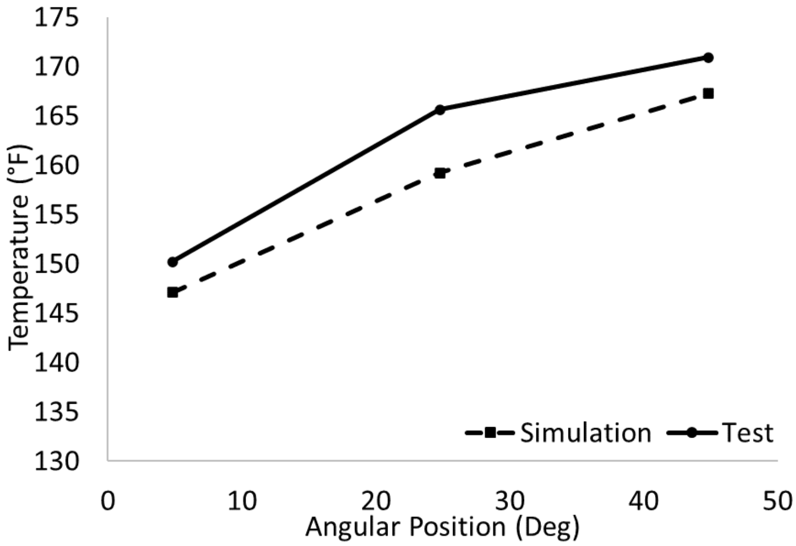

(A)

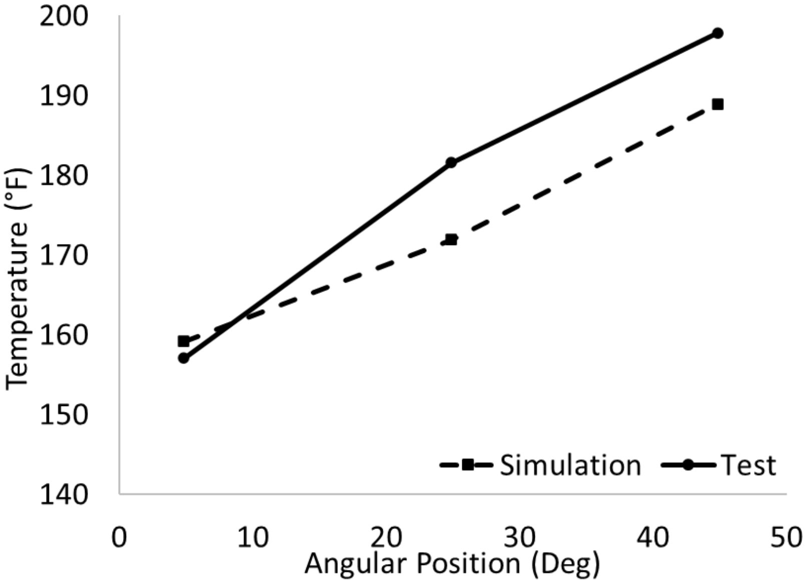

(B)

Figure 28. Pad temperature of the monitoring point: (A) 1500 rpm and 2 MPa bearing load, (B) 3000 rpm with 2 MPa bearing load

2.6 Results

2.6.1 The Influence of Method Three on Oil Lubrication

To summarize these methods, method one is to apply Reichardt's formula from both the upper and lower walls with an equilibrium position to be calculated. Method two sets the equilibrium position directly equal to half the film thickness. Method three is to contain a core region that contains turbulent flow only. The reason for separating method three from methods one and two is that methods one and two are very similar. Their only difference is finding the equilibrium position where the effects of one wall end and the other begin. For method three, a core region exists in the middle to represent a fully turbulent region. Method three determines three inner interfaces in the direction from the pad to the runner: the interface between laminar and turbulent regions in the lower half of the film; the interface in the middle of the film thickness above, which is affected by the upper boundary, under which is affected by the lower boundary; the last interface is between the laminar and turbulent regions in the upper half of the film region.

The influence of method three with oil lubricated conditions was studied by including or excluding method three with either method one or method two. The results are shown in Figure 29 and Figure 30. In Figure 29, method one with or without method three is used for applying Reichardt’s formula, while in Figure 30, method two with or without method three is used to apply Reichardt’s formula. From Figure 29 and Figure 30, the influence of method three is apparent for oil-lubricated conditions. The minimum film thickness with method three excluded is consistently larger. The relative difference between the two sets of cases for each plot is shown in Figure 31 and Figure 32, respectively. From these figures, the minimum film thickness shows more than a 5% difference between including or excluding method three when the Reynolds number reaches around 11229 for method one and 14497 for method two and reaches values near 30% at higher Reynolds numbers. This shows a significant influence of method three in applying Reichardt’s formula.

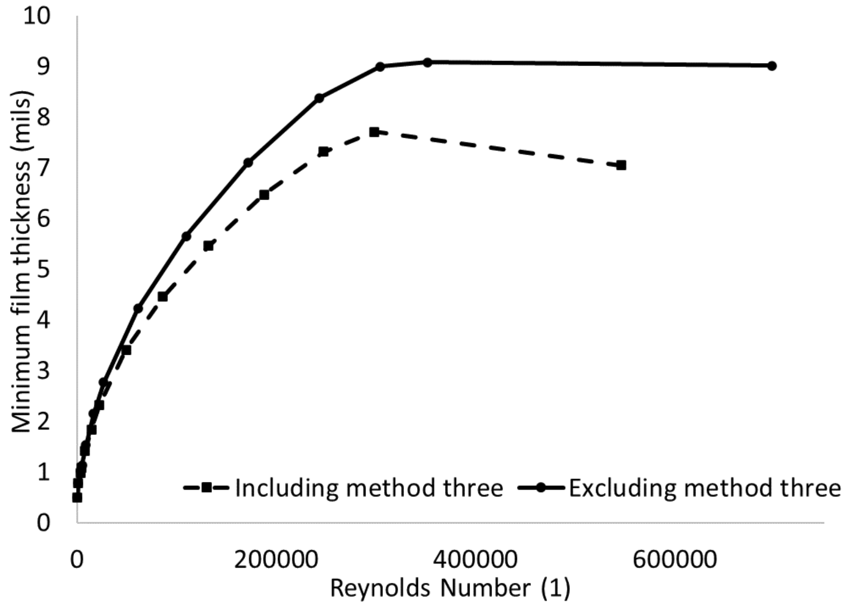

Figure 29. Minimum film thickness using methods one and three for applying Reichardt's formula for oil lubrication

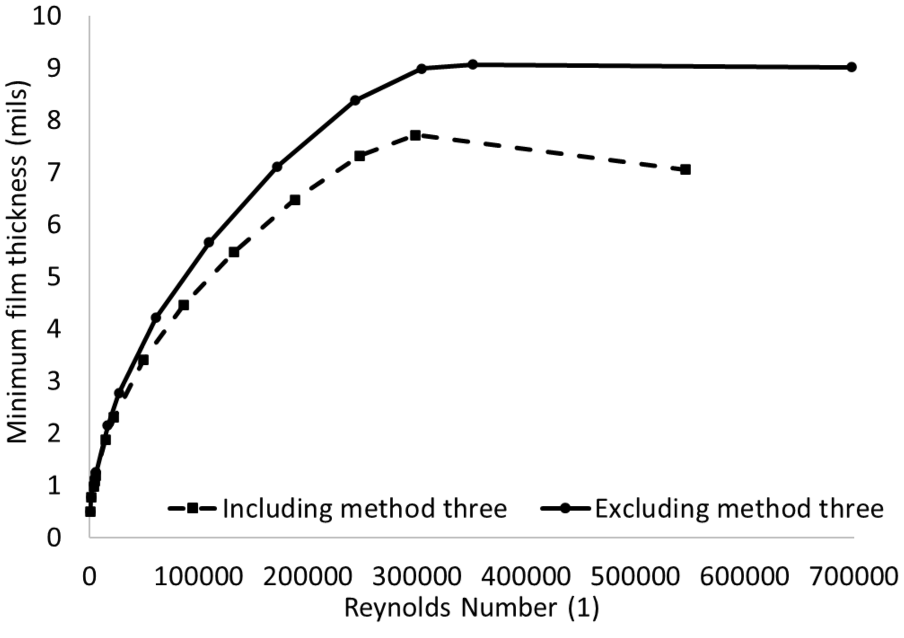

Figure 30. Minimum film thickness using methods two and three for applying Reichardt's formula for oil lubrication

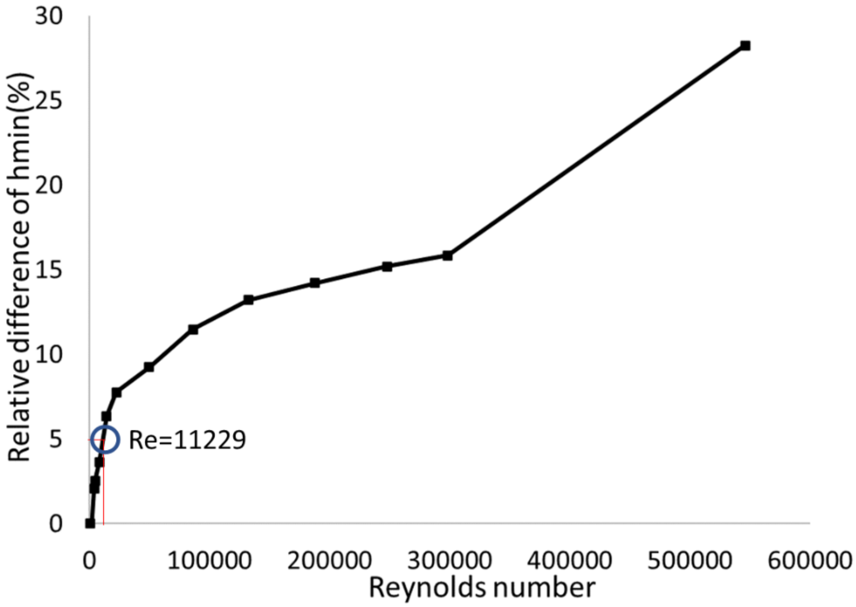

Figure 31. With method one, the relative difference between including and excluding methods three for oil lubrication

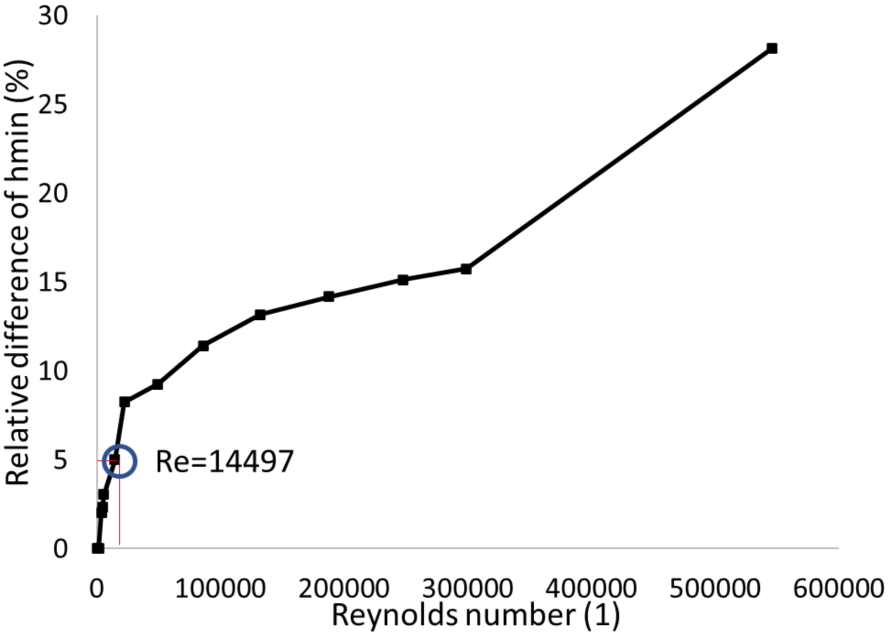

Figure 32. With method two, errors between including and excluding methods three for oil lubrication

2.6.2 The Influence of Method Three on Water Lubrication

The influence of method three with water lubrication was studied by including or excluding method three with either method one or method two. The results are shown in Figure 33 and Figure 34 for method one and method two, respectively. From Figure 33 and Figure 34, for water-lubricated conditions, the influence of method three is not as apparent as that for oil-lubricated conditions. The minimum film thickness with method three excluded is always predicted to be larger, though the difference is not as that large as that for oil-lubricated conditions. The calculated errors between these cases for each plot are shown in Figure 35 and Figure 36, respectively. From Figure 35 and Figure 36, the minimum film thickness shows more than a 5% difference between including or excluding method three for the Reynolds number below 23211 for both methods one and method two, with even higher values of relative difference at lower Reynolds numbers. These results show that overall, choosing method three for applying Reichardt's formula will primarily affect the minimum film thickness prediction. It is also worth noting that the overall trend in error is the opposite of the oil-lubricated case, where the error increased with speed.

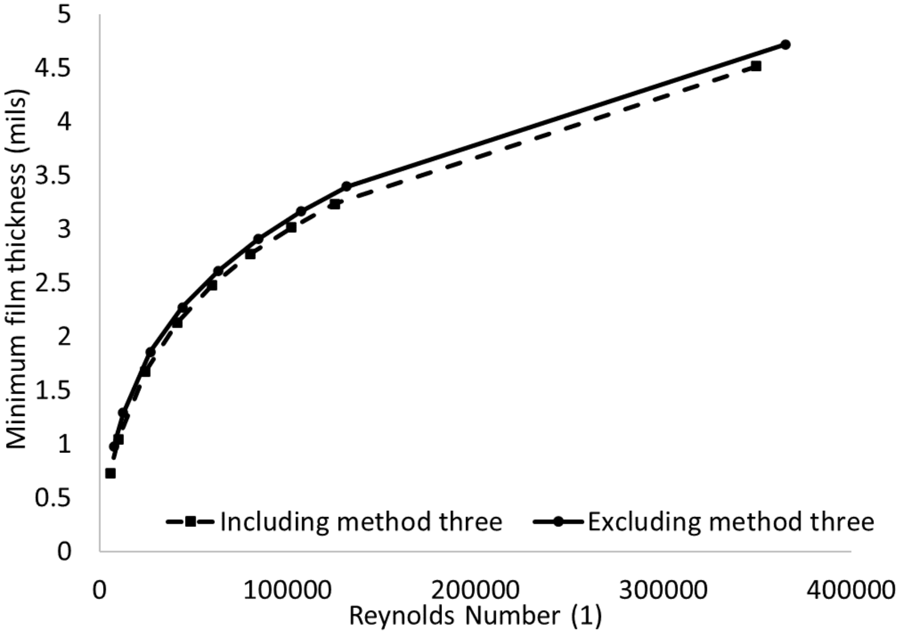

Figure 33. Minimum film thickness using methods one and three for applying Reichardt's formula for water lubrication

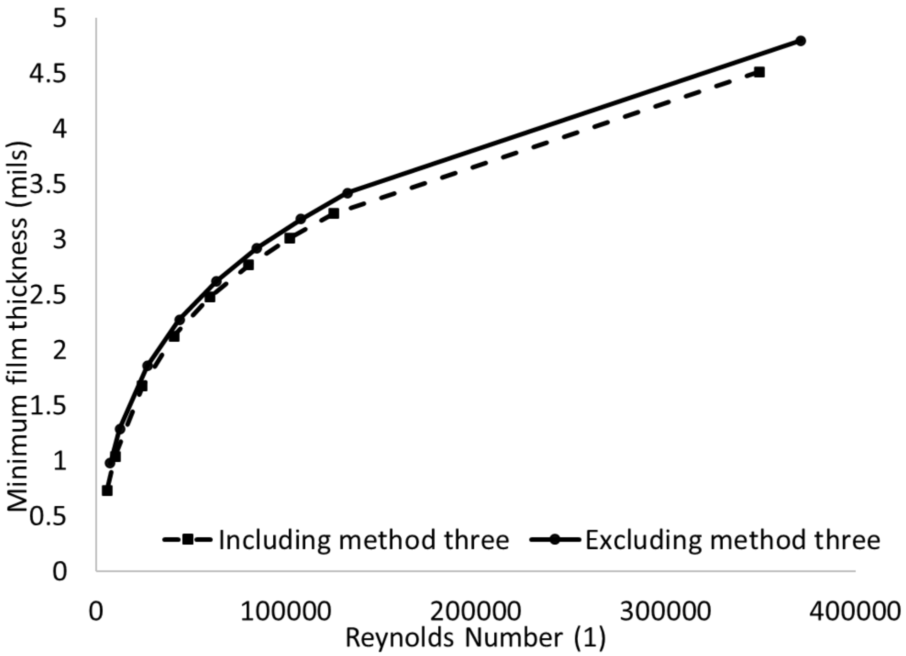

Figure 34. Minimum film thickness using methods two and three for applying Reichardt's formula for water lubrication

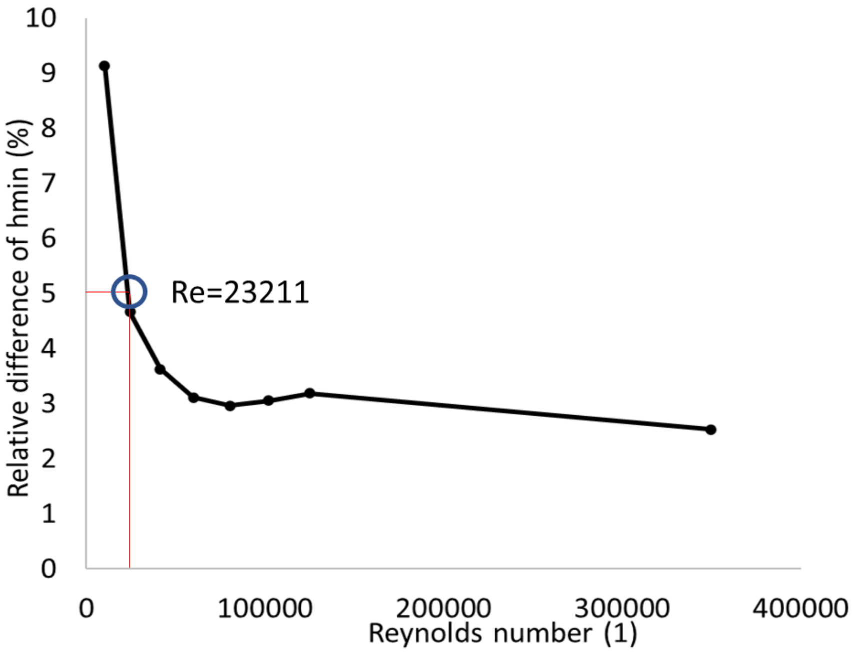

Figure 35. The relative difference between including and excluding method three with method one for water lubrication

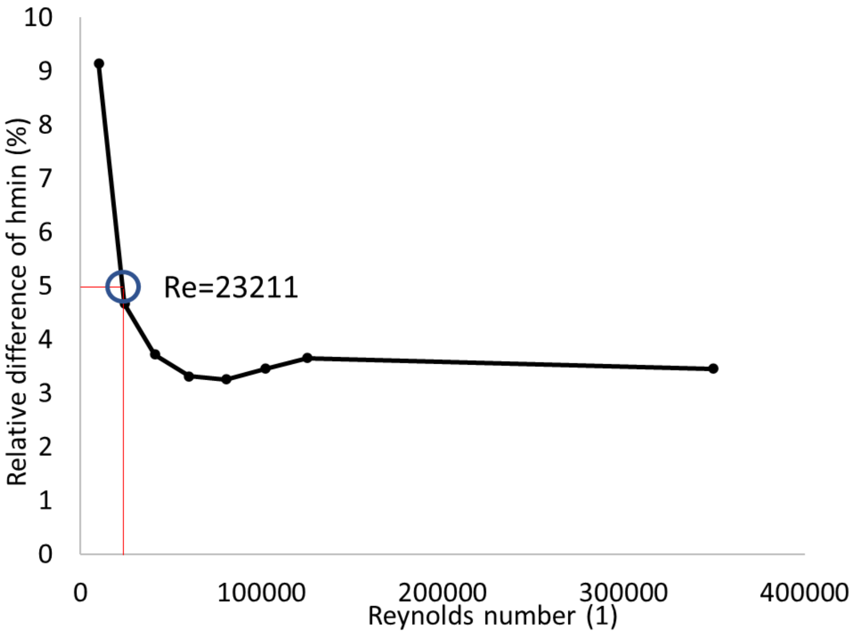

Figure 36. The relative difference between including and excluding method three with method two for water lubrication

2.6.3 The Influence of Methods One and Two

The influence of methods one and two was studied by comparing the minimum film thickness between methods one and two for both the inclusion and exclusion of method three for applying Reichardt's formula in the film, as well as for both oil-lubricated and water-lubricated conditions. The results of this comparison are shown in Figure 37, Figure 38, and Figure 39. In Figure 37, the minimum film thickness is predicted to be the same for method one and method two, with method three either included or excluded for the oil lubricated condition. In Figure 38, the minimum film thickness is predicted to be the same for method one and method two, with method three included or excluded for the water-lubricated condition. From this comparison of methods one and two, shown in Figure 39 and Figure 40, it can be concluded that both methods produce comparable results in their implementation. Method three is the primary source of variation.

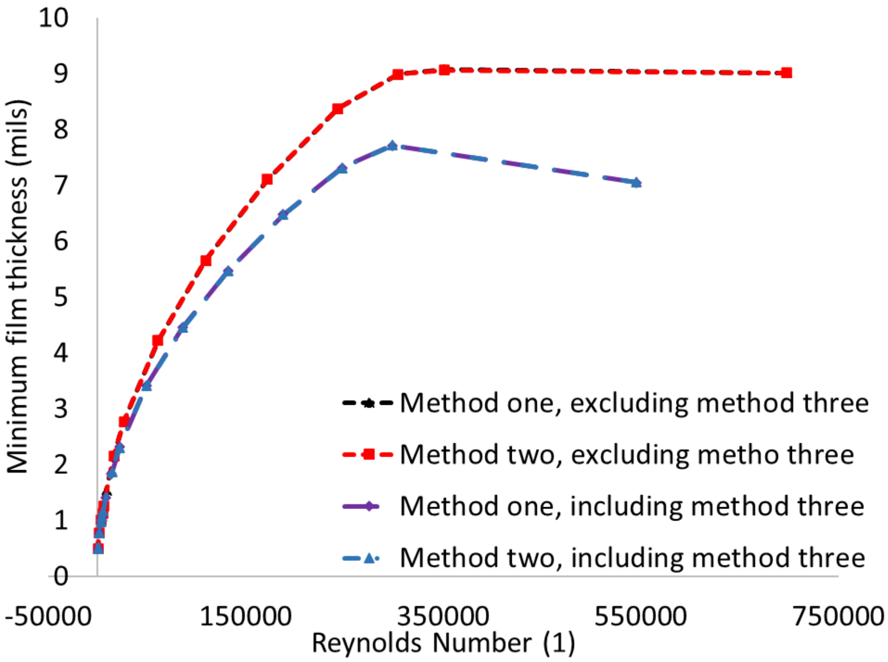

Figure 37. Minimum film thickness versus Reynolds number using method one or method two with method three included or excluded for oil lubrication

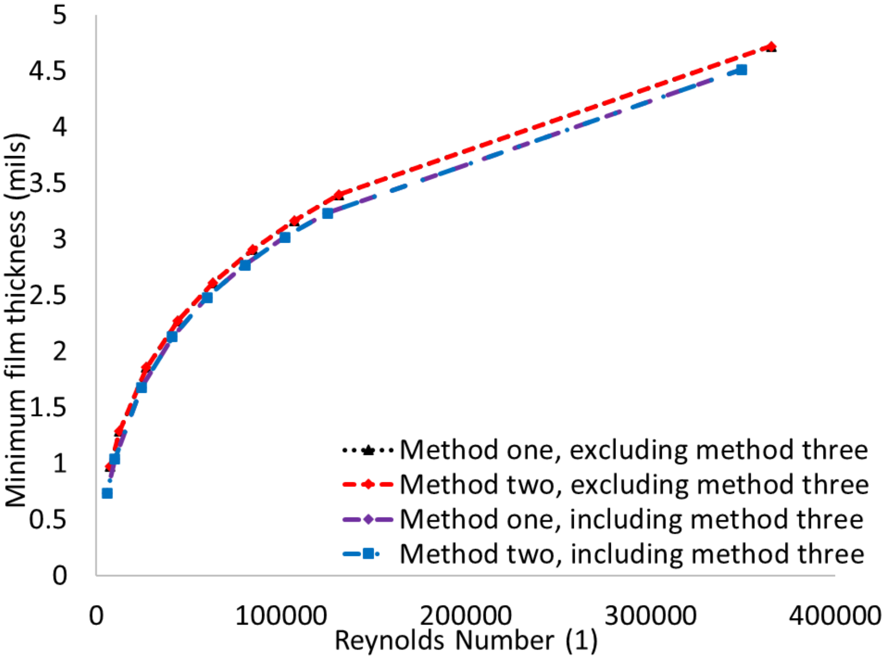

Figure 38. Minimum film thickness versus Reynolds number using method one or method two with method three included or excluded for water lubrication

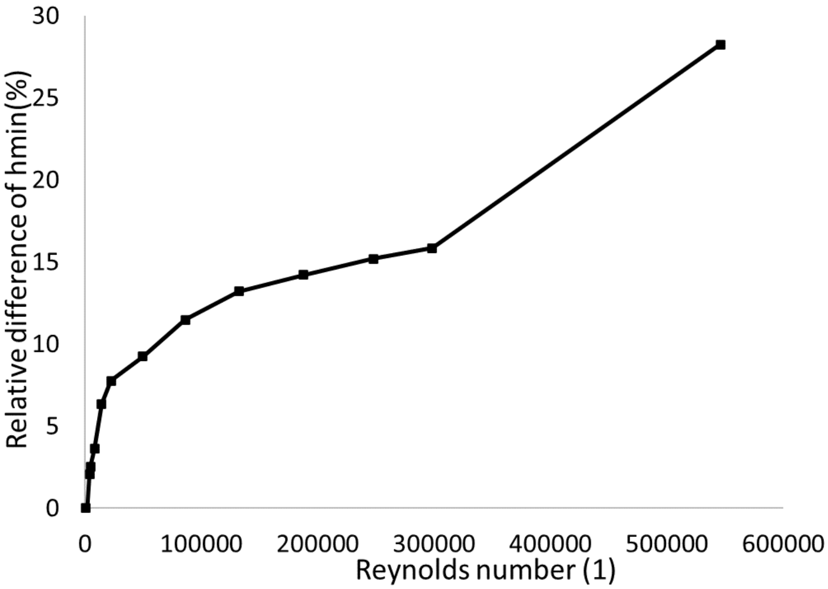

Figure 39. The relative difference between including and excluding method three with methods one and two versus Reynolds number for oil lubrication

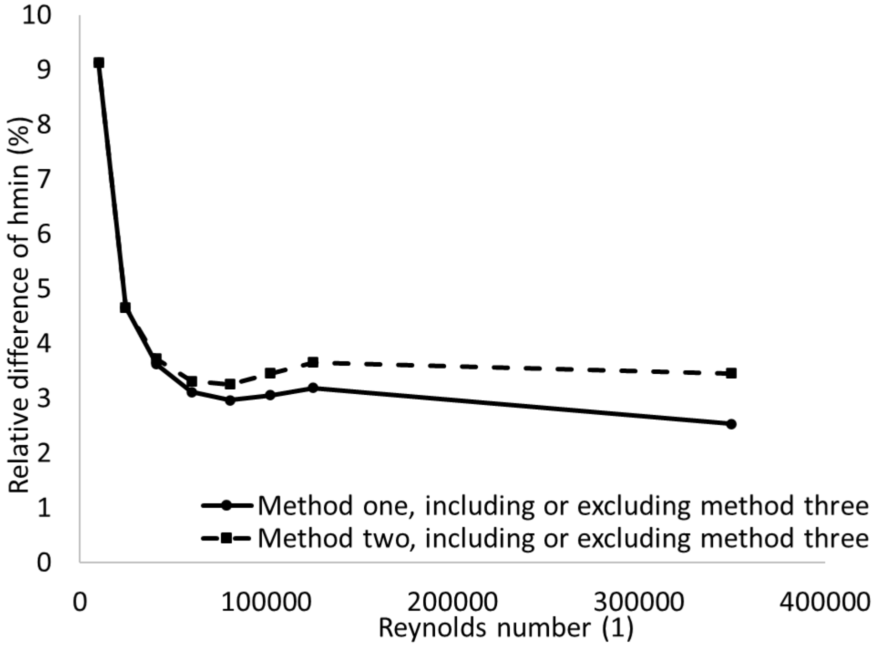

Figure 40. The relative difference between including and excluding method three with methods one and two versus Reynolds number for water lubrication

2.7 Discussion

The accuracy of the turbulence model is critical to modeling fluid film bearings in the high Reynolds region. Methods one, two, and three are various ways to apply Reichardt's formula for the eddy viscosity, which is highly important to turbulent flow calculations. Therefore, improving the accuracy of these methodologies is vital to improving the accuracy of bearing models and their ability to predict velocity and velocity gradients in the film. The accuracy of velocity gradients is a core factor in predicting the film's shear stress. The accuracy of all of these predictions is critical to predicting an accurate equilibrium state in the bearing film, the accuracy of which is vital to predicting load-carrying capabilities and dynamic performance. Creating an accurate model to capture the behavior of these bearings at equilibrium conditions would be of great value to the bearing industry. While a few studies have illustrated these three methods, there have been no model-to-model comparisons for applying Reichardt's formula.

This research work studied the influence of methods one, two, and three on minimum film thickness. The results showed that choosing method three for applying Reichardt's formula largely affected the minimum film thickness for oil-lubricated bearings. In contrast, the effect was less pronounced but still significant for water-lubricated bearings. The minimum film thickness with method three excluded was always predicted to be larger than that of the included case for both oil and water lubrication. The minimum film thickness showed more than a 5% difference between including or excluding method three when the Reynolds number reaches around 11229 for method one and 14497 for method two for oil-lubricated bearings, with more significant variation occurring at higher Reynolds numbers. For water-lubricated bearings, the minimum film thickness showed more than a 5% difference between including or excluding method three for the Reynolds number below 23211 for both method one and method two, with larger errors at lower Reynolds numbers. The only significant difference between method one and method two was that for method two, the minimum film thickness shows more difference between including or excluding method three at higher Reynolds numbers.

The ability to control these three methods applied for eddy viscosity gives engineers significant knowledge to design and model fluid film bearings. This research provides new insight and comparisons of the current state of the art. Improving the accuracy of bearing performance predictions due to eddy viscosity effects is essential, especially considering the increasing application of high Reynold's number oil-lubricated or water-lubricated bearings in high-speed industrial machinery. This control will allow for additional comparisons with experimental data as well.

One significant finding from this study was that the minimum film thickness shows a significant sensitivity to runner thermal deformation, as shown in Figure 41 and Figure 42. As there was no difference between methods one and two, only method one was used here. Figure 41 and Figure 42 are for oil-lubricated conditions, while Figure 43 and Figure 44 are for water-lubricated conditions. As shown in Figure 41, with runner thermal deformation included or excluded, the minimum film thickness shows an initial increase followed by a decrease as the Reynolds number increases. Figure 42 shows a range of relatively low error (of ~10%) caused by including or excluding runner thermal deformation. The minimum film thickness difference in the high Reynolds number flow region increases significantly. As shown in Figure 43 (water lubrication), with runner thermal deformation included or excluded, the minimum film thickness continuously increases as the Reynolds number increases. Figure 44 shows that there is also a relatively consistent difference of ~15% caused by including or excluding runner thermal deformation for the water-lubricated case. In the high Reynolds number flow region, the errors also increase.

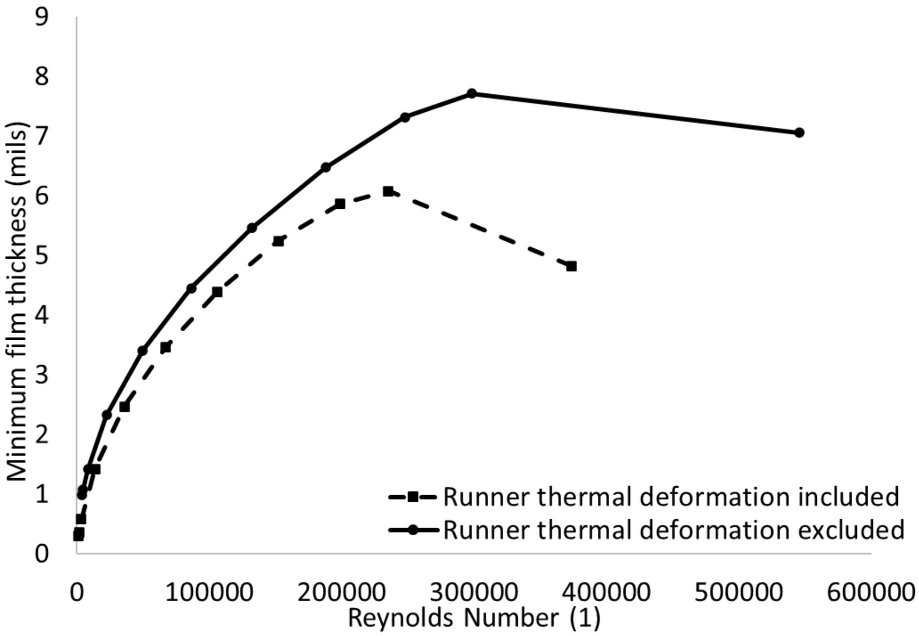

Figure 41. Minimum film thickness versus Reynolds number with runner thermal deformation included and excluded for oil lubrication

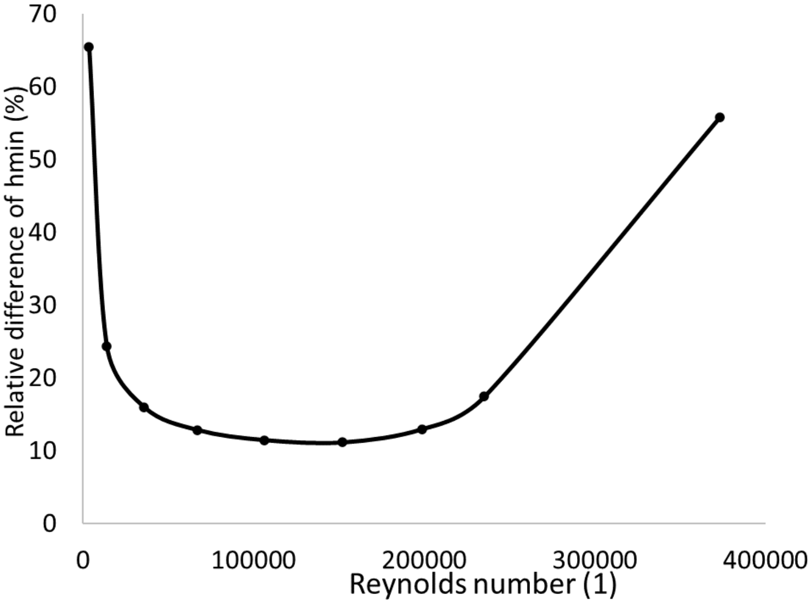

Figure 42. The relative difference between including and excluding runner thermal deformation versus Reynolds number for oil lubrication

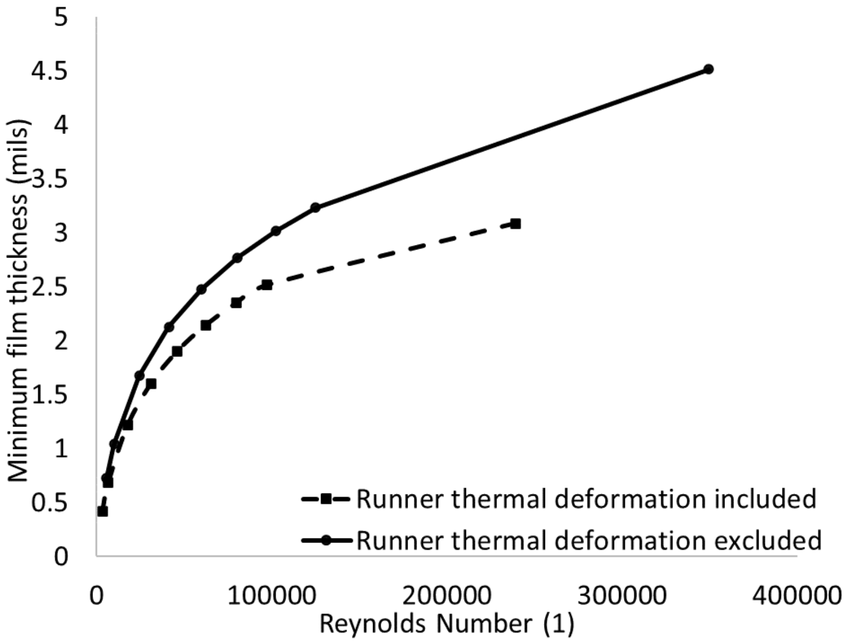

Figure 43. Minimum film thickness versus Reynolds number with runner thermal deformation included and excluded for water lubrication

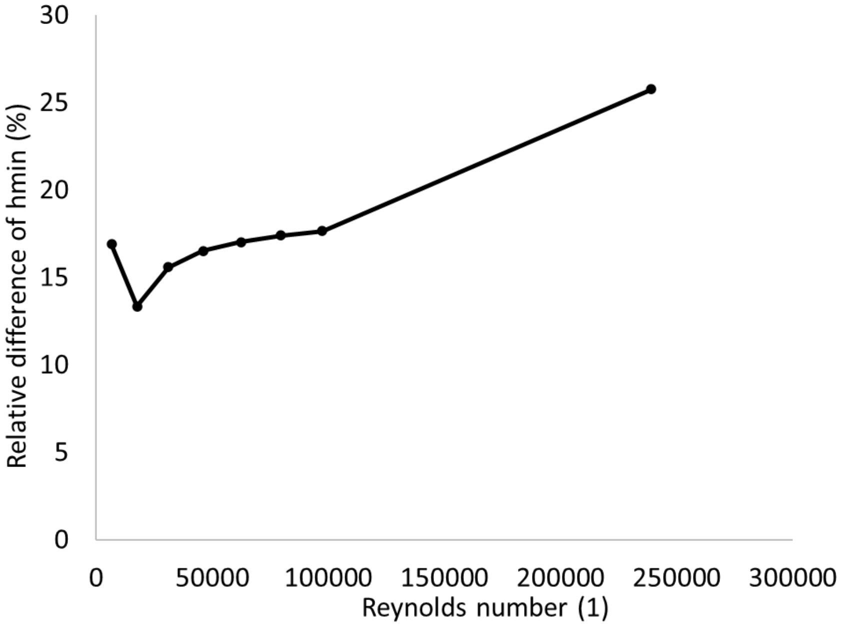

Figure 44. The relative difference between including and excluding runner thermal deformation versus Reynolds number for water lubrication

2.8 Conclusion

This section presented a study of three different methods for applying Reichardt's formula in eddy viscosity calculations for turbulent fluid film bearings. The study focused primarily on eddy-viscosity due to its importance to turbulence models commonly used in bearing analysis tools. A wide range of Reynolds numbers have been analyzed, showing unique behavior at higher and lower Reynolds number flows for oil and water lubricated conditions.

Three methods of applying Reichardt's formula have been analyzed. The shear value in Reichardt's formula was originally intended to be the shear stress at the wall. Method one applies Reichardt's formula from both the upper and lower walls with a calculated equilibrium position separating the effects of each wall. Method two assumes that the eddy-viscosity can be calculated from the local shear stress value in the fluid films. This method applies Reichardt's formula from both the upper and lower walls with an equilibrium position separating the effects of each at the center of the fluid film. The eddy-diffusivity in the upper one-half of the flow is influenced by the upper wall, while the lower wall influences the eddy-diffusivity in the lower half of the flow. The eddy-viscosity in method three is allowed to vary from Reichardt's formula in the core of the flow. The core region is fully turbulent and contains three inner interfaces in the direction from the bearing surface to the runner. This emphasis on eddy-viscosity was due to its importance to turbulence models commonly used in bearing analysis tools. A wide range of Reynolds numbers has been analyzed, showing unique behavior at higher and lower Reynolds number flows for oil and water-lubricated conditions. Including method three in applying Reichardt's formula produced a lower, more conservative film thickness prediction, an essential consideration for design engineers. This lower film thickness is due to a higher temperature (lower viscosity) for method three. The method with a core turbulence region significantly increases the wall shear stress for oil lubrication. For water lubrication, no existing method shows a different effect in predicting wall shear stress. Future work should include additional comparisons with experimental data to further validate these approaches. Overall, this knowledge is valuable and essential to accurately modeling and designing high-speed fluid film bearings used in high-performance industrial applications.

3. Methodology of Turbulence Parameter Correction in Water-Lubricated Thrust Bearings

Oil-lubricated bearings are widely used in high-speed rotating machines such as those found in automotive, power generation, and aerospace industries. However, environmental issues and risk-averse operations result in oil removal and replacement of all sealed oil bearings with reliable water-lubricated bearings. The low viscosity of water increases the Reynolds numbers drastically, making water-lubricated bearings prone to turbulence. This requires finer meshes for finite element modeling when compared to oil-lubricated bearings, as the low-viscosity fluid produces a very thin lubricant film. Analyzing water-lubricated bearings can also produce convergence and accuracy issues in traditional oil-based analysis codes.

Fitting the velocity profile with experiment data having a non-dimensional wall distance y^+ in a specific range, results in Ng-optimized Reichardt's constants k and δ^+. The definition of y^+ can be used to approximate the first layer thickness calculated for a uniform mesh. On the condition that the y^+ is fixed to that of a standard oil bearing for which an oil-bearing code was validated. The number of elements across the film thickness and coefficients used in the eddy-viscosity equation can be adjusted to allow for convergence with fluids other than what the traditional oil-bearing code was designed for. The research questions in chapter three are: Q1 - Is the traditional oil lubrication modeling equation adequate for water lubrication? Q2 - What are the additional modifications needed for water lubrication modeling, due to the different thermal characteristics of oil and water? This study proposed a new methodology to preserve the y^+ value to make water-lubricated thrust-bearing models valid. A method for determining the required number of cross-film elements in water-lubricated bearings was found. The results of this study can be used to improve the numerical model accuracy and thereby aid in improving future performance and designs of water-lubricated bearings.

3.1 Introduction

Bearings are machine elements that allow components to move relative to each other. Bearings are used in many applications, from supporting skyscrapers to allow them to move during earthquakes to enabling the most delicate watches to operate precisely. There are generally two types of bearings: contacting and non-contacting. Contact-type bearings involve mechanical contact between elements. Non-contact bearings include externally pressurized, hydrodynamic fluid-film, and magnetic bearings. The life of non-contact bearings could be virtually infinite if the external power units required to operate them do not fail. In this paper, fluid-film bearings were analyzed.

The industrial revolution was made possible by rotating shafts supported by thin films of lubricant induced by hydrodynamic shear. The working principle of fluid film thrust bearings is shown in Figure 45. A convergent wedge of fluid producing a hydrodynamic lift is generated by the fluid dragged into the gap by viscous shear. With the increase in velocity, the lubrication regime will go through boundary lubrication, mixed lubrication, and hydrodynamic lubrication (full film). In this research work, the analysis focuses on the hydrodynamic lubrication region.

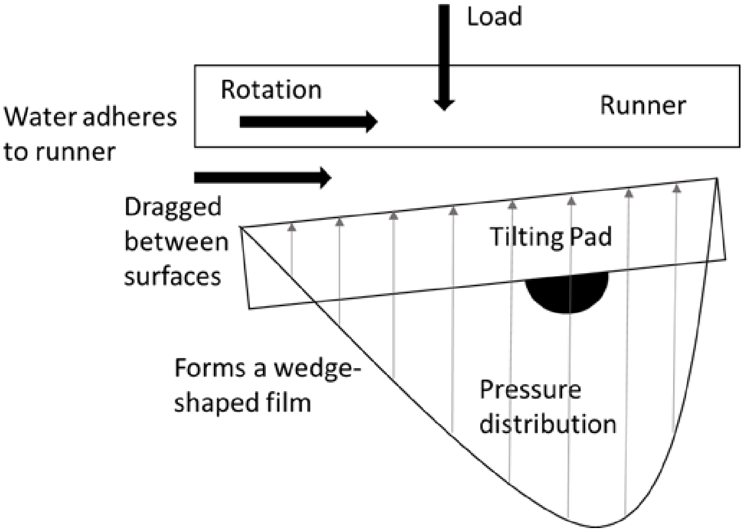

Figure 45. Working principle of fluid film bearings: convergent wedge

There are two well-known approaches to study turbulent lubrication: Prandtl mixing length theory [35] [36] [37] [38] [39] [40] [41] presented by Constantinescu and boundary layer theory presented by Elrod, Ng, and Pan [43] [34] [42] [44] [45]. Constantinescu treated the turbulent shearing stresses by introducing Prandtl's mixing length theory. In contrast, Ng and Pan considered turbulent shear stress by introducing

Prandtl's law of the wall. A common method to model turbulence is by using an eddy-viscosity in the Reynolds equation [34]. The eddy viscosity model is presented as

$$\mu^*(x, y, z) \equiv \mu(1 + \beta \frac{\varepsilon_m}{\nu}) \qquad \text{Eq. 25}$$

In which μ^* is the eddy viscosity, μ is the dynamic viscosity, β is the transition constant, ϵ_m is the wall shear stress, and ν is the kinematic viscosity. Reichardt's formula gives these eddy diffusivities for momentum divided by the kinematic viscosity [48]. Reichardt's formula is presented as

$$\frac{\epsilon_m}{\nu} = \kappa \left[z^+ - \delta^+ \, tanh \left(\frac{z^+}{\delta^+} \right) \right] \qquad \text{Eq. 26}$$

In which κ is an empirically determined constant that ranges from 0.3 to 0.4, δ^+ is also an empirically determined constant. Reichardt originally proposed $\kappa = 0.4$ and $\delta^+ = 11$ [43]. Ng optimized the constants $\delta^+ = 10.7$ based on published experimental data and yielded accurate results over the range $0 < z^+ < 1000$ [34]. Ng stated that κ should decrease to 0.3 as z^+ became greater than 1000.

Some researchers worked on optimizing parameters in Reichardt's formula to optimize turbulence model behavior for water-lubricated thrust bearings. Armentrout [46] developed a method to adjust δ^+ within Reichardt's formula as a function of the Reynolds number at the pad pivot location. The challenge of modeling water lubrication is that Reynolds numbers are almost entirely in the turbulent regime, creating a need for finer meshes as the low fluid viscosity produces a very thin fluid film. Meshing can also cause convergence and accuracy issues in traditional oil-based codes. Cavitation is often suppressed through high ambient pressure in water-lubricated bearings as well. Moreover, there are also challenges posed by the different thermal characteristics between oil and water.

Sun applied a Reynolds-averaged Navier–Stokes (RANS) approach to the turbulence closure of mean and fluctuating variables and entropy production [83]. Huebner presented a numerical scheme to study the effects of temperature-dependent viscosity on the performance of bearings operating in the thermohydrodynamic turbulent regime [76]. Capitao compared Constantinescu's and Ng's approaches and found that numerical results produced by the two turbulence theories were not significantly different for standard tilting pad thrust bearings [60]. Hashimoto theoretically presented a method to solve the turbulent lubrication problems of sector-shaped, tilting-pad thrust bearings with pad deformations and centrifugal forces [84]. Chowdhury studied a wide thrust bearing in the turbulent flow regime theoretically with inertial and thermal effects considered [85]. Deng compared three different methods to apply eddy viscosity with a zero equation turbulent model for turbulent fluid-film bearings [86]. Gohara studied the static characteristics of a water-lubricated hydrostatic thrust bearing with a membrane restrictor without rotation numerically and experimentally [87]. San Andrés detailed a hydrostatic thrust bearing water-lubricated test rig's design, construction, operation, and test results [88]. Lin studied water-lubricated spiral groove thrust bearings using commercial software [89]. No study about the meshing problem in water-lubricated turbulent thrust bearing has been found in the known literature. However, the mesh is a critical parameter to achieve convergence in turbulent water lubrication, especially for traditional oil-lubricated verified finite element thermo-elasto-hydrodynamic (TEHD) codes.

The challenge of modeling water lubrication is that Reynolds numbers are almost entirely in the turbulent regime, creating a need for finer meshes as the low fluid viscosity produces a very thin fluid film. The mesh can also cause convergence and accuracy issues in traditional oil-based codes. Cavitation is often suppressed through high ambient pressure in water-lubricated bearings as well. The challenge also lies in the different thermal characteristics of oil and water. Thermal deformation predominantly affects oil lubrication while having limited effects on water lubrication since the viscosity of the water is low, and the specific heat of the water is significantly larger, even though turbulence in the bearings increases the temperature of the water as well. Mechanical deformation can be more prominent with water lubrication, while its effects are typically lower than thermal deformation with oil lubrication. Therefore, preserving the y^+ value to make water-lubricated thrust bearing models valid is the main concern of this study.

3.3 Methodology

Non-dimensional wall distance y^+ for the wall-bounded flow can be defined in Eq. 27. y^+ is often referred to simply as *y plus* and is commonly used in boundary layer theory and in defining the law of the wall.

$$y^{+} \equiv \frac{u_{*}y}{\nu} \qquad \text{Eq. 27}$$

Where u_{*} is the friction velocity at the nearest wall, y is the distance to the nearest wall, and ν is the local kinematic viscosity of the fluid. Shown in Figure 46, δ^{+} is a dimensionless thickness of viscous sublayer, y^{+} is dimensionless wall distance for the mesh.

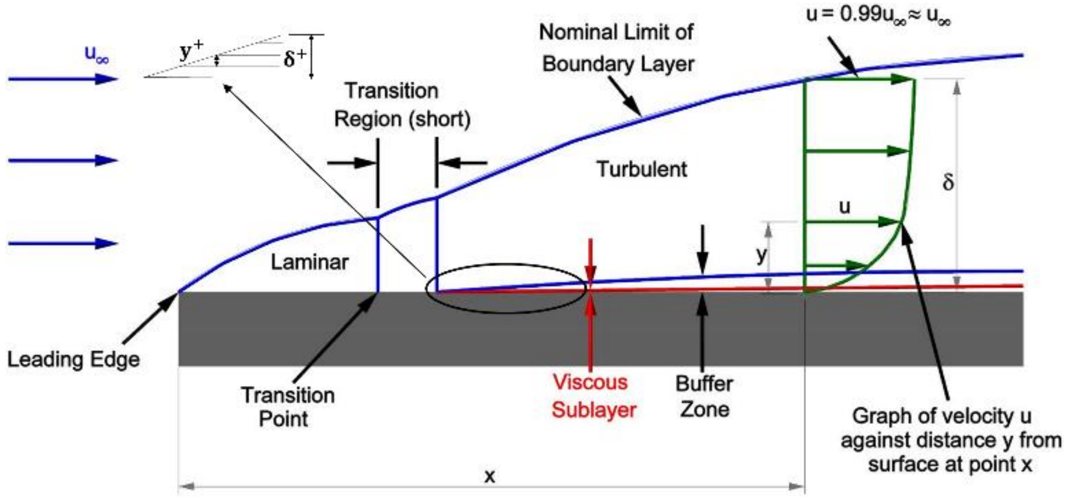

Figure 46. Turbulent boundary layer

Any flow's non-dimensional characteristics should be respected for models to work properly. According to Szeri [90], ε_{m}/ν for the Boussinesq hypothesis is given by Reichardt's formula, fitting the velocity profiles with experiments, with a y^{+} in the range of 0-1000. This results in Ng-optimized Reichardt's constants of $k = 0.4$ and $\delta^{+} = 10.7$ [43]. Szeri states that for $y^{+} > 1000$ theoretical predictions and experiments have greater variance.

Some researchers tried optimizing parameters in Reichardt's formula to optimize the turbulence model for water-lubricated thrust bearings. Armentrout [46] developed a method to adjust δ^{+} within Reichardt's formula as a function of the Reynolds number at the pad pivot location, which they validated with CFD simulations, shown in Eq. 28. The relation between δ^{+} and the Reynolds number at the pad pivot location in a journal bearing is shown in Figure 47. These refinements brought the calculated bearing load capacities and power losses of the conventional Reynolds model into better agreement with those of the CFD model for a broad range of operating conditions [46]. One advantage of the CFD model is that CFD can include film entrance inertia, convective inertia, and temporal inertia [91].

$$\delta^{+} = \alpha e^{-\beta Re_p}$$ Eq. 28

Where

$$Re_p = \frac{\rho u h}{\mu} = \frac{\Omega D h}{\nu}, \alpha = 10.1, \beta = -1.57e-5$$ Eq. 29

In which ρ is the density, u is the moving surface velocity, h is the film thickness, μ is the dynamic viscosity, Ω is the rotor speed, D is the diameter of the rotor, and ν is the kinematic viscosity.

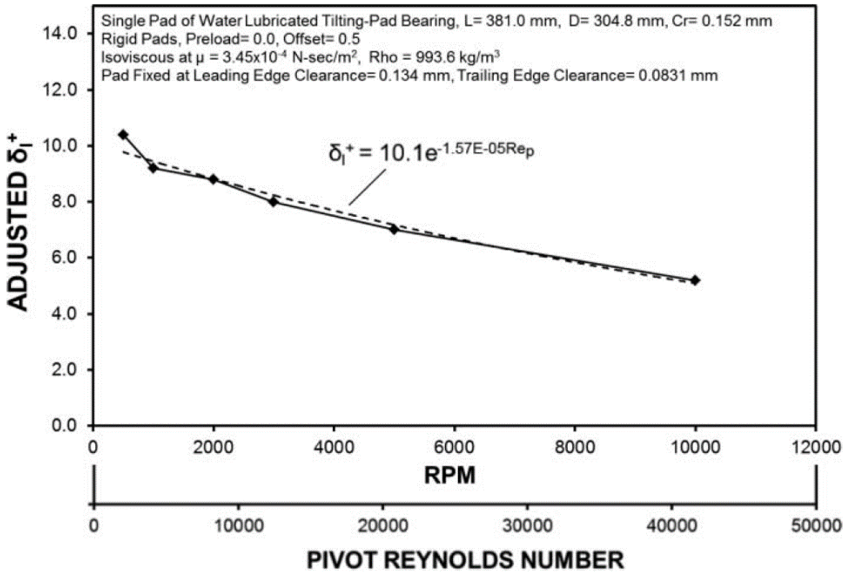

Figure** 47. **Adjusted $\boldsymbol{\delta^+}$ versus pivot Reynolds number [46]

Similarly, the following equation can approximate the definition of y^+ where d^* is the first layer thickness calculated for a uniform mesh, N is the number of elements across the film thickness h, and u is the moving surface velocity.

For a uniform mesh:

$$d^* = \frac{h}{N}$$ Eq. 30

Therefore:

$$y^+ = \frac{ud^*}{\nu} \sim \frac{\Omega D h}{\nu N}$$ Eq. 31

$$u \sim \Omega D$$ Eq. 32

For typical turbulence models, the value of y^+ must be within a specific range to maintain accuracy. Therefore, it can be assumed that if the y^+ is fixed to that of a standard oil-lubricated bearing for which the modeling tool was validated, the following formulation can be used to adjust the mesh number N to allow for absolute convergence with other fluids such as water. Specifically, the kinematic viscosity can be varied for use with different fluids assuming the rotational speed, diameter, and fluid film thickness are within reason from the original experiments used to validate THRUST. By fixing y^+ of the water lubrication equals to y^+ of the oil lubrication, an equation for the required number of elements N across the film for water lubrication can be generated:

$$y^+_{water} = y^+_{oil} \qquad \text{Eq. 33}$$

$$N_{water} = \frac{h_{water}}{h_{oil}} \frac{\Omega_{water} D_{water}}{\Omega_{oil} D_{oil}} \frac{\nu_{oil}}{\nu_{water}} N_{oil} \qquad \text{Eq. 34}$$

Where variables with the subscript 'oil' are for oil-lubricated conditions since most current thrust codes are verified with oil lubrication. The subscript '$water$' is then used for water-lubricated conditions. Converting the kinematic viscosity to the fluid density and dynamic viscosity used by TEHD modeling tools, the equation for the required cross-film element number then becomes:

$$N_{water} = \frac{h_{water}}{h_{oil}} \frac{\Omega_{water} D_{water}}{\Omega_{oil} D_{oil}} \frac{\rho_{water}}{\rho_{oil}} \frac{\mu_{oil}}{\mu_{water}} N_{oil} \qquad \text{Eq. 35}$$

3.2 Modeling

The bearing modeled in this analysis is a water-lubricated sector-pad thrust bearing consisting of six tilting pads, as shown in Figure 48, the inner radius of the pad is 190.5 mm, and the outer radius of the pad is 444.5 mm. The modeling was performed with a thrust bearing code (THRUST) developed by the Rotating Machinery and Controls Laboratory (ROMAC) at the University of Virginia, the theoretical details of which can be found in [71] [92]. An operating speed of 1,800 rpm was used along with an isothermal assumption with constant viscosity. Multiple pad loads were considered, as was the presence of turbulence. The initial guess to the pivot film thickness was a value obtained from a proprietary benchmark code that has been rigorously verified through experimental comparisons and CFD analysis.

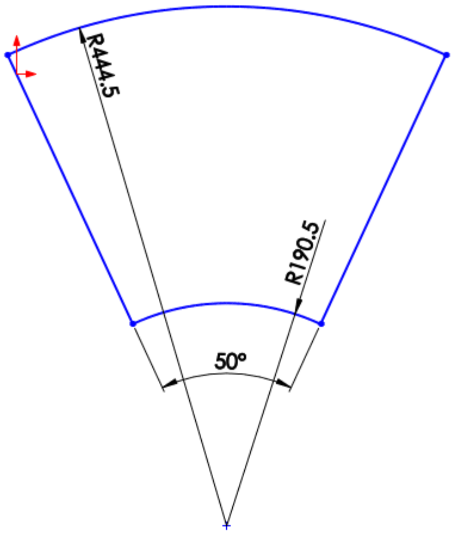

Figure 48. Pad geometry

This thrust bearing code predicts the steady-state operating characteristics of thrust bearings. As a TEHD prediction tool, THRUST assumes Reichardt's formula for the turbulence model, shown in Eq. 26, generalized 2D Reynolds equation for turbulent flow, shown in Equation 27, and 3D energy equation, shown in Equation 28. Turbulence is included by obtaining average values of eddy momentum flux (Reynolds stress) and averaging the influence to a 2D Reynolds equation. Convergence is achieved by iterating on the pad tilting angles and film thickness at the pad pivot location until the integrated pressure matches the load applied to the pad.

The truncation error of individual terms in the governing numerical equations is achieved by evaluating the root mean square (RMS) value. The essential features of the RMS methods are shown in Eq. 38.

$$\frac{1}{r}\frac{\partial}{\partial r}\left(\Gamma_2 r\frac{\partial \hat{p}}{\partial r}\right)+\frac{1}{r}\frac{\partial}{\partial \theta}\left(\Gamma_2\frac{1}{r}\frac{\partial \hat{p}}{\partial \theta}\right)=\omega\frac{\partial}{\partial \theta}\left(\frac{\Gamma_1}{\Gamma_0}\right)-\frac{\partial h}{\partial t}-v_d \qquad \text{Eq. 36}$$

$$c_p\left[\left(u_r\frac{\partial T}{\partial r}\right)+\frac{u_\theta}{r}\frac{\partial T}{\partial \theta}+u_z\frac{\partial T}{\partial z}\right]=\frac{1}{r}\frac{\partial}{\partial r}\left[k^* r\frac{\partial T}{\partial r}\right]+\frac{1}{r^2}\frac{\partial}{\partial \theta}\left[k^*\frac{\partial T}{\partial \theta}\right]+$$
$$\frac{\partial}{\partial z}\left[k^*\frac{\partial T}{\partial z}\right]+Q+\mu^*\left[\left(\frac{\partial u_r}{\partial z}\right)^2+\left(\frac{\partial u_\theta}{\partial z}\right)^2\right] \qquad \text{Eq. 37}$$

$$RMS=\sqrt{\frac{\sum_{i=1}^{n}(\hat{y}_i-y_i)^2}{n}} \qquad \text{Eq. 38}$$

3.4 Results

The results of the comparisons of the minimum film thickness H_{min} and the film thickness at the pad pivot location H_{piv} between the benchmark and TEHD modeling tool, with and without a modified cross-film element number via Eq. 35, are shown in Figure 49 and Figure 50. Experimental comparisons and CFD analysis have rigorously verified the proprietary code used as the benchmark. Both H_{min} and H_{piv} are shown to decrease with an increase in the bearing load. H_{min} from the benchmark was consistently significantly larger than the THRUST results with the cross-film element number unmodified. In contrast, the modified THRUST results with the cross-film element number resulted in an excellent match, particularly for loads above 7.56 kN. H_{piv} from the benchmark code, was also significantly larger than the THRUST results with the cross-film element number unmodified. However, the match between the benchmark and THRUST was significantly improved with the modified cross-film element number. Both H_{min} and H_{piv} from THRUST with a modified cross-film number demonstrated significant increases compared with the unmodified cases.

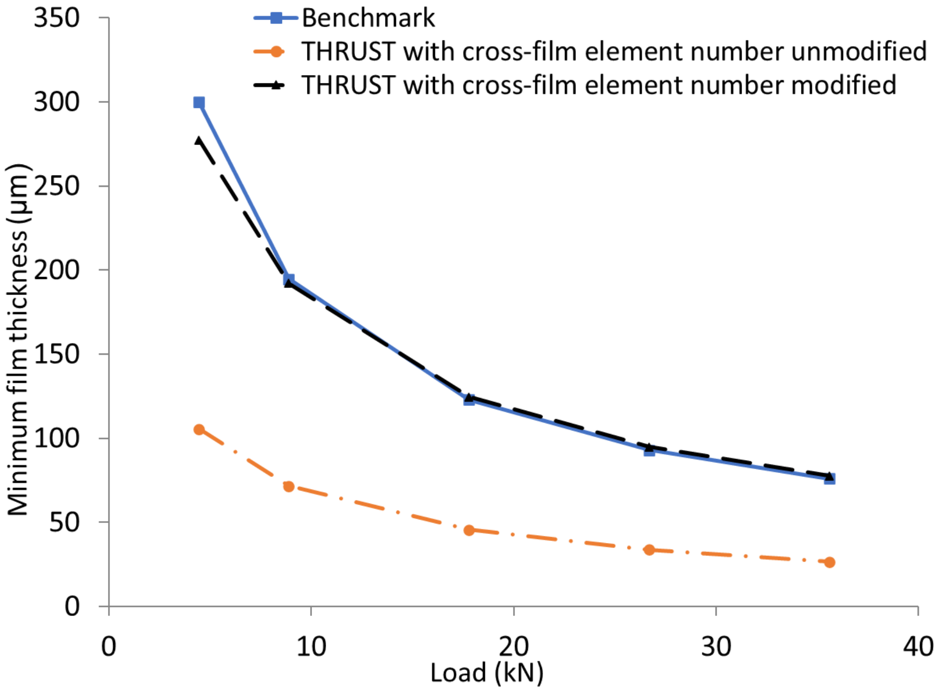

Figure 49. Comparison of minimum film thickness between the benchmark code and thrust bearing code with and without an optimized cross-film element number

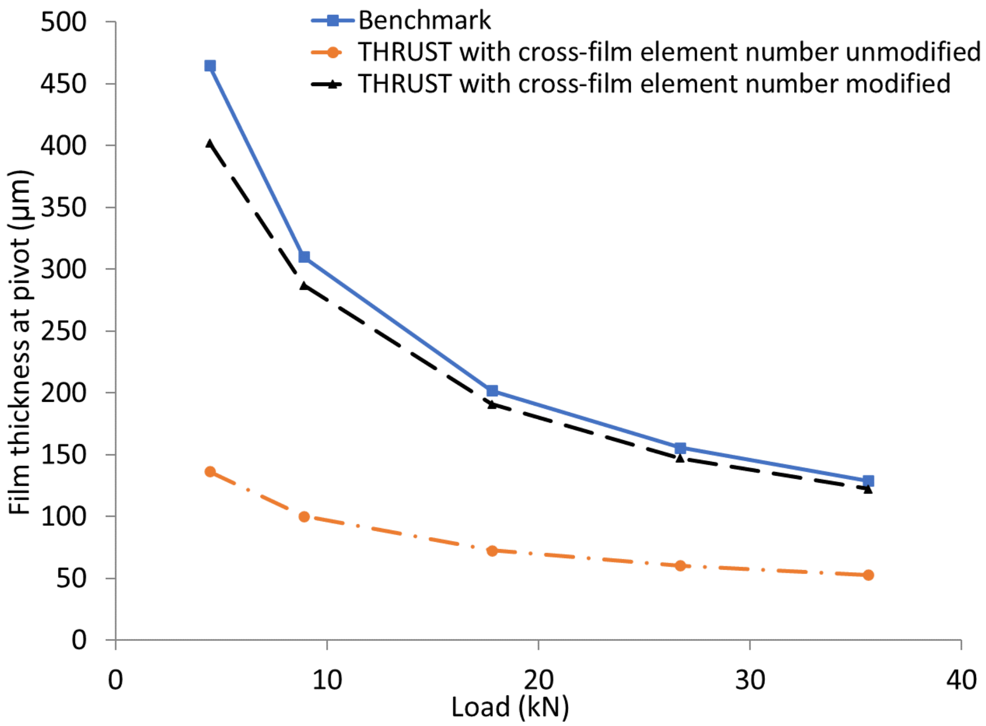

Figure 50. Comparison of pivot film thickness between the benchmark code and thrust bearing code with and without an optimized cross-film element number

Based on the minimum film thickness and film thickness results at the pad pivot location, the absolute values of the relative differences between the benchmark and THRUST with the cross-film element numbers modified and unmodified are shown in Figure 51 and Figure 52. Significant differences are seen between the benchmark and THRUST with an unmodified cross-film element number. However, after optimizing the cross-film element number to obtain an appropriate y^+ value, a good agreement between the benchmark and THRUST was found. For the relative differences in minimum film thickness, most values were found to be less than 3 %, with a slightly higher value at the lowest load case. Only one case exceeded 8% at low load. For the relative differences in film thickness at the pad pivot location, most values were found to be less than 8 %. Only one case exceeded 8% (low load case).

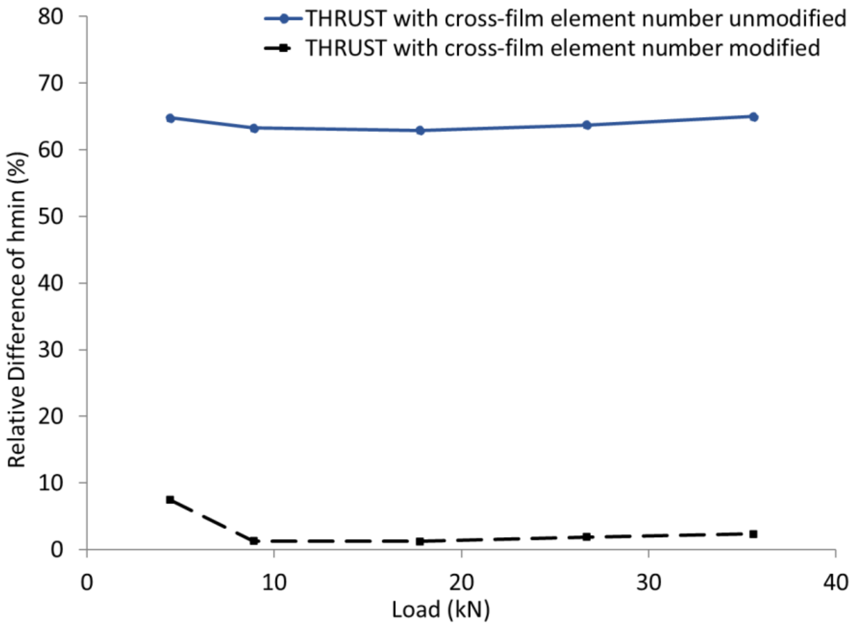

Figure 51. The relative difference of minimum film thickness predictions between the benchmark code and thrust bearing code with and without a modified cross-film element number

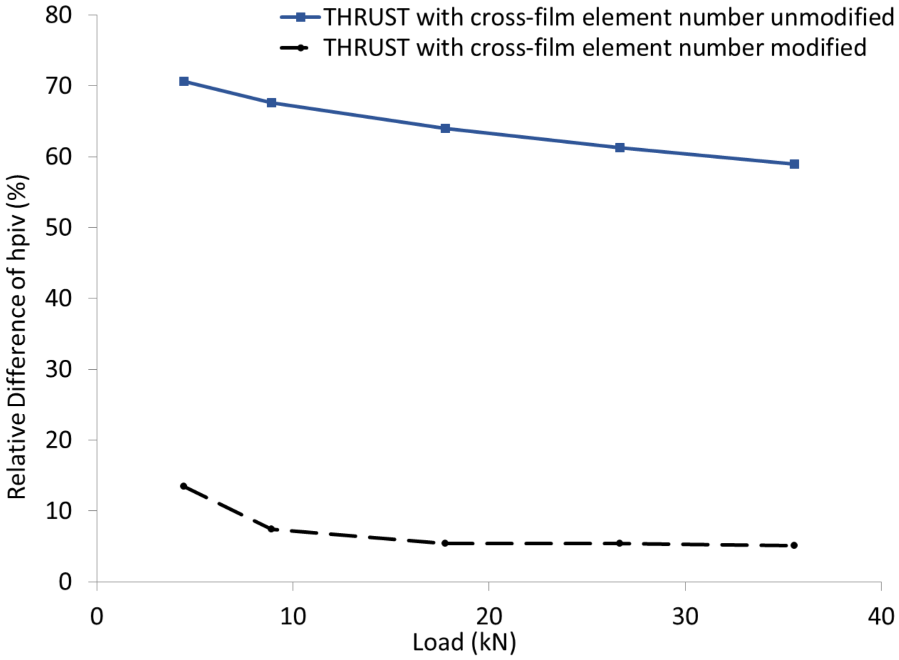

Figure 52. The relative difference of pivot film thickness predictions between the benchmark code and thrust bearing code with and without an optimized cross-film element number

The comparison of the maximum pressure in the fluid film between the unmodified and modified cross-film element numbers is shown in Figure 53. It is known that after optimizing the cross-film element number, the maximum pressure in the fluid film region is very close to the benchmark results and much better than that without optimization. The largest relative difference between the optimized case and benchmark is 2.6 %. The pressure contour of the highest load, THRUST, with an optimized cross-film element number (A) and without (B), is shown in Figure 54. The x and y are the Cartesian coordinates for the pad, and the pressure measurements are expressed in psi. It can be seen from Figure 54 that the pressure profile appears as expected with the optimized cross-film element number. While for the unmodified case, the pressure contour does not appear correct in the following three aspects. First, the overall distribution shape is not correct. Second, the pressure gradient shape near the pad pivot location is too narrow in the circumferential direction. Thirdly, the negative pressure value of the entrance inertia [93] is unrealistically low.

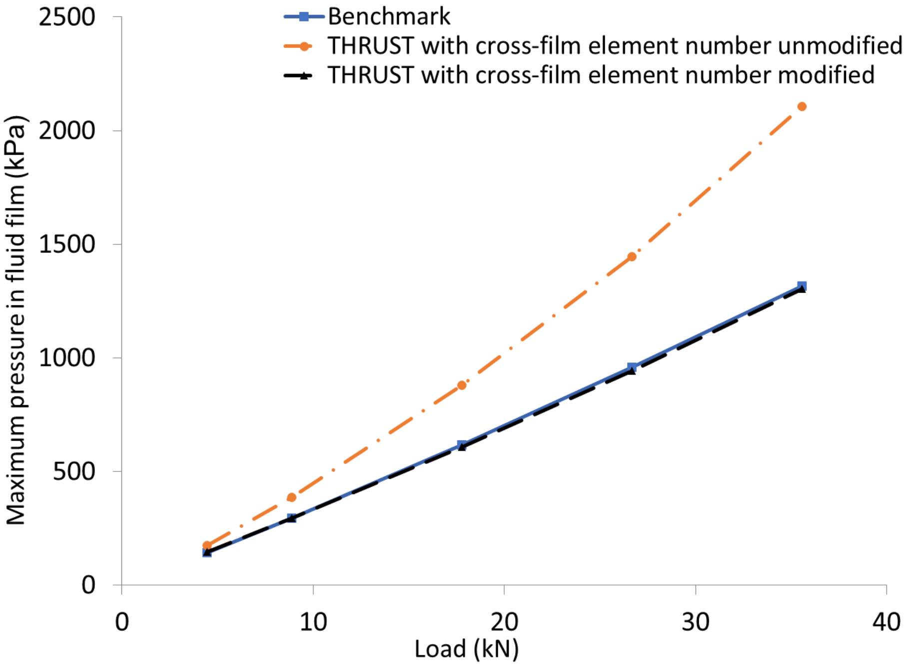

Figure 53. Comparison of maximum pressure in the fluid film between the benchmark code and thrust bearing code with and without an optimized cross-film element number

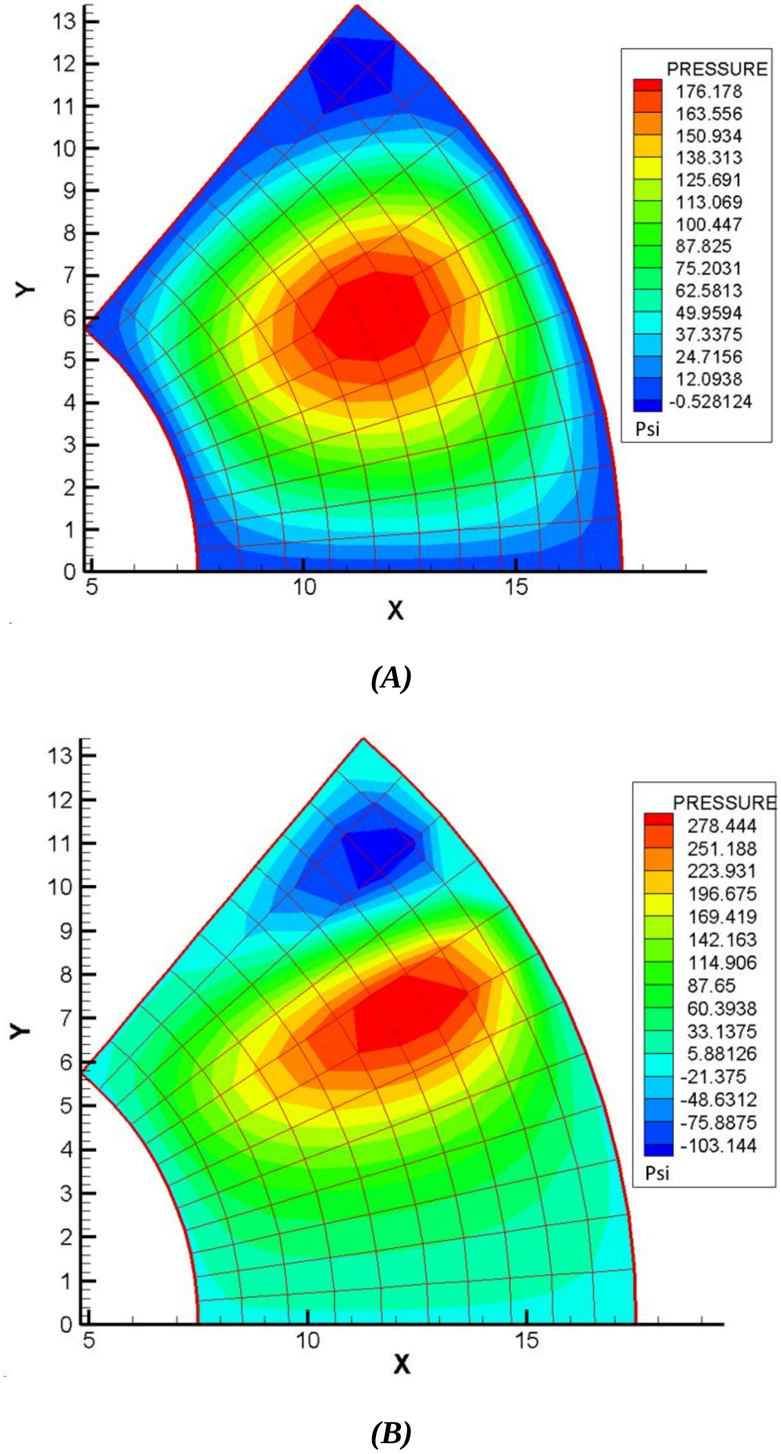

Figure* 54. *Pressure contour of the highest load in thrust bearing code (A) with and (B) without an optimized cross-film element number

The comparison results of the power loss between the benchmark and THRUST, with and without an optimized cross-film element number, are shown in Figure 55. The relative differences in the power loss predictions between the benchmark and THRUST, with and without an optimized cross-film element number, are shown in Figure 56. These two figures show that optimized cross-film element number cases have lower relative differences than unmodified cases. However, after optimizing the cross-film element number, the power loss is underpredicted for the higher loads.

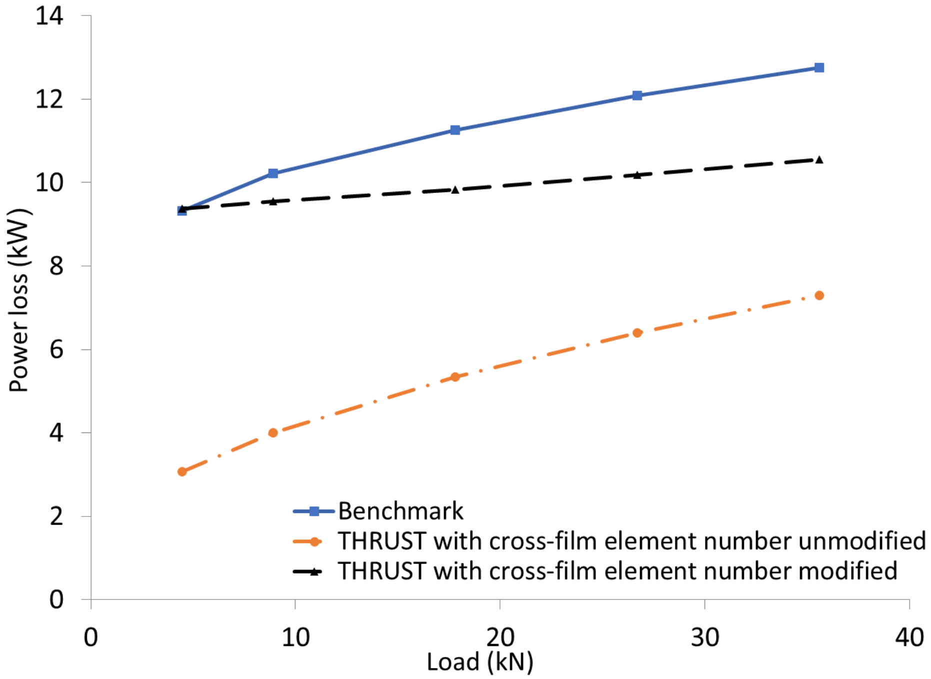

Figure 55. Comparison of power loss between the benchmark code and thrust bearing code with and without an optimized cross-film element number

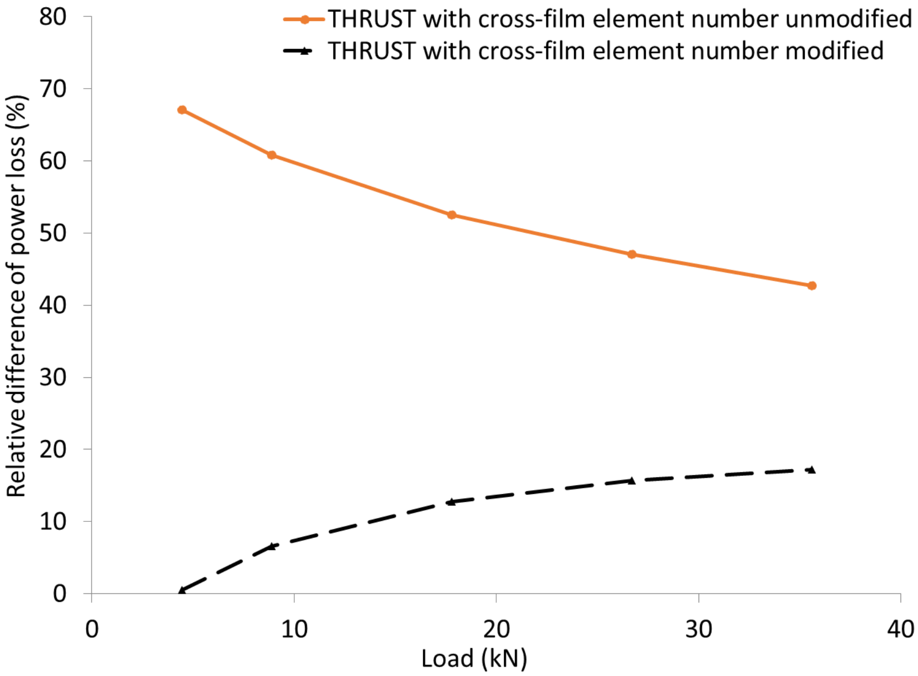

Figure 56. The relative difference of power loss predictions between the benchmark code and thrust bearing code with and without an optimized cross-film element number

The mesh independent study can be applied to oil and water lubrication, shown in Figure 57 and Figure 58. Figure 57 shows that a cross-film element number seven is enough for the oil lubrication, so seven is set for the cross-film element number for the oil lubrication in this paper. Figure 58 shows that the necessary cross-film element number for the water lubrication is known through a mesh-independent study. The cross-film element numbers for each load are shown in Table 4. Table 4 shows that the proposed method overestimated the cross-film element number, which may increase the calculation time but still increase the accuracy, which is the most important concern for researchers. There are two reasons for this difference. The first reason is that the physical meaning of the proposed method in this study is to fix the first mesh layer in the viscous sublayer for both oil and water lubrication, as seen in Figure 46. As the viscous sublayer is relatively small compared to the whole flow region, the impact of this viscous sublayer is overestimated if considering it only. The second reason is that the cross-film element number for the oil lubrication found in this case was relatively small (7). Since this is required to be a whole number, rounding errors can also increase the water-lubricated cross-film element number of the proposed method. Physically, a minimum number of elements is required to resolve the flow profile in the cross-film direction. An insufficient cross-film element number causes oscillating results for oil-lubricated cases.

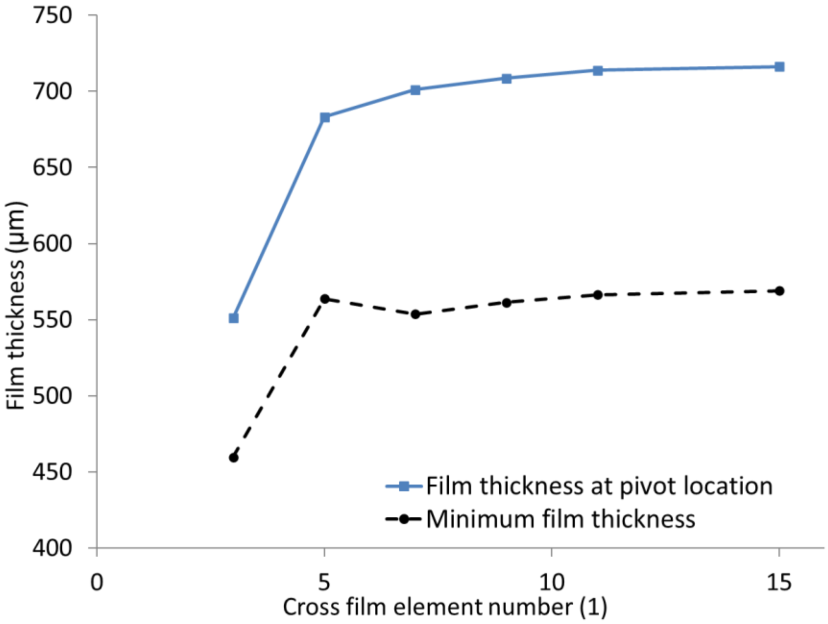

(A)

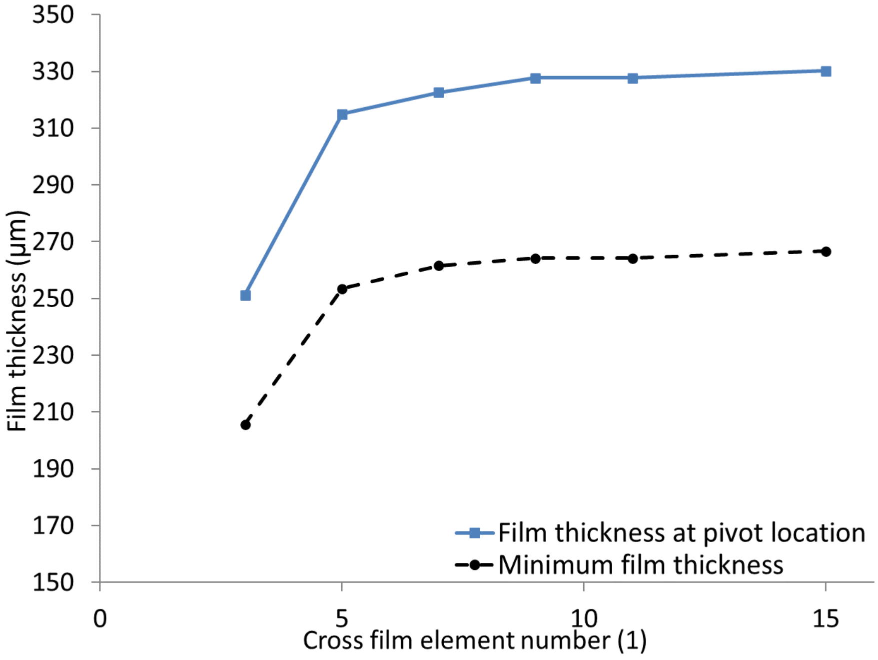

(B)

Figure 57. Mesh independent study with different cross-film element numbers for oil lubrication: (A) lowest load, (B) highest load

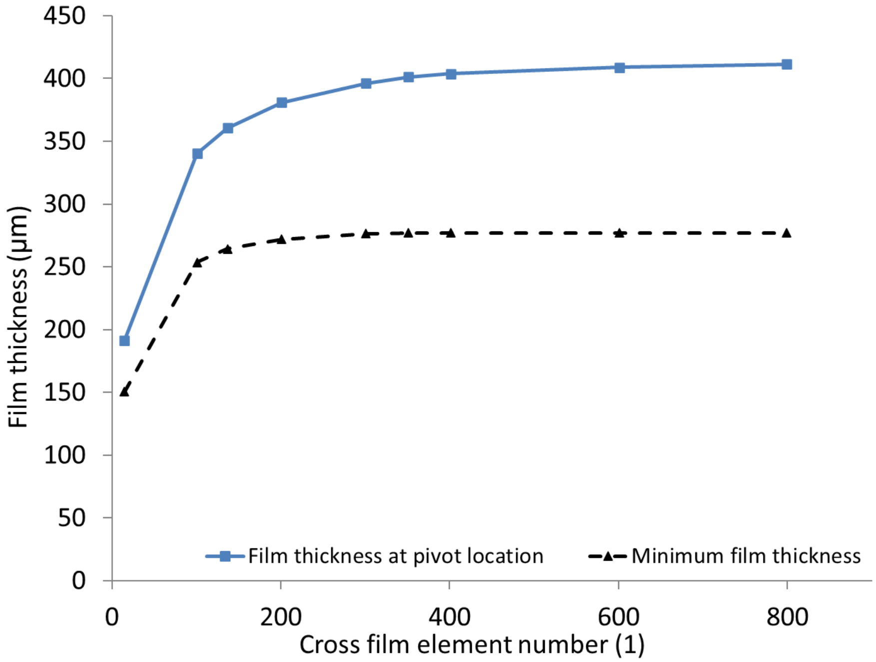

(A)

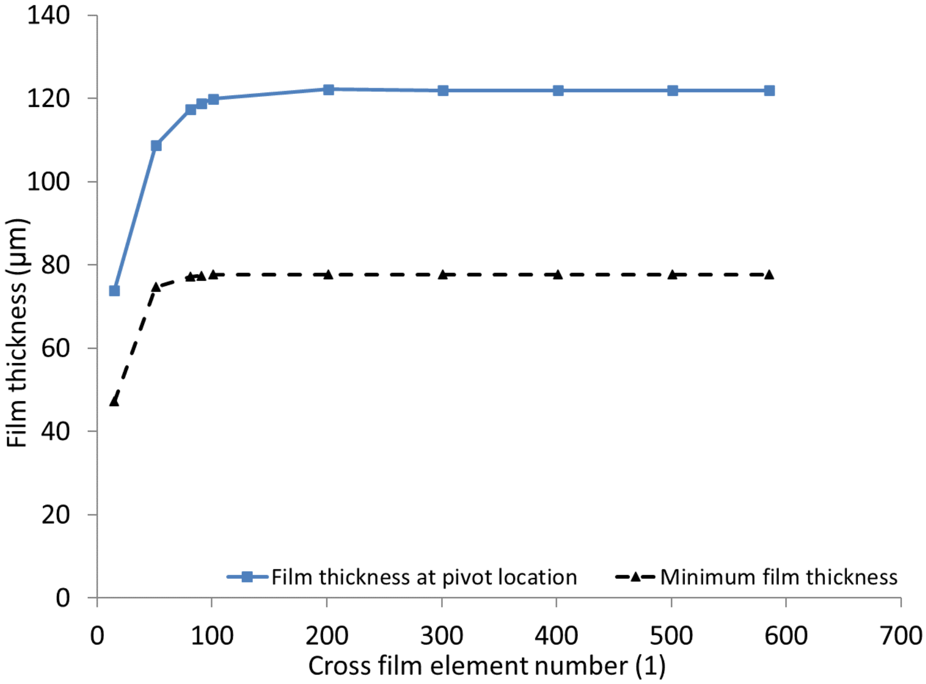

(B)

Figure 58. Mesh independent study with different cross-film element numbers for water lubrication: (A) lowest load, (B) highest load

Table 4. Comparison of cross-film element numbers used

Load (N)	proposed method	Mesh independence	Difference (%)
4448	373	351	5.9
8896	335	251	25
17793	301	201	33
26689	283	151	47
35586	273	101	63

3.5 Experimental validation

Besides the comparison between the thrust bearing and the benchmark codes, the authors also performed the comparison of experimental, thermo-elasto-hydrodynamic (TEHD), and thermal non-deforming computational fluid dynamics (CFD) results in ANSYS CFX for thrust bearings by using THRUST [91] [94], the experimental data is from Glavatskih [79] [80] [81] [82] [95]. This solid case-by-case comparison validated the accuracy of the thrust bearing code and demonstrated a good match between the experiment, THRUST and CFX can be seen in Figure 59.

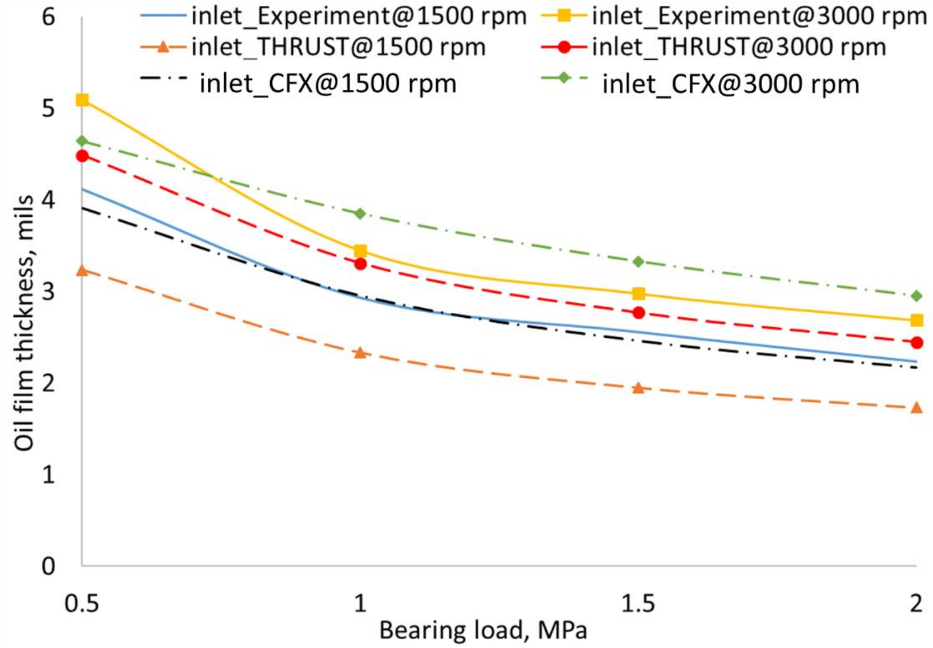

Figure 59: Comparison of inlet film thickness between the experiment, THRUST, and CFD

3.6 Discussion

As shown in Figure 47, the current Eq. 28 does not produce a perfect fit at lower values of δ^+ nor higher Reynolds numbers. Armentrout's equation was generated for a journal bearing. Hence its applicability to thrust bearings and thrust bearing code is questionable. The δ^+ in this study were calculated from Eq. 28 subtracted by 2, as shown in Table 5. This way, a good fit between THRUST and the benchmark could be obtained. Hence, besides the proposed method to preserve the y^+ value to make water-lubricated thrust bearing models valid, this study also did a study of the influence of parameters in Reichardt's formula, and will be introduced in this discussion.

Table 5. Comparison of the dimensionless thickness of viscous sublayer values used

Load (N)	Re_p	Armentrout's eq.'s δ^+	Optimized δ^+
4448	82000	2.79	0.79
8896	54600	4.29	2.29
17793	35600	5.78	3.78
26689	27400	6.57	4.57
35586	22700	7.07	5.07

The eddy viscosity turbulence effect increases with decreasing δ^+, while δ^+ has a minimum physical value as it is defined as the distance across a boundary layer from the wall to a point where the flow velocity has essentially reached the 'free stream' velocity. To develop a new relationship for δ^+ for water-lubrication thrust bearings, modified coefficients were developed to match THRUST to benchmark results. It is proposed that Armentrout's equation has the correct empirical form for δ^+, but it has insufficient accuracy for high Reynolds number cases. The form of α and β should be of a similar form to fit both oil and water data. The coefficients can be solved in Eq. 39 and Eq. 40. From Eq. 39 and Eq. 40, the corresponding constants were found to be: $\alpha = 10.25$ and $\beta = -3.00e-5$.

$$\beta = \left(\frac{1}{Re_{p2} - Re_{p1}}\right) ln(\frac{\delta_1^+}{\delta_2^+}) \qquad \text{Eq. 39}$$

$$\alpha = \delta^+ e^{\beta Re_p} \qquad \text{Eq. 40}$$

Figure 60 shows the fit between the proposed modified equation and the benchmark. THRUST using Armentrout's equation, was selected as the oil benchmark since Armentrout's equation is accurate at low Reynolds number cases, while the benchmark code was selected as the water benchmark. Overall, the proposed modified Armentrout's equation fits well with the benchmark, showing a significant improvement in fit over the original Armentrout's equation at high Reynolds number cases.

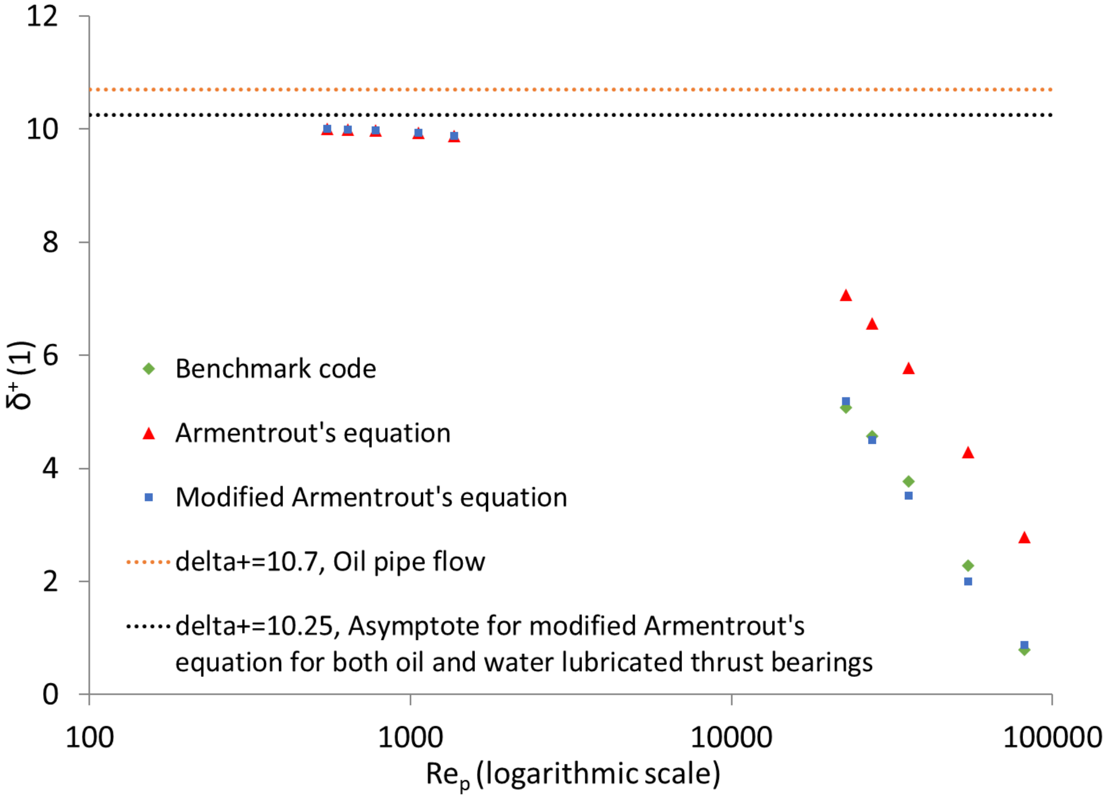

Figure 60. New approximation for δ^+

δ^+ values obtained from the proposed modified Armentrout's equation and the original equation can be compared to the benchmark to show the difference in accuracy. From Figure 60, the $Re_p = 54600$ case was shown to have the largest error. The relative difference between the modified Armentrout's equation and the benchmark at this point was only 12.8 %, while that of Armentrout's original equation was 87.5 %. From this, it is surmised that the new coefficients applied to Armentrout's equation can predict the film thickness at the pad pivot location much more accurately for water bearings than the original equation. The results in Figure 58 also confirm that the change in δ^+ required for a good fit between the proposed modified Armentrout's equation and the benchmark was close to the estimated optimized value of 2.

Figure 61 shows δ^+ used in Reichardt's formula has a significant influence on film thickness prediction. The predicted minimum film thickness values as a function of δ^+ for various loads and Reynolds numbers at the pad pivot location. To fix the Reynolds number at the pivot location to 1500, 6000, 24000, and 96000, the TEHD modeling tool was run iteratively at each load to achieve each Reynolds number by varying the operating speed until the difference between the current and previous iterations was below 1%. From Figure 61, it is shown that the minimum film thickness decreases with the increase of δ^+, with larger values found for lighter loads, From Figure 62, it is shown that the minimum film thickness increases with the increase of Reynolds number at pad pivot location. Figure 61 and Figure 62 highlight the sensitivity of film thickness to both δ^+ and Reynolds numbers at the pad pivot location.

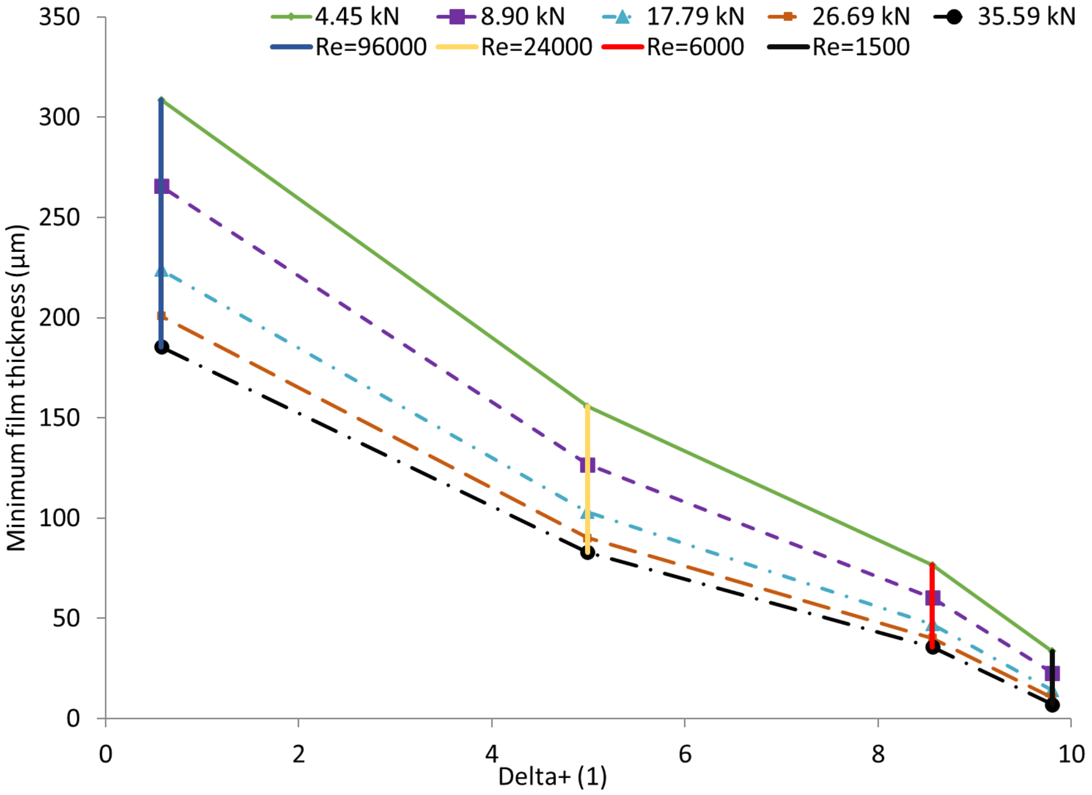

Figure 61. Minimum film thickness sensitivity to δ^+ and load

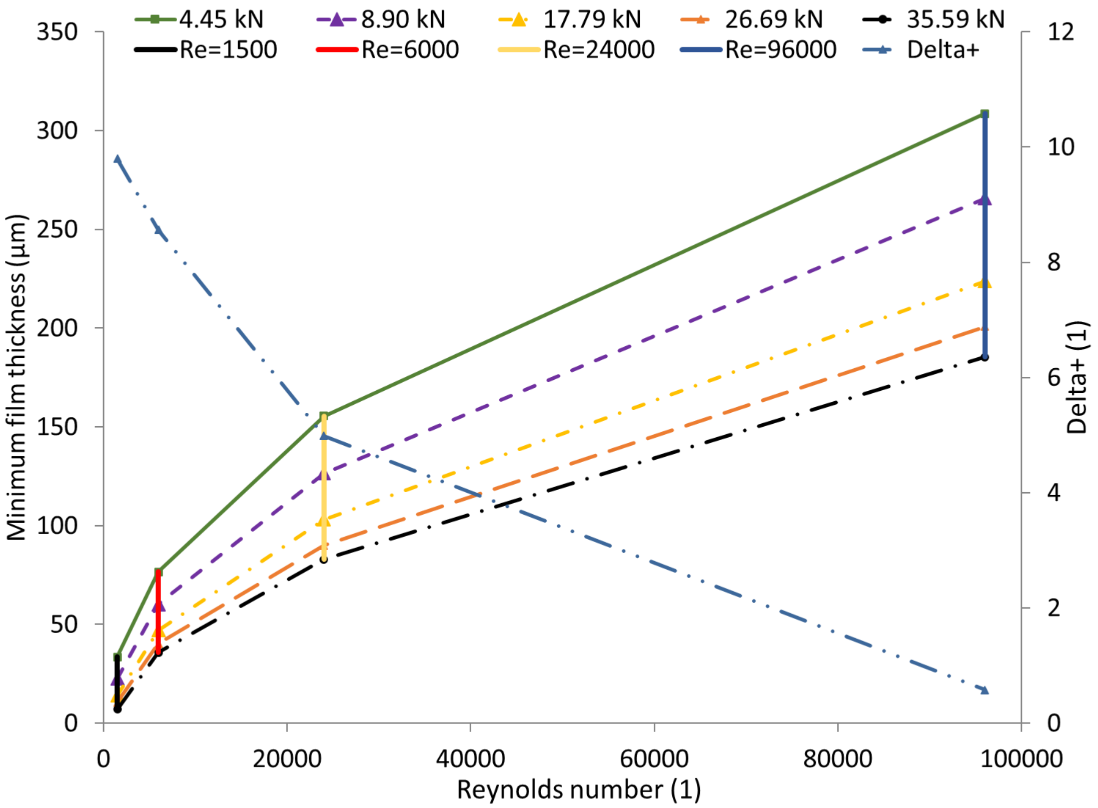

Figure 62. Minimum film thickness sensitivity to pivot Reynolds number and load

Besides the proposed method to preserve the y^+ value to make water-lubricated thrust bearing models valid and the proposed modified Reichardt's formula. Mesh ratio could also be considered to improve the calculation accuracy. To improve the solution accuracy and convergence for the 2D Reynolds equation, the ratio of the radial and circumferential directions in each layer of the cross-film direction divided by the cross-film element number, as shown in Figure 63, could be optimized. The element lengths in the radial and circumferential directions are much larger than in the cross-film direction. The mesh ratio between the radial and cross-film direction and the circumferential and cross-film direction could also be improved to improve the solution quality of the turbulence model. Limiting the skew ratio to 10-1000 depending on the flow physics [72] [96].

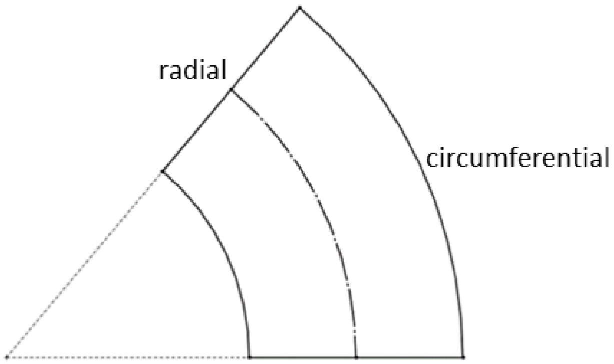

Figure* 63. *Pad plane

3.7 Conclusions

This study proposed a new methodology to preserve the y^+ value to make water-lubricated thrust-bearing models more accurate. A method for determining the required number of cross-film elements in water-lubricated bearings was found. The accuracy of turbulent TEHD results improved significantly after using the proposed methodology. An improved model for determining accurate values of δ^+ used in the turbulence model for water-lubricated thrust bearings was also presented and discussed. Combined, these two enhancements to the thrust bearing TEHD modeling can significantly improve their accuracy in predicting the performance characteristics of water-lubricated thrust bearings. Verifications were performed through the benchmark, mesh independent study, and experiment.

The traditional model for oil lubrication is not adequate for water lubrication. The cross film element number solving Reynolds equation, nondimensional distance, and the coefficients in Reichardt's turbulence need to be refined for water lubrication. An innovative contribution of this work is the establishment of a new perspective in the analysis of water lubrication where Reynolds numbers are large, generating turbulent flow as the dominant flow type as opposed to the traditional laminar flow found in oil lubrication. This perspective creates a new class of functional estimation procedures that parametrically account for the proper mesh characteristics for water-lubricated thrust bearings from oil-lubricated bearing characteristics intuitively and efficiently. These estimation procedures are motivated by the philosophy that the cross film element number and coefficients used in the eddy-viscosity equation should directly target the model convergence in fluids analysis other than that which traditional oil bearing-based analysis methods are designed for. This philosophy was followed by creating estimator functions for the mesh correction within a defined range of dimensionless wall distance induced from the wall-bounded flow. This dimensionless wall distance is used as the basis of a function. Parameters used to control the influence of this function and parameters indexing other aspects of the eddy viscosity are jointly estimated. From an empirical perspective, this is equivalent to assuming a priori that the same dimensionless wall distance for the subject fluid and choosing the hyperparameters controlling uniform mesh prior assumptions to balance the joint estimations.

These estimation procedures were developed in response to the unknown value of required cross-film elements encountered during collaborative projects on water lubrication, as well as to address a dearth of unifying philosophical motivation to improve the analysis of non-traditional fluid lubricants in the analysis of thrust bearings used in turbomachinery. This framework has produced exciting and potentially powerful results in its application to the analysis of water-lubricated machines. While these two techniques have shown to improve accuracy significantly for the range of operating conditions reported in this study, additional experimental validation, bearing designs, lubricating fluids, and operating conditions could be considered for additional verification in future work to establish the domain of usefulness of these approaches more thoroughly.

4. Applying a mixed zero-equation and one-equation turbulence model

4.1 Introduction

Most bearing studies use FE codes to predict bearing characteristics, and most of these codes use a zero-equation turbulence model. Ho and Vohr (1974) [47] used a model in which the eddy-viscosity was proportional to the time-averaged kinetic energy of turbulence and estimated the turbulent length scale from the Van Driest formula (1956) [48]. Van Driest provided a continuous velocity and shear distribution for turbulent flow near a smooth wall. Kosasih (1993) [49] used Prandtl's mixing length theory and Van Driest's mixing length formula in thrust bearings to study inertia and centrifugal forces. Watson-Kassa and Morgan (2020) used one equation and Van Driest formula as the length scale in the seal and referred to this length scale as the “Watson-Kassa” length scale; however, these results are yet to be published and publicly available in the literature at this date.

The research questions in chapter four are: Q1 - Is there a way to remove the two boundary values to decrease the uncertainty? Q2 - If there is more than one other way, what is the best choice? Q3 - How is the new model better than the traditional model? A new thrust-bearing modeling code packet, “ThrustX”, is used for this portion of the research work. ThrustX is a Thermo-Hydrodynamic (THD) code for a fixed film. It consists of looping between turbulence equation, Reynolds’s equation, film energy equation, and pad & runner conduction equation. The hydrodynamic (HD) part of ThrustX is in the innermost loop, and it mainly consists of modeling Reynolds’s equation and the turbulence equation. THD part adds the thermal effects to ThrustX.

4.2 Current Status of Turbulence Study in Thrust Bearings

Recent studies tried to improve the ability to use zero-equation turbulence models to predict the turbulence behavior in thrust bearings [86] [97]. [86] studied an improved method of modeling shear stress. They investigated three methods of applying zero-equation turbulence models. These three methods were intended to predict more accurate shear stress because shear stress is critical to the zero-equation turbulence model. [97]

investigated methods for improving mesh quality. They created a new class of functional estimation procedures that parametrically account for the proper mesh characteristics for water-lubricated thrust bearings from oil-lubricated bearing characteristics intuitively and efficiently. An estimating function was created for the mesh correction within a defined range of dimensionless wall distance induced from the wall-bounded flow.

However, these two studies still did not solve the inherent inevitable shortcomings of these zero-equation models. Therefore, advancement in the turbulence model is needed and should be implemented in the bearing studies to improve accuracy and model prediction capabilities under turbulent and transitional turbulence operating conditions.

4.3 Research Motivation and hypotheses

Fluid flow becomes turbulent when the Reynolds number is high in the lubricant film. The flow pattern (laminar or turbulent) is needed to be known for the appropriate modeling. Turbulence modeling works quite well for the fully turbulent bearing operation. However, significant errors can occur when the flow regime is misidentified, i.e., a turbulent flow bearing is wrongly modeled as laminar or vice versa. The current method of determining turbulence operation is calculating the film's Reynolds number (usually the maximum) and comparing it to the two prescribed threshold values. However, the shortcomings in the current state-of-the-art approach to bearing analysis to advance the design and efficiency of rotating machinery are that there is no consistent or reliable way to accurately prescribe those two threshold Reynolds numbers. In addition, the justification for using the maximum Reynolds number is questionable for a thrust bearing.

There are inherent inevitable shortcomings for these zero-equation models: (1) zero-equation use two empirically determined thresholds [98] [61] [99] [100] [101] [53] to control the boundaries for laminar and turbulent flow. (2) unlike a one-equation turbulent model, zero-equation models cannot calculate the transported turbulence quantity turbulence kinetic energy, which determines the eddy viscosity. With the increase of Reynolds number, the flow progresses from laminar, transitional turbulence to fully turbulent. The two thresholds mean the Reynolds number when: i) transferring from laminar flow to transitional flow, and ii) the Reynolds number for fully turbulent flow.

Furthermore, traditionally, zero-equation turbulence models such as Ng-Pan are used in bearing modeling as they are reasonably accurate, simple, and require less computation time and computing resources. With the improvement of modern computer capabilities, one equation turbulence modeling is now practical to implement and should also enable better accuracy.

4.4 Research tasks

Due to their simplicity and numerical stability, FE-bearing analysis codes widely use the zero-equation turbulence model. However, one and two-equation turbulence models have better accuracy. With advancing computer capabilities, applying one and two-equation turbulence model-based FE bearing codes are now feasible.

Besides the advancement of computing resources, the inevitable weakness of the current zero-equation turbulence models used in FE-bearing codes is that they use two somewhat arbitrary thresholds to control the boundaries for laminar and turbulent flow. As shown in Figure 64, the two vertical lines represent the two thresholds. There are three situations for the flow pattern: (1) if the maximum Reynolds number is smaller than the boundary between laminar and transition, the flow is all laminar; (2) if the minimum Reynolds number is larger than the boundary between transition and turbulent region, all the flow is modeled as turbulent; (3) if the maximum and minimum Reynolds number are within the two thresholds, the flow is in the transition region, which is handled as adding a turbulence scaling factor. These assumptions are problematic because the two threshold numbers are not known in advance. Simply estimating these two threshold numbers could result in significant prediction errors.

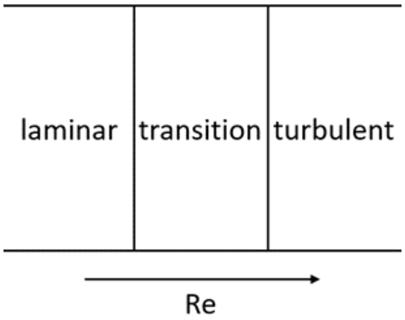

Figure 64: Diagram of two thresholds for controlling the laminar and turbulent flow

In recent studies from the Rotating Machinery and Controls Laboratory (ROMAC) at the University of Virginia [102], it has been found that a one-equation turbulence model can be applied to both laminar flow and low Reynolds number turbulent flow. This discovery, coupled with the weakness of the zero-equation turbulence model in determining the two threshold numbers, suggests that bearing calculations can be improved by replacing the zero-equation turbulence model with one and two-equation turbulence models. This approach removes the need to determine the two threshold numbers.

An n-equation model is a model that requires the solution of n additional differential transport equations in addition to those expressing conservation of mass, momentum, and energy for the mean flow. As shown in Table 6, there are three types of turbulence models contained in this proposal (the stress transport model is not discussed here): (1) zero-equation models, (2) one-equation models, and (3) two-equation models. In modern terminology, we refer to a model based on the mixing-length hypothesis as an algebraic model or a zero-equation model of turbulence. One-equation models use one partial differential equation besides conservation of mass, such as Prandtl's one-equation model (1945) and the Spalart-Allmaras model [103]. Two-equation models use two additional partial differential equations in addition to the mass conservation equation, such as SST [103] [104] [105] [106] [107] [108] [109] [110], k - ε [111] [112] [113] [114] and $k - \omega$ [115] [116]. SST consists of Baseline (BSL) model and a modification to BSL. BSL is a mix of $k - \omega$ and k - ε. SST used a modified near-wall treatment, allowing grid generation. ThrustX is a new Thermo- Hydrodynamic (THD) thrust-bearing finite element (FE) code that will be developed in this proposal. $k - \omega$ and k - ε have issue modeling the near wall region. ThrustX uses state-of-the-art modern coding methods and applies an innovative method to perform a creative zero-equation and one-equation mixed turbulent model.

Table 6. Comparing zero, one, and two-equation turbulence model

Name of Model	Number of turbulent flow transport equations	Turbulence quantities transported
Zero-equation	0	None
One-equation	1	$k \rightarrow \nu_T$

4.5 Modeling

A new thrust-bearing modeling code package, "ThrustX", was used for this portion of the research work, shown in Figure 65. Figure 65 shows Thermo-hydrodynamic (THD) code structure for a fixed film. It consists of looping between turbulence equation, Reynolds' equation, film energy equation, and pad & runner conduction equation. The hydrodynamic (HD) part of ThrustX is in the innermost loop, and it mainly consists of modeling Reynolds's equation and the turbulence equation. THD part adds the thermal effects to ThrustX.

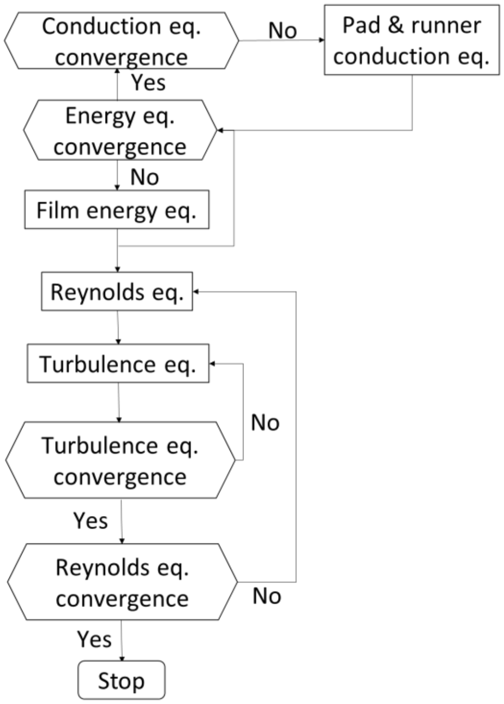

Figure 65: THD code structure in ThrustX

The process of modeling Prandtl's one-equation is shown in Figure 66. After the Reynolds equation is solved, the three velocities u, v, w, and the nine velocity gradients $\frac{\partial u}{\partial x}, \frac{\partial u}{\partial y}, \frac{\partial u}{\partial z}, \frac{\partial v}{\partial x}, \frac{\partial v}{\partial y}, \frac{\partial v}{\partial z}, \frac{\partial w}{\partial x}, \frac{\partial w}{\partial y}, \frac{\partial w}{\partial z}$ are passed to Prandtl's one-equation turbulence model. The inner-most loop of Prandtl's one-equation turbulence model is iterated until the turbulent kinetic energy k is converged. Then it passes the combined laminar viscosity and turbulent dynamic eddy viscosity as the effective turbulent viscosity back to the Reynolds equation as an updated viscosity value. Then this process is repeated until converged pressure and kinetic energy values are achieved.

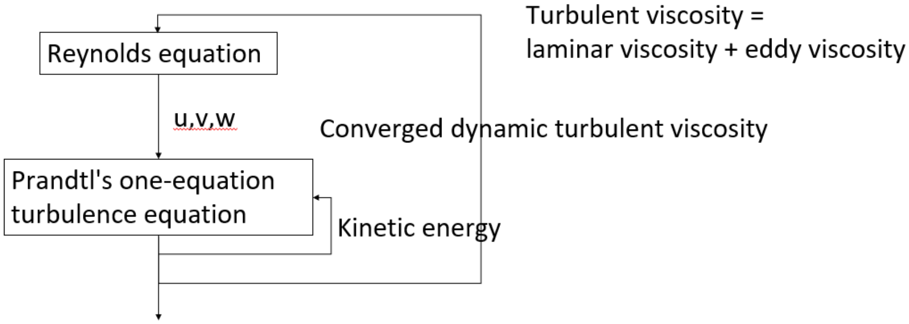

Figure 66: Reynolds eq. and turbulence eq. modeling flowchart

4.5.1 Prandtl equation

Prandtl's one-equation turbulence model solves turbulent kinetic energy through a Partial Differential Equation (PDE) solution and is used in ThrustX to more accurately account for bearing turbulence. Prandtl's one equation turbulence equation is shown in Eq. 41 and Eq. 42. The Watson-Kassa length scale is shown in Eq. 43. The Prandtl one-equation turbulence model is comprised of the following terms: $u_j \cdot \nabla k$ is convection term, $\tau_{ij}\frac{\partial u_i}{\partial x_j}$ is production term, $C_D\frac{k^{\frac{3}{2}}}{l}$ is dissipation term, and $\nabla \cdot \left[\left(\nu + \frac{\nu_T}{\sigma_k}\right)\frac{\partial k}{\partial x_j}\right]$ is viscous and turbulent diffusion terms. k is turbulent kinetic energy, u_j is velocity vector, ∇k and $\frac{\partial k}{\partial x_j}$ are gradient of turbulent kinetic energy, τ_{ij} is the Reynolds stress tensor, $\frac{\partial u_i}{\partial x_j}$ is velocity gradient, $C_D = 0.08$ and $\sigma_k = 1,$ are closure coefficient. l is length scale, an empirical equation shown in Eq. 9. The idea of this function is to model the length scale based on the distance to the runner and pad surface. ν is the viscosity, and ν_T is eddy viscosity. Reynolds stress uses Boussinesis hypothesis to replace fluctuation terms with eddy viscosity term, shown in Eq. 43. S_{ij} is strain-rate tensor, $S_{ij} = \frac{1}{2}(\nabla u + (\nabla u)^T)$, ∇u is velocity gradient tensor, ν_T is eddy viscosity and assumed $k^{\frac{1}{2}}l$, δ_{ij} is Kronecker delta $\delta_{ij} = \begin{cases} 0 \; if \; i \neq j \\ 1 \; if \; i = j \end{cases}$.

$$\frac{\partial k}{\partial t} + u_j \cdot \nabla k = \tau_{ij}\frac{\partial u_i}{\partial x_j} - C_D \frac{k^{\frac{3}{2}}}{l} + \nabla \cdot \left[\left(\nu + \frac{\nu_T}{\sigma_k}\right)\frac{\partial k}{\partial x_j}\right] \tag{Eq. 41}$$

$$\tau_{ij} = 2\nu_T S_{ij} - \frac{2}{3}k\delta_{ij} \tag{Eq. 42}$$

$$l = C\left(1 - e^{-\left(\frac{y^+_{stator}}{A^+}\right)^n}\right)^m \left(1 - e^{-\left(\frac{y^+_{rotor}}{A^+}\right)^n}\right)^m \tag{Eq. 43}$$

Eddy-viscosity transport model (Menter's one-equation model) solves eddy viscosity through PDE and is used in Computational Fluid Dynamics (CFD) software ANSYS CFX. Direct Numerical Simulation (DNS) does not use a turbulence model because the grid and time steps are resolved so that an unsteady solution is possible and is referenced to test Prandtl's one-equation. Reichardt's zero-equation turbulence model is an empirical equation for eddy viscosity. It is used in the previously developed ROMAC thrust bearing modeling tool (THRUST and other similar codes) to compare to ThrustX.

The weak form for the finite element modeling of the Prandtl one-equation turbulence model is shown in Eq. 44, Eq. 45, Eq. 46, Eq. 47, and Eq. 48. The stiffness matrix consists of viscous and turbulent diffusion, convection, and dissipation; the load vector is the production term.

$$\int_v \left(C_2 B^T B + N^T u_i B + C_1 N^T\right) k\,dv = \int_v QN^T dv \tag{Eq. 44}$$

Weak form of Prandtl equation:

$$\int_v \left(C_2 B^T B + N^T u_i B + C_1 N^T\right) k\,dv = \int_v QN^T dv \tag{Eq. 45}$$

$$C_2 = \nu + \frac{\nu_T}{\sigma_k} \tag{Eq. 46}$$

$$C_1 = C_D \frac{k^{\frac{1}{2}}}{l} \tag{Eq. 47}$$

$$Q = \tau_{ij}\frac{\partial u_i}{\partial x_j} \tag{Eq. 48}$$

4.5.2 Energy equation

$$\rho C_p u \cdot \nabla T = \nabla \cdot (k^* \nabla T) + Q + \mu^* \left[\left(\frac{\partial u}{\partial z} \right)^2 + \left(\frac{\partial v}{\partial z} \right)^2 \right] \quad \text{Eq. 49}$$

$$q^* = -k^* \nabla T \quad \text{Eq. 50}$$

Boundary conditions: there are two types of thermal boundary conditions

1. The fixed temperature on the boundary surface S_T: a fixed temperature as $T_s = T_n$
2. Fixed specified heat flow on the boundary surface S_q: a fixed heat flux as $q^* \cdot n = -{q_n}^*$

Weak form:

$$\left(\int_v k^* B^T B dv + \int_v \rho C_p N^T u B dv \right) [T] = \int_v Q N^T dv - \int_{S_T} N^T q^* \cdot n ds + \int_{S_q} N^T {q_n}^* ds \quad \text{Eq. 51}$$

4.5.3 Heat conduction equation

$$\frac{\partial q_x}{\partial x} + \frac{\partial q_y}{\partial y} + \frac{\partial q_z}{\partial z} = Q \quad \text{Eq. 52}$$

$$q = -k \nabla T \quad \text{Eq. 53}$$

There are three types of boundary conditions, as shown below:

1. Fixed temperature on S_T: $T_s = T_n$
2. Fixed specified heat flow on S_q: $q \cdot n = -q_n$
3. Convective S_h: $q \cdot n = h(T_s - T_\infty)$

Weak form:

$$\left(\int_{v} kB^{T}Bdv + \int_{S_h} hN^{T}Nds\right)[T] = \int_{v} QN^{T}dv - \int_{S_T} N^{T}q \cdot nds + \int_{S_q} N^{T}q_{n}ds + \int_{S_h} N^{T}hT_{\infty}ds \qquad \text{Eq. 54}$$

4.6 Turbulence results

Prandtl’s one-equation model is used to model turbulence in bearings FE in this research work. This section shows that Prandtl’s one-equation turbulence model in Couette and Poiseuille flow has been developed and tested. The boundary conditions, the finite element modeling, and the tests are shown in the following paragraph

4.6.1 Test of Prandtl model in Couette flow

The parameter for the model is shown in Table 7:

Table 7. The model parameter in the Couette flow

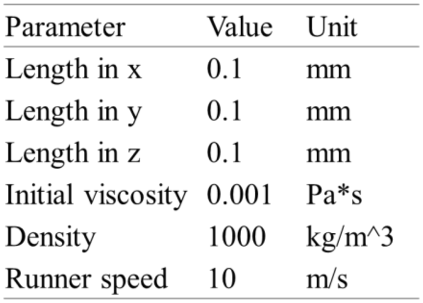

Parameter	Value	Unit
Length in x	0.1	mm
Length in y	0.1	mm
Length in z	0.1	mm
Initial viscosity	0.001	Pa*s
Density	1000	kg/m^3
Runner speed	10	m/s

The boundary surfaces in Couette flow are shown in Figure 67 and are described as follows:

- Leading and trailing surface: $dk/dn = 0$
- Pad surface and runner surface: $k = 0$, and the runner surface speed.
- Inner radius and outer radius surface: $dk/dn = 0$

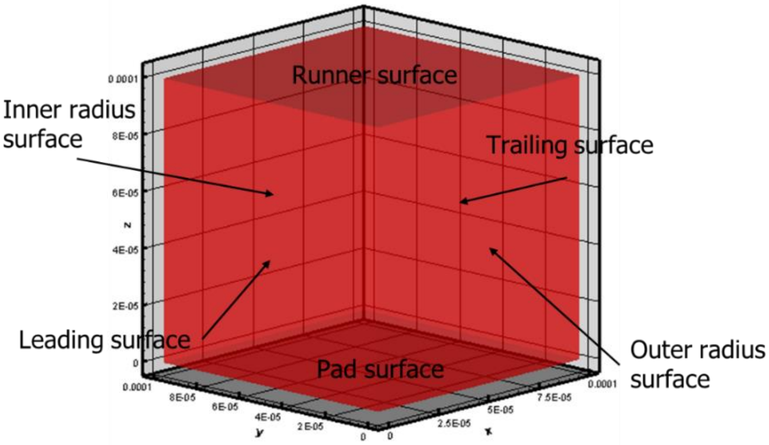

Figure 67: Boundary conditions in Couette flow

The mesh independent check and the mesh at Reynolds number 1600 in ThrustX are shown in Figure 68 and Figure 69. Figure 68 records the maximum and average eddy viscosity difference between each new cross-film element number and the last. It is known from Figure 68 that when the cross film element number is 24, the mesh is independent, with the difference of both maximum and average eddy viscosity below 0.4%. A mesh-independent check at the highest Reynolds number 1600 ensures mesh independence in all lower Reynolds numbers since higher Reynolds numbers require denser meshes.

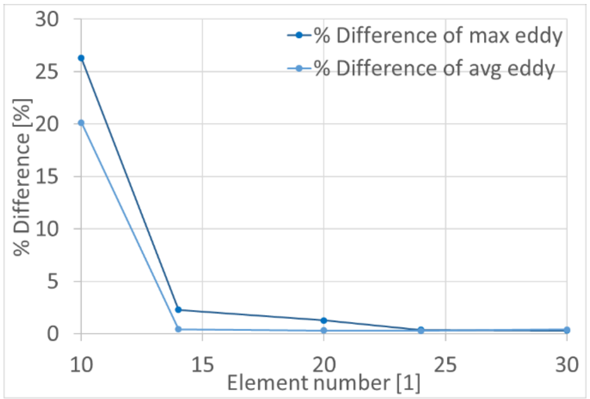

Figure 68: Mesh independent check

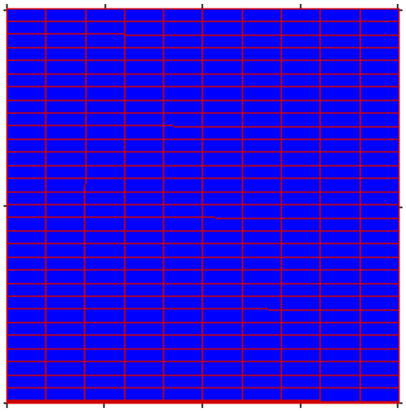

Figure 69: Mesh in ThrustX

ANSYS CFX is chosen to validate the eddy viscosity. The turbulence model in CFX is Menter’s one-equation turbulence model, which requires $y^+<1$. The Reynolds number is controlled by changing the runner's speed. The turbulence numerics is second order. The advection scheme of turbulence is high resolution. The advection scheme of turbulence eddy frequency and turbulence kinetic energy is upwind.

Similar to the mesh independence check in FE, the mesh independent check and the mesh at Reynolds number 1500 in CFX are shown in Figure 70 and Figure 71. Figure 70 records the change of the solution per finest solution of the average and maximum eddy viscosity with different element numbers. The mesh is independent when the total element number is 28594, with the average and maximum eddy viscosity difference below 1% compared to the 15341 element number.

The y^+ of CFX cases with the highest Reynolds number of 1600 is 0.8. This ensures y^+ in all Reynolds number cases is smaller than 0.8 because y^+ is a function of the Reynolds number. The higher the Reynolds number, the denser the mesh needed, which means y^+ is smaller.

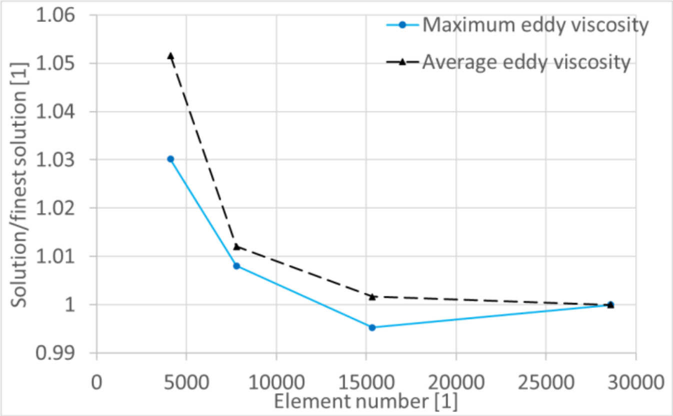

Figure 70: CFX Mesh independent check

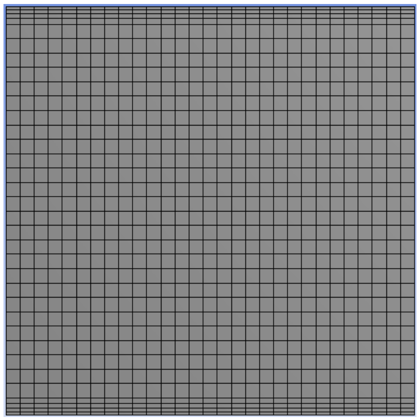

Figure 71: Mesh in CFX

The boundary conditions in CFX are shown in Figure 72:

- Leading surface: inlet, zero static pressure, flow direction: normal to BC
- trailing surface: outlet, zero static pressure
- runner surface: moving no-slip wall
- Pad surface: stationary, no-slip wall
- Inner radius and outer radius surface: symmetry

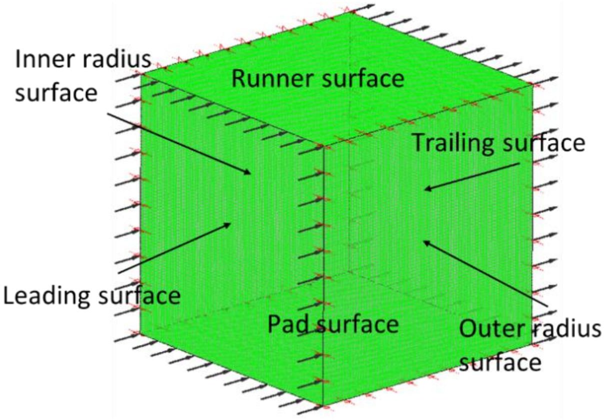

Figure 72: Boundary conditions in CFX

Before validating eddy viscosity in the turbulence model, an intermediate step of validating the velocity profile was performed. A certain number of dynamic viscosities in the cross-film direction were constrained, then the velocity in the flow direction between ThrustX and CFX was compared. The velocity values of ThrustX and CFX are shown in Figure 73, and the values are agreed upon. As shown in Figure 74, velocities in the vertical flow direction and the cross-film direction are zero due to the geometry of the problem.

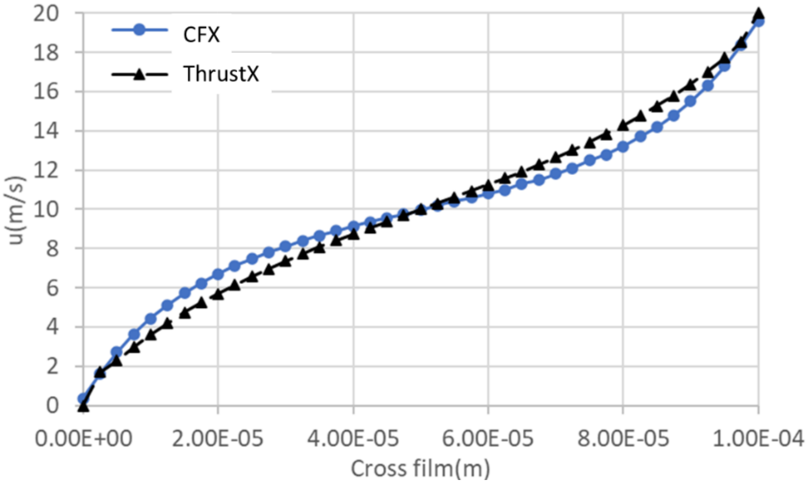

Figure 73: Velocity values of ThrustX and CFX

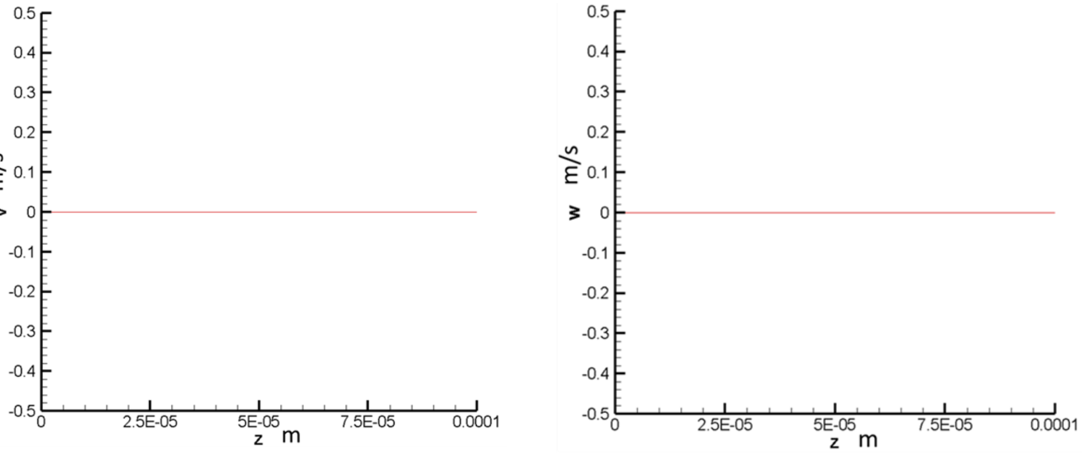

(a) (b)

Figure 74: ThrustX velocity values of (a) vertical to flow direction and (b) cross film direction

The eddy viscosity distribution was tested by comparing mixed zero and one-equation (used in ThrustX), Ng-Pan zero-equation (used in THRUST), Eddy-viscosity transport one equation turbulence model (used in CFX), and DNS values for various Reynolds number. The DNS results were from a collaborator (Cori Watson-Kassa) in ROMAC. The cross-film eddy profile with Re=1000 in Couette flow is shown in Figure 75. This figure shows that the eddy viscosity from the mixed zero-equation and one-equation turbulence model is very close to the Eddy Viscosity Transport (EVT) and DNS results. The mixed zero-equation and one-equation turbulence model and EVT have similar peak eddy viscosity. In contrast, mixed zero-equation and one-equation turbulence models have lower peaks than DNS. The EVT and DNS have similar eddy viscosity profiles in the middle cross-film region. While the mixed zero-equation and one-equation turbulence model has a slightly flatter eddy viscosity profile shape in the middle cross film region compared to EVT and DNS.

The turbulence model of the mixed zero-equation and one-equation turbulence model is much improved compared to Ng-Pan zero-equation. The reason for the improvement is that the shape of Reichardt’s formula is primarily defined by the shape of ‘tanh’ within its formula. The influence of the two shear stresses from the two walls is calculated separately. Therefore, the middle cross-film region calculation is tricky and relatively inaccurate. In contrast, mixed zero-equation and one-equation, and EVT turbulence models are more accurate as they calculate the eddy viscosity through a PDE. DNS essentially uses tiny grids and time steps to resolve all of the terms in the unsteady Navier-Stokes equations. Since turbulence results from unsteady terms, there is no need for a separate turbulence model. Traditional CFD uses the model (zero-equation and one-equation) to eliminate or reduce the unsteady terms and facilitate a solution with fewer grid points and time steps. Assuming the DNS solution is the best baseline. The EVT and mixed zero-equation and one-equation turbulence model solutions should approach the DNS as the mesh density increases.

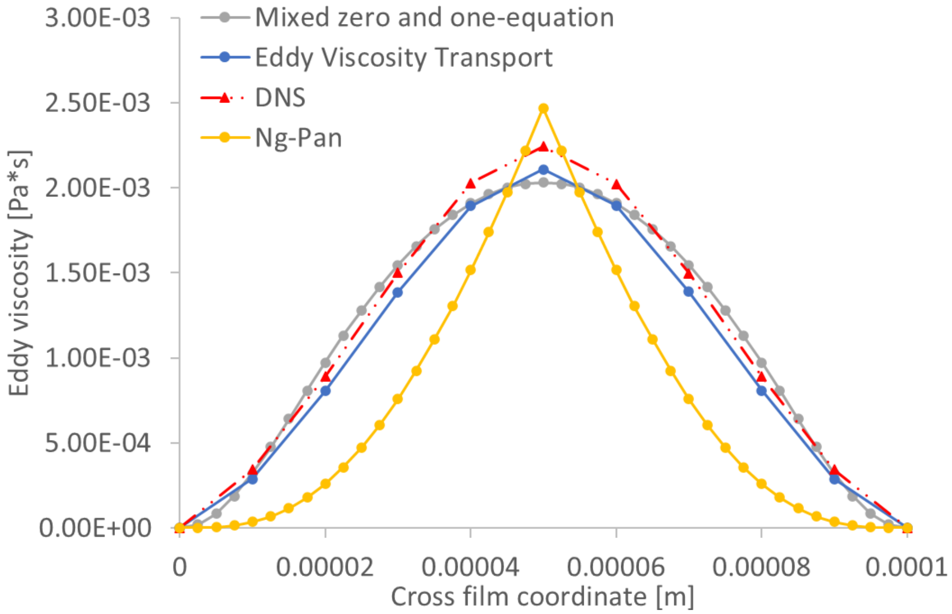

Figure 75: Cross film eddy profile in Couette flow

The comparison of eddy viscosity contour between ThrustX and Eddy-viscosity transport model (Menter’s one-equation model) CFX at a Reynolds number of 1000 is shown in Figure 76. The cross-film eddy viscosity distribution is the same across the flow direction, so only the leading edge surface is shown in Figure 76. The difference in max eddy viscosity between ThrustX and Menter’s one-equation CFX is 1.1%. ThrustX has a wider high cross-film eddy viscosity region than Menter's one-equation CFD. This is because the eddy viscosity profile shape in ThrustX is flatter than CFX in the middle. Therefore the complete eddy viscosity profile of ThrustX was pushed down. This means modeling in the middle cross film region of ThrustX could be further improved, which means the shear stress modeling in the middle cross film region could also be optimized.

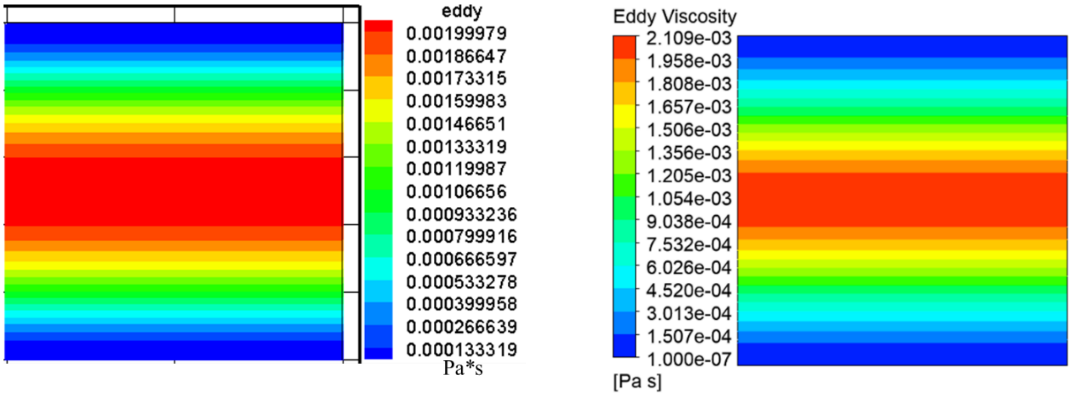

(a) (b)

Figure 76: Eddy viscosity contour of (a)ThrustX and (b) Eddy-viscosity transport model (Menter's one-equation model)

4.6.2 Test of Prandtl model in Poiseuille flow

The boundary surfaces in Poiseuille flow in ThrustX are shown in Figure 77. The detailed boundary conditions are shown below:

- Leading and trailing surface: $dk/dn = 0$. Fixed static pressure, with a pressure difference
- Pad surface and runner surface: $k = 0$.
- Inner radius and outer radius surface: $dk/dn = 0$

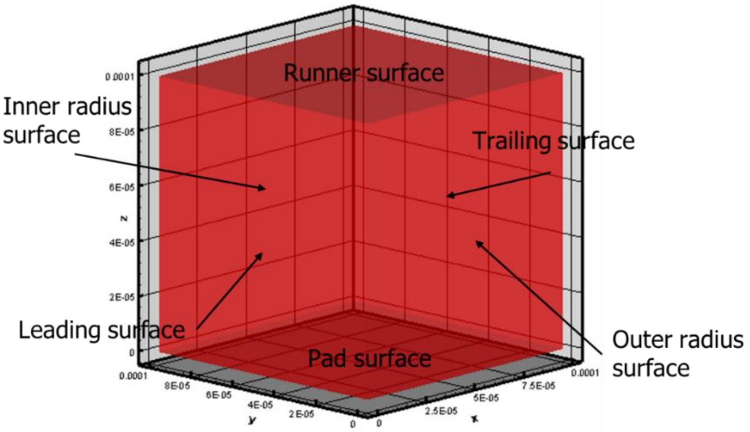

Figure 77: Boundary conditions

The weak form for finite element modeling Prandtl one-equation turbulence model in Poiseuille flow is the same as in Couette flow.

The boundary conditions in of Prandtl model in Poiseuille flow in CFX:

- Leading surface: inlet, fixed value static pressure, flow direction: normal to BC
- trailing surface: outlet, fixed value static pressure
- runner surface: stationary, no-slip wall
- Pad surface: stationary, no-slip wall
- Inner radius and outer radius surface: symmetry

The turbulence numerics is second order. The advection scheme of turbulence is high resolution. The advection scheme of turbulence eddy frequency and turbulence kinetic energy is upwind.

The comparison of eddy viscosity between ThrustX and Eddy-viscosity transport model (Menter's one-equation model) CFX at Reynolds number 500 is shown in Figure 78. The cross-film eddy viscosity distribution is the same across the flow direction, so only the leading edge surface is shown in Figure 78. The difference between the max eddy values is 0.5%. Like the Couette flow results, ThrustX has a wider high cross-film eddy viscosity region compared to Menter's one-equation CFX. This is because the eddy viscosity profile shape in ThrustX is flatter than CFX in the middle. Therefore, the complete eddy viscosity profile of ThrustX was pushed down. This means modeling in the middle cross film region of ThrustX could be improved, which further means the shear stress modeling in the middle cross film region could also be optimized.

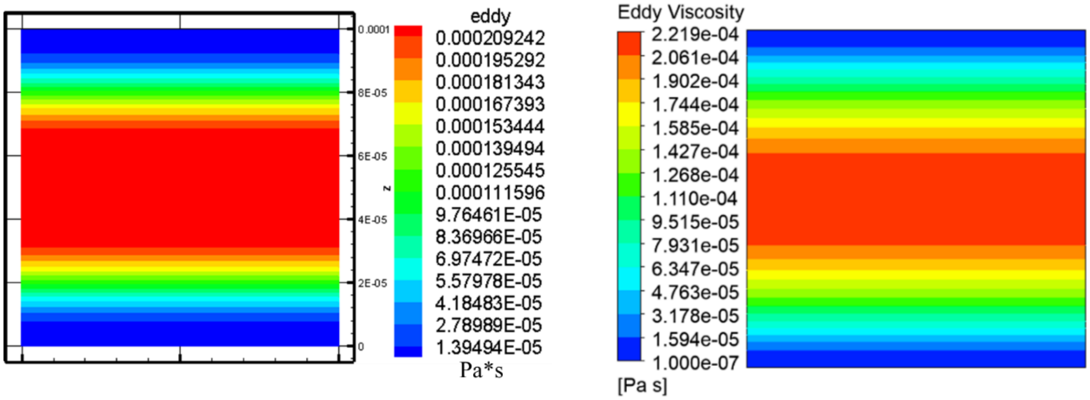

(a) (b)

Figure 78: Eddy viscosity values of (a)ThrustX and (b) Eddy-viscosity transport model (Menter's one-equation model)

4.6.3 Prandtl model in converging region

Figure 79 shows the eddy viscosity contour from solving Prandtl’s one-equation in the converging film. Converging wedge is the working principle of fluid film thrust bearings. After modeling ThrustX in Couette and Poiseuille flow, the next step is to model ThrustX in a converging film. As shown in Figure 79, the eddy viscosity contour on the leading edge is similar to that in the Couette and Poiseuille flow. While as the film is converging, the cross-film eddy viscosity distribution changes across the flow direction. The distribution of the cross-film eddy viscosity demonstrates a parabolic distribution.

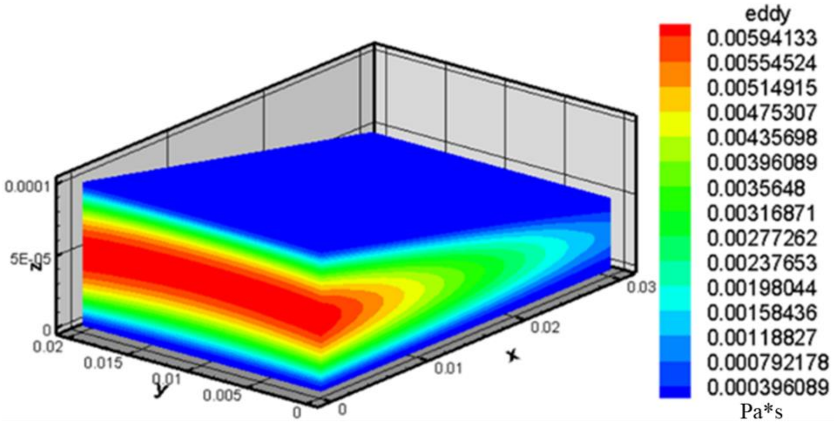

Figure 79: Eddy viscosity contour in ThrustX

4.7 Conclusions

This study proposed a new methodology to model turbulence to make fluid film lubricated thrust bearing models more accurate. A novel mixed zero-equation and one-equation turbulence model was developed for calculating eddy viscosity in fluid film thrust bearings. The accuracy of turbulent THD results improved significantly (compared to the zero equation model) using the proposed methodology. This enhancement to the thrust bearing THD modeling can significantly improve their accuracy in predicting the overall performance characteristics of fluid film lubricated thrust bearings. Verifications were performed through DNS, CFX, and THRUST comparison.

A mixed zero-equation and one-equation turbulence model is an effective and accurate way to remove the two thresholds to decrease the uncertainty. The new model predicts much more accurate eddy viscosity in the cross film. An innovative contribution of this work is the establishment of a novel mixed zero equation and one equation turbulence model in the analysis of fluid film lubrication, where the dominant flow is turbulent. This perspective created a new modeling method for solving Prandtl's turbulence equation with an empirical length scale that solves eddy viscosity. Unlike using an empirical function of Reichardt's equation, this new method physically solves a PDE to calculate eddy viscosity. This new procedure was motivated by the philosophy that a more physical solution is better than empiricism. The length scale was based on the nature of the rotating machinery, which includes two surfaces with relative motion, and shear stress greatly depends on the distance between the two surfaces. This philosophy was followed by combining the Prandtl one equation and empirical length scale, better than a purely empirical zero equation Reichardt's equation, while still not demanding as many computing resources as two-equation turbulence models would. This new mixed zero equation and one equation turbulence model were used in the inner loop with the Reynolds equation. From an empirical perspective, this is equivalent to assuming the length scale is less or equal to the empirical purely zero equation turbulence model value. By adding a Prandtl one equation model and physically solving for eddy viscosity, the new method increases accuracy and decreases empiricism.

This framework has produced exciting and potentially powerful results in its application to the analysis of turbulent fluid film thrust bearings. While the new turbulence model has been shown to improve accuracy significantly for the range of operating conditions reported in this study, additional experimental validation and operating conditions could be considered for additional verification in future work to improve the applicability of this approach further.

5. Modeling Center Pivot Fluid Film Thrust Bearing Temperature Drop in Transitional Region

5.1 Introduction

This chapter examines the temperature drop in the transitional region. The research questions in chapter five are: Is it correct that the temperature drop across a range of increasing velocity can be attributed to the onset of turbulence in the fluid film? (1) If the answer is yes, what turbulence contributes to the temperature drop? Further questions are: (a) What turbulence model should be used? (b) What is the physical mechanism that leads to the temperature drop? Moreover, (2) If the answer to (1) is no, will a laminar flow model correctly capture the temperature drop? Further questions are: for the turbulence model, what happens in the groove that behaves in specific temperature changes in the transitional region? Could the impacting physics be eddy? Conduction? Production? A well-documented, experimental, center-pivot fluid film thrust bearing was selected for the work in this chapter, and a full fluid-solid ANSYS CFX model was built.

An experimentally verified [61] full fluid-solid CFX model was created to answer the research questions. Capitao's experiment [60] is ideal for this work as it provides multiple temperature probes on the pad surface, which were used to validate the CFX model. The validation includes (1) verification of 9 probe temperatures on the pad surface and (2) verification of the temperature drop across the appropriate range of shaft velocity. This full fluid-solid model allows for accurate thermal modeling and analysis and demonstrates the application of a CFX model of the groove to reduce empiricism in hot oil carry-over models typically used in the fluid-film thrust-bearing analysis.

This chapter seeks to fundamentally better understand the transitional region effect in fluid-film thrust-bearings, which is not well captured in current industry state-of-the-art bearing analysis codes. The traditional method [72] of accounting for turbulence is to assign a turbulence scaling factor based on the Reynolds number at one location, which is at the center of the leading edge, as shown in Figure 80. Reynolds number is defined as $Re = \frac{\rho h u}{\mu}$, where ρ is density, h is film thickness, and u is circumferential velocity, μ is dynamic viscosity. The turbulence scaling factor is assumed to be the same for all fluid domains, which may be difficult to justify. For example, the circumferential velocity increases with radius, so the Reynolds number can vary, particularly in large bearings. Likewise, viscosity varies with temperature, and film thickness is not uniform.

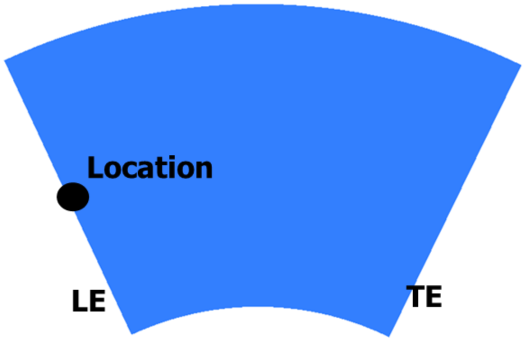

Figure 80: Reynolds number measuring location in legend finite element modeling

The work in this chapter serves to correctly model and understand the flow throughout the fluid-solid domain, including all four groove regions, in addition to answering the research questions listed above. This chapter also demonstrates the variability and sensitivity of center-pivot fluid-film thrust-bearing CFX modeling to the inclusion of crowning modeling. Furthermore, this chapter examines the impact of the film, pad, runner, and groove on bearing calculations and the impact of leading-edge temperature on load capacity.

The flow in the full fluid-solid CFX model is shown in Figure 81. Figure 81a) shows the multiple modeling domains in the circumferential direction, and Figure 81b) shows the multiple modeling domains in the radial direction at the mid-sector surface. There is heat convection in the groove and film. Moreover, there is also heat conduction in the pad and runner, and on the interface between fluid and solid. The groove model includes grooves at the leading edge, trailing edge, inner diameter, and outer diameter.

<table>
<tr><td rowspan="2">Leading edge groove (energy eq.)</td><td>Pad (heat conduction eq.)</td><td rowspan="2">Trialing edge groove (energy eq.)</td></tr>
<tr><td>Film (energy eq.)</td></tr>
<tr><td colspan="3">Runner (heat conduction eq.)</td></tr>
</table>

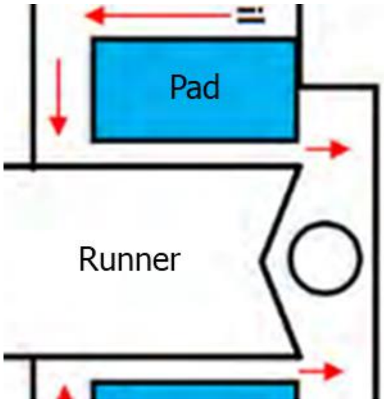

a) Circumferential direction

Shaft (heat conduction eq.)	Inner diameter groove (energy eq.)	Pad (heat conduction eq.)	Outer diameter groove (energy eq.)
		Film (energy eq.)	
	Runner (heat conduction eq.)		

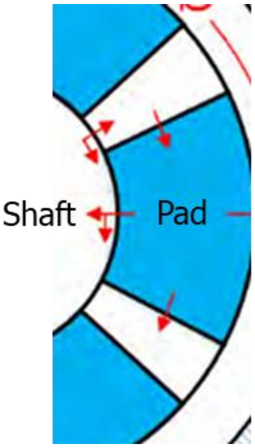

b) Radial direction

Figure 81: Conduction-convection method

5.2 Center pivot experimental model

The bearing modeled is from an experiment [60]. This model is the Capitao center pivot experimental model, six-pad thrust bearing, as shown in Figure 82. The parameters of the Capitao model are shown in Table 8.

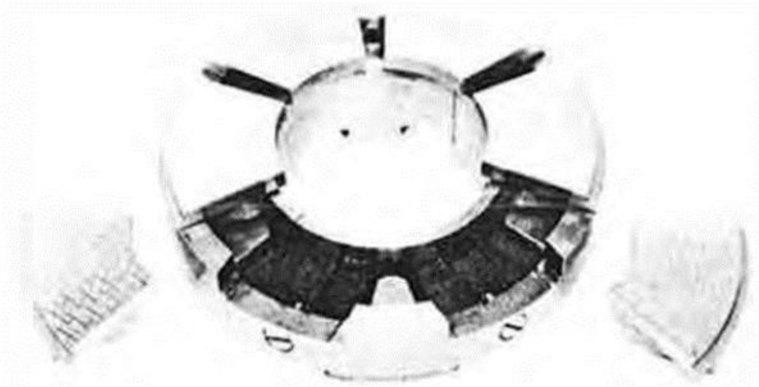

Figure 82: Capitao experimental model

Table 8. Capitao model parameter

Parameter	Value	Units
Pad arc	51	deg
Groove and pad arc	60	deg
Pad number	6	
Pad inner radius	66.5	mm
Pad outer radius	133.5	mm
Single pad area	59.6	cm^2
Pad load	100-400	psi
Groove inner radius (estimated)	65	mm
Groove outer radius (estimated)	135	mm
Sector and ID groove thickness (estimated)	33.3	mm
OD groove thickness (estimated)	6.65	mm
Film thickness	iteration	mm
Runner thickness (estimated)	44.5	mm
Circumferential tilting angle	iteration	deg
Radial tilting angles	iteration	deg
Density	857	kg/m^3
Viscosity	0.027 @ 37.8°C	Pa*s
Viscosity	0.006 @98.9°C	Pa*s
Fluid specific heat capacity (estimated)	2150	J/(kg*K)
Fluid thermal conductivity (estimated)	0.13	W/m*K

supply temperature	46	°C
Shaft speed	9000	rpm

The Capitao experiment provides nine temperature probes on the pad surfaces at a shaft speed of 9000 rpm, as shown in Figure 83. The probe locations on the pad are shown in Figure 84. Nodes 1-3 are near the Outer Diameter (OD), nodes 4-6 are on the Middle Diameter (MD), and nodes 7-9 are near the Inner Diameter (ID). The circumferential and radial percentages of the nine probes are shown in Table 9.

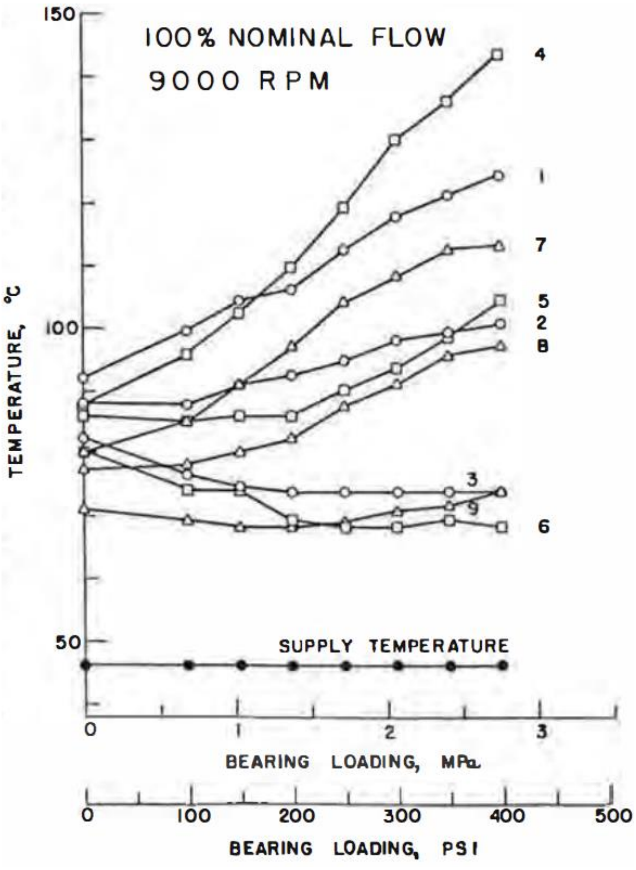

Figure 83: Pad temperature in Capitao experimental model [56]

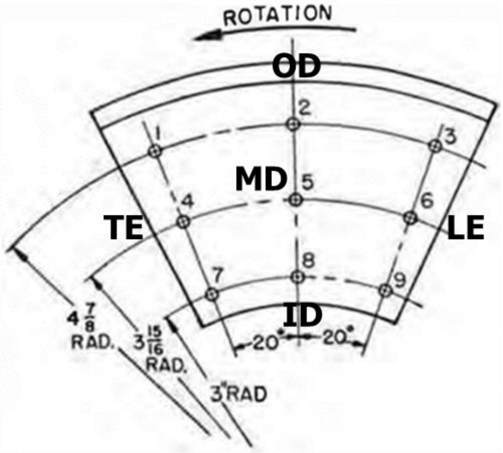

Figure 84: Temperature probes in Capitao experimental model [56]

Table 9. Circumferential and radial percentage of the nine probes

Node number	Circumferential percentage from LE (%)	Radial percentage from ID (%)
1	90	85
2	50	85
3	10	85
4	90	50
5	50	50
6	10	50
7	90	15
8	50	15
9	10	15

With the increase of the shaft speed, there is a temperature drop roughly between 8000 rpm, and 10000 rpm, as shown in Figure 85. This temperature drop region is often referred to as the transitional region. The temperature depicted in the figure is from probe 4, which is located in the middle of the trailing edge. As shown above, data for the other eight temperature probes is only available at 9000 rpm.

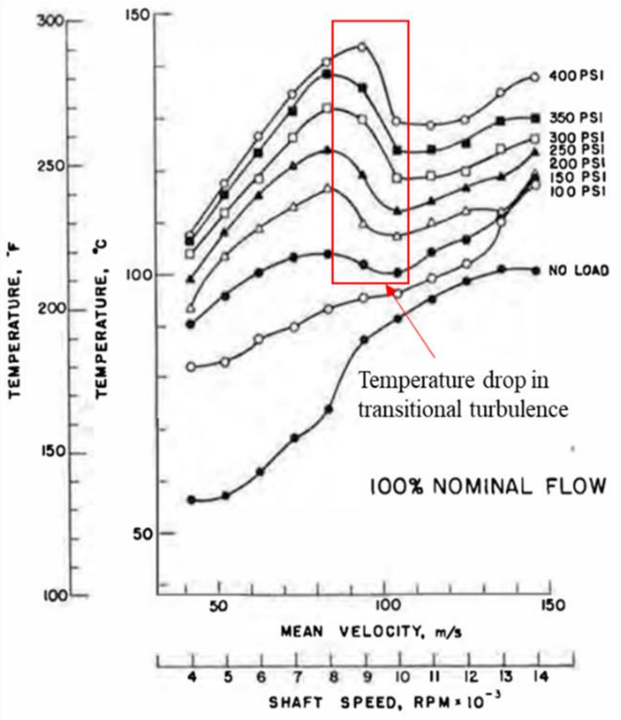

Figure 85: Temperature probes in Capitao experimental model [56]

5.3 Center pivot CFX model

The CFX model is shown in Figure 86. The model has the full fluid domain, including the film, Groove Between Pads (GBP), Outer Diameter Groove (ODG), and Inner Diameter Groove (IDG). Furthermore, the model has a full solid domain, including a pad and runner.

The film profile in the CFX model used a film produced by an industry-standard TEHD benchmark code (Minhui's [72] in-house code) using the finite element method. The pivot film thickness and circumferential and radial tilting angles are shown in Table 10. The film profile in CFX has been rigidly tested by comparing pad deformation and film thickness of four corner points between the CFX model and the benchmark. The location of the four corner points in CFX is shown in Figure 87. Points 1 and 2 are located on the leading edge, and points 3 and 4 are on the trailing edge. Table 11 and Table 12 show the pad deformation and film thickness for the four corner points. The film profile is matched well with the benchmark code film profile.

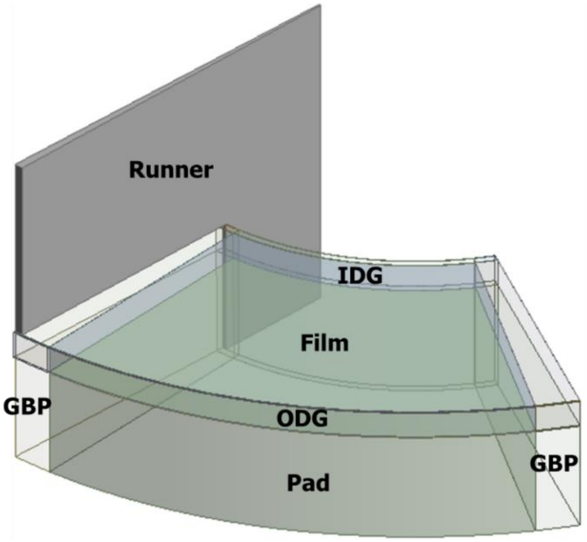

Figure 86: Full fluid-solid CFX model for Capitao experiment

Table 10. Film profile predicted by benchmark code

Pivot film thickness (m)	Circumferential tilting angle (degree)	Radial tilting angle (degree)
0.00008	0.022	0.0053

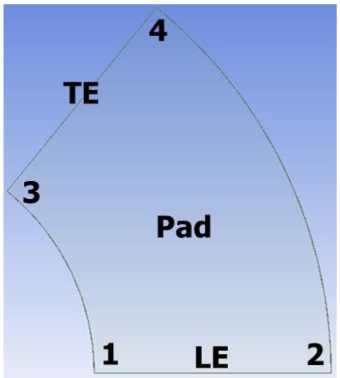

Figure 87: Corner points location

Table 11. Comparison of pad deformation between CFX and benchmark code

	Corner 1	Corner 2	Corner 3	Corner 4
Benchmark code, mm	-1.21e-2	-8.31e-3	-1.33e-2	-9.48e-3
CFX, mm	-1.34e-2	-9.25e-3	-1.34e-2	-9.25e-3

Table 12. Comparison of film thickness between CFX and benchmark code

	Corner 1	Corner 2	Corner 3	Corner 4
Benchmark code, mm	7.54e-2	9.62e-2	5.22e-2	5.07e-2
CFX, mm	7.49e-2	9.60e-2	5.28e-2	5.17e-2

The turbulence model is Shear Stress Transport (SST) with thermal energy. The difference between the thermal and total energy is shown in Table 13. The SST with total energy model was originally designed for gas turbine applications by a Boeing engineer, Menter [106], in 1994. Therefore, SST with total energy is for compressible flow with a Mach number larger than one (supersonic flow). The SST with thermal energy model was created to address numerical stability issues in SST with total energy. SST with thermal energy is suitable for incompressible, low-speed flow and has no stability issues [117].

Table 13. Comparison of film thickness between CFX and benchmark code

Model	Compressibility	Speed	Stability
SST _ total	Compressible	>1 Mach	Stability issue
SST _ thermal	Incompressible	<1 Mach	No stability issue

5.3.1 Meshing

The Capitao center pivot model meshing considered the mesh sensitivity of cross film element number, cross film growth rate, circumferential and radial aspect ratio, and the connection between film and groove regions. Table 14 and Table 15 show the values chosen for the mesh sensitivity study of the cross-film element number in laminar and turbulence. Table 16 and Table 17 show the values chosen for the mesh sensitivity study of cross film growth rate in laminar and turbulence. Table 18 and Table 19 show the values chosen for the mesh sensitivity study of element mesh circumferential and radial aspect ratio to cross film mesh size in laminar and turbulence.

Table 14. Mesh sensitivity study of cross film element number, laminar

Case	Cross film element number, 1
1	8
2	15
3	20
4	35

Table 15. Mesh sensitivity study of cross film element number, turbulence

Case	Cross film element number, 1
1	8
2	15
3	20
4	25
5	30
6	35
7	40

Table 16. Mesh sensitivity study of cross film growth rate, laminar

Case	Cross film growth rate, 1
1	1.05
2	1.1
3	1.15
4	1.2

Table 17. Mesh sensitivity study of cross film growth rate, turbulence

Case	Cross film growth rate, 1
1	1.05
2	1.1
3	1.15
4	1.2

Table 18. Mesh sensitivity study of element mesh circumferential and radial aspect ratio to cross film mesh size, laminar

Case	Element mesh circumferential and radial aspect ratio to cross film mesh size, 1
1	85
2	100
3	125
4	150
5	200

Table 19. Mesh sensitivity study of element mesh circumferential and radial aspect ratio to cross film mesh size, turbulence

Case	Element mesh circumferential and radial aspect ratio to cross film mesh size, 1
1	75
2	100
3	125
4	150
5	200

Figure 88 and Figure 89 show the results of the mesh sensitivity study of cross film element number in laminar and turbulence. The mesh is insensitive when the cross-film element number is 20 for laminar and 35 for turbulence. Figure 90 and Figure 91 show the results of the mesh sensitivity study of cross-film growth rate in laminar and turbulence. The mesh is insensitive in the range of 1.05 – 1.2 for cross film growth rate for laminar. For turbulence, the mesh is insensitive in the range of 1.05 – 1.1 for cross film growth rate. Figure 92 and Figure 93 show the results of the mesh sensitivity study of circumferential and radial aspect ratio to cross film mesh size in laminar and turbulence. The mesh is insensitive when the element circumferential and radial aspect ratio to cross film mesh size is 75 for laminar and 125 for turbulence.

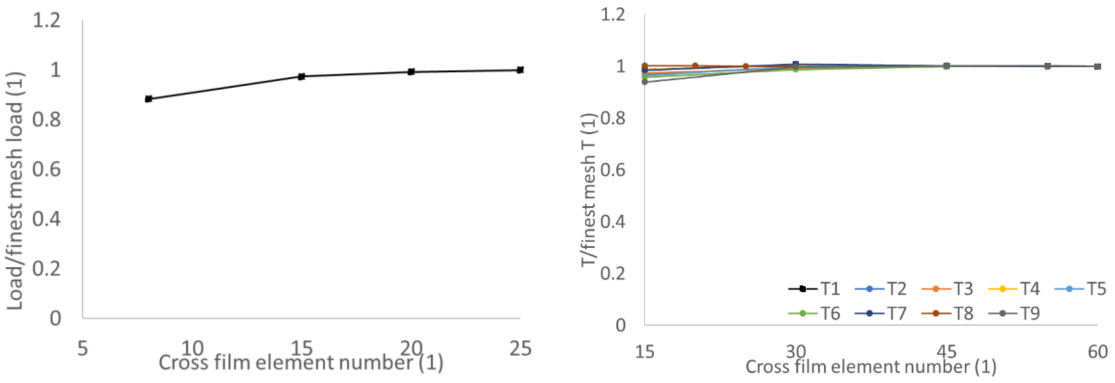

(a) Mesh sensitivity for load (b) Mesh sensitivity for temperature

Figure 88: Mesh sensitivity study results of cross film element number, laminar

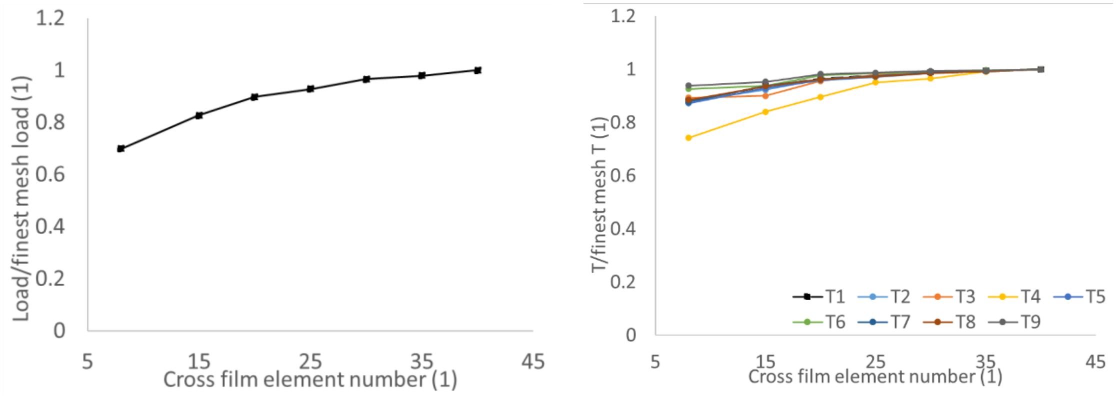

(a) Mesh sensitivity for load (b) Mesh sensitivity for temperature

Figure 89: Mesh sensitivity study results of cross film element number, turbulence

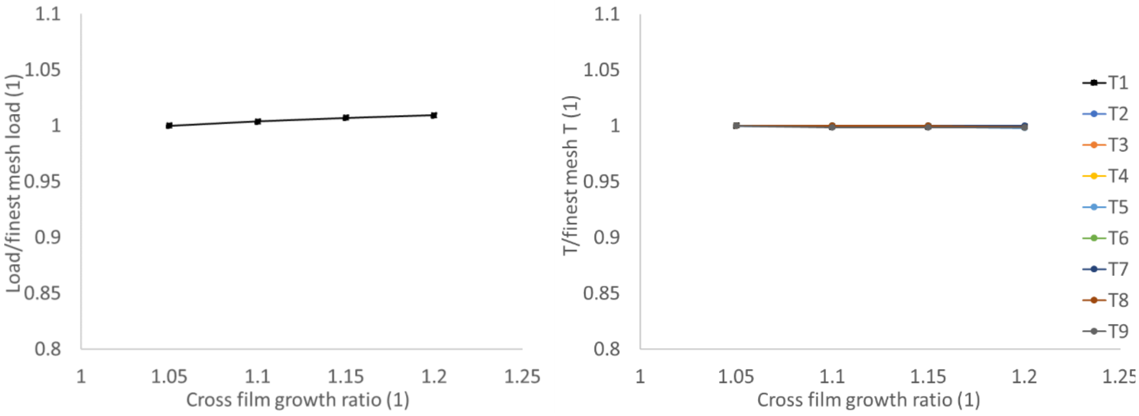

(a) Mesh sensitivity for load (b) Mesh sensitivity for temperature

Figure 90: Mesh sensitivity study results of cross film growth rate, laminar

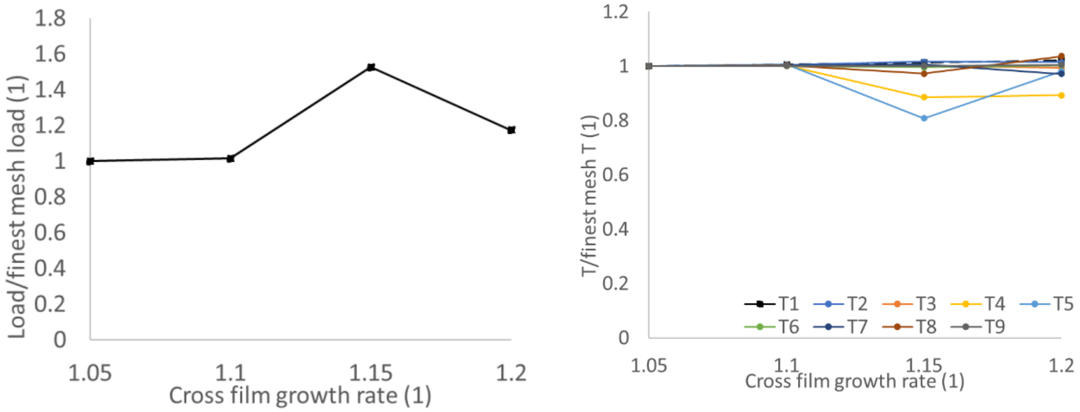

(a) Mesh sensitivity for load (b) Mesh sensitivity for temperature

Figure 91: Mesh sensitivity study results of cross film growth rate, turbulence

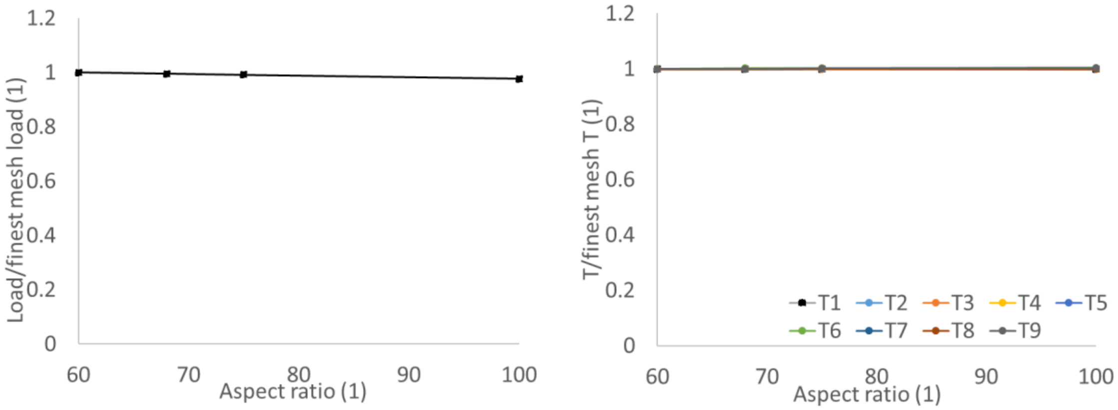

(c) Mesh sensitivity for load (d) Mesh sensitivity for temperature

Figure 92: Mesh sensitivity study results of circumferential and radial aspect ratio to cross film mesh size, laminar

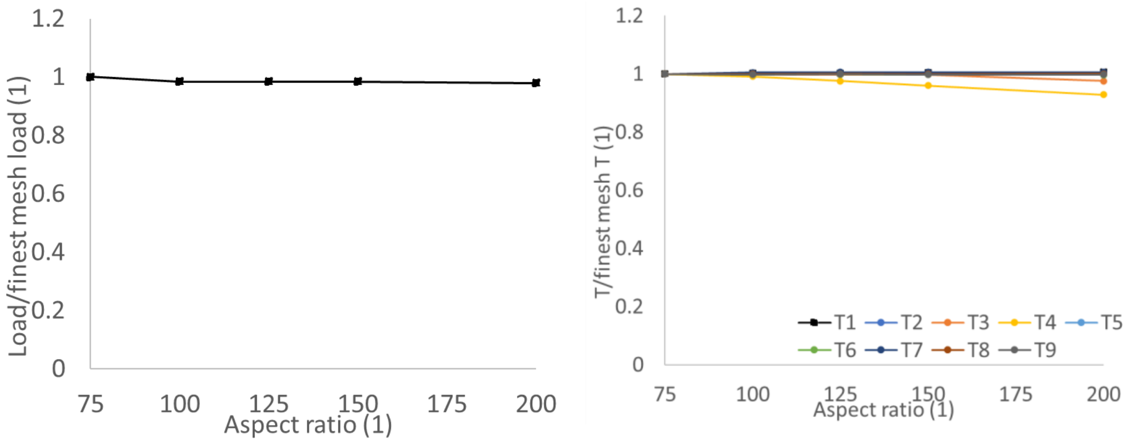

(c) Mesh sensitivity for load (d) Mesh sensitivity for temperature

Figure 93: Mesh sensitivity study results of circumferential and radial aspect ratio to cross film mesh size, turbulence

To improve the flow in the region between the groove and film, referred to the meshing optimization work in seals by Collins [54], inflation was added in both the groove and film in cross film and circumferential directions. The optimized meshing for the groove-film connecting for laminar and turbulence is shown in Figure 94 and Figure 95. The optimized meshing shows a unified mesh in the groove and film regions, which means the mesh has smooth, good growth between film and groove.

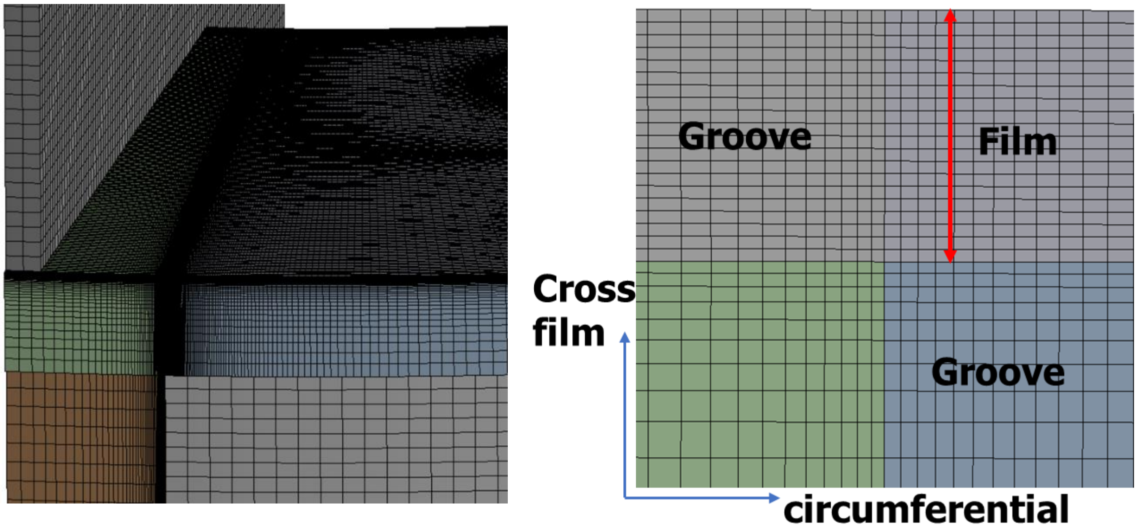

Figure 94: Optimized meshing for the groove-film circumferential connecting, laminar

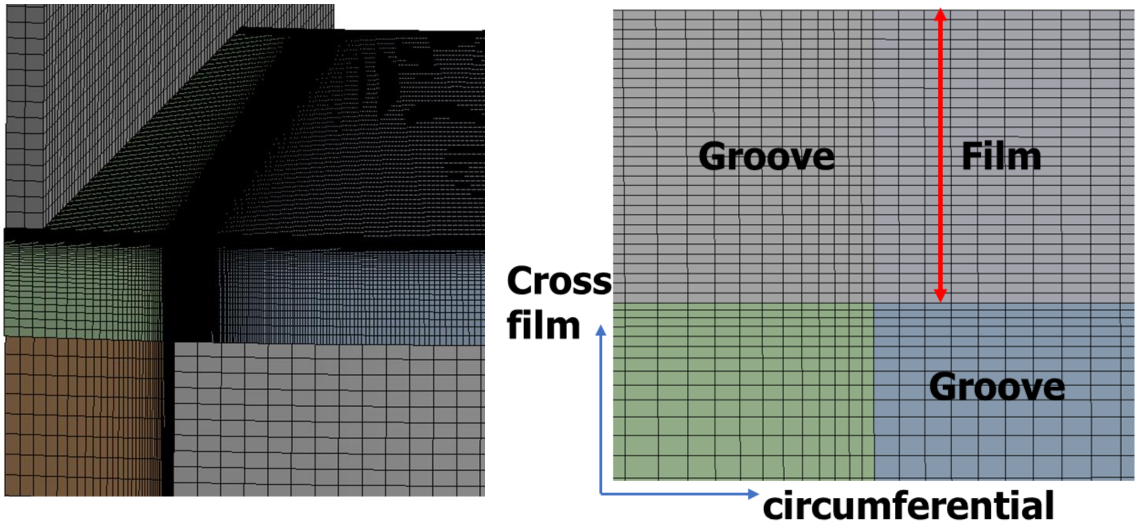

Figure 95: Optimized meshing for the groove-film circumferential connecting, turbulence

The insensitive meshing element number is 4.3 million for laminar and 6.5 million for turbulence. Taking meshing in turbulence as an example, the overall mesh and a close-up look at the mesh in the film, both inner and outer diameter grooves, pad, and runner, are shown in Figure 96.

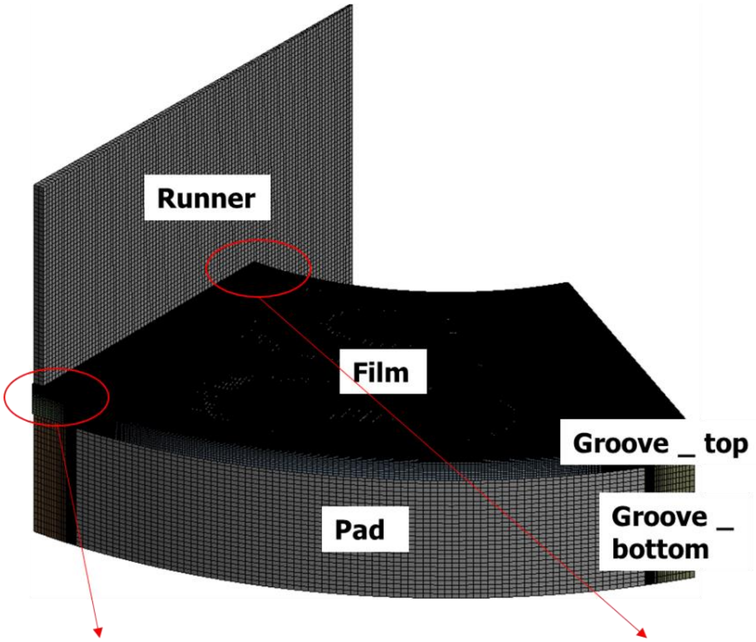

(a) Overall mesh

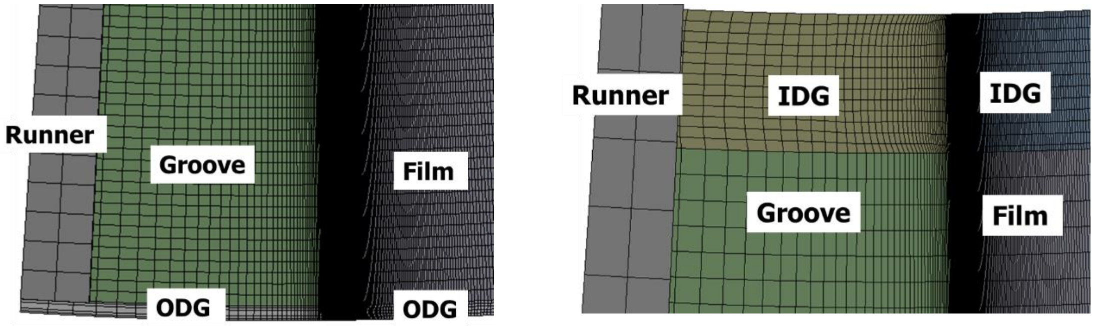

(b) Meshing for film, inner diameter groove, pad, and runner

(c) Meshing for film, outer diameter groove, pad, and runner

Figure 96: Full fluid-solid meshing for Capitao experiment

For a certain turbulence model, to meet the boundary layer flow assumption, the non-dimensional distance to wall value (y+) is required to be in a certain range. For SST, it is below 5. The y+ on the film's pad surface, runner surface, leading edge, and trailing is shown in Table 20. The contours of y+ on the film's pad surface and film's runner surface are shown in Figure 97. Table 20 and Figure 97 show that y+ is below 5, and most y+ on film's boundary surfaces is very small (<1).

Table 20. y+ value for film's boundary surfaces

SST _ thermal	Max y+, 9000 rpm	Avg y+, 9000 rpm
Film's pad surface	2.0	0.60
Film's runner surface	3.0	0.60
Leading edge	2.9	1.0
Trailing edge	2.3	0.46

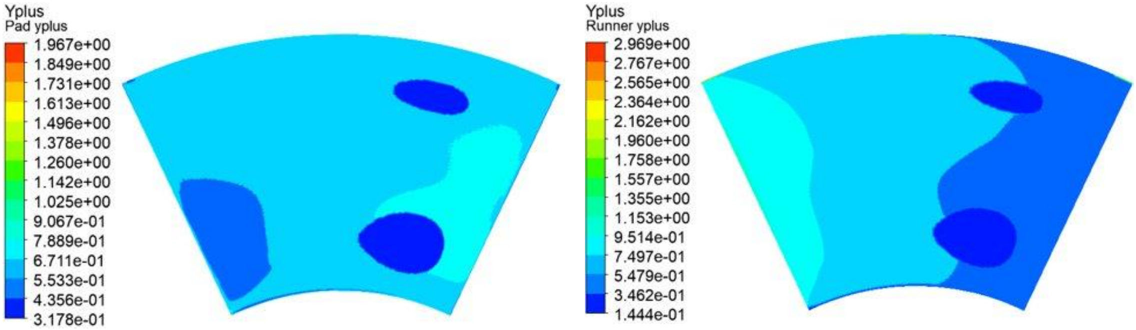

(a) Film's pad y+ (b) Film's runner y+

Figure 97: y+ on film's pad surface and film's runner surface

5.3.2 Boundary conditions

The boundary surfaces of the fluid domain, runner domain, and pad domain are shown in Figure 98, Figure 99, and Figure 100. The boundary conditions for the fluid, runner, and pad domains are below.

Fluid domain:

- Inlet: inlet with mass flow rate, and static temperature is supply temperature. The mass flow rate and inlet temperature values are from the experiment
- Outlet: opening, zero pressure, opening temperature
- Runner: fluid-solid interface, conservative heat flux, rotating speed
- Shaft: fluid-solid interface, conservative heat flux, rotating speed
- Pad: no-slip adiabatic wall, fluid-solid interface, conservative heat flux
- Interface 1 and 2: fluid-fluid interface, rotational periodicity, conservative heat flux
- Fluid wall: adiabatic wall

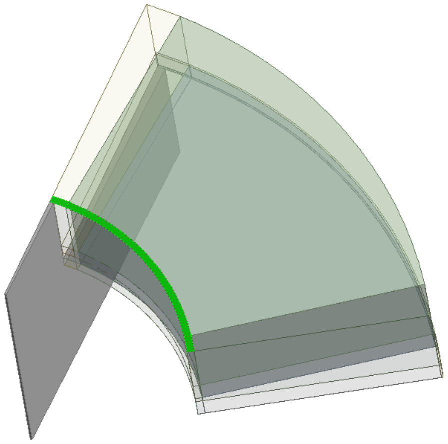

a. Fluid _ inlet

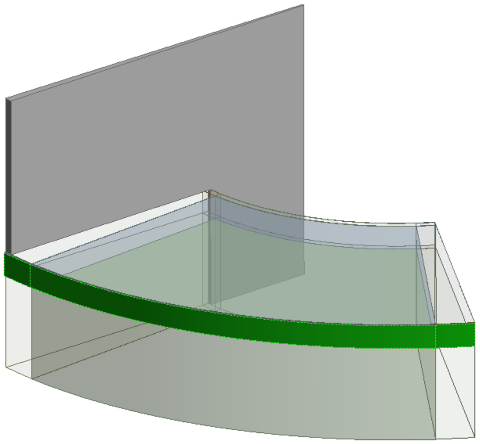

b. Fluid _ outlet

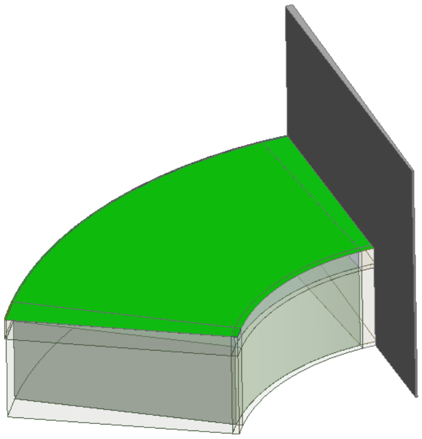

c. Fluid _ runner

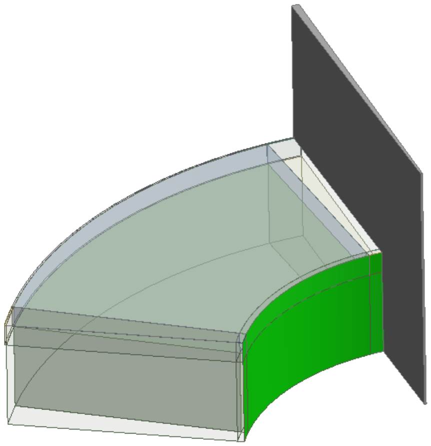

d. Fluid _ shaft

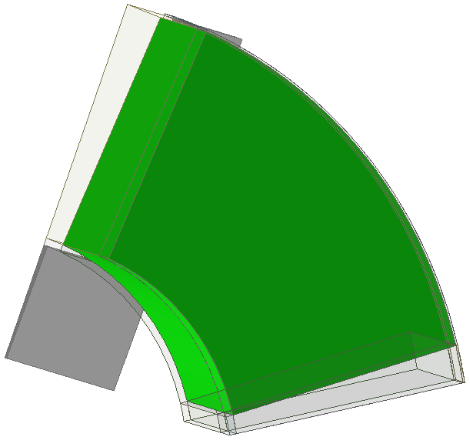

d. Fluid _ pad

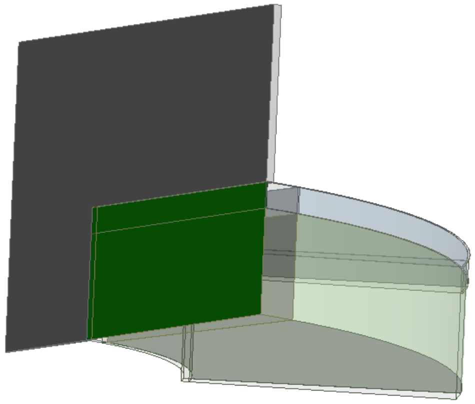

e. Fluid sector interface 1

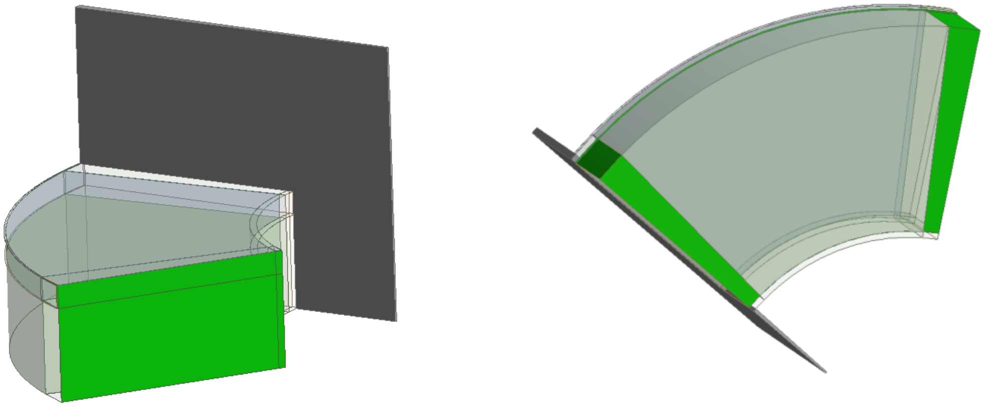

f. Fluid sector interface 2 g. Fluid _ wall

Figure 98: Fluid domain boundary surfaces in CFX model for Capitao experiment

Runner domain:

- Runner: fluid-solid interface, conservative flux
- Shaft: fluid-solid interface, conservative flux
- Runner sector interface: solid-solid interface with rotational periodicity, with conservative flux
- Runner OD: heat convection, ambient temperature is the average of outlet and pad temperature and supply temperature, constant heat conduction coefficient
- Runner top: heat convection, ambient temperature is supply temperature, constant heat conduction coefficient
- Runner bottom: adiabatic wall

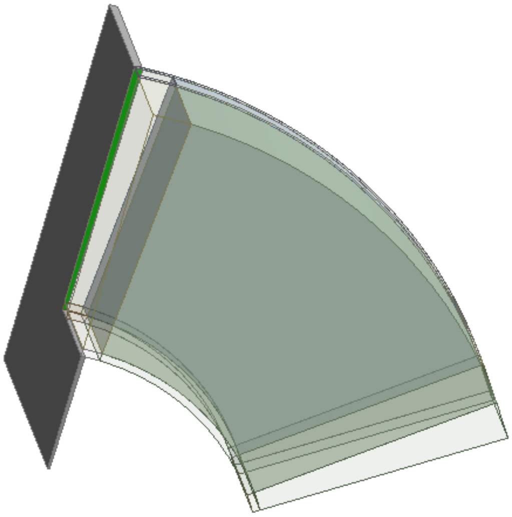

a. Runner _ fluid

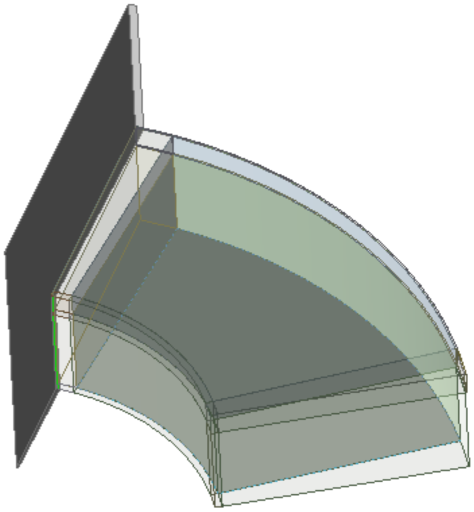

b. Runner _ shaft

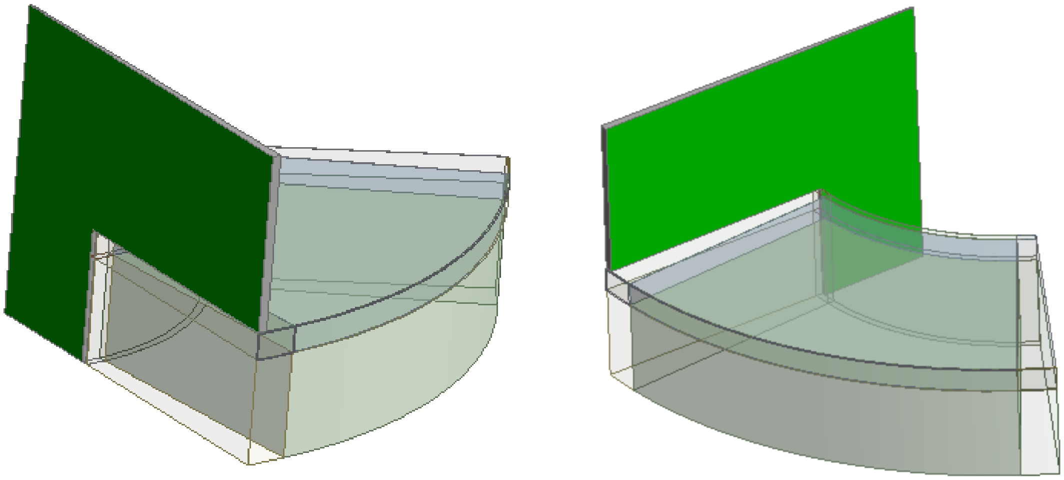

c. Runner sector interface

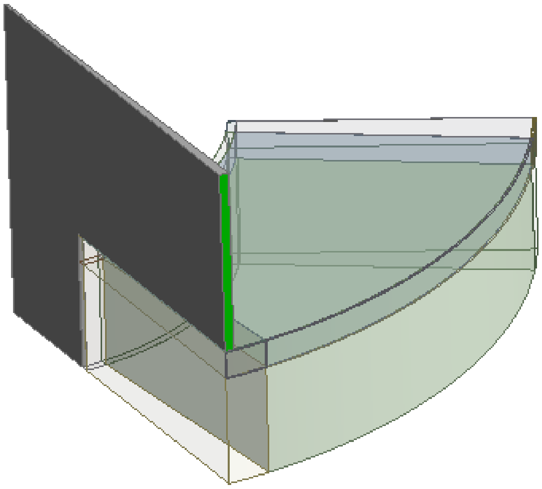

d. Runner _ OD

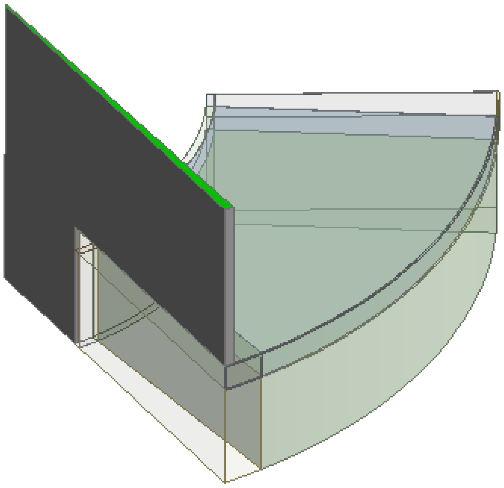

e. Runner _ top

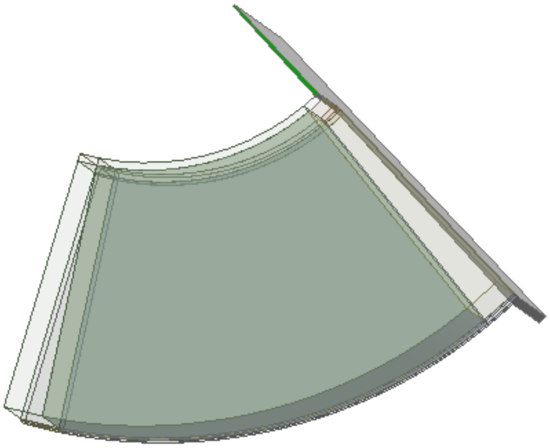

f. Runner _ bottom

Figure 99: Runner domain boundary surfaces in CFX model for Capitao experiment

Pad domain:

- Pad fluid: fluid-solid interface, conservative heat flux
- Pad OD & bottom: heat convection, ambient temperature is supply temperature, constant heat conduction coefficient

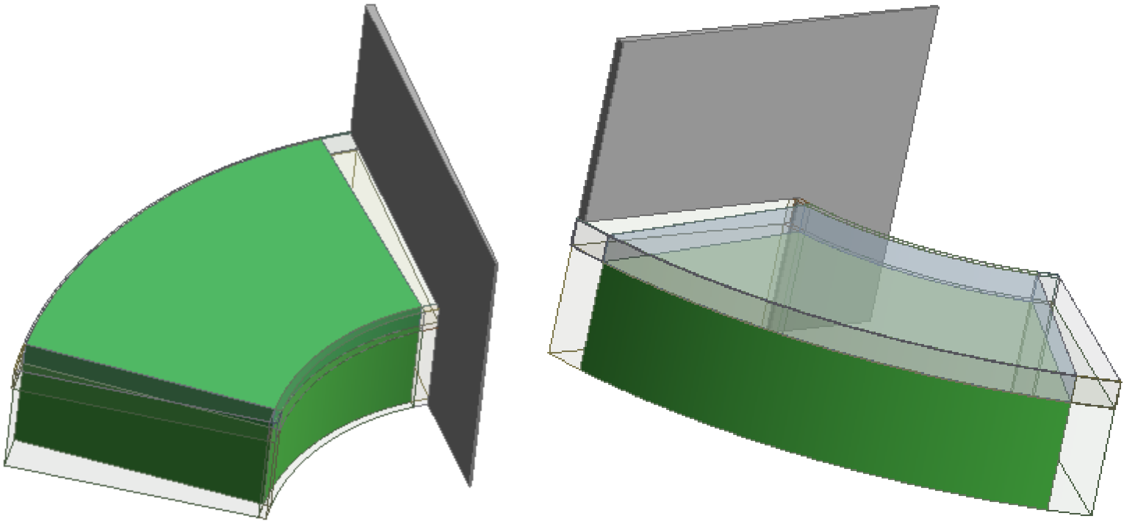

a. Pad _ fluid

b. Pad OD

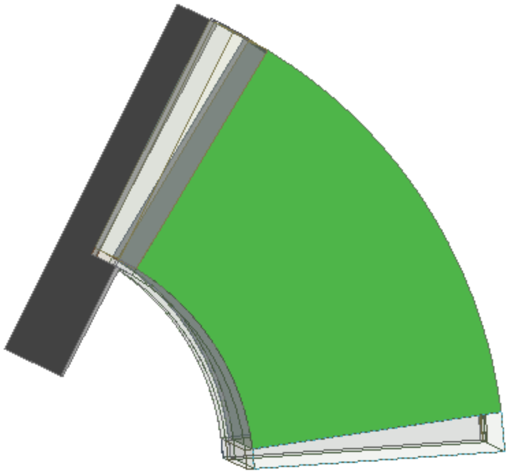

c. Pad bottom

Figure 100: Pad domain boundary surfaces in CFX model for Capitao experiment

5.3.3 Solver

This section introduces the solver control of the laminar and turbulence CFX model in ANSYS CFX. The advection scheme of laminar is high resolution. The turbulence numerics is first order. The advection scheme of turbulence is high resolution. The velocity pressure coupling uses high-resolution Rhie Chow.

Table 21. Equation settings for laminar

Equations	Advection scheme
Continuity	High Resolution
Energy	High Resolution
Momentum	High Resolution

Table 22. Equation settings for turbulence

Equations	Advection scheme
Continuity	High Resolution
Energy	High Resolution
Momentum	High Resolution
Turbulence Eddy Frequency	Upwind
Turbulence Kinetic Energy	Upwind

5.3.4 Convergence

This section introduces the convergence of both the laminar and turbulence CFX model. The convergence of momentum and mass, and heat transfer equations for laminar CFX is shown in Figure 101. The convergence of momentum and mass, and turbulence equations for turbulence CFX is shown in Figure 102. The maximum Root Mean Square (RMS) value for the laminar and turbulence model is on the scale of e-4. From Figure 101 and Figure 102, it is known that the convergence of laminar and turbulence is stable. The CUP time cost for turbulence is very high. It took 720 CPU hours per 700 timesteps' runs for a fixed film. When iterating film to match the load, taking ten runs for a specific speed, for example, is 7200 CPU hours. When calculating multiple speeds, taking three speeds as an example, that is 21,600 CPU hours. When calculating multiple loads, taking two loads as an example, that is 43,200 CPU hours. The University of Virginia only allows 100,000 CPU hours roughly every three months for each lab.

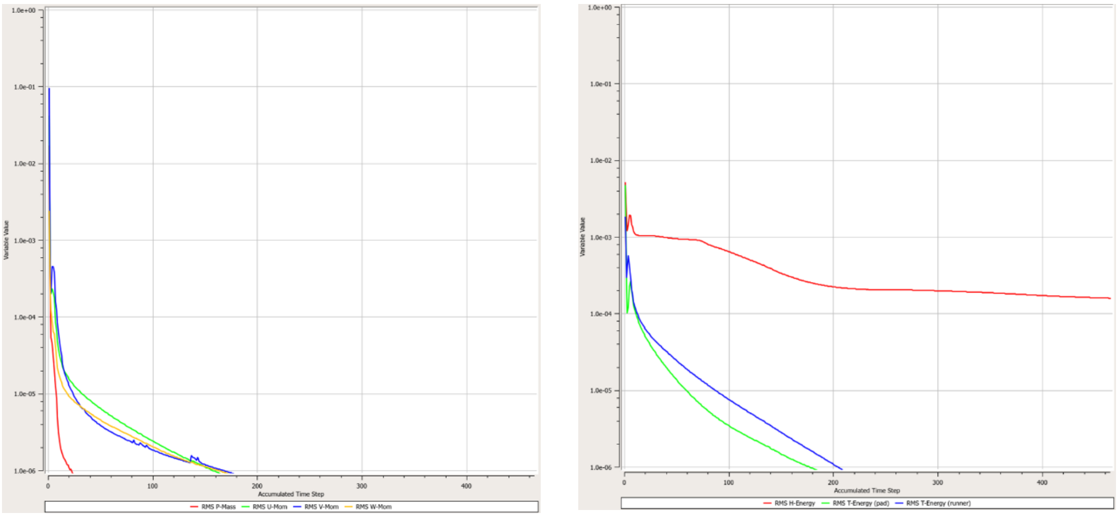

(a) Laminar: Momentum and mass (b) Laminar: Heat transfer

Figure 101: Momentum and mass, and heat transfer convergence in laminar CFX model for Capitao experiment

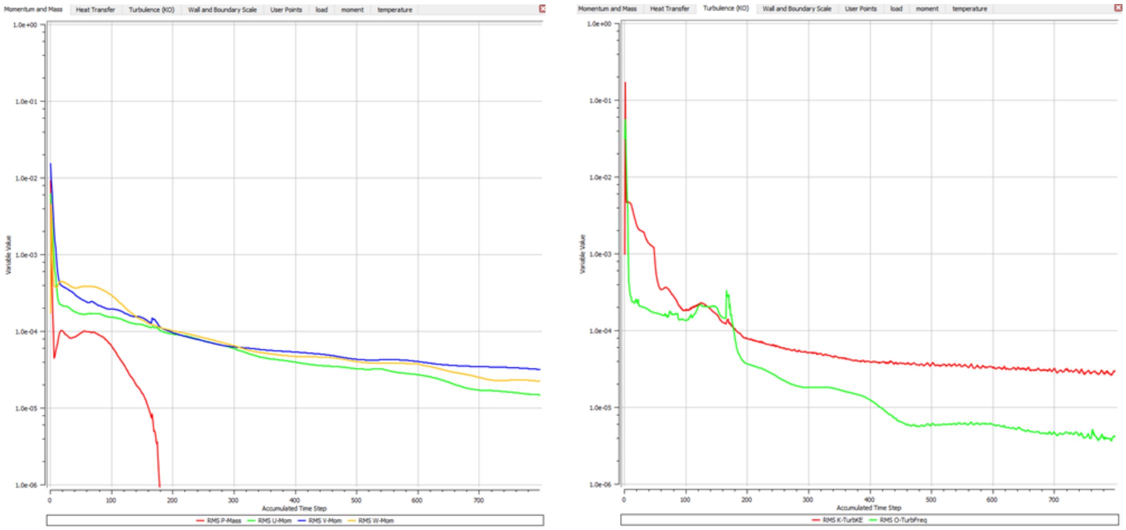

(a) Turbulence: Momentum and mass (b) Turbulence: Turbulence

Figure 102: Momentum and mass, and turbulence convergence in turbulence CFX model for Capitao experiment

The convergence of load and nine probe temperatures for laminar is shown in Figure 103. While Figure 104 shows the convergence of load and temperature for turbulence. From Figures Figure 103 and Figure 104, it is known that load and temperature are converged in both laminar and turbulence.

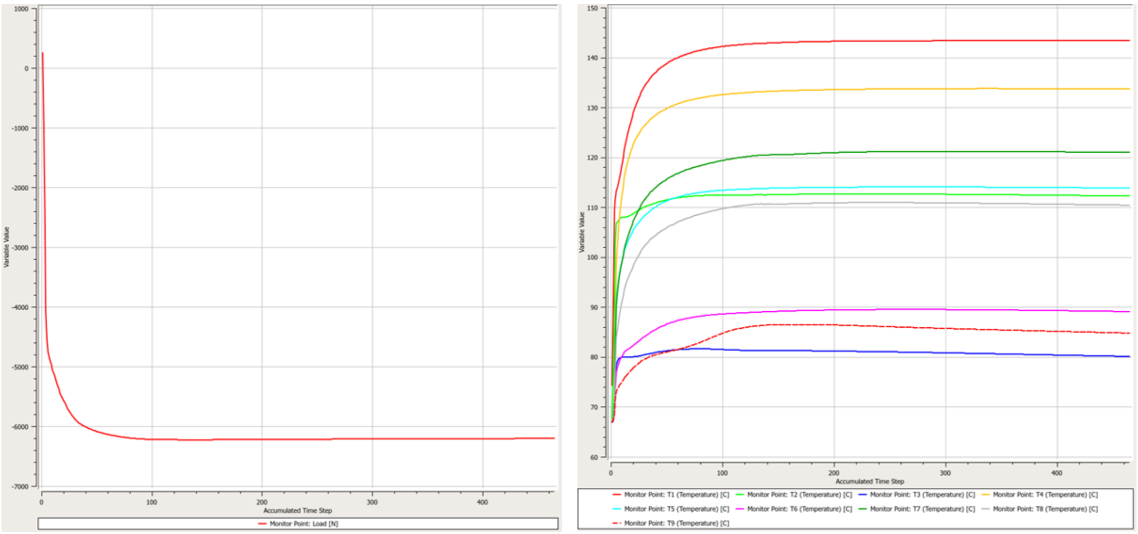

(a) Laminar: load (b) Laminar: temperature

Figure 103: Load and temperature convergence in laminar CFX model for Capitao experiment

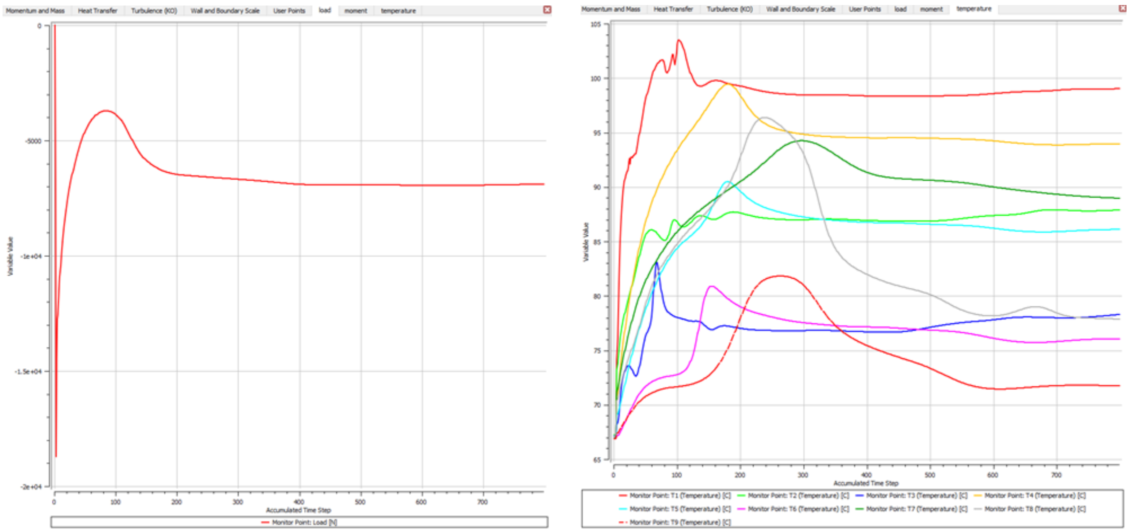

(a) Turbulence: load (b) Turbulence: temperature

Figure 104: Load and temperature convergence in turbulence CFX model for Capitao experiment

5.3.5 Crowning impact

Crowning is a machining technique that cuts material out of the pad surface to change the film thickness on purpose. The simplest pad structure is a flat pad such that there is no crowning on the pad surface. Fillon [59] used taper in a central pivot thrust bearing and stated that the initial geometry of the pad is also of great importance for central pivot thrust bearings. Pivot location affects temperature and pressure [4] [57].

As shown in Figure 105, the pressure shows a negative pressure. The negative pressure is mostly in the leading edge area, and this is a motivation for studying the crowning impact. Abdel-Latif [58] found large load shows negative pressure near the outlet edge.

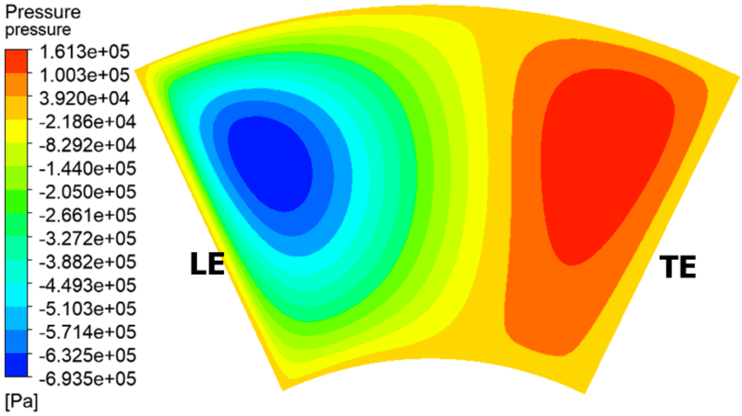

Figure 105: Pad pressure contour in CFX model for Capitao experiment without crowning

This negative pressure is similar to that seen in slider film bearing with a small tilting angle. Historically, parallel thrust bearings were popular as they were easier and less expensive to manufacture. The parallel thrust bearing supporting load was first found by Tower (1891) [118] but was soon forgotten by the bearing industry [119]. It was not until 1946, after World War Two, that researcher Fogg brought considerable attention to the bearing industry about parallel film supporting loads. Fogg experimented and showed that a parallel thrust bearing could support loads. This is the largest single research topic in the history of thrust-bearing research. This phenomenon was known as the “Fogg paradox” [120], as isothermal theory cannot explain it. After the finding of the “Fogg paradox”, people were confused about it because, at that time, people thought the lubrication in bearing was isothermal, and this parallel film holding load cannot be explained with isothermal lubrication theory. So some other researchers started repeating his experiment similar to Fog’s and found the same thing by Kettleborough (1955) in parallel surface thrust bearings [121] [122].

In the meantime, other researchers started thinking about non-isothermal film in slider bearings. Slider bearing is an ideal model for theory building as they are one-dimensional and have minimum shape impact. Therefore, researchers started studying the non-isothermal film in slider bearings. Shaw (1947) [123], Cope (1949) [124], Osterle (1953) [125], Cameron (1958) [126], Currie (1965) [127] studied the thermal impact in supporting loads for parallel film. Variations in lubricant properties can cause significant variations in the pressure distribution. While they also found that sometimes the thermo does not have enough power to hold the loads. The next milestone is the study of thermal tapers. Thermal tapers mean the thermal distortion equals a taper in the leading edge. This thermal taper is nowadays referred to as a mechanical deformation crowning effect. After the study by Swift (1932) [128], Cameron (1963-1975) [129] [21] [130] [119], Neal (1963) [19]. The thermal wedge was found and known to the bearing industry.

Researchers gradually learned the negative pressure in the parallel thrust bearing. For example, Cameron (1958) [126], Dowson and Hudson (1963) studied the infinite slider bearings [131] [132], Neal (1963) [19], and Ettles and Cameron (1965-1966) studied the thermal and elastic distortions in thrust bearings [21] [129] [133], as shown in Figure 106. These researchers experimentally found that parallel thrust bearings have negative pressure unless distortion occurs. The max negative pressure is proportional to the inverse square of film thickness.

(a) (b) (c) (d) (e)

Figure 106: Ettles and Cameron experiment with parallel thrust bearing in multiple film shapes and speeds

In order to test the theory that a no-crowning slider bearing with a small tilting angle behaves similarly to a parallel film, a slider bearing was tested. The pressure profile in the flow direction with Shear Stress Transport (SST) turbulence model is shown in Figure 107. Trailing edge film thickness is fixed as 0.03mm. Case of LE0.3 is parallel film. By increasing the leading edge (LE) film thickness, the film becomes a converging film in cases of LE0.04~LE0.1. Case of LE0.1 is with the largest tilting angle. Figure 107 shows that these pressure profiles are similar to Ettles and Cameron’s experiment results [21]. The experiment shows that the frequency (times of phase from decreasing to increasing) depends on film shape and speed. For slight tilting film, the smaller the LE film, the closer to parallel, then pressure is showing a decreasing then increasing trend in the flow direction.

This highlights the importance of crowning on the performance of central pivot thrust bearings with shallow tilting angles.

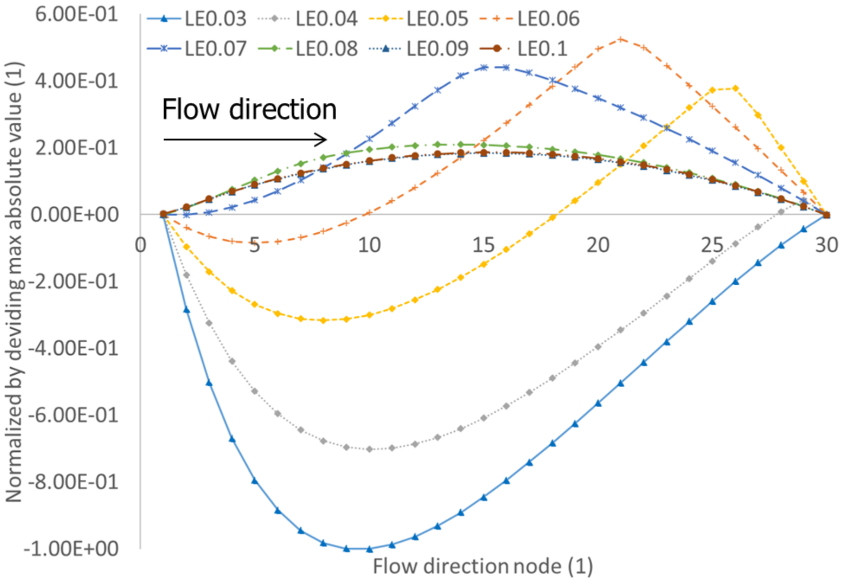

Figure 107: CFX results of slider bearing, film only

After adding crowning, the full fluid-solid model no longer exhibited negative pressures but showed consistent variations compared to the experiment. Therefore, for center pivot thrust bearings, crowning is an essential structure that makes the CFX model work for a slight tilting pad. Crowning functions as deformation in the center pivot thrust bearing, and this is consistent with the traditional knowledge of center pivot only working with deformation included. Fillon [59] stated that the performance of thrust bearings with center pivot pads is more sensitive to pad surface geometry than offset pads. The film-only cases with and without crowning validated the accuracy of this statement. For a flat pad thrust bearing, this sensitivity reflects on the effective deformation incurred by thermal deformation, which is the crowning in this case.

5.4 Fixed film, CFX results at a single speed

5.4.1 Benchmark code results

The load capacity and pad temperature predicted in the benchmark code are shown in Table 23 and Figure 108. Table 21 shows that the benchmark predicts load and pad temperature well, with a reasonable error. The model in benchmark code only has film, pad, and runner, and there is no groove. Benchmark code predicted fully laminar for this case.

Table 23. Load prediction in benchmark

	load, N	experiment load error, %
Benchmark	6334	2.8

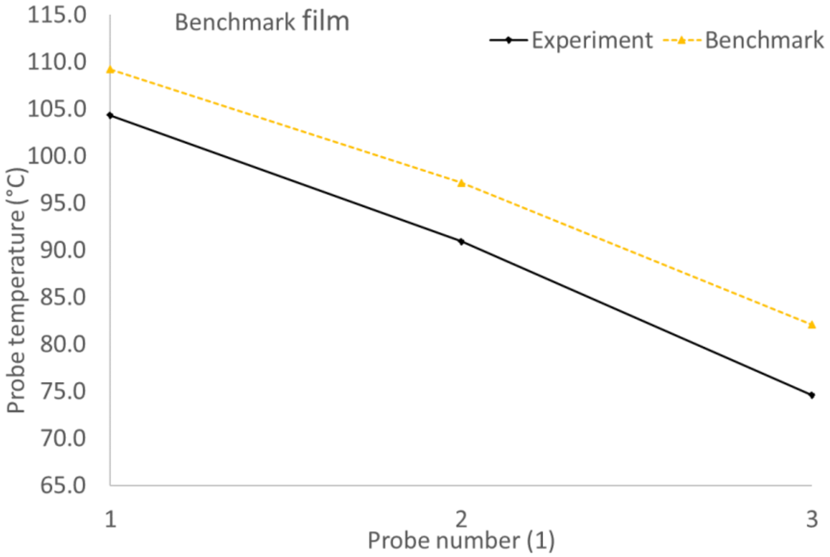

(a) ID

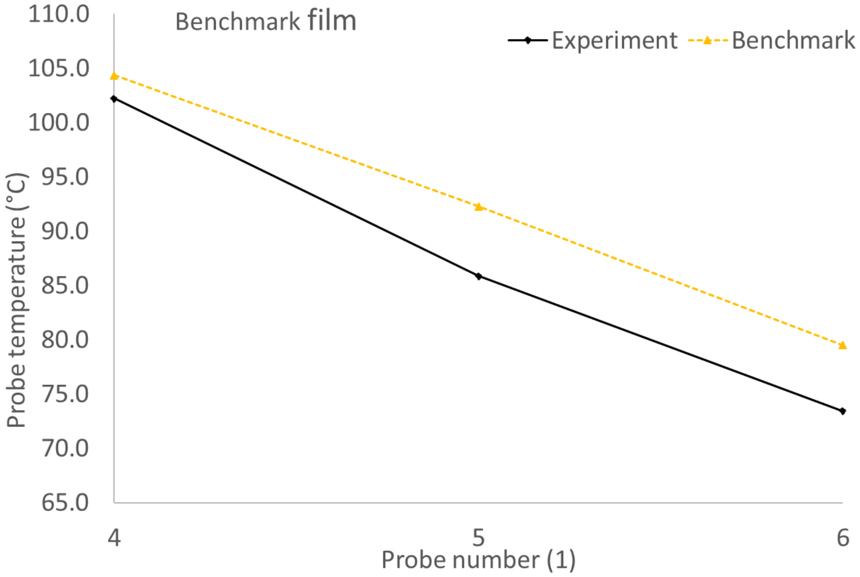

(b) MD

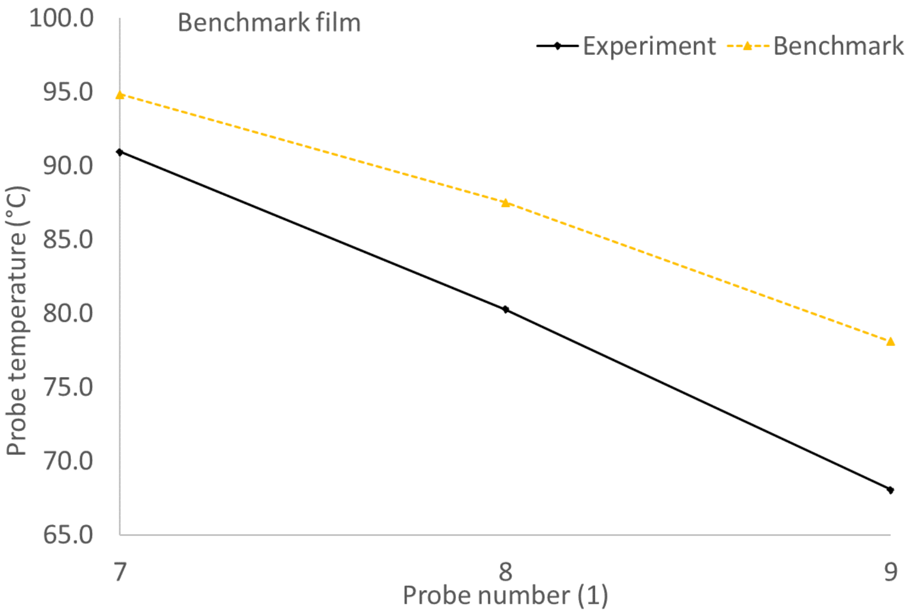

(c) OD

Figure 108: Pad temperature between benchmark code and experiment

5.4.2 No groove CFX in laminar

Besides traditional bearing modeling based on finite element methods, commercial software is becoming more common and popular. In contrast, fundamental bearing studies with commercial CFD have rarely been reported. Therefore, under such practical needs, the physics within the bearing can be better understood by studying the impact between film, pad, and runner. A more accurate model results in a better load capacity, film thickness, and temperature prediction, leading to better dynamic coefficient predictions.

Figure 109 shows a progressive model detail study, including the film CFX model, film + pad CFX model, and film + pad + runner CFX model. The physics of these progressive modeling cases is shown in Table 24. Film-only CFX case is the base model. The film + pad CFX case provides an ideal model for studying the heat conduction between fluid and solid. The film + pad + runner CFX case is an ideal model for studying rotor impact, comparing the film + pad CFX case with film + pad + runner CFX case.

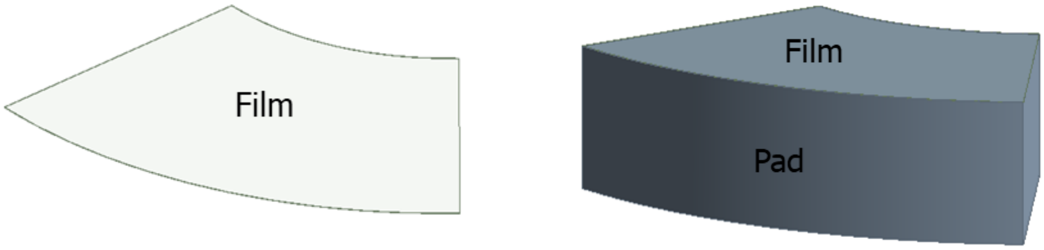

(a) Film CFX model (b) Film + Pad CFX model

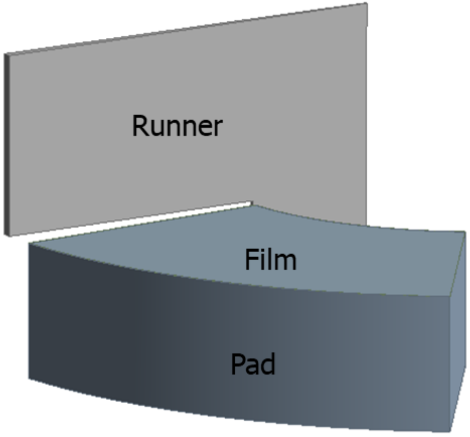

(c) Film + Pad + Runner CFX model

Figure 109: Progressive model detail study

Table 24. Multiple-Component Modeling Domain

	Case	Components	Physics
Leading edge temperature with experimental regression	1	Film	Base model
	2	Film + Pad	Heat conduction between fluid and solid
	3	Film + Pad + Runner	Rotor impact

As shown in Figure 110, the leading-edge temperature is a parabolic regression function (three blue color nodes on the leading edge) varying in the radial direction. The regression function is used to more closely match the experimental data taken slightly away from the actual leading edge. With minimum uncertainty, comparing multiple component cases 1-3 would provide more insights. The leading edge temperature regression function is a quadratic equation of radius, as shown in Table 25. Table 26 shows the regression for calculating the three temperature nodes on the leading edge, and the regression function assumes quadratic functions for both circumferential angle and radius. Therefore, there are eight terms, including first-order terms, second-order terms, and their cross-coupled terms.

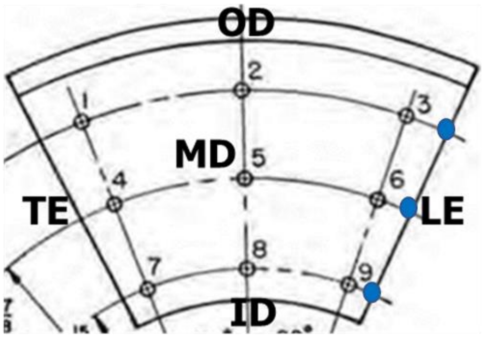

Figure 110: Three temperature locations on the leading edge

Table 25. Regression for leading-edge temperature

Terms	Unit
r	m
r^2	m^2

Table 26. Regression for calculating three leading-edge temperature

Terms	Unit
r	m
θ	degree
r^2	m^2
θ^2	degree^2
$r\theta$	m*degree
$r^2\theta$	m^2*degree
$r\theta^2$	m*degree^2
$r^2\theta^2$	m^2*degree^2

The comparison of load, circumferential and radial moments are shown in Table 27, including benchmark code, film, film & pad, film & pad & runner, and full model. From this table, it is known that film, cases of film & pad, and film & pad & runner, with benchmark code's film profile and leading-edge experimental temperature, are accurate in predicting load capacity with a reasonable error.

Table 27. Comparison of load and moments in CFX, with laminar

	Load, N	Experimental load error, %	Circumferential moment, N*m	Radial moment, N*m
Benchmark code	6334	2.8	5.4e-4	-7.5e-4
Film	5458	-11	4.3	-2.2
Film & Pad	6047	-1.9	3.0	-1.3
Film & Pad & Runner	5947	-3.5	4.4	-1.5

Figure 111 shows the pad temperature comparison between film CFX, film & pad CFX, film & pad & runner CFX, benchmark, and experiment. Figure 111 shows that film only case has the largest temperature error, and the film + pad case has the same pad temperature as the film + pad + runner case. The pad has the largest impact on the overall pad temperature, and the runner has no impact.

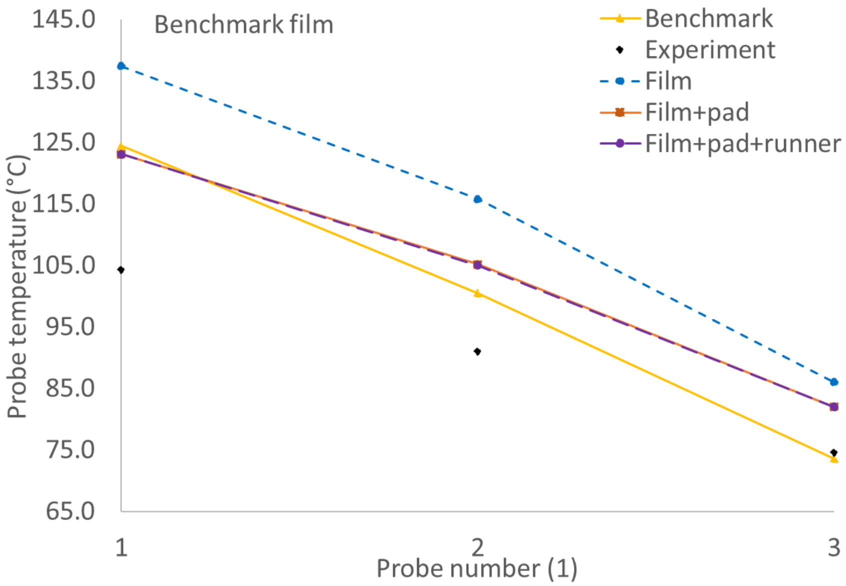

(a) ID

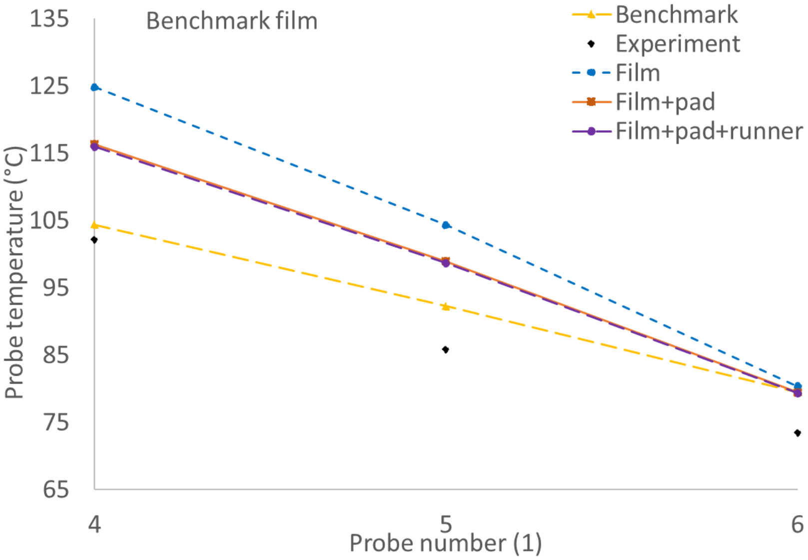

(b) MD

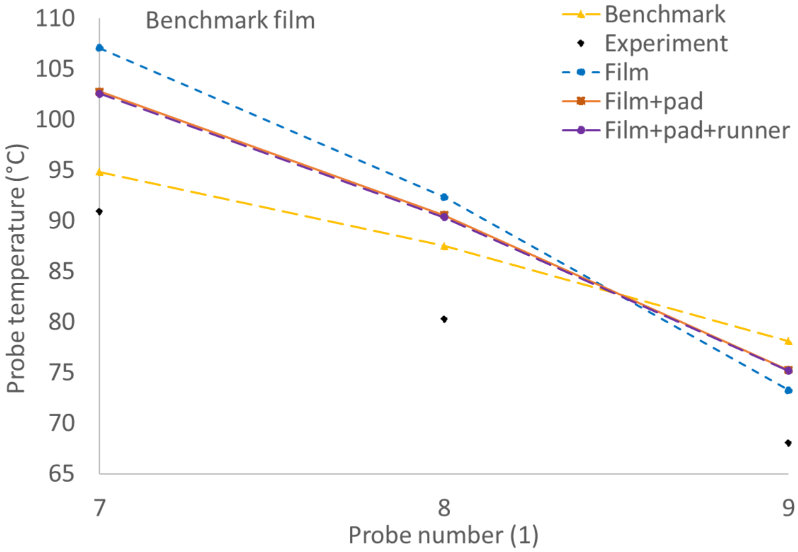

(c) OD

Figure 111: CFX vs. experimental pad temperature comparison, with benchmark film

5.4.3 Groove CFX in laminar and turbulence

As shown in Figure 112, the most inclusive CFX model has the full fluid domain including film, Groove Between Pads (GBP), Outer Diameter Groove (ODG), and Inner Diameter Groove (IDG); and also a full solid domain including pad and runner. The full fluid-solid (groove model) CFX case is an ideal mode for studying the impact of the groove.

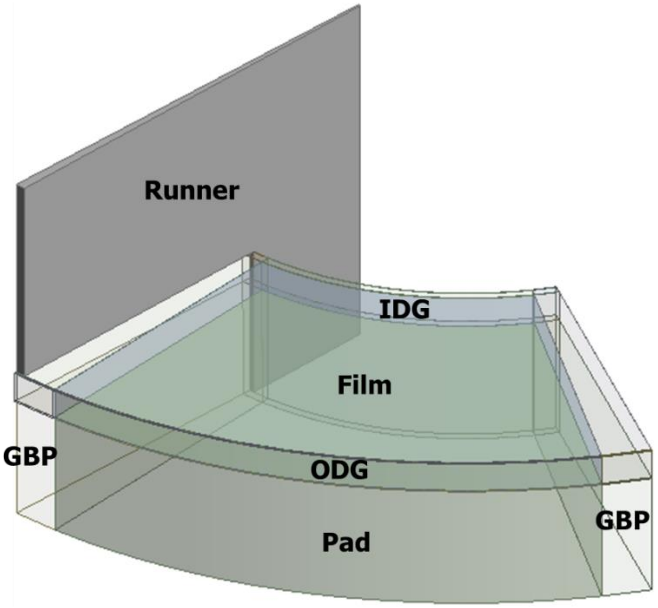

Figure 112: Full model (groove model): Film + Pad + Runner + Groove CFX model

The load capacity of the groove model based on a laminar and turbulence model assumption is shown in Table 28, where the full model in turbulence shows a reasonable load error, while the full laminar model results in a dramatically lower load.

Table 28. The load capacity of the groove model with laminar and turbulence

	Load, N	Experimental load error, %	Circumferential moment, N*m	Radial moment, N*m
Benchmark code	6334	2.8	5.4e-4	-7.5e-4
Turbulence	5898	11.9	8.7	2.6
Laminar	1988	-67.7	1.1	-1.5

Explanation of low load in laminar groove CFX

Figure 113 shows the leading-edge temperature comparison of the laminar groove, turbulence groove, and laminar no groove results, with benchmark's film results, at different locations, including inner diameter (ID), 25% from ID, middle diameter (MD), 75% from ID, outer diameter (OD). The locations are shown in Figure 114. Figure 113 shows that the laminar groove case has a very large cross-film varying leading edge temperature. In contrast, the turbulence groove case is very close to the laminar no groove case for the cross-film temperature distribution. Table 29 compares max leading-edge temperature in laminar no groove and laminar groove cases. Table 30 shows the comparison of max leading-edge temperature in turbulence groove case and laminar groove case. Table 29 and Table 30 show that max leading-edge temperature is dramatically different between the laminar no groove case and laminar groove case and between the turbulence groove case and laminar groove case. This shows a preliminary explanation that the different leading-edge temperatures may influence the low load associated with the laminar groove case.

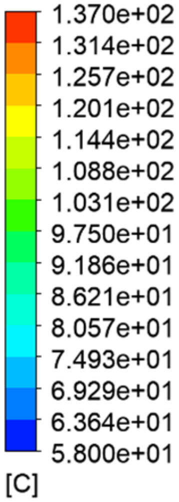

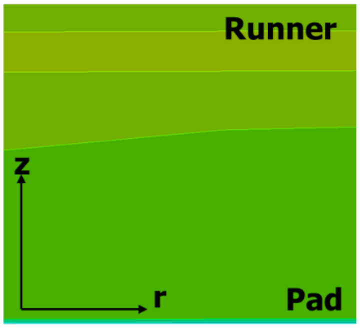

Laminar groove: ID

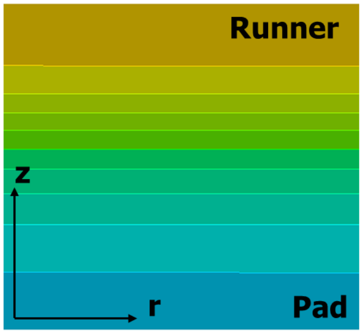

Laminar groove: 25%

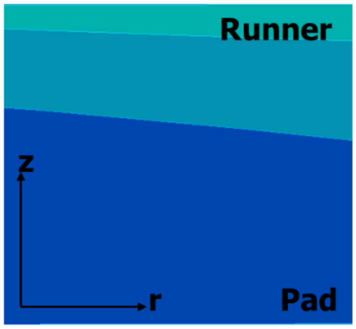

Turbulence groove: ID

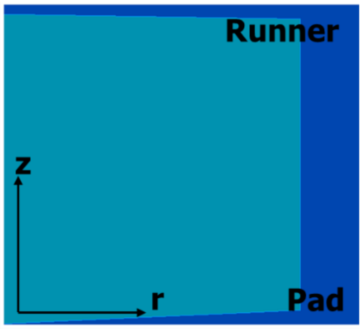

Laminar no groove: ID

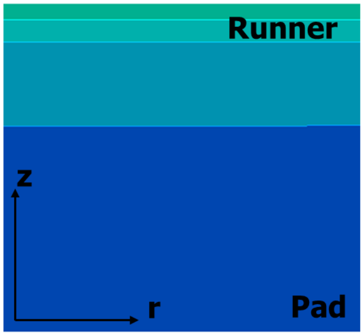

Turbulence groove: 25%

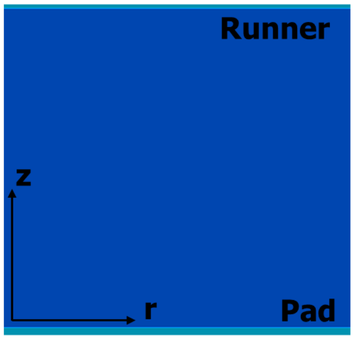

Laminar no groove: 25%

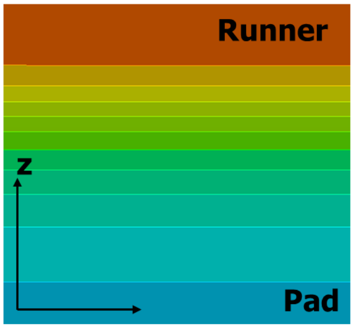

Laminar groove: MD

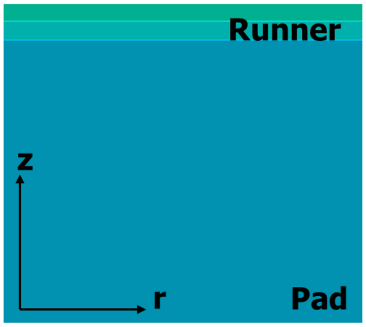

Turbulence groove: MD

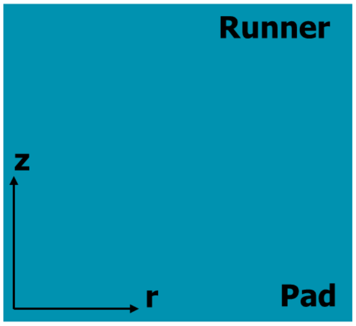

Laminar no groove: MD

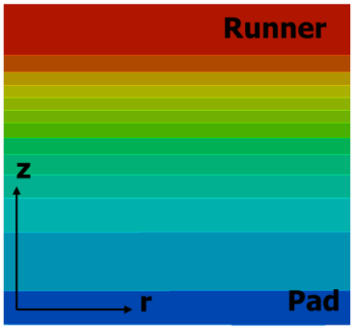

Laminar groove: 75%

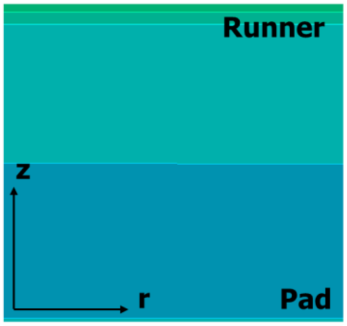

Turbulence groove: 75%

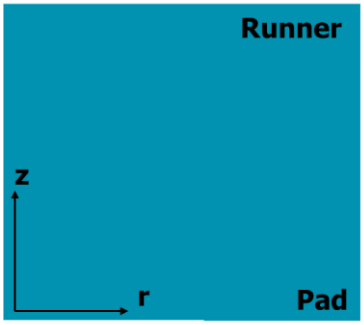

Laminar no groove: 75%

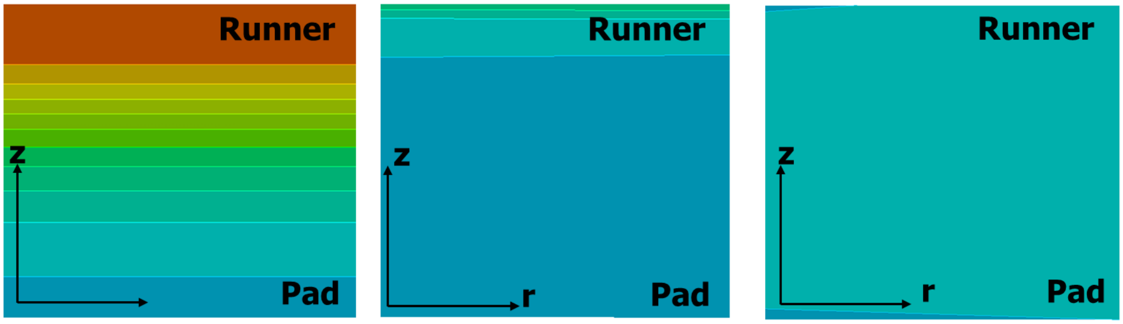

Laminar groove: OD Turbulence groove: OD Laminar no groove: OD

Figure 113: Leading edge temperature comparison of laminar groove, turbulence groove, and laminar no groove, with benchmark's film

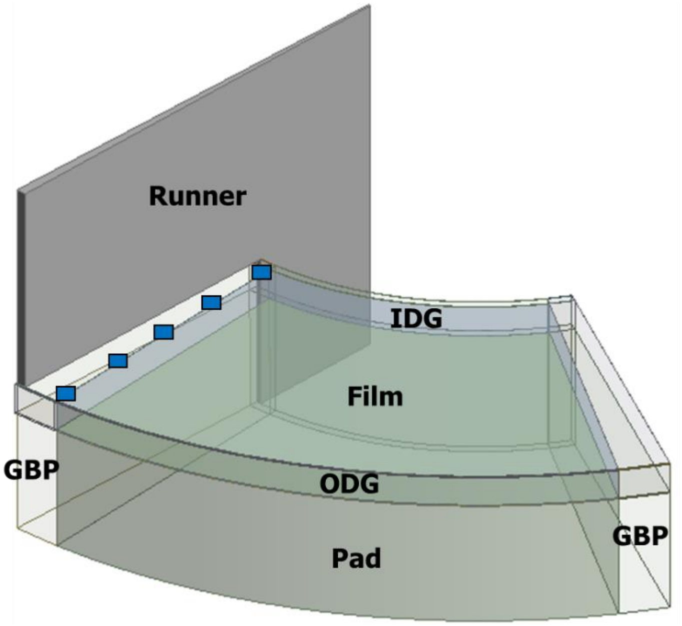

Figure 114: Locations of ID, 25%, MD, 75%, OD on the leading edge

Table 29. Comparison of max leading-edge temperature in laminar no groove case and laminar groove case

Model	Max leading edge temperature, °C	Difference
Laminar _ no groove	80	71%
Laminar _ groove	137	

Table 30. Comparison of max leading-edge temperature in turbulence groove case and laminar groove case

Model	Max leading edge temperature, °C	Difference
Turbulence _ groove	89	54%
Laminar _ groove	137	

A test was performed to have a more robust and convincing explanation for the low load of the laminar groove case. The test was that the case of laminar no groove used the leading-edge temperature distribution in the laminar groove case to test whether the laminar no groove case would have a significantly closer load comparison with the laminar groove case. Pajączkowski [133] looked into the velocity under the impact of the cross-film temperature varying in thrust bearings with commercial CFD. However, he did not study the impact of the cross-film temperature varying on load capacity.

Figure 115 shows the locations for temperature nodes in the laminar groove for calculating the regression function for the leading-edge temperature for the laminar no groove case. The leading-edge temperature varies in radial and cross-film directions with a quadratic regression. Table 31 shows a regression for the leading-edge temperature in the laminar no groove case.

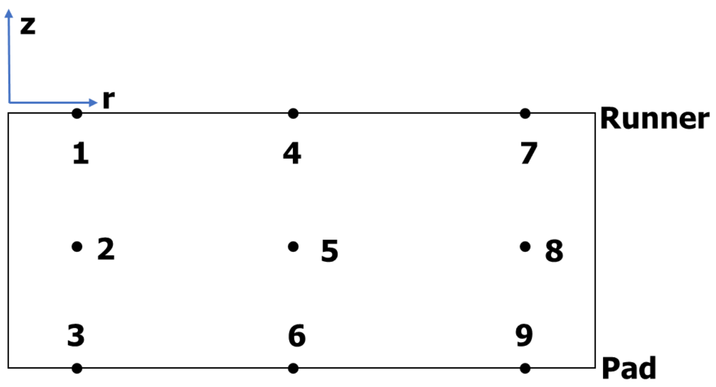

Figure 115: Locations for temperature nodes in the laminar groove for calculating regression function for leading-edge temperature in laminar no groove

Table 31. Regression for leading-edge temperature in laminar no groove case

Terms	Unit
r	m
z	m
r^2	m^2
z^2	m^2
r*z	m^2
r^2z	m^3
rz^2	m^3
r^2z^2	m^4

Table 32 shows the load capacity comparison of the laminar groove and laminar no groove cases using laminar groove leading edge regression temperature, along with the benchmark's film model results. Table 32 shows a solid explanation of the low load in the laminar groove case. The load in the laminar no groove case decreased by 60% using the leading-edge temperature from the laminar groove case. Figure 116 shows the leading-edge temperature comparison of the laminar groove and laminar no groove with laminar groove leading edge regression temperature, with benchmark's film. Figure 116 shows the remaining difference of load between laminar groove and laminar no groove cases, which is due to not having the exact same leading-edge temperature distribution due to regression function mismatch, shown in Table 33.

Table 32. Load capacity comparison of laminar groove and laminar no groove using laminar groove leading edge regression temperature, with benchmark's film

Model	Load, N	Experimental load error, %
Laminar _ no groove	2440	-60.4
Laminar _ groove	1988	-67.7

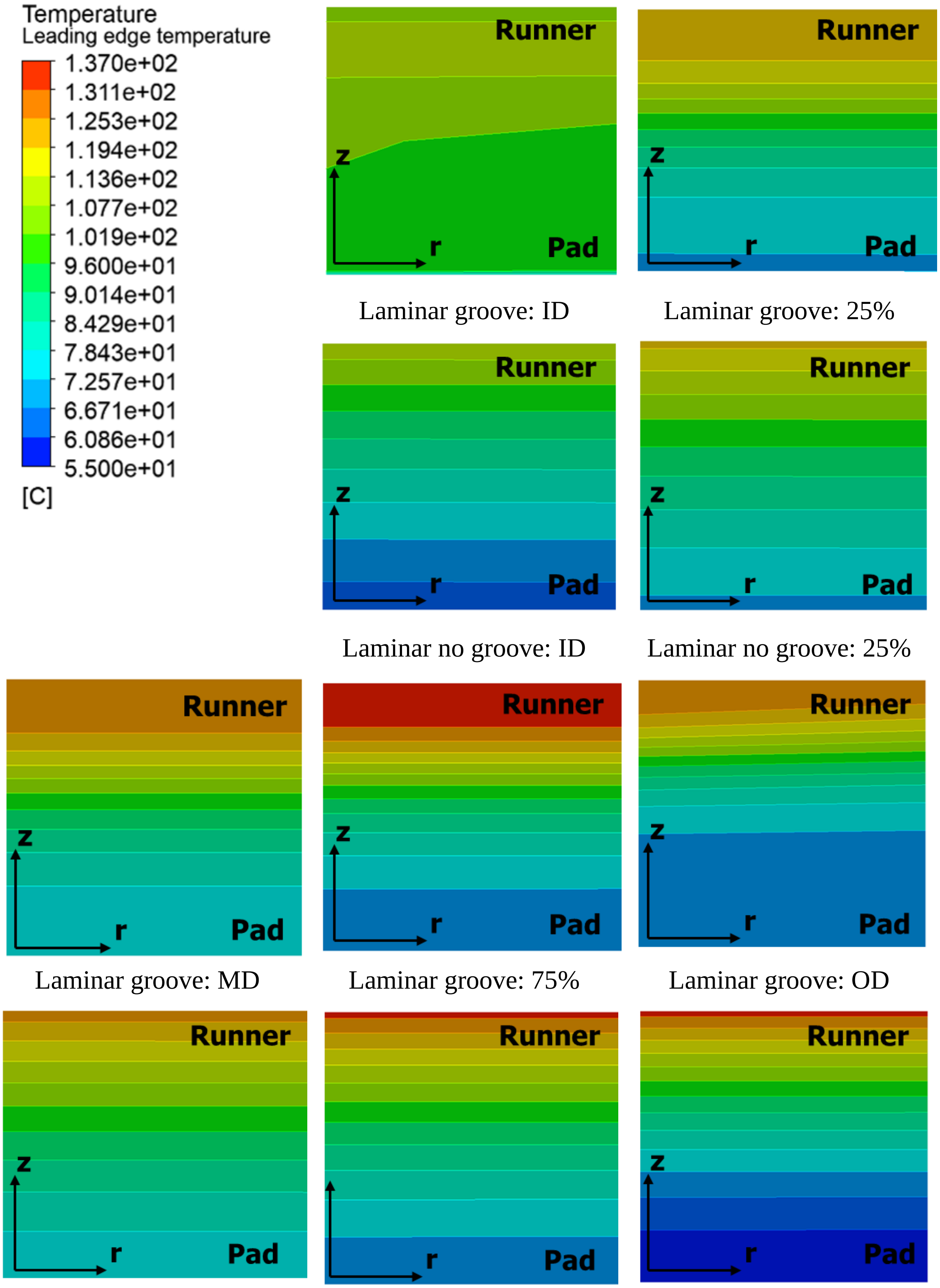

Laminar groove: ID

Laminar groove: 25%

Laminar no groove: ID

Laminar no groove: 25%

Laminar groove: MD

Laminar groove: 75%

Laminar groove: OD

Laminar no groove: MD

Laminar no groove: 75%

Laminar no groove: OD

Figure 116: Leading edge temperature comparison of laminar groove and laminar no groove with laminar groove leading edge regression temperature, with benchmark film

Table 33. The residual output of regression function in laminar no groove case

Observation	Predicted T, °C	Residuals
1	118.6	-0.907
2	88.6	1.81
3	69.4	-0.907
4	129.8	-0.106
5	93.6	0.212
6	73.5	-0.106
7	134.1	0.459
8	86.3	-0.917
9	63.6	0.459

Figure 117 shows the hot oil carry-over model in thrust bearings. Hot oil carry-over mixes two oil flows in the groove: hot oil from pad 1 trailing edge and cold supply oil. Figure 118(a) shows the leading-edge temperature of the benchmark case. As shown in Figure 118(a), the benchmark uses a constant temperature for the whole leading edge, which is an estimated value between the TE hot oil and supply oil temperature values. As shown in Figure 118(b) and Figure 118(c), the turbulence leading edge temperature is close to the leading-edge benchmark temperature, while the laminar leading edge temperature is very different. This difference explains why turbulence predicts a much closer load to the benchmark.

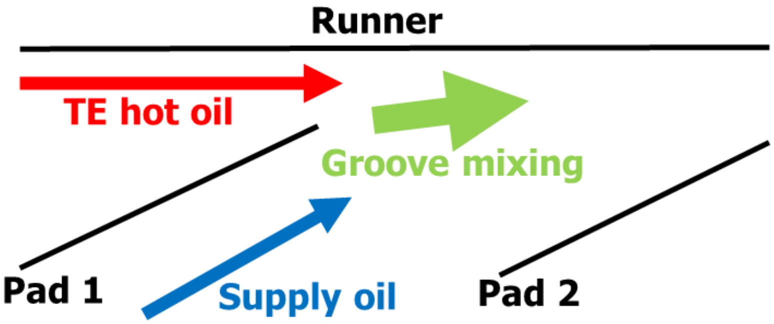

Figure 117: Hot oil carry-over model in thrust bearings

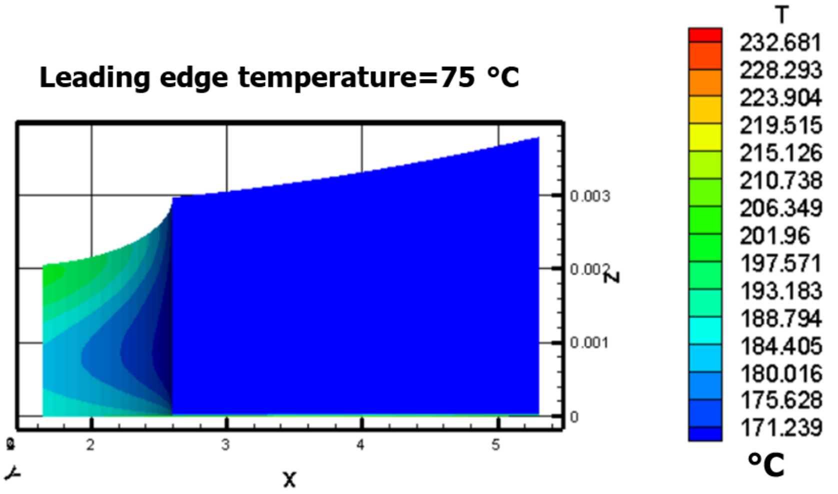

(a) Benchmark

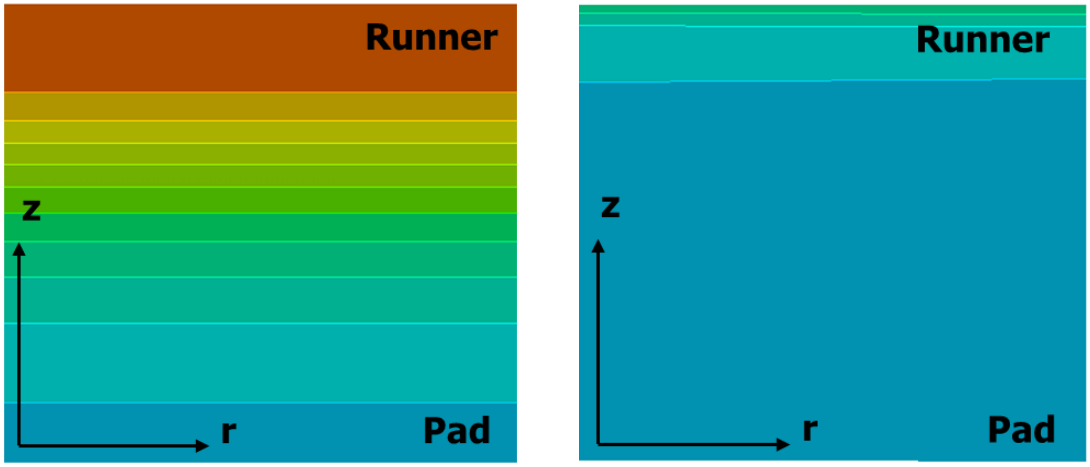

(b) Laminar groove (c) Turbulence groove

Figure 118: Leading edge temperature comparison between benchmark, laminar groove, and turbulence groove cases

Pad temperature with turbulence groove CFX case

Figure 119 shows pad temperature comparison between experiment, benchmark, and turbulence groove cases. Figure 119 shows that the turbulence model (SST) shows equivalent pad temperature with the benchmark. Table 34 shows the circumferential averaged temperature on the runner surface in the turbulence groove case and experiment. Table 34 shows that turbulence and experiment are in good agreement for the circumferentially averaged temperature. The CFX temperature of the three probes, 2, 5, and 8, located in the half length of the circumferential direction, perfectly match the experiment. The CFX temperature of the three probes 3, 6, and 9 in the leading edge are higher than the experiment, showing some cooling effect that the CFX model does not capture. The cooling effect is that the supply oil enters the bottom of the ID groove and then enters the leading edge. The supply oil cooling effect is an open area and could be a future research topic. The slope of SST is the same as with the benchmark in ID and is lower from ID to OD, which leads to lower temperatures of probes 1, 4, and 7 at the trailing edge. It shows that SST predicts more cooling effects toward the OD. This is because the velocity is higher towards OD, and the heat conducted away by turbulence is higher.

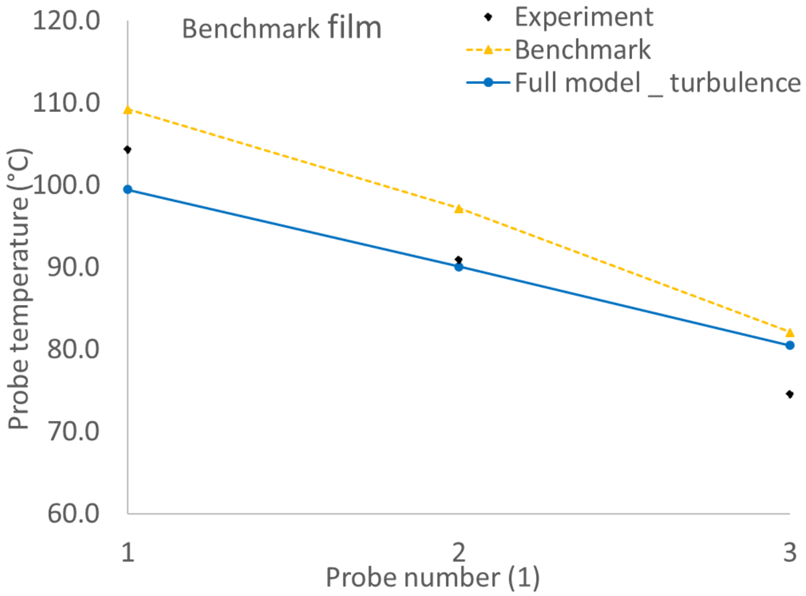

(a) OD

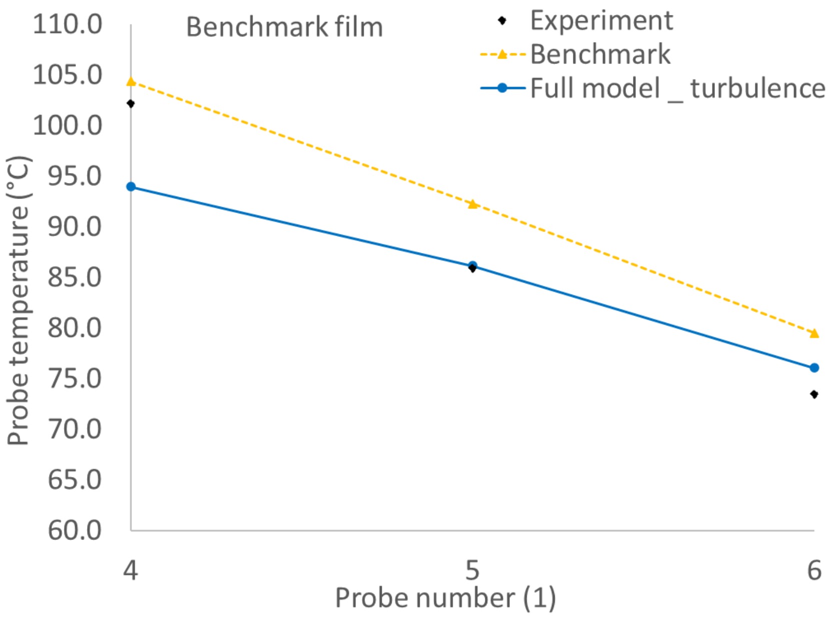

(b) MD

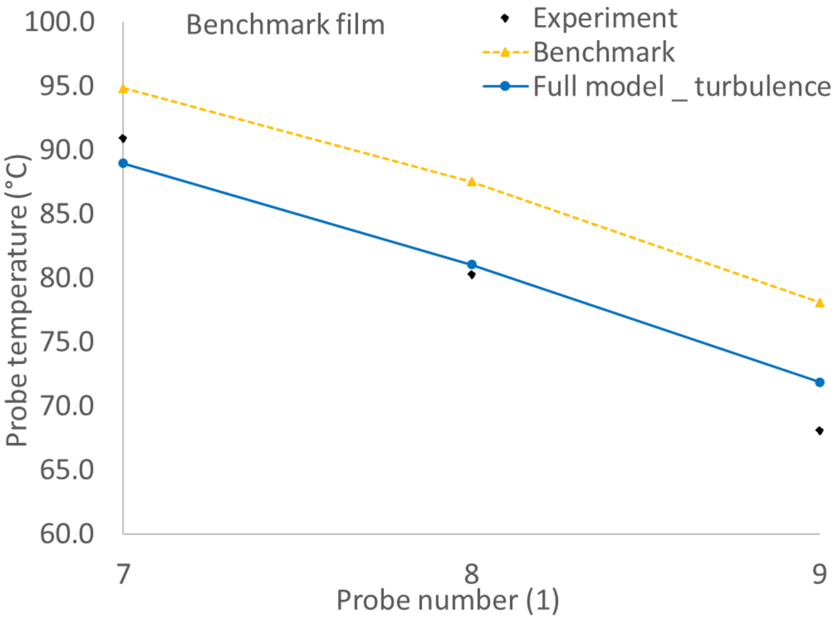

(c) ID

Figure 119: Pad temperature comparison between experiment, benchmark, and turbulence groove, in ID, MD, OD

Table 34. Circumferential averaged temperature on runner surface in turbulence groove case and experiment case

Model	OD, °C	MD, °C	ID, °C
Experiment	89.9	87.2	79.8
Turbulence	90.5	84.8	81.1

5.5 Iterated film, groove CFX results at multiple speeds

Table 35 shows the 8000, 9000, and 10000 rpm loads for the turbulence groove CFX results. Table 36 shows the load at 8000, 9000, and 10000 rpm for laminar groove CFX results. Table 35 and Table 36 show that load at 8000, 9000, and 10000 rpm for both laminar and turbulence groove CFX has been iterated to match the experimental load. Figure 120 shows the temperature drop of the turbulence groove case and the temperature increase of the laminar groove case in the transitional region. From Figure 120, it is known that the turbulence (SST) model was able to capture the temperature drop over the transitional region. In contrast, laminar shows a temperature increase in the transitional region.

Table 35. Load at 8000, 9000, and 10000 rpm for turbulence groove CFX

Speed, rpm	Load, N	Experimental load error, %
8000	6134	-0.49
9000	6125	-0.62
10000	6076	-1.4

Table 36. Load at 8000, 9000, and 10000 rpm for laminar groove CFX

Speed, rpm	Load, N	Experimental load error, %
8000	6114	-0.80
9000	6203	0.65
10000	6072	-1.5

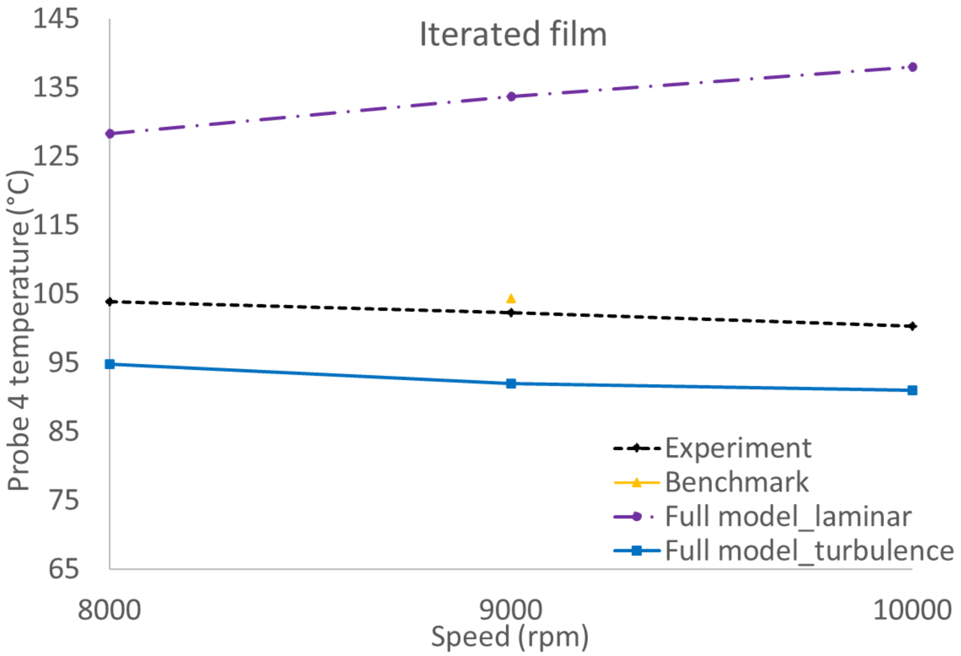

Figure 120: Temperature drop of turbulence groove and temperature increase of laminar groove in the transitional region

Figure 121 shows the leading-edge temperature drop over the transitional region. Eddy viscosity is a flow property, a coefficient in the linear relation between the strain rate and the shear stress. Eddy viscosity represents an extra diffusion due to the turbulence, and turbulent viscosity equals molecular viscosity plus eddy viscosity. Figure 122 shows the average groove eddy increase at the leading edge in the transitional region. Figure 123 shows the leading-edge viscosity comparison over the transitional region speed range. The five locations in Figure 123 are Inner Diameter (ID), 25% from ID, Middle Diameter (MD), 75% from ID, and Outer Diameter (OD). From Figure 121, Figure 122, and Figure 123, it is known that there is a leading-edge temperature drop in the transitional region; the leading-edge temperature drop is due to the increased groove conducting more heat away due to the turbulent conditions within the groove.

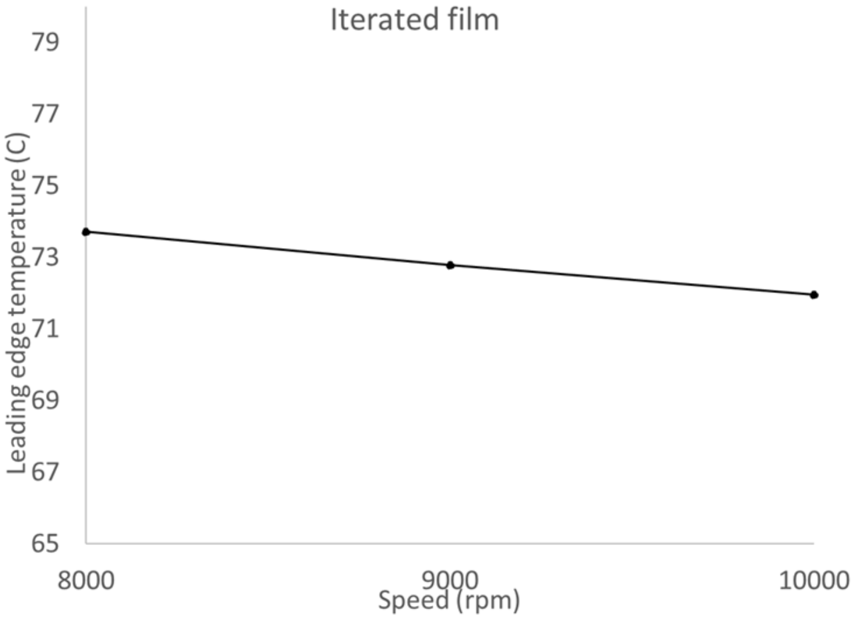

Figure 121: Leading temperature drop in the transitional region

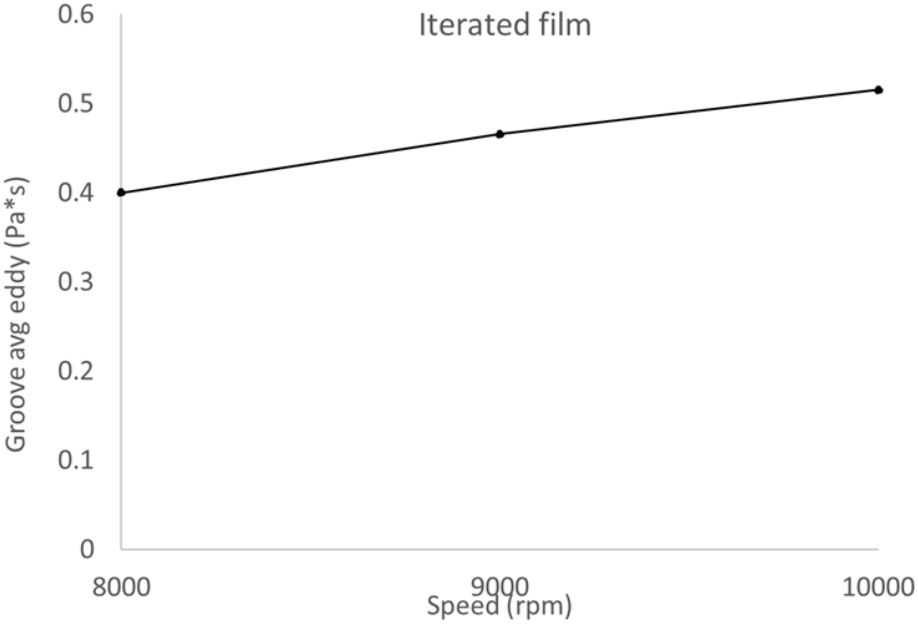

Figure 122: Groove eddy increase in the transitional region

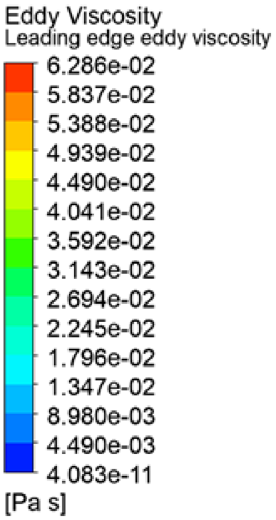

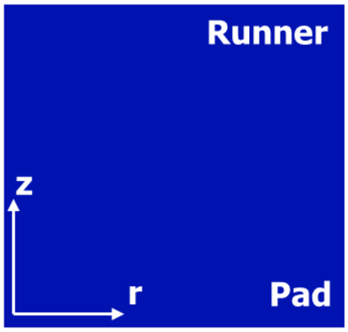

8000 rpm: ID

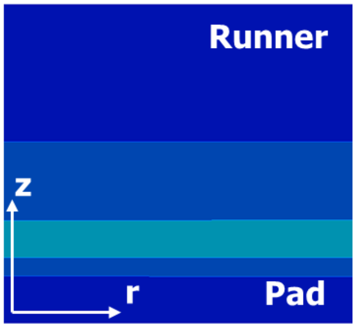

8000 rpm: 25%

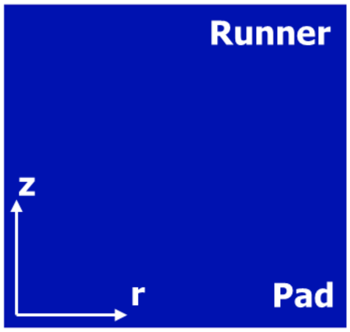

9000 rpm: ID

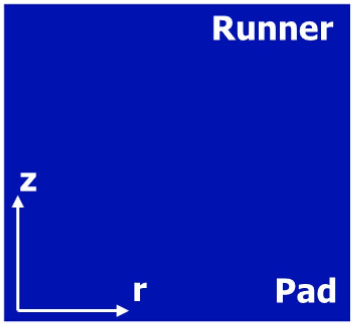

10000 rpm: ID

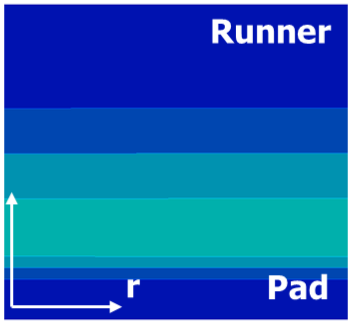

9000 rpm: 25%

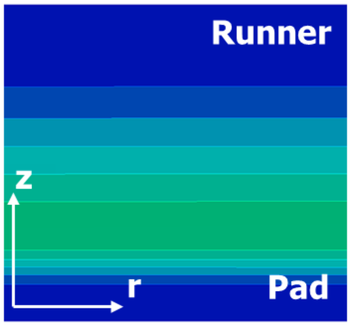

10000 rpm: 25%

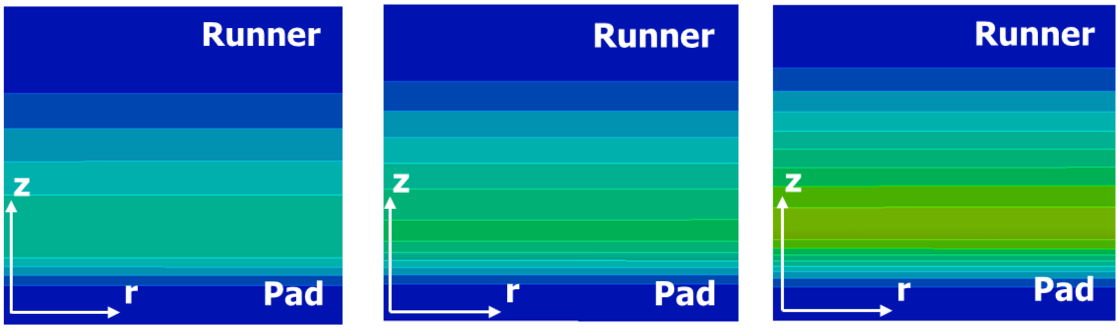

8000 rpm: MD 9000 rpm: MD 10000 rpm: MD

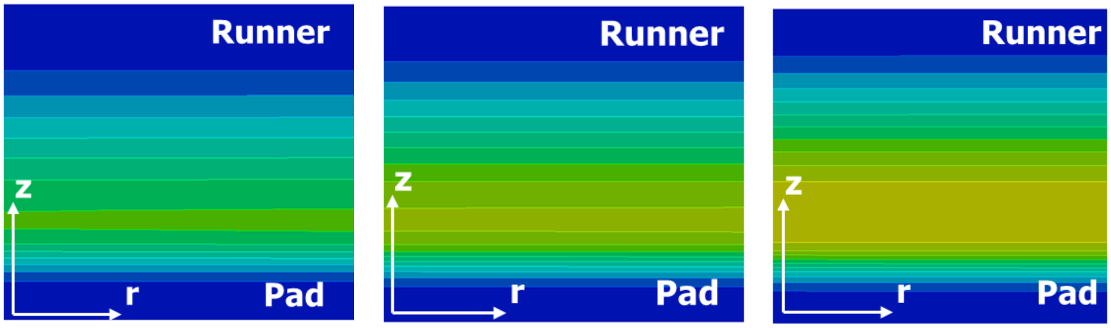

8000 rpm: 75% 9000 rpm: 75% 10000 rpm: 75%

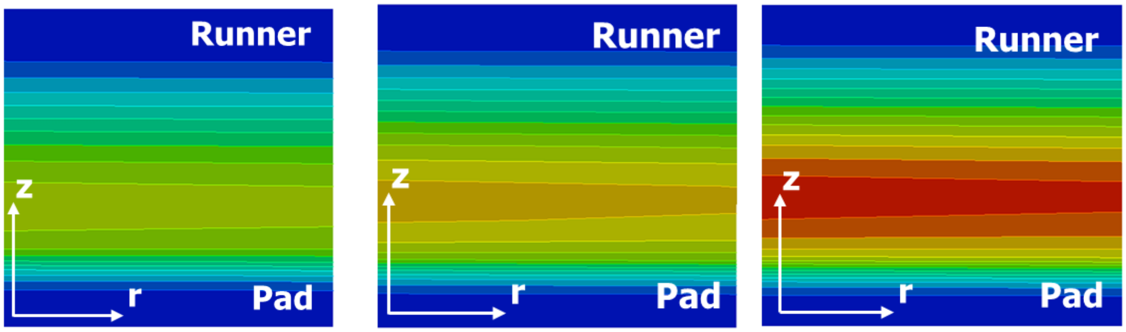

8000 rpm: OD 9000 rpm: OD 10000 rpm: OD

Figure 123: Leading-edge eddy viscosity comparison in the transitional region speed range

Figure 124 shows the eddy viscosity of the groove before the leading edge over the transitional region. The surface in Figure 124 is in the circumferential and cross-film directions. The location is the pivot radius, as shown with a red rectangular shape in Figure 125, and looking from the radial direction, as depicted by the blue arrow in Figure 125. Figure 124 shows that conduction and mixing in the groove turbulence make the leading-edge temperature closer to a constant temperature. Eddy viscosity in the groove before the leading edge is a magnitude larger than that on the leading edge. Unlike the traditional thinking of turbulence in the film region being the cause for the temperature drop, it can be seen from these results that the turbulence in the groove is the primary contributor to the temperature drop.

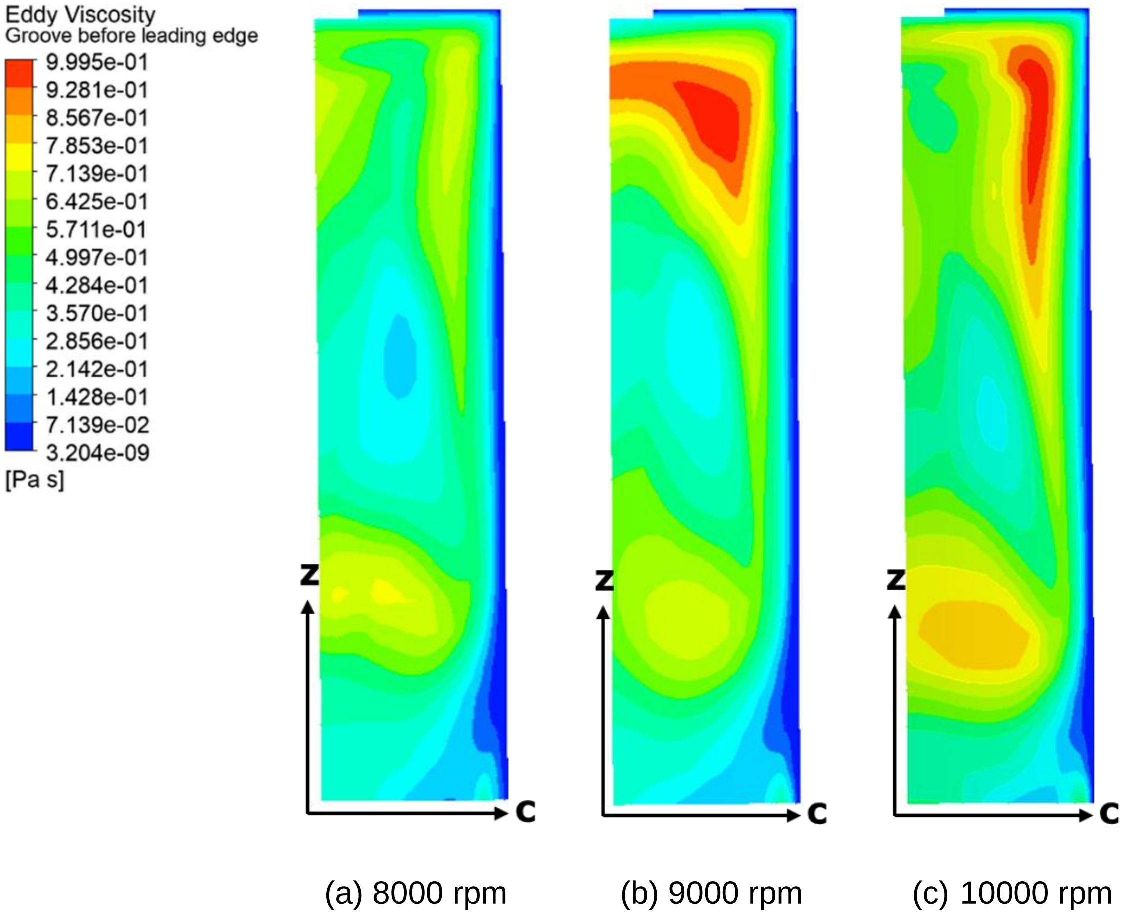

(a) 8000 rpm (b) 9000 rpm (c) 10000 rpm

Figure 124: Eddy viscosity in groove surface before the leading edge, in the transitional region

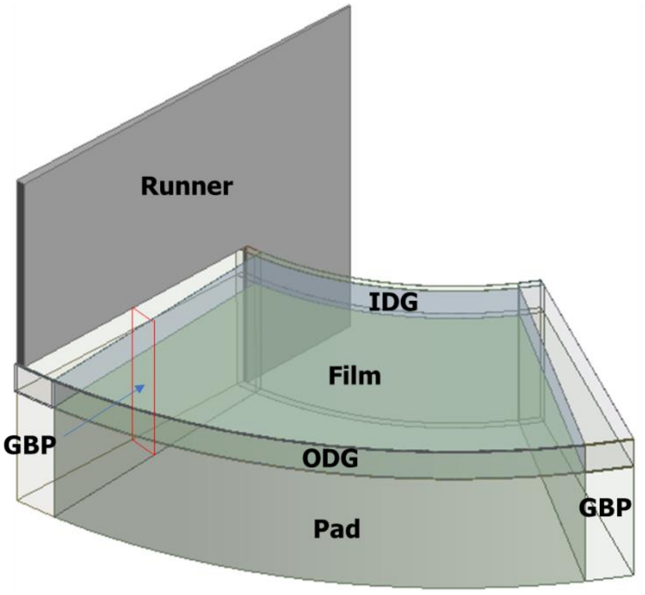

Figure 125: Location of groove surface before leading edge in Figure 124

5.6 Conclusions

This section studied the temperature drop during the transitional region in a center pivot fluid film thrust bearings. A full fluid-solid CFX model was developed for a center pivot fluid-film thrust-bearing experimental model. A novel finding of the physics causing the temperature drop over the transitional region was studied and verified. Thorough verification of CFX with both experiment and benchmark FE code was performed. This chapter focused on a particular model primarily due to its well-documented experimental data, which allows for thorough thermal verification at numerous points on the bearing pad and multiple operating speeds. Nine temperature probes on the pad surface provide a comprehensive temperature map for verifying the CFX model at the nominal speed of 9000 rpm. The highest pad temperature (probe 4) at different speeds spanning the transitional region provides a benchmark for verifying the CFX model in capturing the temperature drop. Results of this study point to the importance of groove turbulence in producing a uniform film temperature at the leading edge of the film. Its proper inclusion in the thrust bearing model can greatly improve the understanding and prediction of overall thermal performance characteristics, improving the dynamic coefficient prediction for fluid-film lubricated thrust bearings.

The SST turbulence model captures the temperature drop in the transitional region. Unlike our traditional understanding that turbulence in the film region is the reason for the temperature drop, it is demonstrated that the groove turbulence itself is the most significant factor that causes the temperature drop. The turbulence in the groove creates eddies in the flow in the groove, and such turbulence mixing and conduction in the groove make the leading-edge temperature more uniform, reducing the temperature. There is a leading-edge temperature drop in the transitional region, due to the increased groove turbulence conduction resulting in more heat being carried away. This chapter also answered what is needed to ensure accurate groove model predictions for center-pivot thrust bearings and the effects that various bearing model components have on prediction capabilities. Pad crowning is essential for center pivot fluid film thrust bearings with shallow tilt angles. The pad has the largest impact on the overall pad temperature, and the runner has essentially no impact on the pad temperature. The groove model results in significant variation of the leading-edge temperature, impacting the bearing load. An inaccurate cross-film leading edge temperature variation can cause more than a 67% error in the load capacity prediction. Studying the leading-edge temperature is also motivated by the philosophy that the inaccurate leading-edge temperature is the largest source of uncertainty in fluid film thrust bearings. This philosophy was followed by assigning a regression function to the leading-edge temperature.

This chapter was developed in response to the unknown processes of turbulence, fluid mixing, and thermal convection and conduction in the groove and to address a dearth of unifying philosophical motivation to improve the accuracy of leading-edge temperature predictions in the analysis of thrust bearings. This framework has produced interesting and potentially powerful results in its application to fluid film thrust bearings analysis. While groove turbulence has proven to greatly improve the accuracy reported in this study, future work should include developing a simplified method to consider the groove turbulence through FE modeling, while still not demanding as many computing resources as full fluid-solid CFX models would. For example, how to use the thin-film equal-length groove to capture the equivalent groove turbulence to have the same impact on the leading edge.

Conclusions

My methodological and applied research, as well as a considerable portion of my theoretical work, addresses the topic of Thermo-elasto-hydrodynamic (TEHD) analysis. The details of the conclusions of the current work are described below.

Chapter two presented a study of three different methods for applying Reichardt's formula in eddy viscosity calculations for turbulent fluid film bearings. The author chose to focus primarily on eddy-viscosity due to its importance to turbulence models commonly used in bearing analysis tools. A wide range of Reynolds numbers have been analyzed, showing unique behavior at higher and lower Reynolds number flows for oil and water lubricated conditions.

Three methods of applying Reichardt's formula have been analyzed. The shear value in Reichardt's formula was originally intended to be the shear stress occurring at the wall. Method one applies Reichardt's formula from both the upper and lower walls with a calculated equilibrium position separating the effects of each wall. Method two assumes that the eddy-viscosity can be calculated from the local shear stress value in the fluid films. This method applies Reichardt's formula from both the upper and lower walls with an equilibrium position separating the effects of each at the center of the fluid film. The eddy-diffusivity in the upper one-half of the flow is influenced by the upper wall, while the lower wall influences the eddy-diffusivity in the lower half of the flow. The eddy-viscosity in method three is allowed to vary from Reichardt's formula in the core of the flow. The core region is fully turbulent and contains three inner interfaces in the direction from the bearing surface to the runner. This emphasis on eddy-viscosity was due to its importance to turbulence models commonly used in bearing analysis tools. A wide range of Reynolds numbers has been analyzed, showing unique behavior at higher and lower Reynolds number flows for oil and water-lubricated conditions. Including method three in applying Reichardt's formula produced a lower, more conservative film thickness prediction, an important consideration for design engineers.

Chapter three proposed a new methodology to preserve the y^+ value to make water-lubricated thrust-bearing models valid. A method for determining the required number of cross-film elements in water-lubricated bearings was found. The accuracy of turbulent

TEHD results improved significantly after using the proposed methodology. An improved model for determining accurate values of δ^+ used in the turbulence model for water-lubricated thrust bearings was also presented and discussed. Combining these two enhancements to the thrust bearing TEHD modeling can greatly improve their accuracy in predicting the performance characteristics of water-lubricated thrust bearings. Verifications were performed through the benchmark, mesh independent study, and experiment.

An innovative contribution of my work is the establishment of a new perspective in the analysis of water lubrication where Reynolds numbers are large, generating turbulent flow as the dominant flow type as opposed to the traditional laminar flow found in oil lubrication. This perspective creates a new class of functional estimation procedures that parametrically account for the proper mesh characteristics for water-lubricated thrust bearings from oil-lubricated bearing characteristics intuitively and efficiently. These estimation procedures are motivated by the philosophy that the efficient functional number of elements across the lubricant film thickness and coefficients used in the eddy-viscosity equation should directly target the model convergence in the analysis of fluids other than that which traditional oil-bearing-based analysis methods are designed for. I adhere to this philosophy by creating estimator functions for the mesh correction within a defined range of dimensionless wall distance induced from the wall-bounded flow. This dimensionless wall distance is used as the basis of a function. Parameters used to control the influence of this function and parameters indexing other aspects of the eddy viscosity are jointly estimated. From an empirical perspective, this is equivalent to assuming a priori the same dimensionless wall distance for the subject fluid and choosing the hyperparameters controlling uniform mesh prior assumptions to balance the joint estimations.

Chapter four proposed a new methodology to model turbulence to make fluid-film lubricated thrust bearing models more accurate. A novel mixed one-equation and zero-equation turbulence model was found for calculating eddy viscosity in fluid film thrust bearings. The accuracy of turbulent THD results improved significantly after using the proposed methodology. This enhancement to the thrust-bearing THD modeling can greatly improve their accuracy in predicting the performance characteristics of fluid-film lubricated thrust bearings. Verifications were performed through DNS, CFX, and THRUST 5.4 comparison.

An innovative contribution of my work is the establishment of a novel mixed zero-equation and one-equation turbulence model in the analysis of fluid-film lubrication where the dominant flow is turbulent. This perspective created a new modeling method for solving Prandtl’s turbulence equation with an empirical length scale that solves eddy viscosity. Unlike using an empirical function of Reichardt’s equation, this new method physically solves a PDE to calculate eddy viscosity. This new procedure is motivated by the philosophy that the physical solution is better than empiricism. The length scale was based on the nature of the rotating machinery, which includes two surfaces with relative motion, and shear stress greatly depends on the distance between the two surfaces. I adhere to this philosophy by combining the Prandtl one-equation and empirical length scale, which is better than purely empirical zero-equation Reichardt’s equation. While still not demanding too many computing resources like two-equation turbulence models. Reynold's equation used this new mixed zero-equation and one-equation turbulence model in the inner loop. From an empirical perspective, this is equivalent to assuming the length scale is less than or at least equal to the purely zero-equation turbulence model. By adding a Prandtl one-equation model and physically solving for eddy viscosity, the new method increases accuracy and decreases empiricism.

Chapter five presented a study of the temperature drop during the transitional region in the center-pivot fluid-film thrust bearings. A full fluid-solid CFX model was developed for a center pivot fluid-film thrust-bearing experimental model. A novel finding of the physics causing the temperature drop over the transitional region was studied and verified. Thorough verification of CFX was performed with both experiment and benchmark FE code. This chapter chose to focus on a particular model primarily due to its well-documented experimental data, which provides for accurate thermal verification. Nine temperature probes on the pad surface provide a comprehensive temperature map for verifying the CFX model. The highest pad temperature at different speeds during the transitional region provides a benchmark for verifying the CFX model in capturing the temperature drop. Results of this study point to the importance of groove turbulence in producing a uniform film temperature at the film leading edge. Its proper inclusion in the thrust bearing model can greatly improve our understanding and prediction of overall thermal performance characteristics and improve the dynamic coefficient predictions for fluid-film lubricated thrust bearings.

The SST turbulence model captures the temperature drop in the transitional region. Unlike our traditional understanding that turbulence in the film region is the reason for the temperature drop, it is shown that the groove turbulence itself is the primary cause of this temperature drop. The turbulence in the groove creates eddies in the groove, such turbulence mixing and conduction in the groove make the leading-edge temperature more uniform. There is a leading-edge temperature drop in the transitional region, and the leading-edge temperature drop is due to the increased groove turbulence conducting more heat away. It was demonstrated that an inaccurate cross-film leading edge temperature variation could cause more than 67% error in the load capacity prediction. Studying the leading-edge temperature is also motivated by the philosophy that the inaccurate leading-edge temperature is the largest source of uncertainty in fluid film thrust bearings. I adhered to this philosophy by assigning a regression function to the leading-edge temperature. This chapter was developed in response to the unknown processes of turbulence, fluid mixing, and thermal convection and conduction in the groove and to address a dearth of unifying philosophical motivation to improve the accuracy of leading-edge temperature predictions in the analysis of thrust bearings. This framework has produced interesting and potentially powerful results in its application to the analysis of fluid-film thrust bearings.

It is the first work studying three different methods of modeling wall shear stress for applying Reichardt's formula in eddy viscosity calculations for turbulent fluid film bearings. It is the first work of a methodology to preserve the y+ value to make water-lubricated thrust-bearing models valid, and a method for determining the required number of cross-film elements in water-lubricated bearings was found. It is the first work of a novel mixed one-equation and zero-equation turbulence model for calculating eddy viscosity in fluid film thrust bearings. It is the first work of finding the physics causing the temperature drop over the transitional turbulence region.

While the new mixed zero-equation and one-equation turbulence model has been shown to improve accuracy significantly for the range of operating conditions reported in this study, additional experimental validation and operating conditions could be considered for additional verification in future work to improve the applicability of this approach further. While groove turbulence has proven to greatly improve the accuracy reported in this study, future work should include developing a simplified method to consider the groove turbulence through FE modeling, while still not demanding as many computing resources as full fluid-solid CFX models would. For example, how to use the thin-film equal-length groove to capture the equivalent groove turbulence to have the same impact on the leading edge.

References

[1] Wikimedia, "Thrust Bearing," 19 January 2022. [Online]. Available: https://en.wikipedia.org/wiki/Thrust_bearing. [Accessed 19 January 2022].

[2] L. S. Andrés and R. Koosha, "A Thermo-Elasto-Hydrodynamic (TEHD) Computational Analysis of Tilting Pad Thrust Bearings: Analytical and FE Pad Structure Models," Texas A&M University, 2019.

[3] M. He and J. Byrne, "Fundamentals of Fluid Film Thrust Bearing Operation and Modeling," in *Asia Turbomachinery & Pump Symposium,* 2018.

[4] J. H. Ball, "Design Considerations for Thrust Bearing Applications," in *Proceedings of the 25th Turbomachinery Symposium,* 1996.

[5] A. M. Mikula, "The Leading-Edge-Groove Tilting-Pad Thrust Bearing: Recent Developments," *Journal of Tribology,* vol. 107, no. 3, pp. 423-428, 1985.

[6] C. Ettles, "Hot Oil Carry-Over in Thrust Bearings," *Proceedings of the Institution of Mechanical Engineers, Conference Proceedings,* vol. 184, no. 12, pp. 75-81, 1969.

[7] S. Dousti, P. Allaire, J. Cao, B. Nichols and T. Dimond, "A Numerical Thermohydrodynamic Study of Fixed Pad Oil Lubricated Thrust Bearings," in *ASME Turbo Expo 2019: Turbomachinery Technical Conference and Exposition*, Phoenix, Arizona, USA, 2019.

[8] T. Hagemann and H. Schwarze, "A Model for Oil Flow and Fluid Temperature Inlet Mixing in Hydrodynamic Journal Bearings," *Journal of Tribology,* vol. 141, no. 2, pp. 021701-1 - 021701-14, 2019.

[9] H. Heshmat and O. Pinkus, "Mixing Inlet Temperatures in Hydrodynamic Bearings," *Journal of Tribology,* vol. 108, no. 2, pp. 231-244, 1986.

[10] J. Mitsui, Y. Hori and M. Tanaka, "Thermohydrodynamic Analysis of Cooling Effect of Supply Oil in Circular Journal Bearing," *Journal of Tribology,* vol. 105, no. 3, pp. 414-420, 1983.

[11] P. B. Kosasih and A. K. Tieu, "An Investigation into the Thermal Mixing in Journal Bearings," *Proceedings of the Institution of Mechanical Engineers, Part J: Journal of Engineering Tribology,* vol. 218, no. 5, pp. 379-389, 2004.

[12] S. Uhkoetter, M. Kursch and C. Beck, "Development and Validation of a Three-Dimensional Multiphase Flow Computational Fluid Dynamics Analysis for Journal Bearings in Steam and Heavy Duty Gas Turbines," *Journal of Engineering for Gas Turbines and Power,* vol. 134, no. 10, pp. 749-758, 2012.

[13] T. Hagemann, C. Zeh, M. Prölß and H. Schwarze, "The Impact of Convective Fluid Inertia Forces on Operation of Tilting-Pad Journal Bearings," *International Journal of Rotating Machinery,* vol. 2017, 2017.

[14] S. I. Moldovan, M. J. Braun and A. M. Balasoiu, "A Three-Dimensional Parametric Study and Numerical/Experimental Flow Visualization of a Six-Pocket

Hydrostatic Journal Bearing," *Tribology Transactions,* vol. 56, no. 1, pp. 1-26, 2011.

[15] J. Mitsui, Y. Hori and M. Tanaka, "An Experimental Investigation on the Temperature Distribution in Circular Journal Bearings," *Journal of Tribology,* vol. 108, no. 4, pp. 621-626, 1986.

[16] O. Pinkus, B. Sternlicht and E. Saibel, "Theory of Hydrodynamic Lubrication," *Journal of Applied Mechanics,* pp. 221-222, 1962.

[17] P. B. Neal, "Analysis of the Taper-Land Bearing Pad," *Journal of Mechanical Engineering Science,* vol. 12, no. 2, pp. 73-84, 1970.

[18] P. B. Neal, "Influence of Film Inlet Conditions on the Performance of Fluid Film Bearings," *Journal of Mechanical Engineering Science,* vol. 12, no. 2, pp. 153-158, 1970.

[19] P. B. Neal, "Film Lubrication of Plane-faced Thrust Pads," *Proc. Inst. Mech. Engrs, Lubrication and Wear Convention,* vol. 52, 1963.

[20] C. Ettles, "The Development of a Generalized Computer Analysis for Sector Shaped Tilting Pad Thrust Bearings," *Tribology Transactions,* vol. 19, no. 2, pp. 153-163, 1976.

[21] C. M. M. Ettles and A. Cameron, "The Action of the Parallel-Surface Thrust Bearing," *Proceedings of the Institution of Mechanical Engineers, Conference Proceedings,* vol. 180, no. 11, pp. 61-75, 1965.

[22] J. H. Vohr, "Prediction of the Operating Temperature of Thrust Bearings," *Journal of Tribology,* vol. 103, no. 1, pp. 97-106, 1981.

[23] J. Yang and A. Palazzolo, "Three-Dimensional Thermo-Elasto-Hydrodynamic Computational Fluid Dynamics Model of a Tilting Pad Journal Bearing—Part I: Static Response," *Journal of Tribology,* vol. 141, no. 6, pp. 061702-1 - 061702-21, 2019.

[24] J. Yang and A. Palazzolo, "Three-Dimensional Thermo-Elasto-Hydrodynamic Computational Fluid Dynamics Model of a Tilting Pad Journal Bearing—Part II: Dynamic Response," *Journal of Tribology,* vol. 141, no. 6, 2019.

[25] J. Yang and A. Palazzolo, "Computational Fluid Dynamics Based Mixing Prediction for Tilt Pad Journal Bearing TEHD Modeling—Part I: TEHD-CFD Model Validation and Improvements," *Journal of Tribology,* vol. 143, no. 1, p. 011801, 2021.

[26] J. Yang and A. Palazzolo, "Computational Fluid Dynamics Based Mixing Prediction for Tilt Pad Journal Bearing TEHD Modeling—Part II: Implementation With Machine Learning," *Journal of Tribology,* vol. 143, no. 1, p. 011802, 2021.

[27] R. Grzegorz and W. Michal, "CFD Analysis of the Lubricant Flow in the Supply Groove of a Hydrodynamic Thrust Bearing Pad," in *ASME/STLE 2007 International Joint Tribology Conference,* San Diego, California, USA, 2007.

[28] A. E. Perry and M. S. Chong, "A Description of Eddying Motions and Flow Patterns Using Critical-Point Concepts," *Annual Review of Fluid Mechanics,* vol. 19, pp. 125-155, 1987.

[29] K. Stawiarski and K. Hanjalić, "A two-scale second-moment one-point turbulence closure," in *Proceedings of the 5th International Symposium on Engineering Turbulence Modelling and Measurements,* Mallorca, Spain, 2002.

[30] M. T. Landahl and E. Mollo-Christensen, Turbulence and Random Processes in Fluid Mechanics, Cambridge, United Kingdom: Cambridge University Press, 1992.

[31] O. Reynolds, "On the Dynamical Theory of Incompressible Viscous Fluids and the Determination of the Criterion," *Philosophical Transactions of the Royal Society of London,* vol. 186, p. 123–164, 1895.

[32] H. Tennekes and J. L. Lumley, A first course in turbulence, Cambridge, Massachusetts: The MIT Press, 1992.

[33] K. Chan and S. Sofia, "Validity Tests of the Mixing-Length Theory of Deep Convection," *Science,* vol. 235, no. 4787, p. 465–467, 1987.

[34] C.-W. Ng and P. CT, "A Linearized Turbulent Lubrication Theory," *ASME Journal of Basic Engineering,* vol. 87, no. 3, pp. 675-682, 1965.

[35] V. N. Constantinescu, "On Turbulent Lubrication," *Proceedings of the Institution of mechanical engineers,* vol. 173, no. 1, pp. 881-900, 1959.

[36] V. N. Constantinescu, "Analysis of Bearings Operating in Turbulent Regime," *Journal of Basic Engineering,* vol. 84, no. 1, pp. 139-151, 1962.

[37] V. N. Constantinescu, "On Some Secondary Effects in Self-acting Gas-lubricated Bearings," *ASLE Transactions,* vol. 7, no. 3, pp. 257-268, 1964.

[38] V. N. Constantinescu, "On Gas Lubrication in Turbulent Regime," *ASME Journal of Basic Engineering,* vol. 86, no. 3, pp. 475-482, 1964.

[39] V. N. Constantinescu, "Theory of Turbulent Lubrication (Turbulent Lubrication Theory Based on Mixing Length Concept to Explain Bearing Behavior)," in *Lubrication and Wear, International Symposium*, Houston, TX, 1965.

[40] V. N. Constantinescu and S. Galetuse, "On the Determination of Friction Forces in Turbulent Lubrication," *ASLE Transactions,* vol. 8, no. 4, pp. 367-380, 1965.

[41] V. N. Constantinescu, "On the Influence of Inertia Forces in Turbulent and Laminar Self-Acting Films," *Journal of Tribology,* vol. 92, no. 3, pp. 473-480, 1970.

[42] H. G. Elrod Jr and C. W. Ng, "A Theory for Turbulent Fluid Films and its Application to Bearings," *Journal of Tribology,* vol. 89, no. 3, pp. 346-362, 1967.

[43] C.-W. Ng, "Fluid Dynamic Foundation of Turbulent Lubrication Theory," *ASLE Transactions,* vol. 7, no. 4, pp. 311-321, 1964.

[44] G. G. Hirs, "A Bulk-flow Theory for Turbulence in Lubricant Films," *Journal of Tribology,* vol. 95, no. 2, pp. 137-145, 1973.

[45] G. G. Hirs, "A Systematic Study of Turbulent Film Flow," *Journal of Tribology,* vol. 96, no. 1, pp. 118-126, 1974.

[46] R. W. Armentrout, M. He, T. Haykin and A. E. Reed, "Analysis of Turbulence and Convective Inertia in a Water-Lubricated Tilting-Pad Journal Bearing Using Conventional and CFD Approaches," *Tribology Transactions,* vol. 60, no. 6, pp. 1-19, 2016.

[47] M.-K. Ho and J. H. Vohr, "Application of Energy Model of Turbulence to Calculation of Lubricant Flows," *Journal of Tribology,* vol. 96, no. 1, pp. 95-102, 1974.

[48] E. R. Van Driest, "On Turbulent Flow Near a Wall," *Journal of the Aeronautical Sciences,* vol. 23, no. 11, pp. 1007-1011, 1956.

[49] P. B. Kosasih and A. K. Tieu, "An Analysis of Sector-shaped Thrust Bearings Operating in the Transition Regime," *Wear,* vol. 160, no. 2, pp. 291-299, 1993.

[50] L. Zhu, W. Zhang, J. Kou and Y. Liu, "Machine Learning Methods for Turbulence Modeling in Subsonic Flows Around Airfoils," *Physics of Fluids,* vol. 31, no. 1, pp. 015105-1 - 015105-14, 2019.

[51] H. Chanson, Applied Hydrodynamics: An Introduction to Ideal and Real Fluid Flows, Leiden, The Netherlands: CRC Press, Taylor & Francis Group, 2009.

[52] H. Schlichting and K. Gersten, Boundary-layer Theory, Springer, 2000.

[53] S. Abramovitz, "Turbulence in a Tilting-pad Thrust Bearing," *Transactions of the American Society of Mechanical Engineers,* vol. 78, no. 1, pp. 7-11, 1956.

[54] M. C. Collins, "Validation and Uncertainty Quantification of CFD Smooth Seal Models: ANSYS and Bulk-Flow," University of Virginia, Charlottesville, VA, 2020.

[55] R. S. Gregory, "Performance of Thrust Bearings at High Operating Speeds," *Journal of Tribology,* vol. 96, no. 1, pp. 7-13, 1974.

[56] J. W. Capitao, R. S. Gregory and R. P. Whitford, "Effects of High-operating Speeds on Tilting Pad Thrust Bearing Performance," *Journal of Tribology,* vol. 98, no. 1, pp. 73-79, 1976.

[57] W. W. Gardner, "Tilting Pad Thrust Bearing Tests—Influence of Pivot Location," *Journal of Tribology,* vol. 110, no. 4, pp. 609-613, 1988.

[58] L. A. Abdel-Latif, "Analysis of Heavily Loaded Tilted Pads Thrust Bearings With Large Dimensions Under TEHD Conditions," *Journal of Tribology,* vol. 110, no. 3, pp. 467-476, 1988.

[59] M. Fillon and S. B. Glavatskih, "PTFE-faced Centre Pivot Thrust Pad Bearings: Factors Affecting TEHD Performance," *Tribology International,* vol. 41, no. 12, pp. 1219-1225, 2008.

[60] J. W. Capitao, "Influence of Turbulence on Performance Characteristics of the Tilting Pad Thrust Bearing," *Journal of Tribology,* vol. 96, no. 1, pp. 110-116, 1974.

[61] J. W. Capitao, "Performance Characteristics of Tilting Pad Thrust Bearings at High Operating Speeds," *Journal of Tribology,* vol. 98, no. 1, pp. 81-88, 1976.

[62] R. S. Gregory, "Factors Influencing Power Loss of Tilting-Pad Thrust Bearings," *Journal of Tribology,* vol. 101, no. 2, pp. 154-160, 1979.

[63] A. M. Mikula and R. S. Gregory, "A Comparison of Tilting Pad Thrust Bearing Lubricant Supply Methods," *Journal of Tribology,* vol. 105, no. 1, pp. 39-45, 1983.

[64] A. M. Mikula, "Evaluating Tilting-pad Thrust Bearing Operating Temperatures," *ASLE Transactions,* vol. 29, no. 2, pp. 173-178, 1986.

[65] A. M. Mikula, "Further Test Results of the Leading-Edge-Groove (LEG) Tilting Pad Thrust Bearing," *Journal of Tribology,* vol. 110, no. 1, pp. 174-179, 1988.

[66] L. Bouard, M. Fillon and J. Frene, "Thermohydrodynamic analysis of tilting-pad journal bearings operating in turbulent flow regime," *Tribology International,* vol. 118, no. 1, pp. 225-231, 1996.

[67] S. Taniguchi, T. Makino, K. Takeshita and T. Ichimura, "A thermohydrodynamic analysis of large tilting-pad journal bearing in laminar and turbulent flow regimes with mixing," *Journal of Tribology,* vol. 112, no. 3, pp. 542-548, 1990.

[68] J. Kim, A. Palazzolo and R. Gadangi, "Dynamic characteristics of TEHD tilt pad journal bearing simulation including multiple mode pad flexibility model," *Journal of Vibration and Acoustics,* vol. 117, no. 1, pp. 123-135, 1995.

[69] T. Hagemann, C. Zeh and H. Schwarze, "Heat convection coefficients of a tilting-pad journal bearing with directed lubrication," *Tribology International,* vol. 136, pp. 114-126, 2019.

[70] D. Dowson, "A Generalized Reynolds Equation for Fluid-film Lubrication," *International Journal of Mechanical Sciences,* vol. 4, no. 2, pp. 159-170, 1962.

[71] T. S. Brockett, L. E. Barrett and P. E. Allaire, "Thermoelastohydrodynamic Lubrication in Thrust Bearings," University of Virginia, Charlottesville, VA, 1995.

[72] M. He and P. Allaire, "Thermoelastohydrodynamic Analysis of Fluid Film Journal Bearings," University of Virginia, Charlottesville, VA, 2003.

[73] T. Suganami and A. Z. Szeri, "A Thermohydrodynamic Analysis of Journal Bearings," *Journal of Tribology,* vol. 101, no. 1, pp. 21-27, 1979.

[74] F. H. Clauser, "The Turbulent Boundary Layer," *Advances in Applied Mechanics,* vol. 4, pp. 1-51, 1956.

[75] A. Z. Szeri, Tribology: Friction, Lubrication, and Wear, New York: McGraw-Hill Book Company, Inc., 1980.

[76] K. H. Huebner, "Solution for the Pressure and Temperature in Thrust Bearings Operating in the Thermohydrodynamic Turbulent Regime," *Journal of Tribology,* vol. 96, no. 1, pp. 58-68, 1974.

[77] T. Suganami and A. Z. Szeri, "A Parametric Study of Journal Bearing Performance: The 80 Deg Partial Arc Bearing," *Journal of Tribology,* vol. 101, no. 4, pp. 486-491, 1979.

[78] O. Pinkus and J. W. Lund, "Centrifugal Effects in Thrust Bearings and Seals under Laminar Conditions," *Journal of Tribology,* vol. 103, no. 1, pp. 126-136, 1981.

[79] S. B. Glavatskikh, "Steady State Performance Characteristics of a Tilting Pad Thrust Bearing," *Journal of Tribology,* vol. 123, no. 3, pp. 608-615, 2001.

[80] S. B. Glavatskih, "Laboratory Research Facility for Testing Hydrodynamic Thrust Bearings," *Proceedings of the Institution of Mechanical Engineers, Part J: Journal of Engineering Tribology,* vol. 216, no. 2, pp. 105-116, 2002.

[81] S. B. Glavatskih, F. M. and L. R., "The Significance of Oil Thermal Properties on the Performance of a Tilting-Pad Thrust Bearing," *Journal of Tribology,* vol. 124, no. 2, pp. 377-385, 2002.

[82] S. B. Glavatskih and R. Larsson, "Performance of Synthetic Oils in the Hydrodynamic Regime—1. Experimental," *Lubrication Science,* vol. 20, no. 1, pp. 15-24, 2003.

[83] J. Sun, D. Kuhn and G. Naterer, "Eddy Viscosity and Reynolds Stress Models of Entropy Generation in Turbulent Channel Flows," *Journal of Fluids Engineering,* vol. 139, no. 3, pp. 034501-1 - 034501-6, 2017.

[84] H. Hashimoto and S. Wada, "Turbulent Lubrication of Tilting-Pad Thrust Bearings With Thermal and Elastic Deformations," *Journal of Tribology,* vol. 107, no. 1, pp. 82-86, 1985.

[85] S. J. Chowdhury and G. Ahmadi, "Thermohydrodynamic Analysis of Wide Thrust Bearings Operating in Turbulent Inertial Flow Regimes," *Journal of Tribology,* vol. 110, no. 2, pp. 327-334, 1988.

[86] X. Deng, B. Weaver, C. Watson, M. Branagan, H. Wood and R. Fittro, "Modeling Reichardt's Formula for Eddy Viscosity in the Fluid Film of Tilting Pad Thrust Bearings," *Journal of Engineering for Gas Turbines and Power,* vol. 140, no. 8, pp. 082505-1 -082505-9, 2018.

[87] M. Gohara, K. Somaya, M. Miyatake and S. Yoshimoto, "Static Characteristics of a Water-lubricated Hydrostatic Thrust Bearing using a Membrane Restrictor," *Tribology International,* vol. 75, pp. 111-116, 2014.

[88] S. L. Andrés, P. S and C. D., "A Water-Lubricated Hybrid Thrust Bearing: Measurements and Predictions of Static Load Performance," *Journal of Engineering for Gas Turbines and Power,* vol. 139, no. 2, pp. 022506-1 - 022506-10, 2017.

[89] X. Lin, S. Jiang, C. Zhang and X. Liu, "Thermohydrodynamic Analysis of High Speed Water-lubricated Spiral Groove Thrust Bearing Considering Effects of Cavitation, Inertia and Turbulence," *Tribology International,* vol. 119, pp. 645-658, 2018.

[90] A. Z. Szeri, Fluid film lubrication, Cambridge, UK: Cambridge University Press, 2010.

[91] X. Deng, C. Watson, M. He, H. Wood and R. Fittro, "Comparison of Experimental, Thermoelastohydrodynamic (TEHD) and Isothermal, Non-Deforming Computational Fluid Dynamics (CFD) Results for Thrust Bearings," in *Fluids Engineering Division Summer Meeting*, Montreal, Quebec, Canada, 2018.

[92] T. S. Brockett, L. E. Barrett and P. E. Allaire, "Thrust Bearing Lubrication -- A Manual for Use with Computer Program THRUST - Version 4.00," Rotating Machinery and Controls (ROMAC), Charlottesville, VA, 1994.

[93] X. Deng, C. Watson, B. Weaver, H. Wood and R. Fittro, "Lubricant Inertia in Water Lubricated Bearings," in *ASME 2017 Fluids Engineering Division Summer Meeting,* Waikoloa, Hawaii, USA, 2017.

[94] X. Deng, C. Watson, M. He, R. Fittro and H. Wood, "Comparison of Experimental, Thermoelastohydrodynamic (TEHD) and Thermal, Non-deforming Computational Fluid Dynamics (CFD) Results for Thrust Bearings: Part II," in *ASME International Mechanical Engineering Congress and Exposition*, Pittsburgh, Pennsylvania, USA, 2018.

[95] D. M. C. McCarthy, S. B. Glavatskih and I. Sherrington, "Oil-film Thickness and Temperature Measurements in PTFE and Babbitt Faced Tilting-pad Thrust bearings," *Proceedings of the Institution of Mechanical Engineers, Part J: Journal of Engineering Tribology,* vol. 219, no. 3, pp. 179-185, 2005.

[96] M. K. Fitzgerald and P. B. Neal, "Temperature Distributions and Heat Transfer in Journal Bearings," *Journal of Tribology,* vol. 114, no. 1, pp. 122-130, 1992.

[97] X. Deng, H. Gates, R. Fittro and H. Wood, "Methodology of Turbulence Parameter Correction in Water-Lubricated Thrust Bearings," *ASME Journal of Fluids Engineering,* vol. 141, no. 7, pp. 071104-1 - 071104-9, 2019.

[98] W. W. Gardner, "Performance Characteristics of Two Tilting Pad Thrust Bearing Designs," in *Proceedings JSLE International Tribology Conference,* Tokyo, Japan, 1985.

[99] M. C. Jeng, G. R. Zhou and A. Z. Szeri, "A Thermohydrodynamic Solution of Pivoted Thrust Pads: Part I—Theory," *Journal of Tribology,* vol. 108, no. 2, pp. 195-207, 1986.

[100] M. C. Jeng, G. R. Zhou and A. Z. Szeri., "A Thermohydrodynamic Solution of Pivoted Thrust Pads: Part II-Static Loading," *A Thermohydrodynamic Solution of Pivoted Thrust Pads: Part II—Static Loading,* vol. 108, no. 2, pp. 208-213, 1986.

[101] M. C. Jeng and A. Z. Szeri, "A Thermohydrodynamic Solution of Pivoted Thrust Pads: Part III-Linearized Force Coefficients," *Journal of Tribology,* vol. 108, no. 2, pp. 214-218, 1986.

[102] M. Branagan, "Computational Modeling of Pad Surface Irregularities in Fluid Film Bearings," University of Virginia, Charlottesville, 2019.

[103] P. Spalart and S. Allmaras, "A One-equation Turbulence Model for Aerodynamic Flows," in *30th aerospace sciences meeting and exhibit*, 1992.

[104] F. R. Menter, R. B. Langtry, S. R. Likki, Y. B. Suzen, P. G. Huang and S. Völker, "A Correlation-Based Transition Model Using Local Variables—Part I: Model Formulation," *Journal of Turbomachinery,* vol. 128, no. 3, pp. 413-422, 2006.

[105] R. B. Langtry, F. R. Menter, S. R. Likki, Y. B. Suzen, P. G. Huang and S. Völker, "A Correlation-Based Transition Model Using Local Variables—Part II: Test Cases and Industrial Applications," *Journal of Turbomachinery,* vol. 128, no. 3, pp. 423-434, 2006.

[106] F. R. Menter, "Two-equation Eddy-viscosity Turbulence Models for Engineering Applications," *AIAA Journal,* vol. 32, no. 8, pp. 1-21, 1994.

[107] F. R. Menter and M. Kuntz, "Adaptation of Eddy-Viscosity Turbulence Models to Unsteady Separated Flow Behind Vehicles," in *The aerodynamics of heavy vehicles: trucks, buses, and trains,* Berlin, Heidelberg, 2004.

[108] F. Menter, M. Kuntz and R. Bender, "A Scale-Adaptive Simulation Model for Turbulent Flow Predictions," in *41st aerospace sciences meeting and exhibit,* 2003.

[109] F. R. Menter, M. Kuntz and R. Langtry, "Ten Years of Industrial Experience with the SST Turbulence Model," *Heat and Mass Transfer,* vol. 4, no. 1, pp. 625-632, 2003.

[110] C. L. Rumsey and P. R. Spalart, "Turbulence Model Behavior in Low Reynolds Number Regions of Aerodynamic Flowfields," *AIAA Journal,* vol. 47, no. 4, pp. 982-1008, 2009.

[111] W. P. Jones and B. E. Launder, "The Prediction of Laminarization with a Two-Equation Model of Turbulence," *International Journal of Heat and Mass Transfer,* vol. 15, pp. 301-314, 1972.

[112] B. E. Launder and B. I. Sharma, "Application of the Energy Dissipation Model of Turbulence to the Calculation of Flow Near a Spinning Disc," *Letters in Heat and Mass Transfer,* vol. 1, no. 2, pp. 131-138, 1974.

[113] T. H. Shih, "An Improved K-Epsilon Model for Near-Wall Turbulence and Comparison with Direct Numerical Simulation," NASA Lewis Research Center, Cleveland, OH, United States, 1990.

[114] F. R. Menter, "Eddy Viscosity Transport Equations and Their Relation to the k-ε Model," *Journal of Fluids Engineering,* vol. 119, no. 4, pp. 876-884, 1997.

[115] D. C. Wilcox, "Formulation of the k-w Turbulence Model Revisited," *AIAA Journal,* vol. 46, no. 11, pp. 2823-2838, 2008.

[116] D. C. Wilcox, "Reassessment of the Scale-determining Equation for Advanced Turbulence Models," *AIAA Journal,* vol. 26, no. 11, pp. 1299-1310, 1988.

[117] ANSYS, "ANSYS CFX-Solver Theory Guide," ANSYS, Canonsburg, PA, 2011.

[118] O. Reynolds, "On the Theory of Lubrication and Its Application to Mr. Beauchamp Tower's Experiments, Including an Experimental Determination of the Viscosity of Olive Oil," *Philosophical Transactions,* vol. 177, pp. 157-235, 1886.

[119] C. L. Robinson and A. Cameron, "Studies in Hydrodynamic Thrust Bearings III. The Parallel Surface Bearing," *Philosophical Transactions of the Royal Society of London. Series A, Mathematical and Physical Sciences,* vol. 278, no. 1283, pp. 385-395, 1975.

[120] A. Fogg, "Fluid Film Lubrication of Parallel Thrust Surfaces," *Proceedings of the Institution of Mechanical Engineers,* vol. 155, no. 1, pp. 49-67, 1946.

[121] C. F. Kettleborough, "Tests on Parallel-surface Thrust Bearings," *Engineering, Lond,* p. 174, 1955.

[122] C. F. Kettleborough, B. R. Dudley, E. Baildon and C. F. Kettleborough, "Micheli Bearing Lubrication: Part I—Experimental Results: Part II—Correlation between Theory and Experiment," *Proceedings of the Institution of Mechanical Engineers,* vol. 169, no. 1, pp. 746-765, 1955.

[123] M. C. Shaw and C. Mass, "An Analysis of the Parallel-surface Thrust Bearing," *Trans. ASME,* vol. 69, pp. 381-387, 1947.

[124] W. F. Cope, "The Hydrodynamical Theory of Film Lubrication," *Proceedings of the Royal Society of London. Series A. Mathematical and Physical Sciences,* vol. 197, no. 1049, pp. 201-217, 1949.

[125] F. Osterle, A. Charnes and A. Saibel, "On the Solution of the Reynolds Equation for Slider Bearing Lubrication-IV—the Parallel Surface Slider Bearing without Side Leakage," *Trans. ASME,* vol. 1, pp. 133-1136, 1953.

[126] A. Cameron and W. L. Wood, "Parallel Surface Thrust Bearing," *ASLE Transactions,* vol. 1, no. 2, pp. 254-258, 1958.

[127] I. G. Currie, C. A. Brockley and F. A. Dvorak, "Thermal Wedge Lubrication of Parallel Surface Thrust Bearings," *jOURNAL,* vol. 87, no. 4, pp. 823-830, 1965.

[128] H. W. Swift, "The Stability of Lubricating Films In Journal Bearings. (Includes Appendix)," *In Minutes of the Proceedings of the Institution of Civil Engineers,* vol. 233, no. 1932, pp. 267-288, 1932.

[129] C. Ettles and A. Cameron, "Thermal and Elastic Distortions in Thrust Bearings," *Inst. of Mech. Engrs,* vol. 7, pp. 60-71, 1963.

[130] C. L. Robinson and A. Cameron, "Studies in Hydrodynamic Thrust Bearings. I. Theory Considering Thermal and Elastic Distortions," *Philosophical Transactions of the Royal Society of London. Series A, Mathematical and Physical Sciences,* pp. 351-366, 1975.

[131] D. Dowson and J. D. Hudson, "Thermohydrodynamic Analysis of the Infinite Slider Bearing: Part I, the Plane Inclined Slider Bearing," *Instn. Mech. Engrs., Lubrication and Wear Convention,* pp. 34-44, 1963.

[132] D. Dowson, "Thermo-hydrodynamic Analysis of the Infinite Slide-bearing: Part II, the Parallel-surface Bearing," *Proc. Inst. Mech. Engrs, Lubrication and Wear Convention,* 1963.

[133] P. Pajączkowski, "Simulation of Transient States in Large Hydrodynamic Thrust Bearings," Gdańsk University of Technology, 2010.

[134] K. Holmberg and A. Erdemir, "Influence of tribology on global energy consumption, costs and emissions," *Friction,* vol. 5, no. 3, pp. 263-284, 2017.

Appendix A

Prandtl One-equation Turbulence Modeling

Fluid film bearings are designed to support the loads applied by the rotor system in turbomachinery. Oil-lubricated bearings are widely used in high-speed rotating machines such as those found in the automotive, oil and gas, and power generation industries. In this study, a Reynolds equation finite element analysis (FEA) model was developed that represents the hydrodynamics for a fluid film sliding bearing under the influence of turbulence. One equation turbulence model was used in the FEA model instead of the algebraic and largely empirical formula currently used in the bearing industry. The pressure and velocities solved from the Reynolds equation were passed to Prandtl's equation, eddy viscosity was calculated from turbulent kinetic energy and combined with laminar fluid viscosity and passed to Prandtl's equation again until convergence was achieved for turbulent kinetic energy. The distributions of turbulent kinetic energy, pressure and velocity in the film will be compared with the results from the commonly used algebraic turbulence model, Reichardt's model, and computational fluid dynamics (CFD). The results of this study will aid in developing further bearing analysis tools that will, in turn, lead to improved bearing and rotating machinery design.

Turbulence models based on the equation for the turbulence kinetic energy have become the cornerstone of modern turbulence modeling research since the 1960s. One equation turbulence model retains the Boussinesq eddy-viscosity approximation but relates the turbulence length scale to some typical flow dimension.

First order PDE of turbulent kinetic energy is shown in Equation (1), $\rho U_j \frac{\partial k}{\partial x_j}$ is convection term, $\tau_{ij} \frac{\partial U_i}{\partial x_j}$ is production term, $C_D \rho \frac{k^{3/2}}{l}$ is dissipation term, $\frac{\partial}{\partial x_j}\left[(\mu + \mu_T/\sigma_k) \frac{\partial k}{\partial x_j}\right]$ is viscous and turbulent diffusion term. C_D and σ_k are closure coefficients.

$$\rho \frac{\partial k}{\partial t} + \rho U_j \frac{\partial k}{\partial x_j} = \tau_{ij} \frac{\partial U_i}{\partial x_j} - C_D \rho \frac{k^{3/2}}{l} + \frac{\partial}{\partial x_j}\left[(\mu + \mu_T/\sigma_k) \frac{\partial k}{\partial x_j}\right] \quad \text{Equation (1)}$$

Convection Production Dissipation Viscous and Turbulent Diffusion

The relation between eddy viscosity and turbulent kinetic energy is shown in Equation (2), l is the length scale

$$\mu_T = \rho k^{1/2} l \qquad \text{Equation (2)}$$

Complete form of Equation (1) & (2) in x,y,z directions is shown in Equation (3)

$$\begin{aligned}
&\frac{\partial}{\partial x}\left[\left(\nu + \frac{k^{1/2}l}{\sigma_k}\right)\frac{\partial k}{\partial x}\right] + \frac{\partial}{\partial y}\left[\left(\nu + \frac{k^{1/2}l}{\sigma_k}\right)\frac{\partial k}{\partial y}\right] + \frac{\partial}{\partial z}\left[\left(\nu + \frac{k^{1/2}l}{\sigma_k}\right)\frac{\partial k}{\partial z}\right] - \left(u\frac{\partial k}{\partial x} + v\frac{\partial k}{\partial y} + w\frac{\partial k}{\partial z}\right) - \\
&\left[\frac{2}{3}\left(\frac{\partial u}{\partial x} + \frac{\partial v}{\partial y} + \frac{\partial w}{\partial z}\right) + \frac{C_D k^{1/2}}{l}\right] k + k^{1/2} l \Bigg[2\left(\frac{\partial u}{\partial x}\right)^2 + 2\left(\frac{\partial v}{\partial y}\right)^2 + 2\left(\frac{\partial w}{\partial z}\right)^2 + \left(\frac{\partial u}{\partial y}\right)^2 + \left(\frac{\partial u}{\partial z}\right)^2 + \\
&\left(\frac{\partial v}{\partial x}\right)^2 + \left(\frac{\partial v}{\partial z}\right)^2 + \left(\frac{\partial w}{\partial x}\right)^2 + \left(\frac{\partial w}{\partial y}\right)^2 + 2\frac{\partial u}{\partial y}\frac{\partial v}{\partial x} + 2\frac{\partial u}{\partial z}\frac{\partial w}{\partial x} + 2\frac{\partial v}{\partial z}\frac{\partial w}{\partial y}\Bigg] = 0 \qquad \text{Equation (3)}
\end{aligned}$$

Referring to the general form of second order PDE in Equation (4)

$$\begin{aligned}
&\frac{\partial}{\partial x}\left[K_x(x,y,z)\frac{\partial T}{\partial x}\right] + \frac{\partial}{\partial y}\left[K_y(x,y,z)\frac{\partial T}{\partial y}\right] + \frac{\partial}{\partial z}\left[K_z(x,y,z)\frac{\partial T}{\partial z}\right] + M_x(x,y,z)\frac{\partial T}{\partial x} + \\
&M_y(x,y,z)\frac{\partial T}{\partial y} + M_z(x,y,z)\frac{\partial T}{\partial z} + P(x,y,z)T + Q(x,y,z) = 0 \qquad \text{Equation (4)}
\end{aligned}$$

Let

$$\begin{aligned}
&\nu + \frac{k^{1/2}l}{\sigma_k} = C_1, \frac{2}{3}\left(\frac{\partial u}{\partial x} + \frac{\partial v}{\partial y} + \frac{\partial w}{\partial z}\right) + \frac{C_D k^{1/2}}{l} = C_2, k^{1/2} l \Bigg[2\left(\frac{\partial u}{\partial x}\right)^2 + 2\left(\frac{\partial v}{\partial y}\right)^2 + 2\left(\frac{\partial w}{\partial z}\right)^2 + \\
&\left(\frac{\partial u}{\partial y}\right)^2 + \left(\frac{\partial u}{\partial z}\right)^2 + \left(\frac{\partial v}{\partial x}\right)^2 + \left(\frac{\partial v}{\partial z}\right)^2 + \left(\frac{\partial w}{\partial x}\right)^2 + \left(\frac{\partial w}{\partial y}\right)^2 + 2\frac{\partial u}{\partial y}\frac{\partial v}{\partial x} + 2\frac{\partial u}{\partial z}\frac{\partial w}{\partial x} + 2\frac{\partial v}{\partial z}\frac{\partial w}{\partial y}\Bigg] = C_3
\end{aligned}$$

Then

$$\begin{aligned}
&\iiint \Bigg[\left(\frac{\partial N_i}{\partial x}C_1\frac{\partial k}{\partial x} + \frac{\partial N_i}{\partial y}C_1\frac{\partial k}{\partial y} + \frac{\partial N_i}{\partial z}C_1\frac{\partial k}{\partial z}\right)k_i - \left(N_i u\frac{\partial k}{\partial x} + N_i v\frac{\partial k}{\partial y} + N_i w\frac{\partial k}{\partial z}\right) - N_i C_2 k + \\
&N_i C_3\Bigg] dv = 0 \qquad \text{Equation (5)}
\end{aligned}$$

Coefficient of second derivative solving parameter:

$$[A_{2'}] = [B]^T[C_1][B] \qquad \text{Equation (6)}$$

Coefficient of first derivative solving parameter: $[A_{1'}] = [N]^T[u][B]$ Equation (7)

Coefficient of first order solving parameter:

$$[A_1] = [N]^T[C_2][N] \tag*{Equation (8)}$$

Coefficient of solving parameter:

$$[A] = [A_{2'}] - [A_{1'}] - [A_1] \tag*{Equation (9)}$$

The coefficient of the load vector is shown in Equation (10), $[N_i]$ is shape function, as shown in Equation (15). $[J]$ is Jacobian matrix

$$[B] = [N_i]^T[C_3] \tag*{Equation (10)}$$

$$[A_{2'}] = \begin{bmatrix} \frac{\partial N_1}{\partial x} & \frac{\partial N_1}{\partial y} & \frac{\partial N_1}{\partial z} \\ \vdots & \vdots & \vdots \\ \frac{\partial N_{20}}{\partial x} & \frac{\partial N_{20}}{\partial y} & \frac{\partial N_{20}}{\partial z} \end{bmatrix} \begin{bmatrix} C_1 & & \\ & C_1 & \\ & & C_1 \end{bmatrix} \begin{bmatrix} \frac{\partial N_1}{\partial x} & \cdots & \frac{\partial N_{20}}{\partial x} \\ \frac{\partial N_1}{\partial y} & \cdots & \frac{\partial N_{20}}{\partial y} \\ \frac{\partial N_1}{\partial z} & \cdots & \frac{\partial N_{20}}{\partial z} \end{bmatrix} \tag*{Equation (11)}$$

$$[A_{1'}] = \begin{bmatrix} N_1 \\ \vdots \\ N_{20} \end{bmatrix} [u \quad v \quad w] \begin{bmatrix} \frac{\partial N_1}{\partial x} & \cdots & \frac{\partial N_{20}}{\partial x} \\ \frac{\partial N_1}{\partial y} & \cdots & \frac{\partial N_{20}}{\partial y} \\ \frac{\partial N_1}{\partial z} & \cdots & \frac{\partial N_{20}}{\partial z} \end{bmatrix} \tag*{Equation (12)}$$

$$[A_1] = C_2 \begin{bmatrix} N_1 \\ \vdots \\ N_{20} \end{bmatrix} [N_1 \quad \cdots \quad N_{20}] \tag*{Equation (13)}$$

$$[k_i] = \begin{bmatrix} k_1 \\ \vdots \\ k_{20} \end{bmatrix} \tag*{Equation (14)}$$

$$[N_i] = \begin{bmatrix} N_1 \\ \vdots \\ N_{20} \end{bmatrix} \tag*{Equation (15)}$$

$$[B] = \begin{bmatrix} \frac{\partial N}{\partial x} \\ \frac{\partial N}{\partial y} \\ \frac{\partial N}{\partial z} \end{bmatrix} = [J]^{-1} \begin{bmatrix} \frac{\partial N}{\partial r} \\ \frac{\partial N}{\partial s} \\ \frac{\partial N}{\partial t} \end{bmatrix} = [J]^{-1} \begin{bmatrix} \frac{\partial N_1}{\partial r} & \cdots & \frac{\partial N_{20}}{\partial r} \\ \frac{\partial N_1}{\partial s} & \cdots & \frac{\partial N_{20}}{\partial s} \\ \frac{\partial N_1}{\partial t} & \cdots & \frac{\partial N_{20}}{\partial t} \end{bmatrix} \tag*{Equation (16)}$$